Biophysical characterizations of the periplasmic and cytosolic proteins of a few ABC transporters of *Vibrio cholerae*

Thesis submitted for the Degree of

Doctor of Philosophy (Science)

In

Biotechnology

By

INDRILA SAHA

Post Graduate and Research Department of Biotechnology

St. Xavier's College (Autonomous), Kolkata

Affiliated to the University of Calcutta

2024

Dedicated to My parents, & Late grandparents

Acknowledgement

"Dreams transform into thoughts, and thoughts lead to action," as Dr. A.P.J. Abdul Kalam wisely observed. Completing this Ph.D. thesis has been a challenging yet immensely rewarding journey, and it would not have been possible without the support, guidance, and encouragement of numerous individuals. Words fall short in expressing my deep gratitude to the Almighty for guiding me to this significant milestone in my academic career.

First and foremost, it is a genuine pleasure to extend my heartfelt thanks to Dr. Jhimli Dasgupta for guiding me with her valuable expertise and suggestions. This work would not have been possible without her direction, motivation, and invaluable advice. My immense gratitude goes to ma'am, who has not only allowed me to learn from her but has also ensured that I leave the lab with far more knowledge and scientific integrity than I began with. Her continuous support, motivation, and deep knowledge in the field of structural biology have made my journey not just achievable but truly accomplished. It is only due to her support and guidance that I have been able to successfully complete my Ph.D., and I am truly grateful for your mentorship.

I am extremely grateful to Dr. Biplab Ghosh, Scientific Officer at RRCAT, Indore. His expert advice and invaluable assistance have been pivotal throughout my research. His guidance in the collection of crystallization data and introduction to the world of MD simulation have significantly shaped my understanding and skills in this area. The knowledge I have gained is largely due to his mentorship. Furthermore, I deeply appreciate his friendly and supportive demeanor, which has made my research journey all the more rewarding. Thank you sir for your suggestions, encouragement and guidance.

I am profoundly grateful to Prof. Udayaditya Sen of the Saha Institute of Nuclear Physics (SINP), Kolkata, for his unwavering support and assistance with any chemical or instrumental needs at any time. His methodical approach to analysing experiments and his systematic interpretation of results not only provided essential guidance but also offered significant encouragement throughout my research.

I am grateful to Rev. Dr. Dominic Savio, SJ, Principal of St. Xavier's College, Kolkata, for granting me the permission and providing the facilities to conduct my doctoral research here. I would also like to extend my thanks to Ronita Ma'am, Sayak sir, Chandana Ma'am, Uma Ma'am, Sudipa Ma'am, Dipankar Sir, Aniruddha Sir, Aryadeep Sir, Souvik Sir, and Priyanka Ma'am, Ditipriya Ma'am, the esteemed faculty members of the Post Graduate Department of Biotechnology, for their guidance and encouragement. Additionally, I am thankful to at the Central Research Facility (CRF), and Central Research Facility (CIF) of St. Xavier's College, Kolkata.

I am very grateful and blessed to have had Dr. Shrestha Chakraborty as my lab colleague and dear friend. Whether it was for experimental help, navigating tough times, or sharing her knowledge about our field, she has been an unwavering source of support. Beyond the lab, we have enjoyed many memorable moments together, enriching our experiences and strengthening our bond. Now she has become family to me. May your journey ahead, be filled with success, fulfilment, and new opportunities. I am also thankful to my lab colleague and friend Peeali Mukherjee for her invaluable support and assistance throughout my journey. We always enjoyed spending time together at chai pe charcha, where we shared both professional and personal insights. Her help has been greatly appreciated, and I wish her all the best for her future endeavours.

I would also like to acknowledge the support and camaraderie of my lab juniors, Ruchira and Arnab. Their enthusiasm and persistent dedication have made the lab environment vibrant and enjoyable. I have no doubt that their passion for research will lead them to great success.

Additionally, I extend my thanks to the wonderful group of seniors, my colleagues and fellow researchers who have enriched my Ph.D. experience: Sreeparna Di, Arnab Da, Senjuti Di, Shehnaz Di, Anagh Da, Sourabh Da, Sonia Di, Aheli Di, Pooja Di, Preeti, Anirban, Indira, Drishti, Saptarshi, Priyabrata, Swarnavo, Sushmita, and Aparajita. Their support and friendship have been invaluable. I am also grateful to the interns who worked under my supervision: Ananya, Anik, Tuhina. Their cooperation and hard work have greatly contributed to the research. Thank you all for making my Ph.D. journey a memorable and fulfilling experience.

I would also like to extend my gratitude to the lab members of Udayaditya Sir's lab for their invaluable support. Dr. Kamalendu Pal and Dr. Tulika Chakraborty have been exceptionally helpful whenever I have conducted experiments in their lab. Additionally, I am thankful to the staff members of our department, Abhijit Da, Bidesh Da, Rajkumar Da for their support and cooperation.

I am deeply grateful to the UGC-DAE-CSR fellowship, Swami Vivekananda Merit-cum-Means Scholarship and CSIR-SRF fellowship for their financial support. Their assistance has been crucial in enabling me to focus on my research.

I would also like to mention a special person, my most supportive friend who has now become my husband, Sandipan. He has been my constant strength, helping me navigate through all the difficult situations. Thank you, Sandipan, for being my rock and steadfast supporter, for enduring my temper, and for making me smile even on the toughest days. Your love, and belief in me throughout my Ph.D. journey have been a tremendous source of strength and inspiration.

This thesis is the result of collective efforts and I am deeply appreciative of the contributions from everyone who has been a part of this journey. Thank you all for your invaluable support.

~Indrila

Content

Abbreviations

ABC	ATP-binding cassette
PBP	Periplasmic binding protein
TMD	Transmembrane domain
NBD	Nucleotide binding domain
OF	Outward Facing
IF	Inward Facing
Occ	Occluded
ECF	Energy Coupling Factor
CT	Cholera toxin
AMP.PNP	Adenosine 5'-(β,γ-imino) triphosphate
PCR	Polymerase Chain Reaction
IPTG	Isopropyl β-D-1-thiogalactopyranoside
SDS-PAGE	Sodium dodecyl sulfate-Polyacrylamide gel electrophoresis
SD	Standard deviation
K_d	Dissociation constant
PDB	Protein Data Bank
MD	Molecular Dynamics
RMSD	Root Mean Square Deviation
RMSF	Root Mean Square Fluctuation
DMPC	Dimyristoylphosphatidylcholine
DMSO	Dimethyl sulfoxide
PpIX	Protoporphyrin IX
MR	Molecular Replacement
PEG	Polyethylene glycol
SEC	Size exclusion chromatography
ITC	Isothermal titration calorimetry

List of Tables

List of Figures

Figure 3.3: **ATP binding by HutD.** (a,b) Fluorescence quenching demonstrated significant change in fluorescence upon AMP.PNP binding to HutD; (λ_{exc} = 280 nm, λ_{em} = 295–400 nm) with slit widths of 5 nm for both excitation and emission Plots of $\Delta F/\Delta F_{max}$ against ligand AMP.PNP (μM) obtained a K_d value of 94±0.024 μM; (c) Slope of the *straight line* indicates 1:1 binding stoichiometry between HutD and AMP.PNP.

Figure 3.4: **ATP hydrolysis by HutD.** (a) The release of inorganic phosphate (*Pi*) was estimated against the standard curve of KH_2PO_4; (b) Significant ATP hydrolysis of HutD were observed in Malachite green assay; (c) Reaction velocity of HutD were plotted against ATP concentrations (μM) as per Michaelis-Menten equation with 'One site-specific binding' model. Error bars in, (b) and (c) are SD values obtained from at least three replicates.

Figure 3.5: **Identification of functionally crucial residues of HutD by mutagenesis.** (a) Loss of function of the mutants R18A, K44A, D166A, E167A compared to HutD, as evident from the measurement of ATPase activities with 100 μM and 500μM ATP at three time points (1,3,5 minutes); (b) ATPase activities of HutD and mutants measured with an extended incubation time of 20 minutes with 100μM and 500μM of ATP.

Figure 4.1: **Sequence analysis of HutC and HutD.** (a) Sequence alignment of HutC from *Vibrio cholerae*, HmuU from *Yersinia pestis* and BhuU from *Burkholderia cenocepacia*. Numbering is based on HutC sequence. (b) Sequence alignment of HutD from *Vibrio cholerae*, HmuV from *Yersinia pestis* and BhuV from *Burkholderia cenocepacia*. Numbering is based on HutD sequence. Important motifs and conserved residues are individually coloured/marked. Semi-conservation inside important motifs are shaded in grey. Some important residues are marked with '*'.

Figure 4.2: **Models of HutD, HutC in different states and lipid embedded assembly.** Ribbon representation of the models of (a) HutD dimer in the OF state, Nucleotide-binding domains (NBDs, dimer of HutD) are shown in brown and cyan, conserved Walker-A motif or P-Loop is shown in magenta of each NBD. Two ATP molecules are shown in stick; (b) HutD dimer in the IF state; (c) Zoomed view of the docking of Mg^{2+}-ATP in HutD OF dimer and related interactions; (d) Mg^{2+}-ATP bound HutCD dimeric assembly in the OF state; Zoomed view of different regions of HutCD are shown in e-g. (e) Interactions between L-loop of HutC1(salmon) with Q-loop of HutD1 (magenta); (f) Disposition of binding motifs such as A-loop, Walker-A (green), Walker-B (maroon) around Mg^{2+}-ATP. ABC signature motif is shown in cyan; (g) Arrangements of transmembrane helices in HutCD-OF model is shown from the periplasmic side. TM5 helices of each TMD is

shown in green, H5a in yellow; (h) Model of HutCD assembly in IF state; (i) Model of HutCD assembly embedded in solvated DMPC lipid bilayer.

Figure 5.1: **MD simulation parameters of building lipid-protein system.** (a) Time averaged electron density profile of the DMPC bilayer extracted from the heme bound simulation. Both the leaflets of the bilayer were intact and maintained the bilayer thickness during the course of dynamics; (b) The time evolution of the average area per lipid molecule is plotted. Fluctuations of the average lipid area about a mean value indicate convergence and stability of the bilayer during the course of simulation.

Figure 5.2: **MD simulation results of HutD in the OF state.** (a,b) Cα-RMSD values of HutD1 and HutD2 as part of HutD dimers and as part of HutCD assemblies in the IF and OF states; (c,d) B-factors of HutD1 and HutD2 as part of HutD dimers and as part of HutCD assemblies in the IF and OF states.

Figure 5.3: **MD simulation results of HutD in the OF state.** (a) ATP binding in HutD OF at 200 ns showing involvement of the residues of A-loop, Walker-A and Walker-B motifs; (b) Interaction between D-loops of two HutD monomers at 108 ns of simulation run on HutD dimer in the OF state; (c) Disposition of H200 at 150 ns of the simulation run on HutD dimer in the OF state.

Figure 5.4: **MD simulation showed OF to IF transition in HutCD.** (a,b) Cα-RMSD values of HutC1 and HutC2 as part of HutCD assemblies in IF and OF states; (c) Superposition of snapshots showing overall movement in HutCD OF state. PLBP binding site using an arrow.

Figure 5.5: **Synchronised conformation shift observed HutCD OF state.** (a) Superposition of snapshots showing proximity between L-loop (cyan) of HutC and Q-loop (pink) of HutD during dynamics; (b) Snapshot of 150 ns shows interaction of F151 of HutC with ATP and Y15 of A-loop of HutD that causes cytoplasmic gate opening.

Figure 5.6: **MD simulation results of HutCD in the OF state.** (a) TM5 helices (green) of HutCD OF at the beginning of MD run; (b) Zoomed view of TM5 helices (green) and H5a (yellow) of the beginning frame from periplasmic side; (c) Superposition of snapshots of HutCD OF starting frame (green) and 150 ns (magenta) shows increased inter TM5-TM5 distance at leading to cytoplasmic gate opening.

Figure 5.7: **IF state of HutCD culminated to occluded state.** (a) Ribbon representation of HutCD-IF model at 1 ns, showing axes of H5A(Yellow), and TM5(green), of each TMD in HutC dimer. (b) HutCD IF turned to

to the inter-dimeric pocket. Formation of occluded state constricts the pocket and releases heme.

Figure 8: Type-I G6P VCA0625-27 ABC transporters of *Vibrio cholerae*.

Figure 9.1: **Cloning, Overexpression and purification profile of VCA0625.** (a) 1% Agarose gel showing the band of PCR product of VCA0625; (b) 12% SDS PAGE profile of induced and uninduced VCA0625 expressing BL21(DE3) cells; (left) I: Induced cells, U: uninduced cells; M: Marker (right); (c) 12% SDS PAGE showing purification profile of VCA0625 (Lane 1: Marker, Lane 2-8: 10 – 150 mM imidazole gradient); (d) 12% SDS PAGE showing concentrated VCA0625 (Lane 1: Marker, Lane 2-3: 2µl and 4µl of concentrated protein.

Figure 9.2: **Crystallization and diffraction data collection profile of VCA0625**. (a) Crystals of PLBP VCA0625;(b) X-ray diffraction image of VCA0625 crystals; the crystal diffracts to a highest resolution of 1.6 Å.

Figure 9.3: **Structure determination of VCA0625.** (a)$2F_0$-Fc density map (contoured at 1σ) around G6P bound to VCA0625; (b) Ribbon diagrams of VCA0625 complexed with β-G6P.

Figure 9.4: **Interactions profile of VCA0625.** (a) Crystal structure of Holo-VCA0625; (b) Ligand binding region in solved crystal structure of VCA0625; (c) Superposition of G6P bound AfuA structure (PDB code: 4R73) (gray) on VCA0625 (gold). G6P is shown in ball and stick.

Figure 10.1: **MD simulation results of VCA0625 in free and G6P bound state.** (a) Plot of the RMSD values for the Cα atoms are shown for apo-VCA0625 (blue) and holo-VCA0625 (green) up to 1µs simulation range. (b) RMSF of the Cα atoms was calculated from the simulation trajectories.

Figure 10.2: **VCA0625 execute both 'open to close' and swinging motions**. (a–b) Superposition of the snapshots of overall MD trajectories (a) in apo VCA0625 and (b) holo VCA0625; (c–d) Snapshots aligned with respect to the N-lobe to shows the inter-domain movement for apo VCA0625 in (c) and G6P bound VCA0625 in (d); (e–f) Movement of R34 side chain during simulation in apo and G6P bound VCA0625.

Figure 11.1: 10% SDS PAGE showing concentrated 4µl of VCA0625 and its mutants after removal of G6P from proteins through partial denaturation.

Figure 11.2: **Binding affinity studies by ITC**. (a) VCA0625 showed significant binding with G6P resulting a K_d value of 17.45 ± 0.45 µM; (b,c) Thermograms of R34A, Y103A indicated insignificant interaction.

Figure 12.1: **Cloning, Overexpression and purification profile of VCA0627.** (a) 1% Agarose gel showing the band of PCR product of VCA0627; (b) 10% SDS PAGE showing purification profile of VCA0627 (Lane 1-9: 10–250 mM imidazole gradient); (c) 10% SDS PAGE showing concentrated VCA0627 (Lane 1, 2: 2µl and 4µl of concentrated protein).

Figure 12.2: **Bioinformatic analysis of VCA0627.** (a) Consensus sequence logo generated (using Skylign followed by ClustalW alignment) from VCA0627 of *V. cholerae* and nearest structural homologs; (b) The overall superposition of CysA, PH0022, MalK, on model of VCA0627, whereas substantial similarities were observed between regulatory domains of PH0022 and VCA0627 (right panel).

Figure 12.3: **ATP binds to VCA0627.** (a) Fluorescence quenching demonstrated significant change in fluorescence upon AMP.PNP binding to VCA0627; (λ_{exc}=280 nm, λ_{em} =295–400 nm) with slit widths of 5 nm for both excitation and emission; (b) Plots of $\Delta F/\Delta F_{max}$ against ligand AMP.PNP (µM) obtained a K_d value of 140±0.043 µM.

Figure 12.4: The ATPase domain VCA0627 showed negligible ATPase activities in Malachite green assay even with an elevation of ATP concentration to 0.5mM.

Figure 12.5: **Bioinformatic studies on VCA0626.** (a,b) The models of VCA0626 and VCA0626-27 assembly. Arrangements of transmembrane helices in atypical VCA0626 model is shown from the periplasmic side in (a); (c) Multiple sequence alignment of VCA0626 and similar transmembrane proteins of 27 gram-negative bacteria showed strict sequence conservation. Residue numbering is as per VCA0626 of *V. cholerae.*

Figure 13: G6P importing type-I ABC transporter VCA0625-27 of *Vibrio cholerae*.

SUMMARY

Essential nutrients like iron, vitamin B12, and sugar-phosphate are crucial for the growth and survival of *Vibrio cholerae*, the etiological agent of cholera. ABC transporters actively move these nutrients across the plasma membrane. This process involves cognate periplasmic binding proteins (PBPs) that specifically bind the nutrients, while ATP hydrolysis by the cytosolic ATPase subunit supplies the energy needed to transport the ligands through the transmembrane components into the cytosol. This study explores the mechanisms of two distinct ABC importers in *V. cholerae*: the type-I G6P VCA0625-27 transporter and the type-II heme HutCD-B transporter.

Heme internalization is crucial for the survival of many bacteria, including *Vibrio cholerae*, as the host limits iron availability as a strategy to combat pathogenic invasion. Understanding the mechanism of heme transport by HutCD-B, therefore, can provide valuable insights into developing antimicrobial strategies. Although the structure of the PBP HutB has previously solved, the mechanism of heme transport through HutCD remained unclear. We have performed biochemical studies on ATPase HutD and its mutants, along with molecular modeling, docking and unbiased all-atom MD simulations on lipid-solvated models of permease-ATPase complex HutCD. The results demonstrated mechanisms of ATP binding/hydrolysis and trapped transient and global conformational changes in HutCD, necessary for heme internalization. ATPase HutD forms a dimer, independent of the permease HutC. Each HutD monomer canonically binds ATP in a 1:1 stoichiometry. MD simulations demonstrated that a rotational motion of HutC dimer occurs synchronously with the inter-dimeric D-loop interactions of HutDs. F151 of TM4-TM5 loop of HutC, packs with ATP and Y15 of HutD, initiating ‘cytoplasmic gate opening’ which mimics an ‘outward-facing’ to ‘inward-facing’ conformational switching upon ATP hydrolysis. The simulation on ‘inward-facing’ HutCD culminates to an ‘occluded’ state. The simulation on heme-docked HutCD indicated that the event of heme release occurs in ATP-free ‘inward-facing’ state. For the first time, this study explores the heme release mechanism in *V. cholerae*, uncovering new insights into its heme internalization process. Simulation studies revealed that heme release is primarily driven by interactions between the propionate groups and polar residues in the HutC–HutD dimeric pocket. Analysis of simulation data predicted interactions between heme and NBD HutD residues, such as the D-loop, Walker-A, Q-loop, and the 'ABC signature motif,' which was later confirmed through several biochemical results. We have also observed that heme

binding inhibits ATP hydrolysis by HutD while binding of ATP itself was less compromised. This confirmed that during internalization heme engages the residues required for ATP hydrolysis. Therefore, heme release to cytosol presumably takes place in ATP free state of HutD. Interestingly, the key residues involved in heme and ATP interactions were found to be conserved across NBDs in various gram-negative bacteria, indicating a shared mechanism for heme transport.

Sugar phosphates are potential sources of carbon and phosphate for bacteria, especially in phosphate-limiting condition in aquatic environment. Despite that, the process of G6P internalization through plasma membrane remained elusive in several bacteria. VCA0625-27, made of PBP VCA0625, an atypical monomeric permease VCA0626, and cytosolic ATPase VCA0627, recently emerged as hexose-6-phosphate uptake system of *Vibrio cholerae*. Here we report high resolution crystal structure of VCA0625 in G6P bound state. High-resolution crystal structures of VCA0625, combined with MD simulations, on VCA0625 in apo and G6P bound states unravelled an 'open to close' and swinging bi-lobal motions, which are diminished upon G6P binding. Site-directed mutagenesis and isothermal titration calorimetry provided further details on residue roles in ligand binding. Mutagenesis followed by biochemical assays on VCA0625 underscored that R34 works as gateway to bind G6P. Biochemical assays on the NBD VCA0627 showed that it binds ATP but is ATPase-deficient when not associated with VCA0625 and VCA0626. These features are indicative of a type-I ABC importer. Furthermore, modeling, docking and systematic sequence analysis allowed us to envisage the existence of similar atypical type-I G6P importer with fused monomeric permease in 27 other gram-negative bacteria. Overall, our studies on two ABC transporter systems VCA0625-27 and HutCD-B helps us to elucidate the mechanistic insights of G6P and heme internalization for gram negative pathogenic bacteria.

Chapter 1

INTRODUCTION

1.1 Nutrient uptake in pathogenic bacteria

Bacteria require various chemicals and elements of the environment which are referred to as nutrients or nutritional requirement including of C, H, O, N, S. P, K, Mg, Fe, Ca, Mn, Zn, Co, Cu, and Mo. These elements are acquired from water, inorganic ions, small molecules and macromolecules. Beside this, pathogenic bacteria require important micronutrients like iron, sugar-phosphate, vitamins, manganese, calcium for their growth. To accomplish such requirements, bacteria have developed various transport mechanisms to uptake these nutrients from their surroundings. The mechanism includes passive diffusion, facilitated diffusion and active transport mechanism (1-2). Active transport, where ATP hydrolysis driven energy is utilized to move molecules against their concentration gradients, is essential for acquiring nutrients that are present at lower concentrations outside the cell compared to inside. In general, nutrient uptake in bacteria is governed by a variety of transport mechanisms and regulatory strategies to ensure the survival and growth of bacterial cells in their respective environments. The ability of bacteria to effectively persist and procure essential nutrients from their environment holds significant epidemiological implications, yet remains not well understood.

Pathogenic bacteria have developed various mechanisms to acquire nutrients from their hosts, aiding their survival and proliferation within the host environment (Fig.1.1). Example are as follows: (i) Iron is essential for bacterial growth but tightly regulated and restricted in the host environment. Pathogens use siderophores to scavenge iron from host proteins like transferrin and lactoferrin (3); (ii) Some bacteria also extract iron-bound heme from haemoglobin, aiding survival in iron-limited environments (4); (iii) Bacteria consume host derived metabolites like sugars, amino acids, and nucleotides, utilizing specialized transporters and enzymes for efficient nutrient uptake (5); (iv) Certain virulence factors produced by these bacteria can serve as nutrient sources, like toxins and enzymes degrade host tissues, releasing nutrients for bacterial assimilation (6); (v) Bacteria may metabolize host lipids such as fatty acids and cholesterol, providing alternative carbon sources for energy and growth (7); (vi) Pathogens adapt to varying nutrient availability in the host by employing regulatory systems that facilitate switching between metabolic pathways, optimizing nutrient utilization (8); (vii) During chronic conditions, bacteria form biofilms—protective communities embedded in extracellular substances. These biofilms create microenvironments that retain and recycle nutrients, significantly enhancing bacterial survival within the host (9).

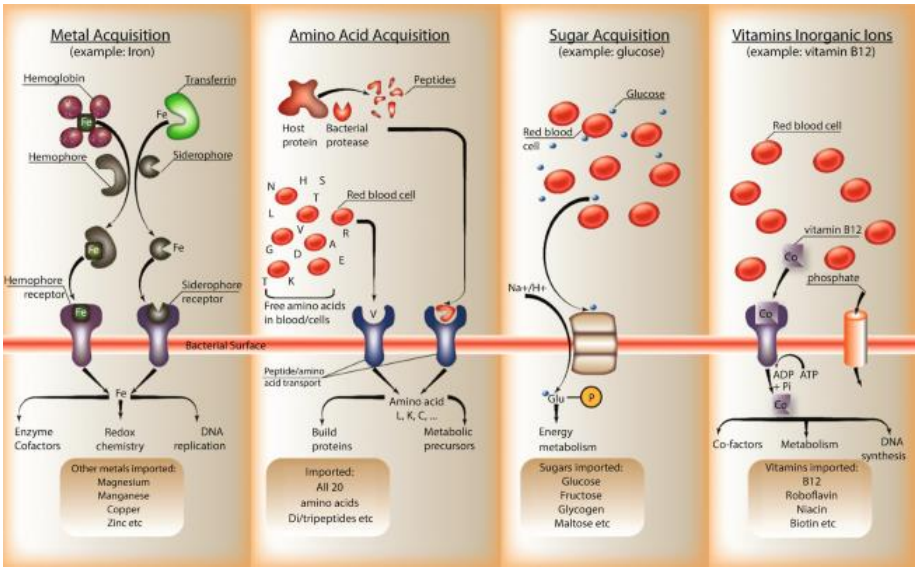

Figure 1.1: Pathogenic bacteria employ various approaches to acquire and consume nutrients from their host (10).

1.2 Transport of the essential nutrients

The selective permeability of nutrients across cell membranes, a fundamental characteristic of living cells, is facilitated by transport proteins known as permeases. These proteins can be categorized into four types: (i) passive channels that aid in transport along a concentration gradient (more prevalent in eukaryotes) (11), (ii) primary active transporters utilizing ATP as a direct energy source (12), (iii) secondary active transporters that rely on ion gradients (like sodium or proton motive force) as an indirect energy source (12) and (iv) group translocators that chemically alter their substrates during transport (2).

1.3 Different transport mechanism in Gram negative bacteria

Gram-negative bacteria utilize diverse mechanisms for nutrient acquisition, including diffusion of small molecules like oxygen and sugars through channels in the outer membrane, active transport powered by ATP hydrolysis, group translocation for phosphorylating sugars, siderophore-mediated iron uptake via specific receptors, and specialized transport systems for vitamins, cofactors, lipids, and lipopolysaccharides essential for cellular function and adaptation to various environments (13).

Specific outer membrane receptors for siderophores, heme, and vitamin B12 have been identified in gram-negative bacteria (13). These substrates are transported across the outer membrane facilitated by an energy-dependent mechanism involving the TonB, ExbB, and ExbD proteins embedded in the cytoplasmic membrane (14). These proteins assemble into the

Ton complex, which harnesses the proton motive force of the cytoplasmic membrane (15, 16) to energise receptor-mediated transport of the substrates. This process may involve direct binding to specific outer membrane receptors or the involvement of bacterial homophors that capture heme from host carriers and deliver it to TonB-dependent outer membrane receptors (17).

1.4 ABC transporter

The ABC (ATP binding cassette) transporter superfamilies are ubiquitous integral membrane proteins, and stand as one of the most extensive groups within transport proteins. ABC transporters are widely found across all domains of life: archaea, bacteria, and eukaryotes (18, 19) (Fig.1.2). These proteins are important clinically and economically and their dysfunction leads to a number of human genetic diseases, and the ability of some to pump cytotoxic molecules from cells confers resistance to antibiotics, herbicides and chemotherapeutic drugs (19). Several ABC transporters have been identified as pivotal virulence factors in pathogenic species (Fig. 1.2). This further suggests that these microorganisms cannot thrive in the host environment unless they secure specific nutrients. Overall, ABC transporters are crucial for bacterial survival and adaptation to various environmental conditions by enabling efficient uptake of essential nutrients and maintaining cellular homeostasis. Their importance is underscored by their conservation and diverse roles in bacterial physiology and pathogenesis. Inclusively, the combination of specificity, accessibility, conservation, and potential to overcome resistance makes ABC transporters attractive targets for drug development aimed at combating bacterial infections (18).

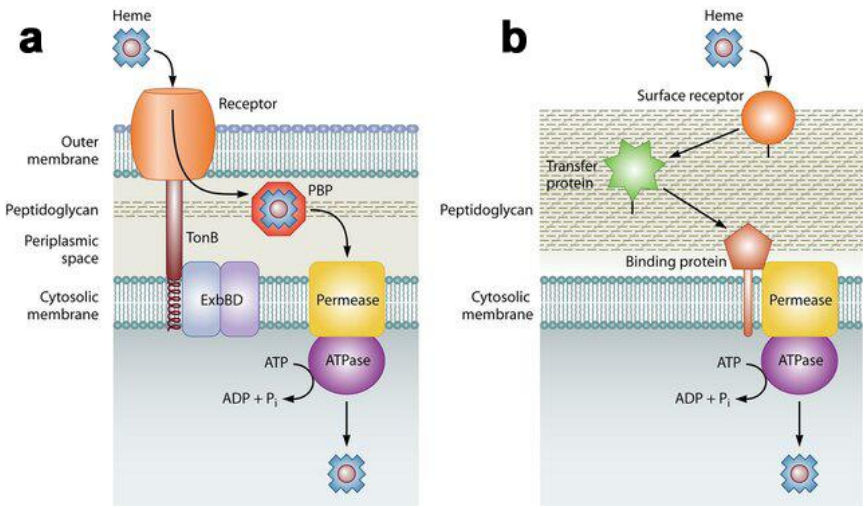

Figure 1.2: Schematic of bacterial ABC transport system of (a) Gram-positive (b) Gram-negative bacteria (20).

1.4.1 Structural Diversity of ABC transporters

ABC transporters typically comprise of two cytoplasmic nucleotide-binding domains (NBDs) that function as an ATP-driven motor, along with two transmembrane domains (TMDs) that create a conduit for substrates (Fig. 1.3). The NBDs are usually well conserved across different types of ABC transporters, whereas the TMDs exhibit considerable diversity in structure and composition. Each NBD features classical nucleotide-binding motifs such as Walker A and B, alongside a characteristic LSGGQ signature motif that is indicative of ABC ATPases (21). Additionally, the NBDs contain a Q loop which plays a crucial role in facilitating interactions between the TMDs and the NBDs within ABC transporters (22). ABC transporters are majorly classified into two classes as importers and exporters depending on the direction of substrate transport (Fig. 1.3). ABC importers facilitate the uptake of nutrients in prokaryotes and archaea, whereas ABC exporters are responsible for removing unwanted cytoplasmic substances like drugs and lipids in organisms ranging from bacteria to humans. So that, ABC importers represent promising targets for drug development because they are predominantly found in bacteria and are accessible without penetrating the cytoplasmic membrane (23).

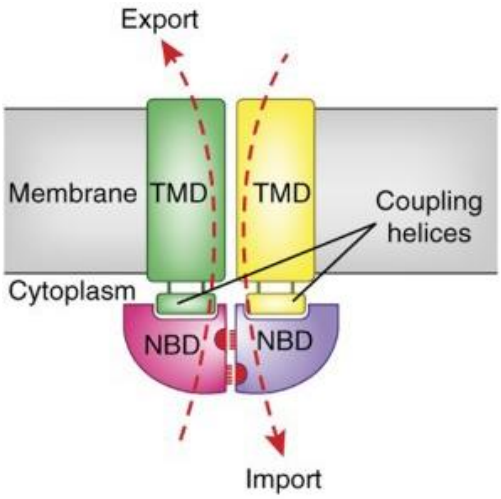

Figure 1.3: Overview of the general structure of ABC transporters family (24).

1.4.1.1 Diversity within ABC importers

ABC importers are a diverse group of membrane transport proteins primarily found in prokaryotes and archaea. They utilize ATP hydrolysis driven energy to transport a wide range of substrates across cellular membranes, playing crucial roles in nutrient uptake and cellular homeostasis. The functionality of most ABC importers necessitates an additional Periplasmic Binding Protein (PBP) for efficient substrate recognition and transport. Structural and

biochemical studies have led to the classification of different types of ABC importers: type-I, type-II and energy coupling factor (ECF) importers (also named type-III importers) (Fig. 1.4). All three types of ABC importers are found only in the prokaryotes (25).

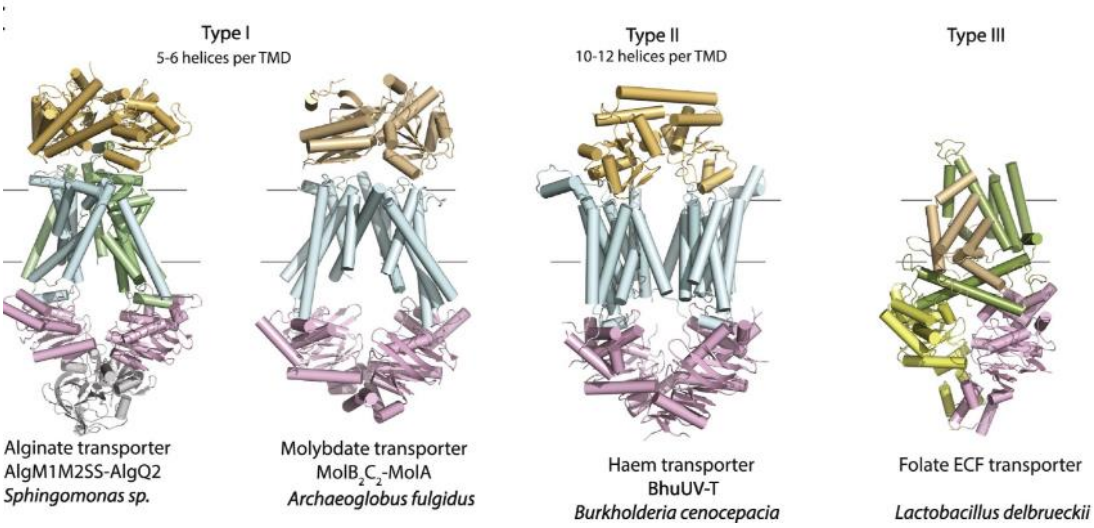

Figure 1.4: ABC transporter assembly for type-I, II and III importers (26).

- **Type-I ABC importers** primarily import a wide range of substrates such as amino acids, peptides, sugars, ions and compatible solutes into the cell (27). Typically, type-I importers exhibit 5-8 TM helices in each TMD subunit and facilitate the translocation of small molecules. In type-I systems, the interaction between the PBP and the transporter is transient and characterized by low affinity, as seen in the cases of Mal (28), His (29), Met (30), Opp (31), and Mod (32). Conversely, type-II systems such as FhuBC-D, BtuCD-F, HmuUV-T form stable, high-affinity complexes (ranging from nanomolar to picomolar) with their PBPs, demonstrating a much stable and more enduring interaction (33-35). In the absence of PBPs, type-I transporters exhibit minimal ATPase activity, but this activity is significantly enhanced upon binding of PBPs loaded with ligands (36). Unlike the NBDs, TMDs do not exhibit significant sequence conservation but maintain a similar topology within their transporter class. The variability in TMD sequences reflects the diverse substrates they transport. Despite variations in the number of TMD helices in type-I importers, they all utilize the ‘alternating access’ mechanism to transport substrates. The reorientation of the TMDs from an IF to an OF conformation involves significant rigid body conformational changes, which aligns with the "alternating access" mechanism. The maltose transporter $MalFGK_2$, a well-studied type-I system, provides a clear example of this transport mechanism (37). Additionally, some type-I importers possess a regulatory domain (RD) attached to the highly conserved NBDs, which regulate their function.

Structures of other type-I ABC importers, such as ModBC from *Archaeoglobus fulgidus* (38) and MetNI (39), have validated this mechanism by showing the transporters in a resting state, with substrate-loaded PBP but without nucleotide. Additionally, the structure of MaModBC (40) reveals a trans-inhibited state with tungstate ions bound to the RD of the ModC NBD dimer. Furthermore, different arrangements of TMDs (homodimeric or heterodimeric) allow type-I ABC importers to adopt different substrate specificities and transport requirements. The structural diversity of TMD configurations contributes to the functional versatility of these transporters (37).

- **Type-II ABC importers** primarily import trace non-metabolites such as iron-siderophore complexes, heme and vitamin B12 etc (33-35, 41). Type-II transporters differ from type-I in several aspects. They typically possess 10-12 TM helices of each monomer compared to type-I (38, 42), with specific core helices undergoing distinct conformational changes for substrate transport (37, 43). These core helices are crucial for regulating access to the translocation pathway and play a central role in the transport mechanism. Additionally, type-II often exhibits weak association with PBP due to the presence of the substrate in the substrate binding groove of the PBP (44, 45). Despite sharing common characteristics, there is increasing evidence of mechanistic variability within the type-II sub-family (37). The diversity in substrate size, ranging from molybdate to vitamin B12, may contribute to the observed differences among type-II transporters. The conformational decoupling observed in type-II importers, implies that these systems are capable of undergoing at least two separate catalytic cycles of ATP hydrolysis. In the uncoupled cycle, where the PBP is not present, the NBDs undergo opening and closing, resulting in ATP hydrolysis. However, this activity does not influence the TMD gates. Conversely, during the complete catalytic cycle, when the substrate is present, the NBDs continue to open and close, but those movements also affect the TMD gates. Considering their overall structure and transport mechanism, well-studied type-II ABC importers include: the BtuCD vitamin B12 importer (44) and iron-siderophore importer FhuBCD from *Escherichia coli* (35), the heme importers HmuUV from *Y. pestis* (33) and BhuUV from *Burkholderia cenocepacia* (46). The structures and mechanisms of type-II transporters have become increasingly diverse. A major area of uncertainty for type-II transporters is their regulation. As research into the type-II subfamily progresses, further diversity is likely to be uncovered.

- **Type-III ABC importers** play a vital role in the uptake of micronutrients by bacteria and archaea. ECF transporters, similar to type-I and II transporters, include two nucleotide-

binding domains (EcfA and EcfA0), a transmembrane coupling domain (EcfT), and a distinct substrate-binding component called EcfS. Unlike type-I and II ABC importers, which use a substrate-binding protein to guide compounds to the translocation pathway, ECF transporters specifically depend on EcfS (47). This integral membrane protein exhibits high-affinity substrate binding in the nanomolar range (48). Some structurally characterised type-III transporters include riboflavin importing RibU from *S. aureus* (48), thiamine and biotin importing ThiT and BioY from *L. lactis* and folate transporter from *L. delbrueckii* (37).

1.4.1.2 Different states acquired by ABC importers during nutrient translocation

ABC transporters undergo conformational changes as they transition through various states during their transport cycle (Fig. 1.5). These states include (23, 49):

Inward Facing (IF) state: In this state, the substrate-binding site of the transporter is accessible from the inside of the cell or the cytoplasmic side of the membrane providing an open pathway for substrate translocation into the cytoplasm. This state is crucial for substrate binding and initial steps of transport.

Outward Facing (OF) state: In this state, the substrate-binding site is oriented outward towards the extracellular environment or the periplasm in prokaryotes. Consequently, the translocation pathway is directed towards the opposite side of the membrane. This conformation enables substrate release or interaction with periplasmic binding proteins.

ATP hydrolysis transition state: where the NBD dimer is in a closed conformation for hydrolysis, and the TMDs have repositioned to accept substrate from the binding protein.

Occluded State (OCC) state: A conformational transition from IF to OF conformation occurs via an occluded (OC) state, leading to the release of the substrate to the outside. This state is characterized by the absence of substrate or nucleotide binding and may coexist in equilibrium with other conformations.

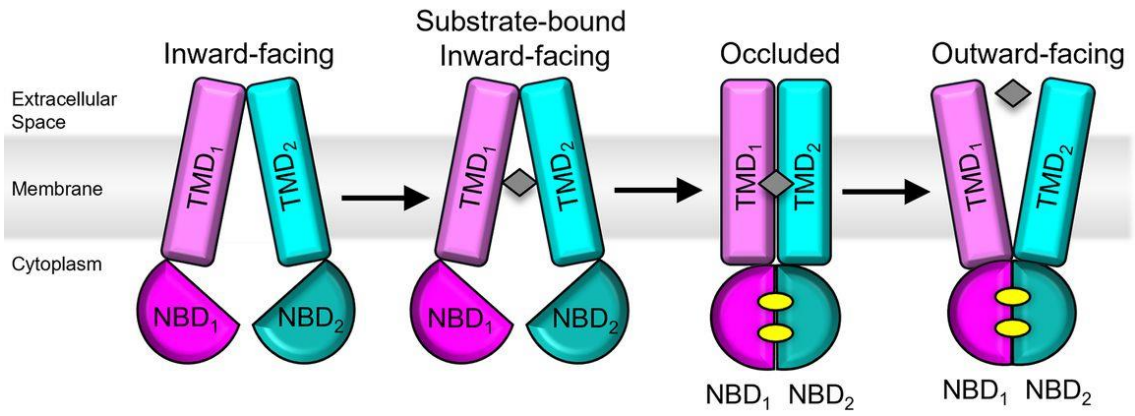

Figure 1.5: ABC importer in different conformation states (50).

1.5 *V. cholerae*, and human disease cholera

Cholera, a severe and potentially life-threatening diarrheal disease, is caused by *Vibrio cholerae,* a curved, rod-shaped Gram-negative bacterium. This highly motile organism moves via a single, polar sheathed flagellum and typically infects humans through contaminated food or water sources. In its natural aquatic habitat, *V. cholerae* faces various environmental stresses like nutrient scarcity, temperature extremes, and oxidative conditions. To cope with these challenges, the bacterium has evolved diverse survival strategies, including the formation of biofilms, which enhance its resilience in aquatic environments (51). *V. cholerae* utilizes its fast-swimming polar flagellum as a screw-like propeller to navigate in water (51). Once inside the human body, bacterium withstands the acidic environment of the stomach and reaches the nutrient-rich small intestine. Using its polar flagellum, *V. cholerae* penetrates the mucus lining of the intestine and adheres to the epithelial cells on its surface (52). Successful colonization requires the expression of the toxin co-regulated pilus (TCP), which serves as the primary adhesion factor (53). The cholera toxin (CTX), is the primary virulence factor found in toxigenic strains of *V. cholerae*. It is comprising of the catalytic A subunit (CTX-A) and the pentameric receptor-binding B subunit (CTX-B) (54**).** These subunits are encoded by the ctxA and ctxB genes, which reside in the filamentous bacteriophage CTXϕ (54). CTX coordinated with TCP expression, triggers host epithelial cells to produce adenylate cyclase, resulting in the secretion of large volumes of watery diarrhoea (55, 56). Within the host, *V. cholerae* replicates, releases CTX and induces disease symptoms. Eventually, the bacteria detach and exit the host via the profuse diarrhoea, characteristic of cholera. Reflecting its dependency on iron, *V. cholerae* encodes numerous iron transport systems (57, 58), underscoring the importance of iron acquisition for its pathogenicity. In summary, *V. cholerae*'s adaptation to

environmental stresses and its sophisticated strategies for host colonization and toxin production contribute to the severity and persistence of cholera as a global health concern.

1.6 ABC importers of *V. cholerae*

Transporting nutrients through the periplasm and across the inner membrane in *V. cholerae* requires a periplasmic binding protein-dependent ATP-binding cassette (ABC) transport system. As for example, in *V. cholerae*, siderophores, including the hydroxamate siderophore ferrichrome (59), are transported via the FhuBCD system (35). Siderophores, which have a very high affinity for iron, support growth in iron-limited conditions but their production is energy-intensive. The FeoABC system, found in all *Vibrio* species (60), is one of the earliest discovered bacterial iron transport systems which import ferrous iron transport. Additionally, *V. cholerae* utilizes the FbpABC system, another ABC transporter, for ferric (Fe^{3+}) iron transport (4). Furthermore, *V. cholerae* transports free heme and hemoglobin-associated heme through the action of the HutCD-B system (61, 62) and it also transports cobalamin through the action of BtuFCD system. For iron transport, *V. cholerae* produces and releases vibriobactin, a catechol siderophore, into its surroundings. The outer membrane receptor ViuA/VctA and the penicillin-binding protein ViuP/VctP facilitate the transport of the iron-vibriobactin complex by the ABC transporters ViuABCD or VctABCD (63). Moreover, *V. cholerae* utilizes hexose-6P as a carbon and phosphate source for biofilm formation and survival under phosphate-limiting conditions. Recent studies have identified three genes (VCA0625-27) in *V. cholerae* as part of an ABC transport system for hexose-6P, previously known as iron transport genes, which help to uptake and utilize hexose-6P as a carbon and phosphate source (64).

Although several ABC transporters for nutrient uptake have been identified in *V. cholerae*, differences in protein sequences and predicted structures suggest that these complexes may assemble and function uniquely. Therefore, understanding the structure and function of these ABC transporters are crucial for grasping the molecular mechanisms of nutrient uptake.

Chapter 2

Heme internalisation in type-II HutCD-B ABC transporter of *Vibrio cholerae*

2.1 Diversity inside type-II ABC importer

Several ABC importers have been recognized as pivotal virulence factors in pathogenic species, suggesting that these microorganisms cannot thrive in the host environment without specific nutrients. Examples of such importers include the heme transporter in *Staphylococcus aureus* (65), the glutamine transporter in *Salmonella enterica* serotype Typhimurium and *Streptococcus agalactiae* (66), and the maltodextrin transporter in *Streptococcus pyogenes* (67), heme transporter in *Vibrio cholerae* (68) and vitamin B12 transporter BtuCD-F (69).

Interestingly, despite their common basic architecture, molecular mechanisms of ATP binding and hydrolysis mediated alteration of nutrient translocation pathway are remarkably diverse even for the type-II importers, which are well known for the uptake of iron-siderophores, vitamin B12 and heme (33-35). So far, structural details of heme transporting ABC importers are restricted to HmuUV of *Yersinia pestis* and BhuUV-T of *Burkholderia cenocepacia* (33, 46). Crystal structure of HmuUV of *Y. pestis* demonstrated an 'outward-facing' (OF) conformation of the permeases with the translocation pathway opening to the periplasmic side of the membrane. The structure of BhuUV-T of *B. cenocepacia*, on the other hand, was obtained in 'inward-facing' (IF) conformation with the substrate translocation pathway open to the cytoplasm (46). Recently, a targeted MD simulations on BhuUV-T with bound ATP in the IF state yielded an 'occluded' (Occ) state, in which both the cytoplasmic and periplasmic sides of heme translocation channel remained closed (70, 71). So that, ABC importers represent promising targets for drug development because they are predominantly found in bacteria and are accessible without penetrating the cytoplasmic membrane.

2.2 Iron import in pathogenic bacteria

Motile pathogenic bacteria acquire iron, the essential metal cofactor for several cellular processes, aiming at successful colonization and growth inside a host (4, 72). Animal hosts attempt to limit iron availability through 'nutritional immunity' thereby combating the colonization of pathogens (73). This results in free-iron levels as low as 10^{-24} M (74). To refute this, many pathogens develop various efficient strategies to obtain iron from the host-derived molecules during infection. Pathogenic bacteria primarily acquire iron through two main strategies: directly extracting Fe^{3+} from specific host iron-containing complexes like lactoferrin, transferrin, haemoglobin, or hemin, and/or by producing small Fe^{3+} chelating molecules known as siderophores (75, 76). Heme is a vital coordination complex featuring an iron ion bound to a porphyrin acting as a tetradentate ligand, along with one or two axial ligands

(Fig. 2.1). Heme functions as an essential prosthetic group in a wide array of metalloproteins that feature porphyrin structures (77). Heme or hemin is considered beneficial for pathogens due to its abundance within the host environment, especially when the pathogen lacks the ability to synthesize heme, as observed in the case of some heme auxotrophs (78). The mechanisms by which pathogenic bacteria acquire iron are especially important because they can be adapted for the 'Trojan Horse' strategy in antibiotic delivery, potentially overcoming drug resistance related to permeability issues (79). Unlike siderophores that bind iron tightly but cannot extract it from heme compounds, many pathogenic bacteria, such as *Vibrio cholerae,* possess mechanisms to directly utilize heme, whether from free heme or various heme-containing proteins (80).

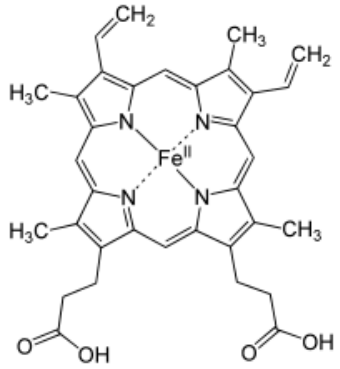

Figure 2.1: Chemical Structure of Heme

Gram-negative bacteria typically transport heme using ABC transporters. Heme's availability promotes growth under iron-restricted conditions, making it a favoured iron source for organisms equipped with heme transport systems. Significantly, the enzyme heme oxygenase, which can release iron from heme, has been detected in certain pathogenic bacteria, including *Staphylococcus aureus*, *Neisseria meningitidis*, *Corynebacterium diphtheriae,* and *Pseudomonas aeruginosa* (81-84). Interestingly, *Vibrio cholerae* and other enteric bacteria lack identifiable heme oxygenase activity or genes homologous to known heme oxygenases in sequenced genomes. Whether these bacteria employ an undiscovered enzyme for iron extraction from heme or possess alternative heme utilization strategies remains an open question (85).

The structure of the cellular envelope of gram-negative bacteria requires heme to be trafficked across the outer membrane, through the periplasm, and across the inner membrane before reaching the cytosol. Import of heme across the outer membrane of bacteria is accomplished by a TonB-dependent system with the help of proton motive force (86). Active

transport of the nutrients across the plasma membrane is achieved by various ATP binding cassette (ABC) transporters. Generally, periplasmic ligand binding protein (PLBP) captures nutrient, cytosolic nucleotide binding domains (NBDs) utilise ATP hydrolysis driven energy to cause large-scale conformational changes in the permeases to facilitate uptake of nutrients.

2.3 Heme ABC importer, HutCD-B of *V. cholerae*

Vibrio cholerae encodes multiple iron acquisition systems, reflecting the importance of iron for this pathogen. These include the synthesis and transport of the catechol-type siderophore vibriobactin, transport of exogenous siderophores such as enterobactin and the acquisition of heme of the host system (87). Based on that, ABC type transport system HutCD-B has been identified as the system of *V. cholerae* for heme transportation through the inner membrane (85). Analysis of the hut genes indicated that HutCD-B (Fig. 2.1), which encodes a periplasmic binding protein (HutB), a cytoplasmic membrane permease (HutC) and an ATPase (HutD) are required to reconstitute the *V. cholerae* heme-transport system in *Escherichia coli* (88). However, the structure, dynamics and mechanism of ATP-dependent heme translocation through this system of *V. cholerae* remains unknown. As an early step to understand the molecular basis of HutCD-B mediated heme transport, previously we solved the crystal structure of periplasmic heme-binding protein HutB in our lab before (68). Structural studies coupled with biochemical analysis indicated parallel binding of two heme molecules to HutB in a pH-dependent manner which attributed to its storage (62). Nonetheless, the mechanism of heme internalization is still unknown in *V. cholerae*. Understanding the mechanism of this HutCD-B transporter provides insights into the bacterium's biology, develop new antibiotics or adjuvant therapies, and combat antibiotic resistance effectively.

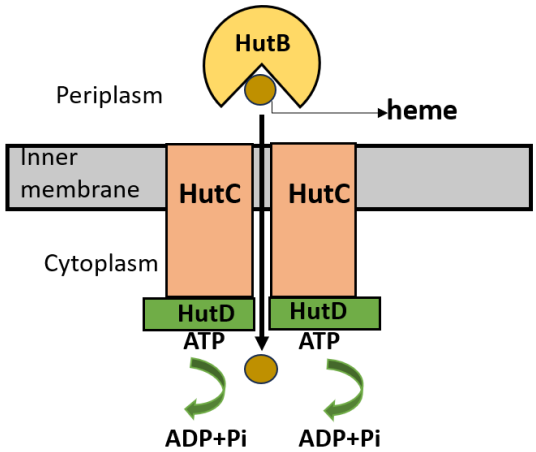

Figure 2.2: Type-II Heme ABC transporter HutCD-B of *V. cholerae*

2.4 Objectives: Revelation of the mechanism of Heme transport in *V. cholerae*

Till date, the understanding of nutrient uptake mechanisms in *V. cholerae* remains limited, with a particular lack of detailed knowledge regarding its iron uptake mechanism. Moreover, in ABC transporters, the nature of conformational changes is largely specific to the species and the nutrients. Studies on nutrient transport mechanisms in *V. cholerae* have focused on how the vibriobactin (a catechol-type siderophore) binding protein ViuP operates in both its unbound (apo) and bound (holo) states (89). However, how *V. cholerae* transports heme at the molecular level remains elusive yet. Understanding the mechanism of this HutCD-B transporter provides insights into the bacterium's biology, develop new antibiotics or adjuvant therapies, and combat antibiotic resistance effectively.

Therefore, the objectives of my study were: (i) to conduct structural characterization and biochemical studies on the NBD, HutD and its mutants belonging to the HutCD-B transporter system. (ii) to understand the structure and dynamics of HutCD assemblies through molecular modeling, docking, and MD simulations. (ii) to identify the pivotal residues involved in ATP binding and hydrolysis of HutD, and to capture the ATP hydrolysis driven transient and global conformational changes necessary for heme internalization through biochemical studies and MD simulations. (iii) to study the conformational shifts expected in the heme transportation pathway in the presence or absence of Mg^{2+}-ATP. (iv) to elucidate the probable pathway and identify the interacting residues of HutD with heme during ejection through MD simulations on the heme-docked HutCD complex.

Chapter 3

Cloning, Overexpression, Purification and Biochemical assays of HutD and its mutants

Summary

HutD, like the other NBDs, exhibits sequence and structure conservations across the transporter family (23), and contains several conserved functional motifs such as Walker-A (WA) and Walker-B (WB), along with ABC transporter-specific or ‘‘signature’’ motif that remains adjacent to the ATP binding site. To confirm their functional roles in ATP binding/hydrolysis, we have prepared four points mutants of HutD. R18A, K44A are from Walker-A motif while D166A and E167A belong to Walker-B. This chapter covers the details of the isolation of *V. cholerae* O395 genomic DNA, cloning, overexpression and purification of HutD and its mutants. This chapter also contains the state of oligomerisation of HutD in the presence and absence of non-hydrolysable ATP analogue Adenosine 5’-(β,γ-imino) triphosphate (AMP.PNP). This chapter also describes the details of binding studies of HutD with ATP (or AMP.PNP) through fluorescence quenching as well as ATP hydrolysis by HutD and its mutants by Malachite green assay.

3.1 Genomic DNA preparation

The genomic DNA for cloning was extracted from *V. cholerae* serotype O1 (strain ATCC 39541 / Classical Ogawa 395 / O395) using a high salt SDS-based protocol (90). The extraction process involved TE buffer (Tris-EDTA), 10% (w/v) sodium dodecyl sulphate (SDS), 20 mg/ml proteinase-K, a 1:1 mixture of phenol and chloroform, a 10:1:0.6 solution of supernatant/3M sodium acetate/isopropanol, 70% ethanol, and TE-RNase (Fig. 3.1a).

3.2 Cloning, Overexpression and Purification of Nucleotide Binding protein HutD and mutants R18A, K44A, D166A and E167A

The NBD HutD was inserted into the kanamycin-resistant pET28a$^+$ vector (Novagen) using specific primers: forward primer 5'-GACTGAGACATATGGTGGATATCACCTTGCGCTGTGGC-3' and reverse primer 5'-CATTCGGGATCCTCAAGCTGGATAAACCATTGGG-3'. These primers, synthesized by SahaGene, included *NdeI* and *BamHI* restriction sites. Genomic DNA from *V. cholerae* strain O395 served as the template to amplify the full-length HutD region (259 amino acids, residues 1-259, Accession code: A0A0H3ADP8). The 780 bp HutD PCR product (Fig. 3.1b-c) and the pET28a$^+$ vector were both digested with *NdeI* and *BamHI*, then purified from a 1.0% agarose gel using a gel-extraction kit (Qiagen). The digested DNA fragments were ligated with T4

DNA ligase, and the ligation products were transformed into kanamycin-resistant *E. coli* XL1-Blue cells for cloning.

The recombinant protein with an N-terminal 6×His-tag was overexpressed in BL21 (DE3) cells using a T7 RNA polymerase-IPTG induction system and purified via Ni^{2+}–NTA affinity chromatography. Briefly, a single colony was used to inoculate 10 ml of LB broth with kanamycin, which was then grown overnight at 310 K with shaking. This overnight culture was used to inoculate 1 liter of LB broth containing kanamycin, and the culture was further incubated at 310 K until the OD_{600} reached 0.6. Protein expression was induced with 1 mM IPTG and the culture was grown for an additional 3 hours at 310 K. Cells were harvested by centrifugation at 4500×g for 20 minutes at 277 K, and the pellet was resuspended in 8 ml of ice-cold lysis buffer-L (50 mM Tris–HCl, pH 8.0, 300 mM NaCl, 5 mM $MgCl_2$, 10% (v/v) glycerol). PMSF (1 mM) and lysozyme (1 mg/ml) were added, and the solution was lysed by sonication on ice. The lysate was centrifuged at 13,000 RPM for 45 minutes at 277 K. The supernatant was applied to a Ni–NTA affinity column (Qiagen) previously equilibrated with buffer-L. The 6×His-tagged recombinant proteins were eluted using a gradient of 50–200 mM imidazole (Fig. 3.1e). Imidazole was removed by buffer exchange using Amicon centrifugation units, and the protein was concentrated to 500 μM. The purity of the proteins was assessed by SDS–PAGE (Fig. 3.1f). The construct was verified by restriction digestion analysis and commercial DNA sequencing.

The mutants, R18A, K44A, D166A and E167A were prepared by two-step PCR amplification using previously cloned wt HutD plasmid as template. These mutant amplicons were also cloned in $pET28a^+$ vector using *NdeI* and *BamHI* as restriction sites (Fig. 3.1d). Sequences of the mutants were verified by commercial sequencing. These recombinant proteins with N-terminal 6×His-tag were overexpressed in *E. coli* BL21(DE3) by IPTG induction. All mutants were purified using the buffer containing 50 mM Tris–HCl pH 8.0, 300 mM NaCl, 10% (v/v) glycerol with the same protocol and concentrated up to 500 μM. The homogeneity of the purified proteins was checked using SDS-PAGE with 12% polyacrylamide concentration. The mutants were verified by restriction digestion analysis and commercial DNA sequencing.

Table 3: Primers used to clone the mutants of HutD

HutD mutants	Primer sequence 5′ ➡ 3′
R18A (1-259 aa)	FP: ACCTACGGCTCTGCCCAAGTGCTC RP: ATGATCGAGCACTTGGGCAGAGCCGTA
K44A(1-259 aa)	FP: AACGGAGCCGGGGCAAGTACCTTA RP: CTTCAGTAAGGTACTTGCCCCGGCTCCGTT
D166A (1-259 aa)	FP: ATTTTGATGCTGGCTGCGCCAACA RP: TGCTGATGTTGGCGCAGCCAGCATCAA
E167A (1-259 aa)	FP: TTGATGCTGGCTGCGCCAACATCA RP: GAGTGCTGATGTTGGCGCAGCCAGCAT

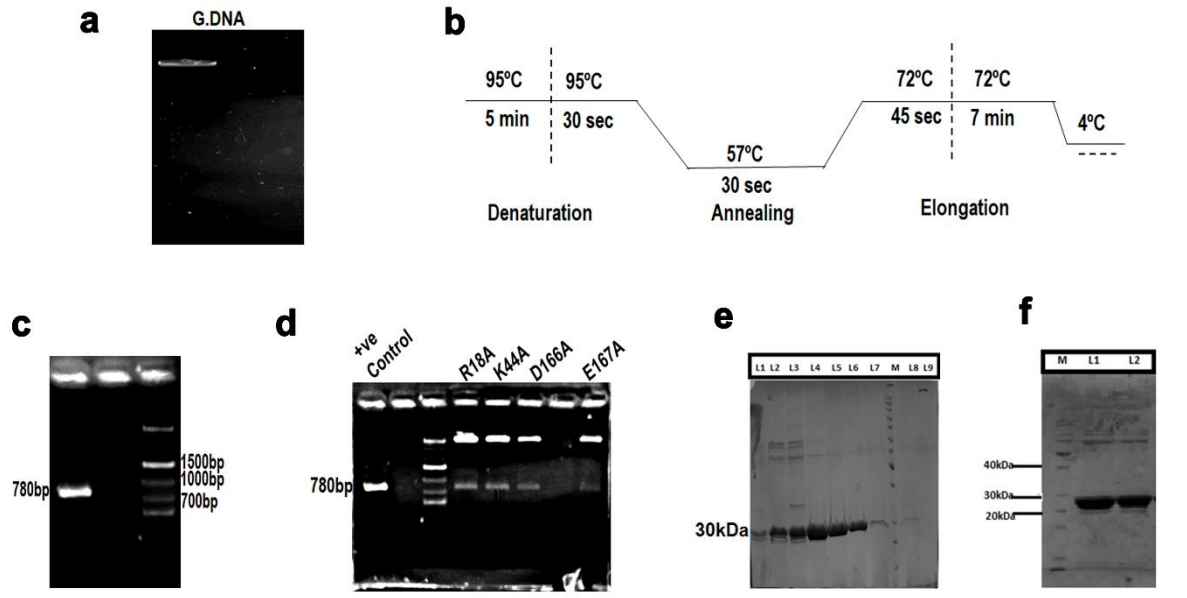

Figure 3.1: Cloning, overexpression and purification profile of HutD & its mutants. (a) Agarose gel showing the band of isolated genomic DNA *V. cholerae* serotype O395; (b) Reaction conditions for PCR of HutD from the template genomic DNA; (c) 1% Agarose gel showing the band of PCR product of HutD; (d) 1.2% Agarose gel showing the confirmation bands of the HutD mutants by restriction digestion with *NdeI* and *BamHI*, Lane 1, HutD PCR product; lane 3, DNA ladder; (e) 12% SDS gel showing bands of L(1-9): elution fractions with imidazole gradient(10-200mM) of HutD after Ni/NTA, M: marker; (f) The homogeneity of the concentrated HutD also was checked on 12% SDS–PAGE, lane 1(M), molecular weight marker; lane 2(L1), 4µl of concentrated HutD and lane 3(L2), 2µl of concentrated HutD.

3.3 Study of oligomerisation of HutD by crosslinking and SEC

3.3.1 In-solution chemical cross-linking: methodology

For the detection of oligomeric state, crosslinking experiments had been carried out with HutD in the presence and absence of non-hydrolysable ATP analogue AMP.PNP using Glutaraldehyde (Sigma-Aldrich) as crosslinker. HutD was purified in cross-linking buffer (50 mM Na-Phosphate pH 8.0 and 150 mM NaCl) followed by incubation with AMP.PNP (20 mM) on ice for 1.5 h. Increasing amounts of glutaraldehyde were added to the mix to a final concentration range of 0.0025–0.04%. The reaction mixture was further incubated at room temperature for 15 min. Crosslinking reactions were quenched by adding 50 mM Tris–HCl pH 8.0, followed by incubation at 97 °C for 10 min in standard SDS loading dye. Reaction products were separated by electrophoresis and analysed on 10% SDS-PAGE polyacrylamide gel.

3.3.2 Size exclusion chromatography using Superdex column: methodology

Size exclusion chromatography was conducted using a Superdex 200 Increase 10/300 GL column with an AKTA purifier (Cytiva). Blue dextran was utilized to determine the void volume of the column. Calibration was performed with a molecular weight standard kit (GE Healthcare) that included Ferritin (440 kDa), Aldolase (160 kDa), Ovalbumin (45 kDa), and Lysozyme (14.3 kDa). A standard curve was created plotting relative elution volume (Ve/Vo) on the x-axis, where Ve represents the elution volume and Vo is the void volume, against the logarithm of molecular weight on the y-axis. For the AMP.PNP bound state analysis, 250 µM HutD was incubated at 4°C for 1.5 hours with 500 µM AMP.PNP in buffer-L. In each chromatographic run, 500 µl of the protein solution was injected into the SEC column, which had been pre-equilibrated with a buffer containing 50 mM Tris–HCl (pH 8.0), 300 mM NaCl, and 5 mM $MgCl_2$, and the run was carried out at a flow rate of 0.5 ml per minute. The peak fractions were collected and analysed by 12% SDS-PAGE.

3.3.3 Crosslinking and size exclusion chromatography suggest dimerization of HutD

Migration pattern, analysed by 10% SDS/PAGE gel, after crosslinking experiments with HutD in the presence and absence of AMP.PNP (where Glutaraldehyde was as crosslinker) (Fig. 3.2a) showed the presence of dimer (~60kDa) along with monomer of HutD (30kDa) (Fig. 3.2a). However, tendency of forming dimer is prevalent in the presence of

AMP.PNP (Fig. 3.2a). HutD, that was used for cross-linking experiments was pure and functional, and little bit of anomaly in movement of proteins in SDS-PAGE (which is observed in case of HutD dimer) is not very uncommon upon cross-linking or chemical modifications.

To further validate the results of cross-linking experiments, we performed size exclusion chromatography (SEC) using Superdex 200 increase column 10/300 with HutD in free and AMP.PNP treated states (Fig. 3.2b-c; apo and AMP.PNP treated HutD are shown in red and green respectively). In free state, peak-II of Fig. 3.2b having elution volume of 15.36 ml was indicative of monomer along with a trace of dimer. However, incubation with AMP.PNP showed a clear shift of peak-II towards dimer with elution volume of 14.68 ml (Fig. 3.2b-c). This indicates that AMP.PNP binding facilitates dimerization which corroborates with the observations of cross-linking experiments. In both experiments of SEC, peak-I probably denotes little impurities in the samples and/or soluble aggerates.

So far, HutCD was known as a putative type-II ABC importer of heme, based on sequence comparisons. Our observations authenticated that like other type-II importers HutD is capable to form dimer in the absence of the permease, HutC and ATP binding facilitates dimerization of HutD.

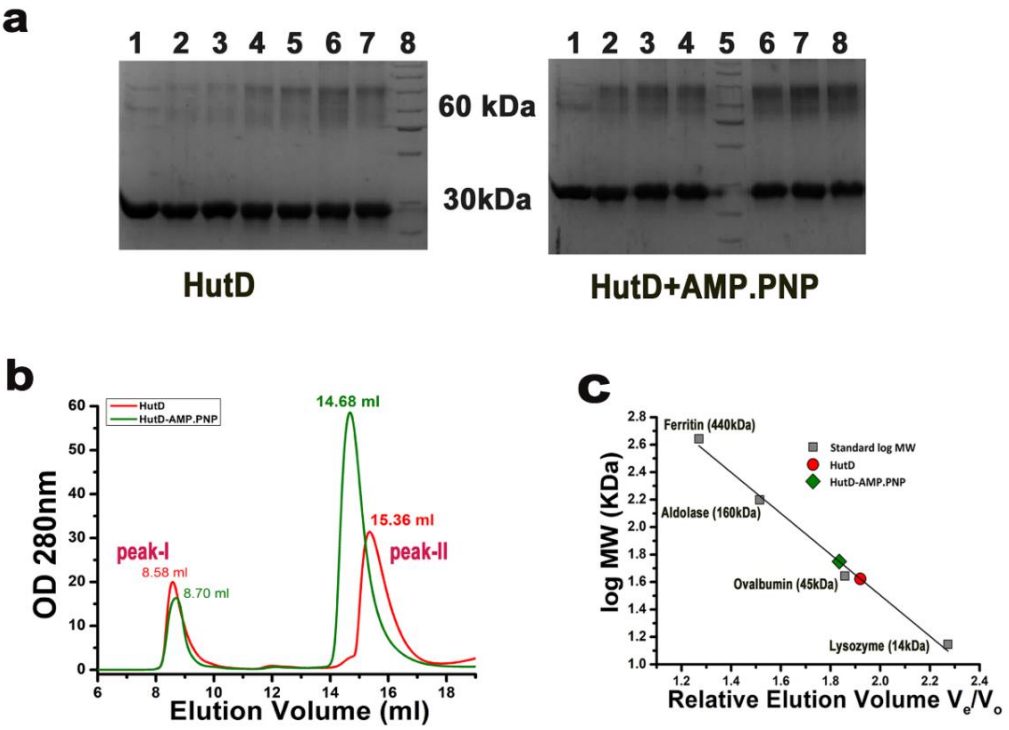

Figure 3.2: Dimerization profile of HutD. (a) Crosslinking of HutD with Glutaraldehyde in Nt-free state (left) and after incubation with AMP.PNP showed prevalent dimerization upon incubation with AMP.PNP; *left:* (L1: Control, L2-L7: after treatment with 0.005-0.04% of Glutaraldehyde, L8: MWM), right:

(L1: Control, L2-L4: after treatment with 0.005%, 0.01%, and 0.02% of Glutaraldehyde, L5: MWM, L6-L8: after treatment with 0.03%, 0.035%, and 0.04% of Glutaraldehyde); (b) Size exclusion chromatography elution profiles of HutD in Nt-free and upon incubation with AMP.PNP; (c) the molecular weights of the peaks were determined from the calibration curve prepared using molecular weight standards. Elution volumes suggest strong dimeric shift upon AMP.PNP binding to HutD.

3.4 Measurement of binding affinity of HutD to AMP.PNP by Fluorescence Spectroscopy

3.4.1 Intrinsic fluorescence Spectroscopy: methodology

Fluorescence measurements were performed using a Hitachi F-7000 spectrofluorometer with 1 cm path length quartz cuvettes. The Tyr residue fluorescence was excited at 280 nm, and emission spectra were recorded from 295 nm to 400 nm with slit widths set to 5 nm for both excitation and emission. All experiments were conducted at 298 K in a buffer consisting of 50 mM Tris-HCl (pH 8.0) and 300 mM NaCl. Equilibrium titrations of HutD were carried out with AMP.PNP as the ligand and the changes in fluorescence emission intensity were measured in the presence of increasing concentration of ligand. The concentration of HutD was 2.5μM and ligand concentrations varied from 0 to 2mM.

The binding stoichiometry was determined using the protocol described in Mani et al (91). The plot of $\log(F_0 - F)/(F - F_\infty)$ against log [AMP.PNP], where F_0, F, and F_∞ are the fluorescence intensities of HutD alone, HutD in the presence of various concentrations of AMP.PNP, and HutD saturated with AMP.PNP, respectively, yielded a straight line whose slope was a measure of the binding stoichiometry. The dissociation constant, K_d was determined using nonlinear curve fitting analysis as per equations [1] and [2] (91). All experimental points for the binding isotherms were fitted by the least-squares method:

$$K_d = \{[C_0 - (\Delta F/\Delta F_{max}) \bullet C_0] \bullet [C_P - (\Delta F / \Delta F_{max}) \bullet C_0]\} / \{(\Delta F / \Delta F_{max}) \bullet C_0\} \quad [1]$$

$$C_0 \bullet (\Delta F/\Delta F_{max})^2 - [(C_0+C_P+K_d) \bullet (\Delta F/\Delta F_{max})] + C_P = 0 \quad [2]$$

C_0 and C_p denotes the input concentrations of the ligand and HutD respectively. ΔF is the change in fluorescence intensity at 334nm (λ_{ex}=280nm) for each point of titration curve and ΔF_{max} is the same parameter when ligand is totally bound to the protein. A double-reciprocal plot of $1/\Delta F$ against $1/(C_p - C_0)$, as shown in equation [3] was used to determine the ΔF_{max}.

$$1/\Delta F = 1/\Delta F_{max} + K_d/ [\Delta F_{max} (C_P - C_0)] \quad [3]$$

ΔF_{max} was calculated from the slope of the best fit line corresponding to the above plot. All experimental points for the binding isotherms are fitted by least square methods using OriginPro 8.0 software.

3.4.2 Binding of AMP.PNP with HutD

Participation of A-loop, Walker-A and Walker-B is well known in the ATP binding in the NBDs of type-II ABC importers (PDB codes: 4G1U, 1L2T). Sequence alignment followed by structural model (shown later in Fig. 4.1b, 4.2a) indicated proximity of Y15, the Tyr of A-loop to the ATP binding site. We, therefore, decided to investigate the interactions of AMP.PNP, the non-hydrolysable ATP analogue, with HutD by monitoring the intrinsic fluorescence quenching at an excitation wavelength of 280 nm (λ_{ex} = 280 nm, λ_{em} = 295–400 nm) accounting the contributions of tyrosine residues present at the ligand binding site. Interestingly, with significant fluorescence quenching HutD has shown considerable interactions with AMP.PNP with a dissociation constant, K_d of 94±0.024 μM (Fig. 3.3a-b). Calculation of stoichiometry indicated binding between HutD and AMP.PNP in a 1:1 molar ratio (Fig. 3.3c). Negligible quenching upon excitation at wavelength of 295 nm (λ_{exc} = 295 nm, λ_{em} = 308–400 nm), that accounts the contribution only of Trp, ruled out the participation of the Trp residues in ATP binding and established that the Trp residues are located beyond the forster distance of ATP binding site of HutD.

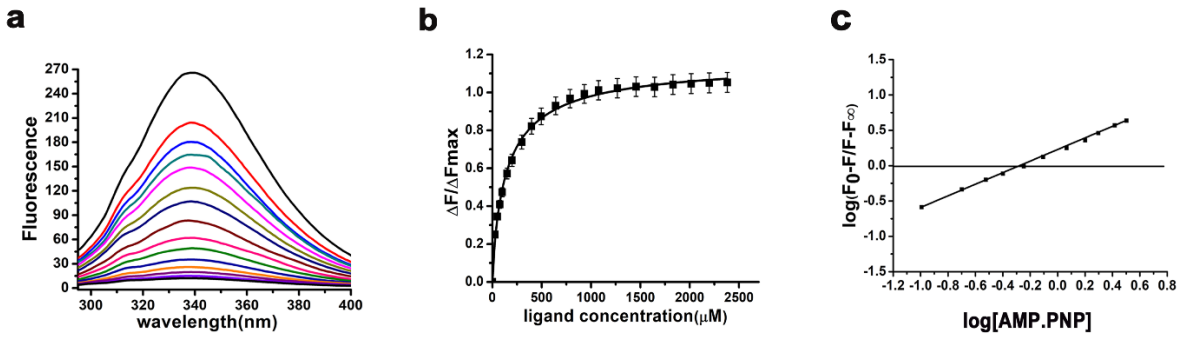

Figure 3.3: ATP binding by HutD. (a,b) Fluorescence quenching demonstrated significant change in fluorescence upon AMP.PNP binding to HutD; (λ_{exc} = 280 nm, λ_{em} = 295–400 nm) with slit widths of 5 nm for both excitation and emission Plots of $\Delta F/ \Delta F_{max}$ against ligand AMP.PNP (μM) obtained a K_d value of 94±0.024 μM; (c) Slope of the *straight line* indicates 1:1 binding stoichiometry between HutD and AMP.PNP.

3.5 Measurement of the ATPase activity of HutD, and reaction velocity through time course experiments

3.5.1 Methodology to measure ATPase activity

ATPase activitiy of purified HutD was determined spectrophotometrically using Malachite green assay by measuring the release of inorganic phosphate (Pi). The reaction mixture with final protein of 2.5 µM and buffer containing 50 mM Tris–HCl (pH 8.0), 300 mM NaCl, and 5 mM $MgCl_2$ were incubated with ATP (Sigma Aldrich), of concentration ranging from 100 to 500 µM at 298 K. Malachite Green solution was freshly prepared by adding 0.44 g of Malachite green in 0.3 M H_2SO_4, 2.5 ml of 7.5% ammonium molybdate, and 0.2 ml of 11% Tween 20 to a final volume of 10 ml. 200 µl of aforesaid solution was added to the reaction mixture to a final volume of 1 ml. The absorbance was measured at 630 nm within 5 min of adding the colouring reagent. Pi standard curve was prepared by using KH_2PO_4 and plotting OD_{630} against release of Pi using OriginPro 8.0 software (92). The total Pi released by each protein upon ATP hydrolysis was obtained from the standard curve. Each reaction was checked with Malachite green dye without ATP to measure the contaminant inorganic phosphate if any, and the minor absorbance thus obtained at 630 nm was subtracted from the absorbance produced by that protein upon hydrolysis of added ATP. The ATP hydrolysis without protein has served as another negative control to nullify the effect of the contaminating inorganic phosphate with ATP. All the experiments were minimally performed in triplicate.

3.5.2 Significant ATP hydrolysis by HutD

HutD has shown substantial ATP hydrolysis while tested using Malachite green assay (Fig. 3.4b). 2.5 µM HutD and 0.1 mM ATP (Sigma Aldrich) were incubated at 298 K for 20 minutes (Fig. 3.4b). The release of inorganic phosphate (Pi) was measured at 630 nm upon incubation with Malachite green as per the protocol described earlier (92). Released Pi from each reaction was quantified by comparing with a Pi standard curve prepared using KH_2PO_4 (Fig. 3.4a). HutD without ATP addition served as the control reaction. The experiments were minimally performed in triplicates.

3.5.3 Calculations of reaction velocity (V_{max}) and Michaelis constant (K_M) through time course ATPase assays of HutD

HutD was assayed for reaction velocity (V_{max}) and Michaelis constant (K_M) through ATPase activity using Malachite green assay, as described in the section 3.5.1. Considering linearity of Pi production during time course experiment, reaction velocity was measured upon incubation of HutD with increasing ATP concentrations (up to 800 μM) through a time scan up to 5 mins. Reaction velocity (V_0) in terms of Pi release was then plotted against ATP concentrations (Fig. 3.4c). Kinetic parameters, like the maximal velocity (V_{max}) and Michaelis constant (K_M), were determined by non-linear curve fitting employing Michaelis-Menten plot using OriginPro 8.0 software. Fitting of ATPase activities in Michaelis-Menten equation resulted in V_{max} of 3.42 ± 0.10 μM min^{-1} and K_M of 74.15 ± 9.46 μM for HutD (Fig. 3.4c).

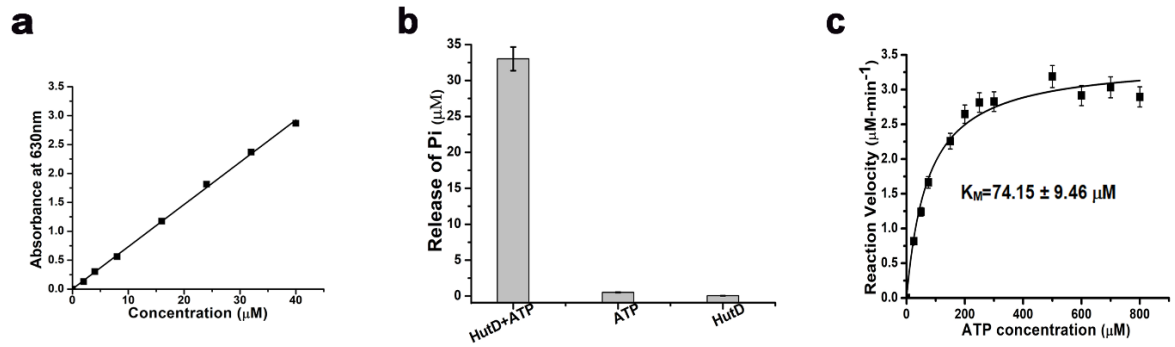

Figure 3.4: ATP hydrolysis by HutD. (a) The release of inorganic phosphate (*Pi*) was estimated against the standard curve of KH_2PO_4; (b) Significant ATP hydrolysis of HutD were observed in Malachite green assay; (c) Reaction velocity of HutD were plotted against ATP concentrations (μM) as per Michaelis-Menten equation with 'One site-specific binding' model. Error bars in, (b) and (c) are SD values obtained from at least three replicates.

3.5.4 Identification of pivotal functional residues of HutD through mutagenesis

Based on sequence similarity, we could presume functionally important residues of HutD (Fig. 4.1b). To confirm our propositions, we have prepared four points mutants of HutD namely R18A, K44A, D166A and E167A, and investigated their ATP hydrolysis capacity using Malachite green assays. Time course experiments showed that the amount of Pi produced by wild type HutD during ATP hydrolysis increased approximately linearly with incubation time for the first 5 minutes (Fig. 3.5a). However, the ATPase activity using 100 μM of ATP of the mutants R18A, K44A, D166A and E167A were drastically low compared to wt HutD and remained constant throughout for different incubation times varying from 1 min to 5 min (Fig.

3.5a). The concentration of ATP inside the bacterial host may elevate up to 1 mM under certain conditions (93). Therefore, we have measured ATPase activities of wt HutD and the variants upon elevating ATP concentrations to 0.5 mM. All four mutants showed negligible ATPase activities even with an elevation of ATP concentration to 500 μM (Fig. 3.5a *right panel*). The increase of incubation time to 20 minutes also did not affect the ATP hydrolysis pattern of the mutants and wt HutD (Fig. 3.5b).

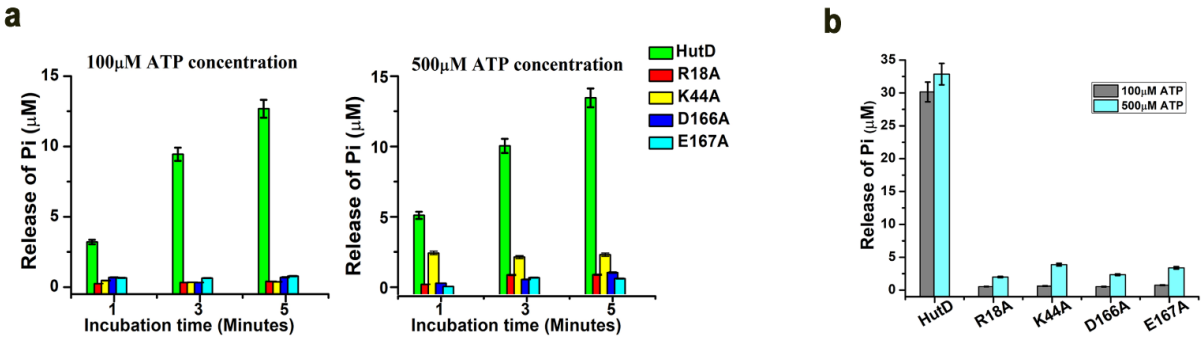

Figure 3.5: Identification of functionally crucial residues of HutD by mutagenesis. (a) Loss of function of the mutants R18A, K44A, D166A, E167A compared to HutD, as evident from the measurement of ATPase activities with 100 μM and 500μM ATP at three time points (1,3,5 minutes) (b) ATPase activities of HutD and mutants measured with an extended incubation time of 20 minutes with 100μM and 500μM of ATP.

Chapter 4

Structural characterisation and modeling of HutCD complex

Summary

This chapter covers characterization of HutCD assembly (made of dimer of HutC and the dimer of HutD) through sequence analysis and structural modeling. HutD, the cytosolic ATPase, exhibits conservation of functional motifs typical of ABC transporters. Using templates from known structures, models of HutD and HutCD were prepared in different conformation states.

4.1 Sequence analysis of HutC and HutD

To structurally characterize HutCD of *V. cholerae* we have performed a BLAST search against PDB with the amino acid sequences of the TMD, HutC (Accession code: C3LWH8) and the NBD, HutD (Accession code: A0A0H3ADP8), and aligned the sequences with their close structural homologs using Clustal Omega (Fig. 4.1). HutC has shown 45% identity (and 67% similarity for 303aa) with heme transporting permease HmuU of *Y. pestis*, and 45% identity (63% similarity for 339 aa) with BhuU, of *B. cenocepacia* (Fig. 4.1a). In addition to the heme transporters, HutC sequence also showed 41% identity (58% similarity for 293 aa) with BtuC, the ABC transporter permease involved in vitamin B12 uptake. HutD, the cytosolic ATPase showed a maximum identity of 45% (62% similarity for 242 aa) with HmuV while identity with BhuV of *B. cenocepacia* was relatively less (36% identity and 51% similarity for 276 aa). Identity of HutD with BtuD of BtuCD was 36% (52% similarity for 217 aa). The significant extent of identity with the heme and vitamin B12 ABC transporters of different prokaryotic systems strongly indicates that HutCD is expected to possess a similar overall fold and belongs to the type-II class of ABC transporter. The predicted topology of HutC with ten transmembrane helices appears to correspond to the transmembrane segment of the permeases of the type-II class (marked in Fig.4.1a). Similarly, HutD, like the other NBDs, exhibits sequence and structure conservation across the transporter family (37) and contains several conserved functional motifs such as Walker-A (WA) and Walker-B (WB) motifs, an ABC transporter-specific or ‘‘signature’’ motif, and two shorter sequences containing conserved glutamine and histidine residues (namely Q-loop and H-loop respectively) (Fig. 4.1b).

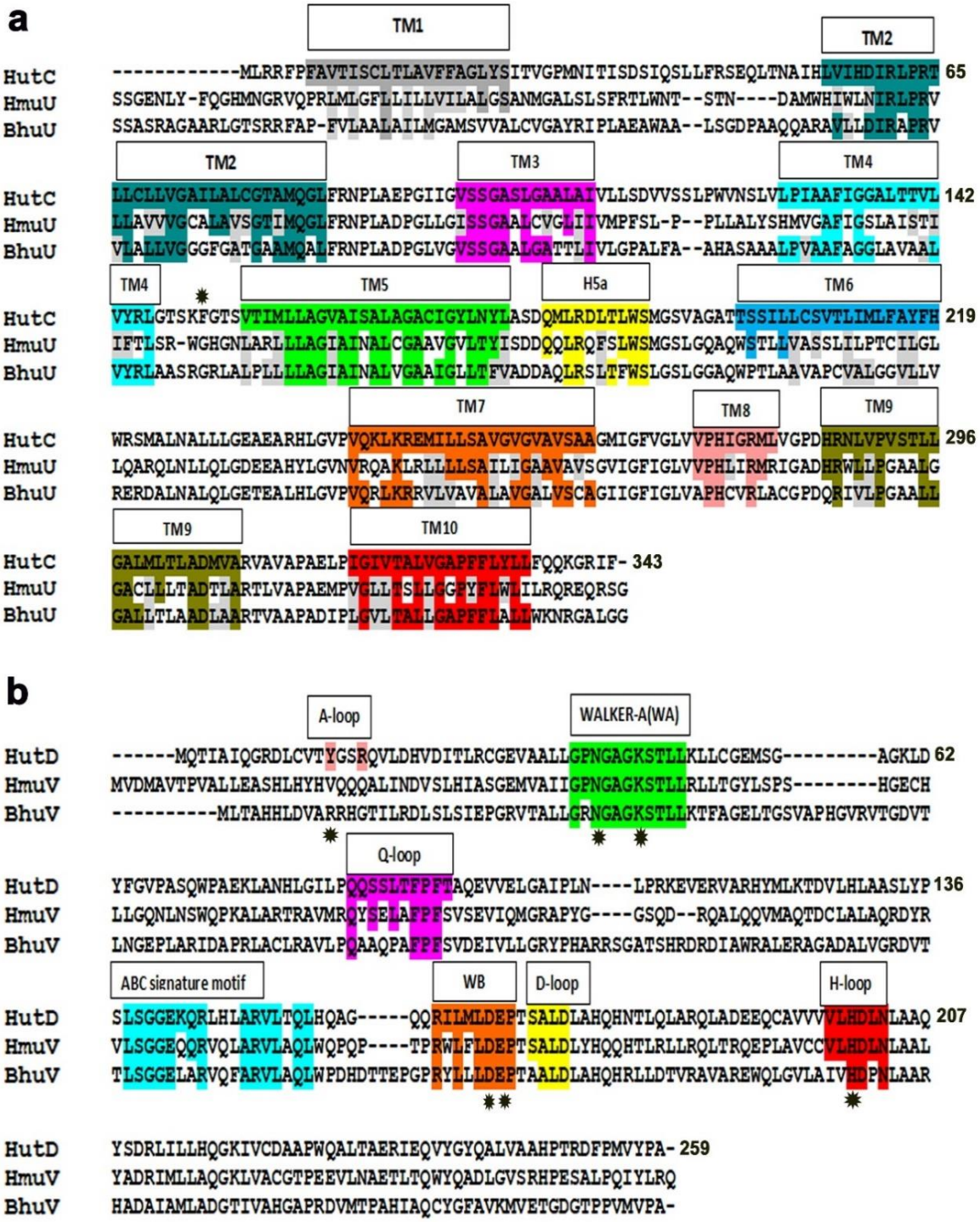

Figure 4.1: Sequence analysis of HutC and HutD. (a) Sequence alignment of HutC from *Vibrio cholerae*, HmuU from *Yersinia pestis* and BhuU from *Burkholderia cenocepacia*. Numbering is based on HutC sequence. (b) Sequence alignment of HutD from *Vibrio cholerae*, HmuV from *Yersinia pestis* and BhuV from *Burkholderia cenocepacia*. Numbering is based on HutD sequence. Important motifs and conserved residues are individually coloured/marked. Semi-conservation inside important motifs are shaded in grey. Some important residues are marked with '*'.

4.2 Modeling of HutD and HutCD in OF and IF conformational states

Oligomeric states of NBD of ABC transporters, and mechanism of ATP binding/hydrolysis differ significantly in the case of type-I and type-II importers. While in the case of the type-I importers dimerization of NBDs are influenced by interactions with permeases, type-II NBDs can form dimer independently (37). Sequence comparisons proposed HutCD as a type-II importer (Fig. 4.1). Our biochemical results established that HutD forms stable functional dimer (that can bind and hydrolyse ATP) in the absence of the permease HutC (Fig. 3.2). Therefore, we decided to investigate the dynamic nature of HutD dimers in the OF and IF states.

The structures of the two type-II Heme importers, HmuUV of *Y. pestis* (PDB code: 4G1U) and BhuUV from *B. cenocepacia* (PDB code: 5B57), in two different conformational states, served as templates to prepare the models of HutD and HutCD in both the outward facing (OF) and inward facing (IF) states. First, we prepared the models of HutD dimers in OF and IF conformations (Fig. 4.2a-b). Previous studies on type-II ABC transporters suggested that ATP hydrolysis mainly occurs in the OF state (34). Therefore, knowledge-based docking of two Mg^{2+}-ATP molecules was performed with HutD in the OF state (Fig. 4.2a-c) where coordinates and binding mode of ATP in MJ0796 NBD dimer (PDB code 1L2T) was treated as template. Dimers of HutC in OF and IF states were also modelled in a similar manner. All models were prepared initially using ps2v2 (94) and later verified by Alphafold2 (95). HutCD assemblies in IF and OF states were then generated considering the assembly structures of HmuUV and BhuUV (Fig. 4.2d-i).

Altogether, we have prepared five sets of complexes: (1) Mg^{2+}-ATP bound HutD dimer in OF state; (2) HutD dimer in IF state; (3) lipid bilayer embedded Mg^{2+}-ATP bound HutCD assembly in OF state; (4) lipid bilayer embedded HutCD in IF state; (5) Heme bound lipid bi-layer embedded HutCD in IF state. Each MD simulation was carried out for 1 μs with the Amber-18 and AmberTools-18 software packages (96). We have used DMPC (1,2-dimyristoyl-sn-glycero-3-phosphocholine) molecules for constructing the bilayer and CHARMM-GUI (97) was used to prepare the solvated protein-embedded lipid bilayer system before simulations. An embedded model is shown in Fig.4.2i. However, the lipid bilayer and the solvents molecules were not shown in the subsequent figures to maintain clarity.

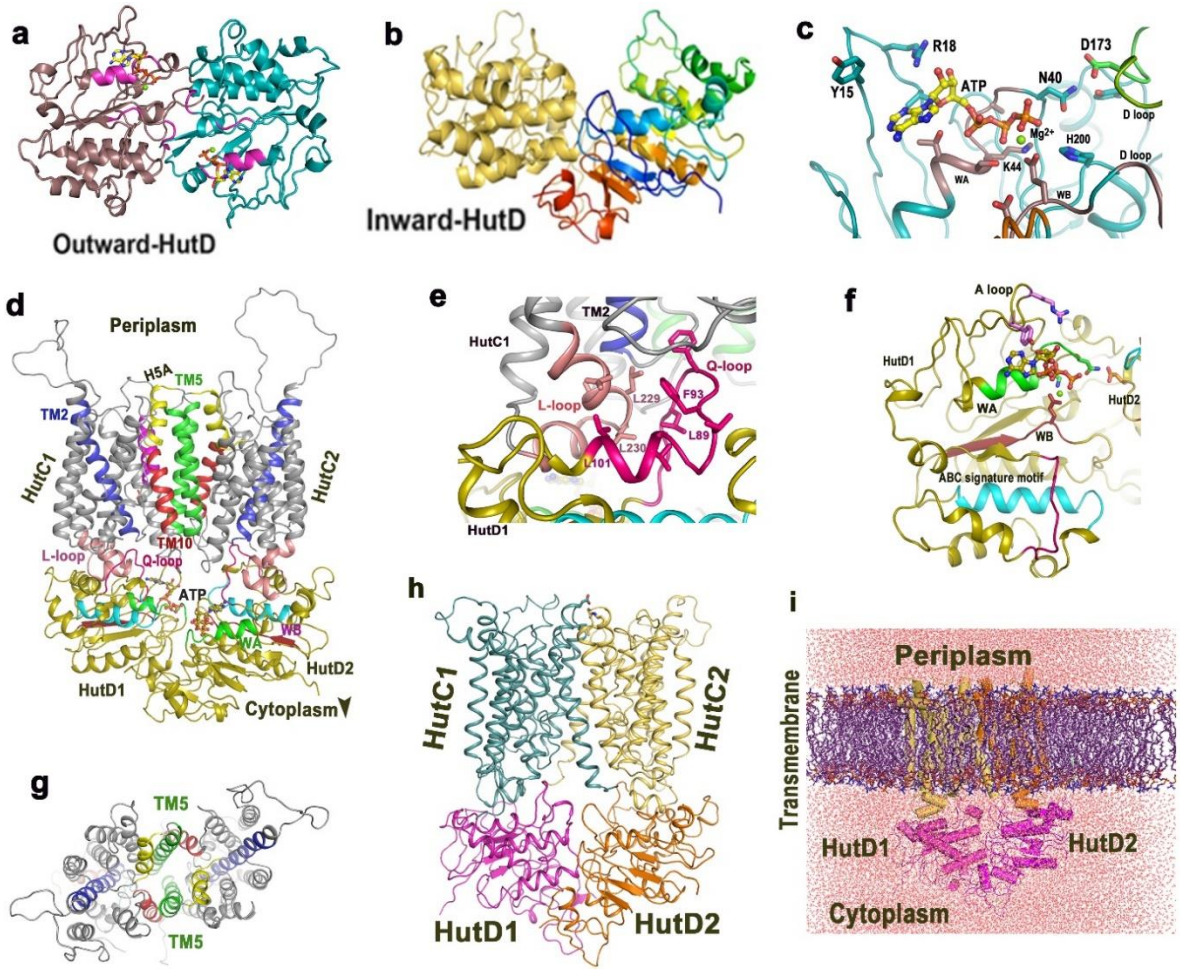

Figure 4.2: Models of HutD, HutC in different states and lipid embedded assembly. Ribbon representation of the models of (a) HutD dimer in the OF state, Nucleotide-binding domains (NBDs, dimer of HutD) are shown in brown and cyan, conserved Walker-A motif or P-Loop is shown in magenta of each NBD. Two ATP molecules are shown in stick; (b) HutD dimer in the IF state; (c) Zoomed view of the docking of Mg^{2+}-ATP in HutD OF dimer and related interactions; (d) Mg^{2+}-ATP bound HutCD dimeric assembly in the OF state; Zoomed view of different regions of HutCD are shown in e-g. (e) Interactions between L-loop of HutC1(salmon) with Q-loop of HutD1 (magenta); (f) Disposition of binding motifs such as A-loop, Walker-A (green), Walker-B (maroon) around Mg^{2+}-ATP. ABC signature motif is shown in cyan; (g) Arrangements of transmembrane helices in HutCD-OF model is shown from the periplasmic side. TM5 helices of each TMD is shown in green, H5a in yellow; (h) Model of HutCD assembly in IF state; (i) Model of HutCD assembly embedded in solvated DMPC lipid bilayer.

Chapter 5

MD simulation studies on HutC, HutD and HutCD assembly in different conformation states

Summary

This chapter has depicted MD simulations on HutD dimers in free and HutC-bound states. We have evaluating RMSD values and B-factors to assess stability and flexibility induced by Mg^{2+}-ATP binding. Interactions near the ATP binding site of HutD dimers were explored, highlighting specific residues and motifs involved in ATP hydrolysis and dimerization. Additionally, the conformational dynamics of HutCD in the ATP-Mg^{2+} bound state were studied, revealing synchronized shifts between HutD and HutC subunits, mediated by inter-domain interactions and structural rearrangements. Moreover, the study identified heme release pathway in the inward-facing (IF) state of HutCD.

5.1 Methodology: Molecular Dynamic Simulation

5.1.1 MD Simulation steps and parameters

Unbiased MD simulations were carried out using pmemd.cuda, the GPU version 10 of MD engine within the Amber package. The protein backbone and side chains were treated with the FF parameters from ff14SB (98), and lipid14 FF (99) was used for the DMPC bilayer. All the simulations were carried out in explicit solvent with the three-point transferable interatomic potential (TIP3P) for waters (100). In simulations involving only protein (i.e., the cases where bilayer was absent), a truncated octahedron box was used for solvation such that the edge of the box was at-least 10 Å away from the protein. A suitable number of Na^+ or Cl^- ions were added to neutralize the solvated system. Periodic boundary conditions were used on every side of the solvated box. Bonds containing H-atoms were restrained using the SHAKE algorithm (101) which enabled us to use a time step of 2 *fs* for the integrator. The pressure and temperature were controlled using a weak coupling to an external bath. The solvated system was coupled to a Berendsen barostat (102) with a relaxation time of 2 *ps*, for maintaining a constant pressure of 1 *atm*. The particle mesh Ewald summation (102) was employed for calculating the electrostatic interactions part of the total Hamiltonian. We applied a distance cutoff of 10 *Å* for calculations of the long-range electrostatic interactions. The temperature of the system was allowed to fluctuate around a mean of 310 *K* by employing Langevin dynamics (103) with a collision frequency of 2 ps^{-1}. Standard simulation protocols were used for the solvated protein cases (104).

For the protein-lipid multicomponent system, the following simulation protocols were used. We followed rigorous energy minimization steps [3] to “relax” the system by eliminating

any energetically unfavourable interactions that might have occurred while preparing the system using CHARMM-GUI. Minimisation was done in three steps: (i) minimised the solvent molecules holding the lipids and protein fixed by using position restraints with a force constant of 250 *kcal/mol/Å*^{2}, (ii) minimised the solvent and the lipid keeping the protein fixed and (iii) finally all the atoms in the systems were set free of restraints and allowed to relax. We ran 5000 cycles of minimization steps in all three segments. The temperature of the energy minimised system was increased to 310*K* linearly in two steps (0-100*K*, 100K-310*K*). To avoid excessive solute fluctuations, we applied a weak restraint (10 *kcal/mol/Å*^{2}) on the protein and lipid residues. Langevin dynamics with a collision frequency of 1.0 ps^{-1} was applied for temperature equilibration at constant volume. Each of the equilibration steps involved 100 *ps* of MD runs in NVT ensembles. After the heating steps, the weak restraints on the protein and lipid residues were released in steps by carrying out four MD simulations, each of 500*ps*, in NPT ensembles. Monte Carlo barostat (barostat=2) with pure semi-isotropic (ntp=3) pressure scaling was used to achieve a constant pressure of 1 *atm*. To reduce buckling of the bi-layer, a constant surface tension (0.0 dyne/cm) was applied at the membrane-liquid (csurften=3) interface (106). Finally, we ran MD "production run" for 1000 ns with an integration time step of 2 *ps* in NPT ensemble.

5.1.2 Building the lipid-protein system

The principal axis of the HutCD complex was aligned with the Z-axis, while the lipid bilayer spanned the XY plane. The HutCD complex was translated by 20 Å along the Z-axis to correctly place the TMD part within the hydrophobic region of the bilayer such that the polar head groups and hydrophilic lipid trails make contact with the specific residues of the transmembrane protein (107). The multicomponent complex was enclosed in a tetrahedral box (approximate dimensions: a = 120 Å, b = 120 Å, c = 170 Å) and solvated in explicit water with a minimum water thickness of 22.5 Å on the top and bottom of the complex. A suitable number of neutralizing ions (Na^+ or Cl^-, depending upon the cases) were added by replacing solvent molecules using the Monte Carlo method. The number of DMPC molecules in a leaflet was in the range of 180 to 210, depending upon the protein being embedded (Fig. 5.1a). The number of DMPC molecules on the upper and lower leaflets was slightly different (the maximum difference was 10). The area per lipid was calculated (108) by multiplying the sides of the simulation box in the XY-plane and dividing it by the average number of lipid molecules in a leaflet (Fig. 5.1b). The coordinate of the solvated multicomponent system was saved in PDB format and was modified afterward to make it consistent with the AMBER naming scheme.

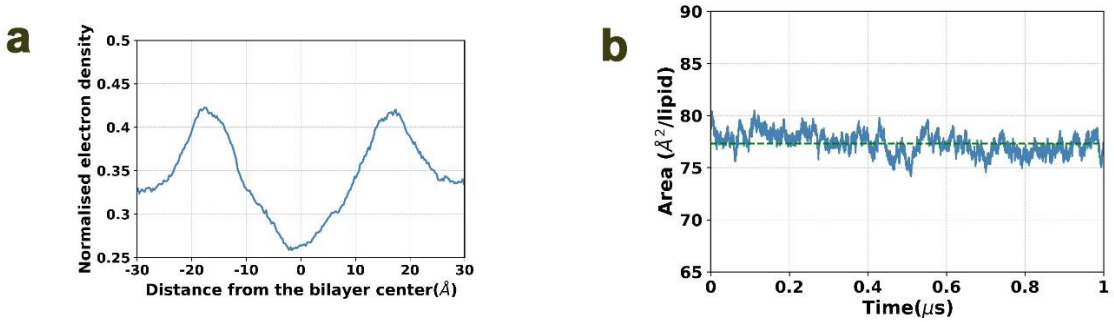

Figure 5.1: MD simulation parameters of building lipid-protein system. (a) Time averaged electron density profile of the DMPC bilayer extracted from the heme bound simulation. Both the leaflets of the bilayer were intact and maintained the bilayer thickness during the course of dynamics; (b) The time evolution of the average area per lipid molecule is plotted. Fluctuations of the average lipid area about a mean value indicate convergence and stability of the bilayer during the course of simulation.

5.1.3 Force field for the ligands

All atom force field (FF) for the ATP cofactor was taken from the AMBER parameter database maintained by the Bryce group. ATP molecules were first made fully deprotonated and then hydrogens were added using “reduce" available in the Amber Tools. All the phosphate atoms in ATP were deprotonated and the total charge was -4*e*. The atom names in ATP were also changed to match the naming convention of this FF. We used antechamber (109) and MCPB.py (110) to create the FF for the heme group. In the heme group, the iron metal coordinates to four nitrogen atoms. We have used a bonded model (99) where Fe is bonded to four sp3 hybridised nitrogen. The antechamber program was used with the AM1-BCC charge method (111) to assign charge by treating heme as having a charge of -4*e* and the atoms were treated with GAFF atom types (112). The procedure we followed to treat the heme group within the AMBER software package is described in detail in one of the Amber tutorials (99).

5.1.4 Docking

Docking of heme with HutCD in the IF state has been performed using AutoDock Vina (113) software. Coordinates of heme was retrieved from docking of Heme molecule in the pocket of HutCD was performed using a grid box of dimension 65 Å×40 Å×52 Å centred at (−29,+14,+15) Å.

5.2 Analysing the MD simulation results

5.2.1 Software used for analysis

Software used for data analysis are Origin, PyMol, UCSF chimera and Adobe photoshop.

5.2.2 Dynamics of HutD dimer in free and in HutC bound states

In order to understand the collective internal motions of HutD dimers in the OF and IF states, we have calculated root-mean-square deviations (RMSDs) of the Cα atoms from the snapshots of the trajectories up to 1 μs for the two chains of NBDs of HutD dimer and HutCD dimer (Fig. 5.2a-b). In all cases, RMSD values converged well to a constant value afer approximately 75 ns. RMSD values of the two HutD protomers (named as HutD1 and HutD2) were plotted separately (Fig. 5.2a-b). The RMSD values for HutD1 of HutCD OF, HutCD IF, and HutD IF and OF were steady around 3.0 to 3.5 Å (Fig. 5.2a). However, HutD2 in OF state showed relatively lower RMSDs ranging around 2 Å (Fig. 5.2b). This indicates that NBDs acquire stability upon Mg^{2+}-ATP binding, although asymmetric movements were observed between the monomers (Fig. 5.2a-b). B-factors of the two chains of HutD were also plotted separately. The highest B-factors were observed for HutD and the B-factors were lowest for HutD of HutCD in ATP-Mg^{2+} bound state (Fig. 5.2c-d). HutD of HutCD IF state showed intermediate flexibility (Fig. 5.2c-d). Further analysis of B-factors of the two monomers of HutD showed asymmetry/dissimilar movements. Reduction in fluctuations in the residues 100–115 of HutD1 in HutCD indicates that not only ATP-Mg^{2+} but the TMDs also help in stabilization of the complex, because of the interactions between L-loop of HutC and Q-loop of HutD (Figs. 4.2e, 5.1c-d). The flexibility and asymmetric nature of the A-loop (residues 12–23, Fig. 4.1b) are also evident for all the states, which is more distinct in case of HutD1 compared to HutD2 (Fig. 5.2c-d). As evident from large B-factor values, high flexibility was observed in certain surface exposed regions of HutD (Fig. 5.2c-d).

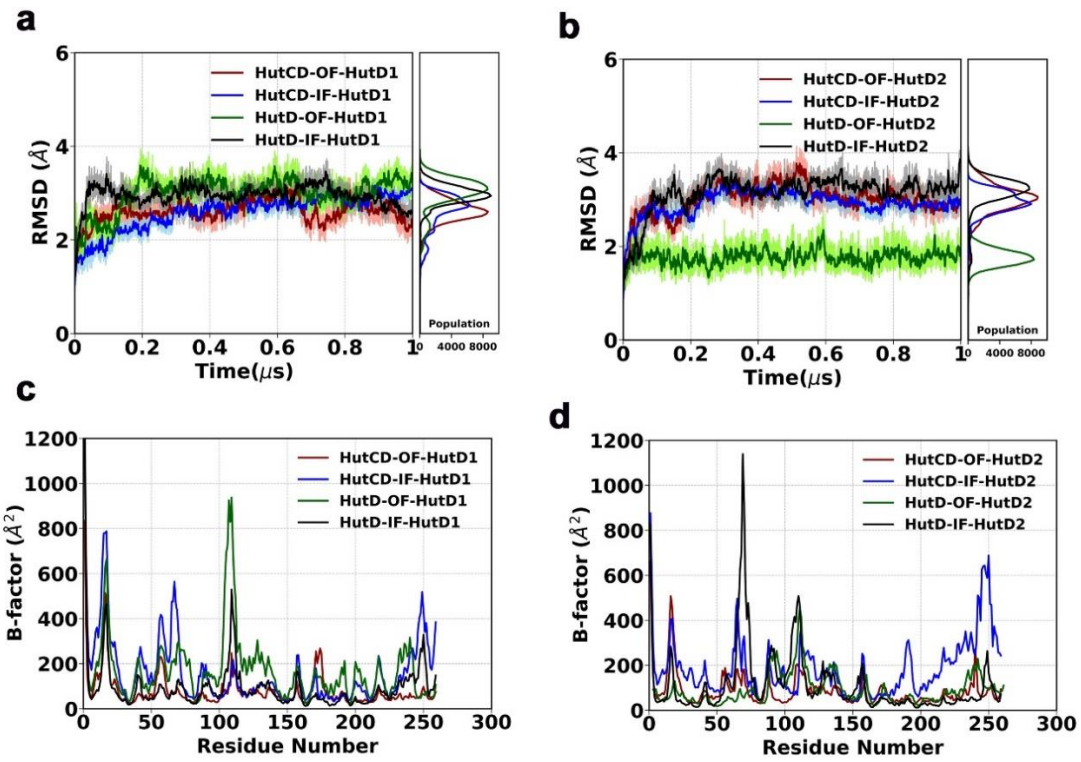

Figure 5.2: MD simulation results of HutD in the OF state. (a,b) Cα-RMSD values of HutD1 and HutD2 as part of HutD dimers and as part of HutCD assemblies in the IF and OF states; (c,d) B-factors of HutD1 and HutD2 as part of HutD dimers and as part of HutCD assemblies in the IF and OF states.

5.2.3 Interactions near ATP binding site of HutD dimer

Analysis of the simulation trajectory of HutD dimer in the presence of Mg^{2+}-ATP bound OF state revealed that Y15 of the A-loop packs hydrophobically with the adenine base of ATP where R18 interacts with the ribose sugar of ATP (Fig. 5.3a). During dynamics, Mg2+ consistently remains bound to E167 of Walker-B and is poised to hydrolyse ATP (Fig. 5.3a-b). D166, the neighbouring residue, interacts with S45 of Walker-A and thereby stabilizes the Walker-A conformation. K44 acts as the pivotal residue of Walker-A that interacts and stabilizes β- and γ-phosphates of ATP (Fig. 5.3a). These observations corroborate with abrogation of ATP hydrolysis of R18, K44, D166 and E167 to Ala (Fig. 3.2). In the OF state, the D-loops of the two HutD monomers interact with each other at the dimeric interface which is mediated primarily by T169 and S170 (Fig. 5.3b). H200 also participates in dimerization (Fig. 5.3c). H200 of both the chains interacts with the D-loops belonging to the trans protomer (Fig. 5.3c). N40 is found to play a dual role. Tis residue is capable of interacting both with the γ-phosphate of bound ATP and D173 of the D-loop belonging to the trans-acting HutD (Fig. 5.3b-c). ATP binding was found to be assisted by 'ABC signature motif' in BtuCDF (34).

However, we have hardly observed any contribution of 'ABC signature motif' in ATP binding for HutCD (Fig. 5.3b).

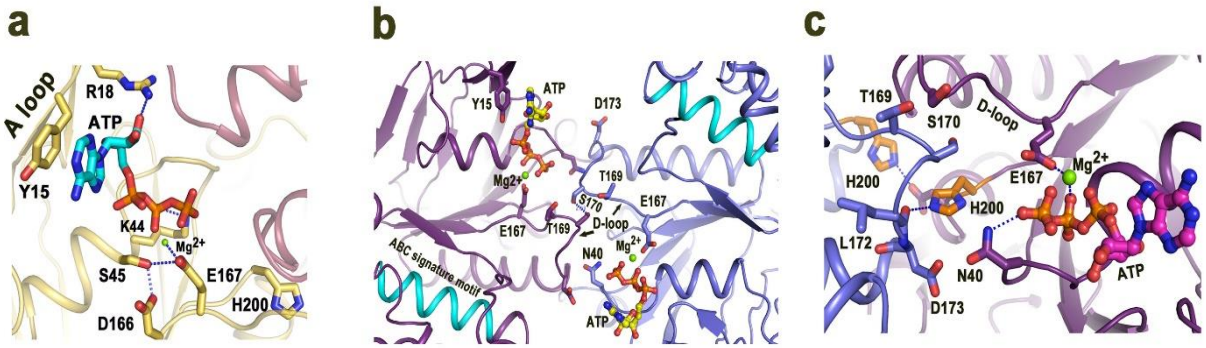

Figure 5.3: MD simulation results of HutD in the OF state. (a) ATP binding in HutD OF at 200 ns showing involvement of the residues of A-loop, Walker-A and Walker-B motifs; (b) Interactions between D-loops of two HutD monomers at 108 ns of simulation run on HutD dimer in the OF state; (c) Disposition of H200 at 150 ns of the simulation run on HutD dimer in the OF state.

5.*2.4 Dynamics of HutCD in the OF state*

We observed that RMSDs of the two HutD chains of HutCD converged after 75 ns and remained steady around 2.5 Å and 3 Å respectively. To investigate the flexibility and conformational shift of TMDs in HutCD, we have calculated the RMSDs of HutC1 and HutC2 in OF and IF states from MD trajectories run up to 1 μs. RMSD plots of two TMD chains (Fig. 5.4a-b) indicated that the values converged after approximately 75 ns. While RMSD values of HutCs in the IF state remained stable around 3 Å (Fig. 5.4a-b), significant fluctuations were observed in the RMSDs of HutCs in the OF state, ranging between 4 and 5 Å. Overall superposition of the snapshots in OF state (ranging between 100 and 750 ns) demonstrated high flexibility of the loops exposed to periplasmic side and encompassing the PLBP binding site (aa 30–55 of HutC) (Fig. 5.4c). Although these loops of both HutC monomers were apparently in the upright conformation in the staring model (Fig. 4.2d), after dynamics they culminated in different conformations (Fig. 5.4c). In one HutC monomer, this loop region was found in upright conformation whereas in the other it acquired an inclined conformation (Fig. 5.4c). Asymmetric movement of this loop in two HutC monomers might be attributed to ease the accommodation of the PLBP.

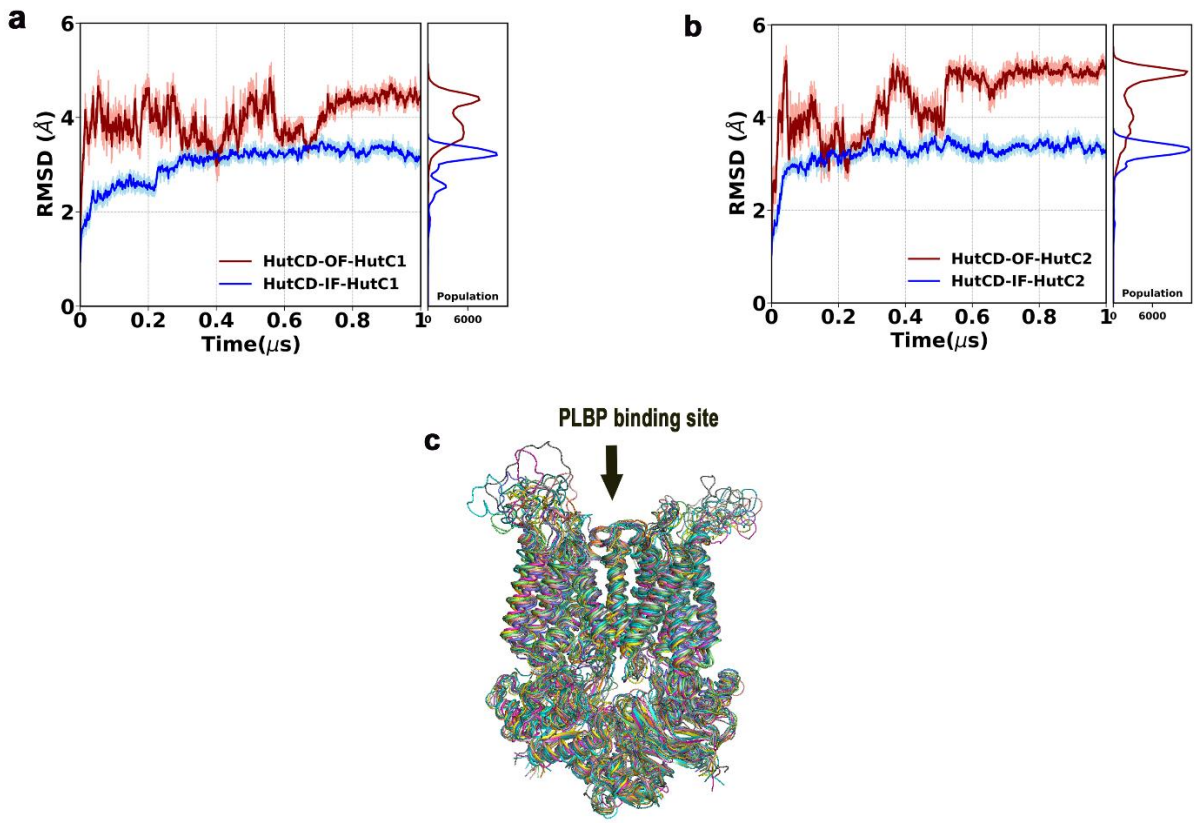

Figure 5.4: MD simulation showed OF to IF transition in HutCD. (a,b) Cα-RMSD values of HutC1 and HutC2 as part of HutCD assemblies in IF and OF states; (c) Superposition of snapshots showing overall movement in HutCD OF state. PLBP binding site using an arrow.

5.2.5 Synchronized conformational shift of HutD and HutC in ATP-Mg^{2+} bound OF state HutCD

Analysis of the simulation trajectory of HutCD OF state indicated that the interactions between the D-loops of the two HutD monomers are instrumental in the transmission of conformational shift to HutC. In HutCD, the distance between S170 of the SALD motif of the D-loops of the two monomers varied from 2.9 (103 ns) to 17 Å (606 ns) (Table 5.1). Upon proximity, the D-loops interacted with each other through H-bonding between S170 and/or T169 (Fig. 5.3b). N40 stabilized the γ-phosphate of ATP and interacted with D173 belonging to the 'SALD motif' of the D-loop of trans-acting protomer (Fig. 5.3b-c). However, this interaction was inversely related to inter HutD interactions through the D-loops, which is evident from Table 5.1. Upon proximity of the D-loops of the two monomers of HutD, N40 interacted with the γ-phosphate of ATP practically facilitating ATP hydrolysis. Available structures suggest that a cytoplasmic loop, called L-loop that is located between TM6 and TM7 helices of TMD, shares extensive contacts with the complementary groove on the NBD surface

and is proposed to be critical in TMD-NBD communication (37). Such interactions were evident in HutCD as well (Fig. 4.2d). Superposition of the snapshots, collected from 50 to 580 ns of the simulation run of HutCD, established retention of proximity and hydrophobic interactions between L-loop of HutC and Q-loop of HutD (Fig. 5.5a). The conserved Q85 of the Q-loop of HutD was also found to interact with the cis-acting D-loop. The conformational shifts in HutD dimer, caused by the position and the interactions of the D-loops, therefore, relayed to the L-loop of HutC through the Q loop of HutD. Trajectories of HutCD in OF state between 140 and 300 ns showed vigorous structural movements, and after 300 ns there has been a continuous loosening and widening of the overall structure, with concomitant dissociation of HutD1–HutD2 interface by distancing of D-loops (Table 5.1).

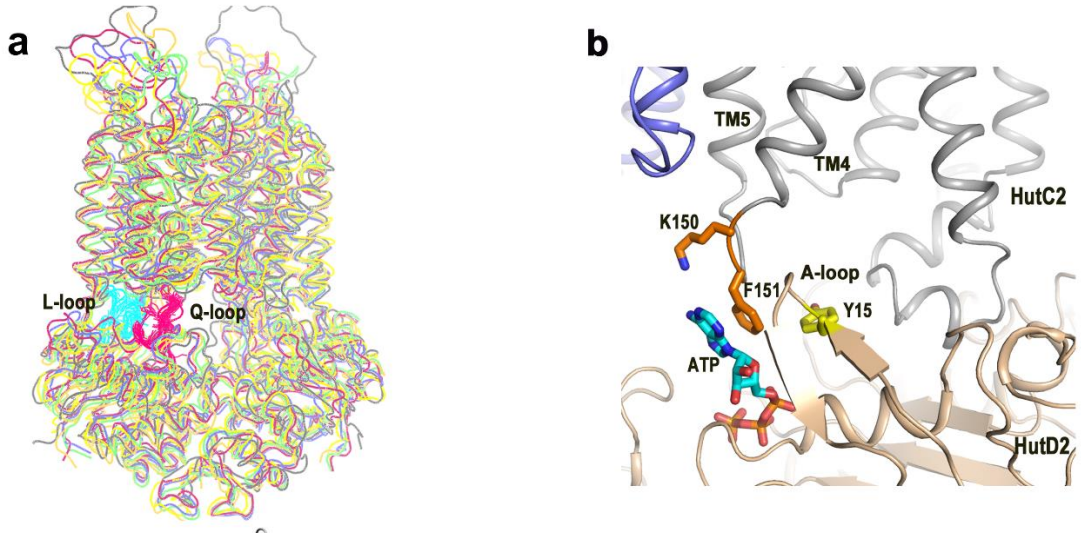

Figure 5.5: Synchronised conformation shift observed HutCD OF state. (a) Superposition of snapshots showing proximity between L-loop (cyan) of HutC and Q-loop (pink) of HutD during dynamics; (b) Snapshot of 150 ns shows interaction of F151 of HutC with ATP and Y15 of A-loop of HutD that causes cytoplasmic gate opening.

Table 5.1: Random frames taken to see any proximities between S170 of HutD1:N40 of HutD2, N40 of HutD1:S170 of HutD2 and S170 of HutD1:S170 HutD2

Trajectory of HutCD OF state	S170 of HutD1 / N40 of HutD2 (Å)	N40 of HutD1 / S170 of HutD2 (Å)	D-loop distance S170-S170
79 ns	11.65	5.49	4.6
98 ns	11.15	5.21	5.0
103 ns	7.2	5.38	2.92
117 ns	10.7	7.2	3.5
127 ns	7.64	7.56	2.93
136 ns	5.15	4.17	9.48
141 ns	4.02	2.81	8.65
151 ns	4.79	2.63	8.24
184 ns	3.88	5.15	8.09
342 ns	4.67	4.92	11.69
381 ns	2.89	4.47	9.93
400 ns	4.70	2.92	10.30
420 ns	3.71	3.88	11.22
450 ns	3.36	4.96	10.020
481 ns	4.70	4.76	11.889
500 ns	3.36	3.158	11.550
553 ns	4.863	4.653	12.052
595 ns	4.66	4.82	12.299
606 ns	5.80	6.9	17.26

5.2.6 Opening of the 'cytoplasmic gate'

The 'cytoplasmic gate' that resides in cytoplasmic side of TM5 is known to be instrumental in heme translocation, as evident from the structures of HmuUV and BhuUV (33, 71). F151 that belongs to the loop between TM4 and TM5 of HutC located near cytoplasmic gate is found to be important in terms of transmission of the signal. At the beginning of simulation, this loop was 13 Å away from HutDs. During dynamics, F151 was seen to pack with adenine base of ATP and Y15 of the A-loop of HutD (Fig. 5.5b). Interestingly, the involvement of F151 in such hydrophobic packing is not consistently simultaneous in each HutC–HutD duo. In early stage of simulation, such as 80 ns to 150 ns, the interaction remained simultaneous in both HutC1–HutD1 and HutC2–HutD2. However, after 200 ns the interactions were not that consistent. Subsequently, F151 of HutC packs with Y15 of HutD but adenine base of ATP remains sufficiently away from those residues. In these stages of the trajectory, such interaction was observed in one HutC–HutD, while in the other, the TM4-TM5 loop was away from the ATP binding site. At the beginning of MD simulation 'cytoplasmic gate' was closed (Fig. 5.6a) and as expected with OF structure, periplasmic side of the heme uptake

channel was open (Fig. 5.6b). During the progress of the simulation run, packing of F151 of HutC with ATP and Y15 of HutD increases the distance of TM5 in cytoplasmic side essentially opening the cytoplasmic gate (Fig. 5.6c). A superposition of the snapshots at 150 ns on that of frame 1 depicts such opening of the 'cytoplasmic gate' (Fig. 5.6c). This conformational shift made us hypothesise that ATP binding and hydrolysis facilitates opening of the 'cytoplasmic gate' for heme uptake.

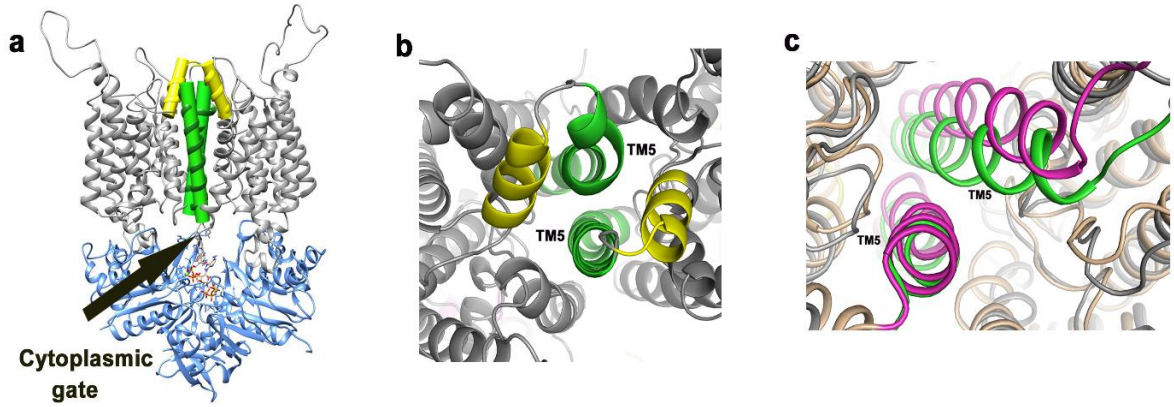

Figure 5.6: MD simulation results of HutCD in the OF state. (a) TM5 helices (green) of HutCD OF at the beginning of MD run; (b) Zoomed view of TM5 helices (green) and H5a (yellow) of the beginning frame from periplasmic side; (c) Superposition of snapshots of HutCD OF starting frame (green) and 150 ns (magenta) shows increased inter TM5-TM5 distance at leading to cytoplasmic gate opening.

5.2.7 Occluded state is observed in the simulation of ATP-free IF state of HutCD

As expected, the HutCD IF model showed inward facing orientation of the TM5 helices (Fig. 5.7a). Overall RMSD values of HutC and HutD dimers remained around~3 Å during simulation. Throughout the dynamics, the periplasmic side remained tightly sealed by salt bridge interactions between D182 and R186 along with hydrophobic packing between L185 of two H5a helices. Although the crossing angle of H5a–H5a was little lower (50.8°) than the structure of BhuUV (73.1°), like BhuUV, the position of H5a helices remained almost unchanged during dynamics. Notable transition in the orientation of the TM5 helices was observed from 277 ns (Fig. 5.7b). At this stage and onward, drastic reduction in the inter TM5–TM5 crossing angle occurred from 23.9° to 6.4° (Fig. 5.7b). Superposition of the snapshots of HutCD IF, collected at~277 ns, with the occluded ATP bound crystal structure of vitamin B12 importer BtuCD (PDB Code: 4FI3) showed a RMSD of 3 Å, indicating their gross resemblance (Fig. 5.7c). Maximum differences were observed among the NBDs, while orientation of the

TM5 helices of the two structures were outstandingly similar to each other (Fig. 5.7c-d). The crossing angle/distance of TM5 axes was 6.4°/16.2 Å in case of HutCD, and that of the ATP bound occluded structure of BtuCD is 11.2°/19.0 Å (PDB Code: 4FI3). These observations suggest that unbiased MD simulation of the HutCD in IF state leads to gradual transition to the ostensible occluded state from~277 ns by exclusive movement of the inter TM5 helices (Fig. 5.7b). The NBD domains of HutCD IF state remained oriented throughout dynamics, where the main flexible portion were the A-loops (Fig. 5.2c). In IF state, the trans-acting 'ABC signature motif' was found near the Walker-A, although the distance was not equal in case of the two protomers. Gradual proximity of the Walker-A and trans-acting 'ABC signature motif 'with the progress of simulation provided compactness to the NBD dimer. The D loops at the NBD interface were less flexible than the D-loops of Mg^{2+}-ATP bound OF state HutCD. In contrast to the OF state where D-loops of HutDs were found to interact, in the IF state, inter D-loop distance was ranging from 6 to 11 Å in most of the frames.

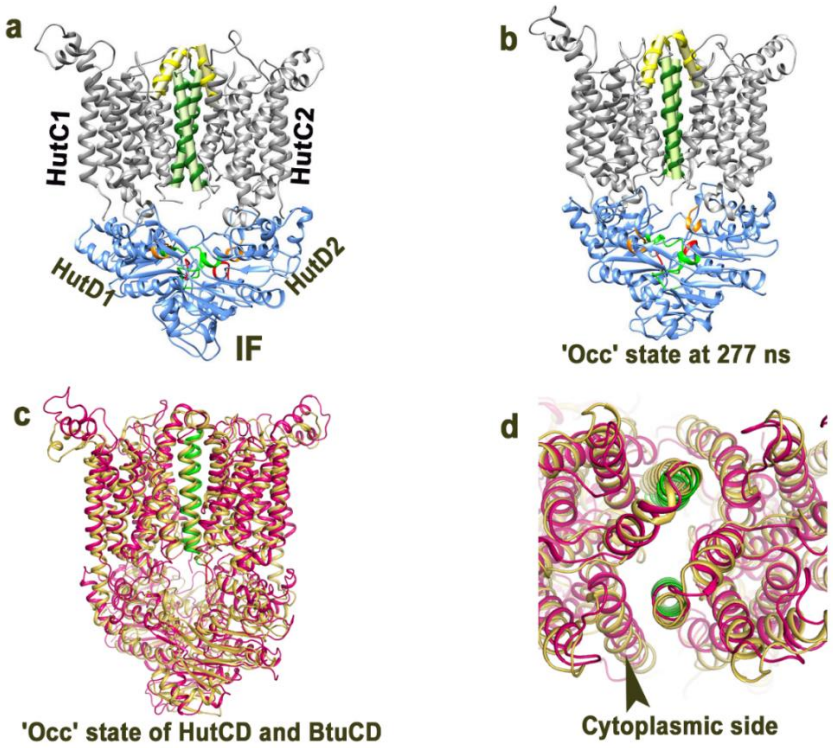

Figure 5.7: IF state of HutCD culminated to occluded state. (a) Ribbon representation of HutCD-IF model at 1 ns, showing axes of H5A(Yellow), and TM5(green), of each TMD in HutC dimer. (b) HutCD IF turned to 'occluded' state, snapshot taken at 277 ns from the unbiased MD study. Both in 'a' and 'b', D-loop, Walker-A and 'ABC signature motif' of HutD are shown in red, green and orange respectively. (c) Superposition of the 'occluded' state snapshot of HutCD IF at 277 ns on the 'occluded' state crystal structure of BtuCD (PDB code: 4FI3) (d) Zoomed view of (c) from cytoplasmic side showing similar orientation of TM5 helices (shown in green in case of HutCD).

5.2.8 Identification of heme release pathway in HutCD IF state

Naoe et al. stated that D112 of the TM2– TM3 loop of the permease BhuU of *B. cenocepacia* is the only charged residue exposed to the inward facing heme translocation pathway of BhuUV and plays critical role in the heme translocation process, because mutation of this residue to the hydrophobic residues impaired transport activity (46). Corresponding residue of HutC is E92 and as expected, this residue of both the HutC monomers are exposed to the heme translocation channel in the IF model of HutCD to impart polarity (Fig. 4.1a, 5.8a). We, therefore, intended to investigate the binding pattern and movement of heme, after it reaches the 'cytoplasmic gate'. For that reason, heme was docked near the cytoplasmic gate of inward facing HutCD using Autodock Vina (113) (Fig. 5.8b-c). The hydrophobic site was made of L159 and V163 of TM5 along with L90 of TM2–TM3 loop. One propionate group was hydrogen bonded with R87 of the TM2–TM3 loop (Fig. 5.8d). Soon after beginning of simulation, the heme molecule moved to the pocket between two HutC-HutD dimers (Fig. 5.8e–g). At this stage, the propionate group was interacting with the backbone NH groups of the Q-loop residues L89 and T90 of HutD1. Heme stayed inside this pocket 'flip-flopping' around for a significant period. Subsequently, heme was found to interact with N40 of Walker-A and the D-loop residues of HutD. Polar interactions of the propionates of heme with Q86, S88, T90 of HutD (HutD1) were steady from 350 to 430 ns (Fig. 5.8f). Additionally, F151 of HutC was found to pack with heme (Fig. 5.8g). Notably, F151 of HutC was crucial for cytoplasmic gate opening during ATP hydrolysis by HutCD in OF state. The pocket between two HutC-HutD dimers started squeezing around 455 ns. Around 465 ns the heme changed orientation and moved near the other HutD monomer (HutD2) where the propionates were interacting with S138 of HutD2 (Fig. 5.8g). Heme was on the verge of release to cytosol around 472 ns where heme was in contact with S138 of the 'ABC signature motif' of HutD2. At 473 ns, the propionate group of heme had polar interaction with S136 followed by H128 and the molecule is finally released to the cytosol (Fig. 5.8e–i). A detailed list of interactions between HutCD and heme is given as Table 5.2. During the process of heme release, no significant structural change occurred in the TMDs except orientation of TM5 (Fig. 5.8h). After 400 ns, the TM5 helices started acquiring an occluded conformation which was prominent around 460 ns (Fig. 5.8i). Attainment of occluded state is evident from the superposition of the snapshots collected at 85, 121, 410 and 468 ns (Fig. 5.8i). Here, conformation of TM5 remained unchanged in HutC1 where cytoplasmic side of TM5 of HutC2 shifted about 5 Å towards central axis of the translocation channel (Fig. 5.8i).

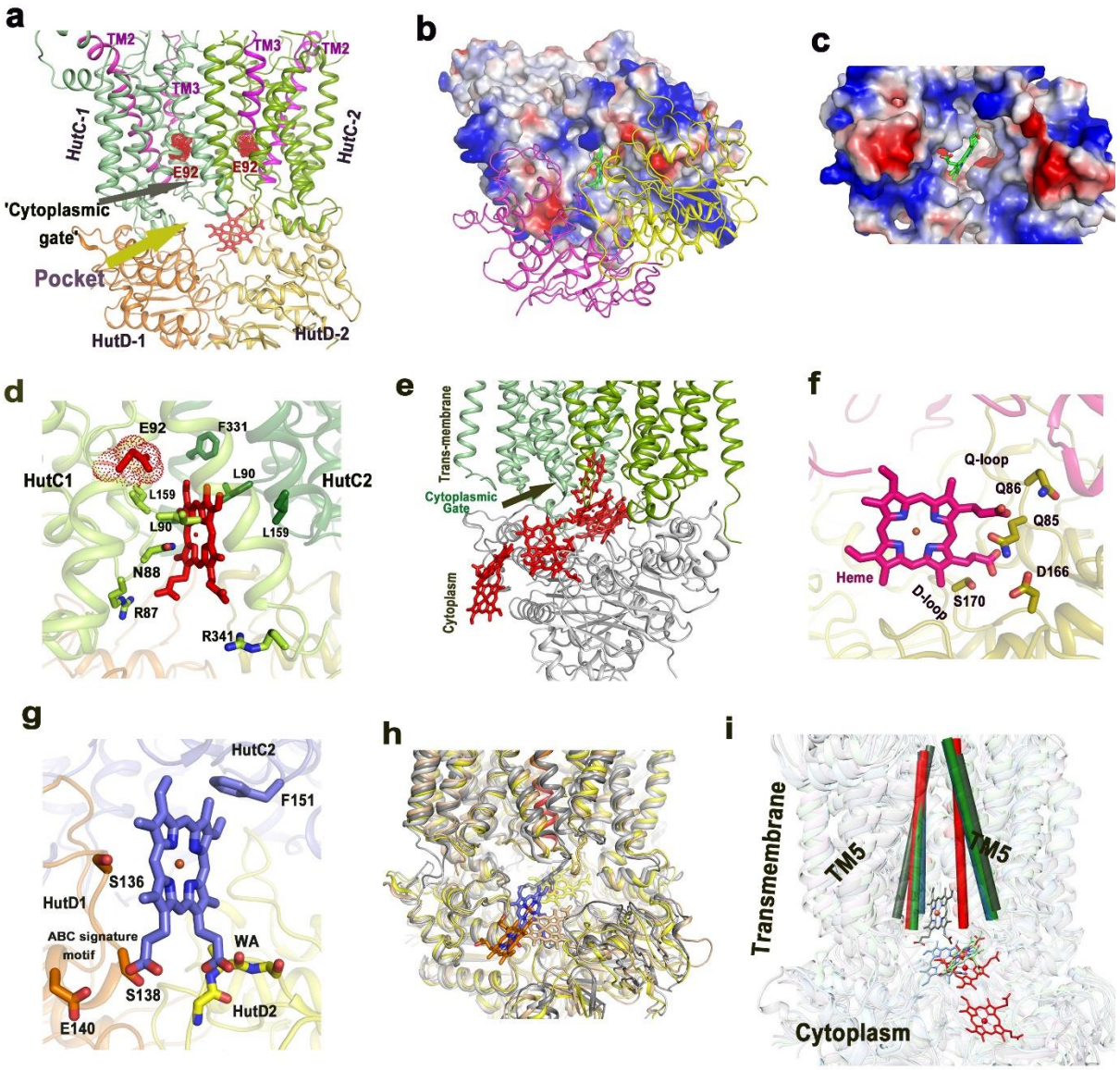

Figure 5.8: Heme release pathway from 'cytoplasmic gate' to cytosol. (a) Ligand release pocket between the two dimers, HutC1-HutD1 and HutC2-HutD2 and cytoplasmic gate is shown here.TM2, TM3 of each HutC monomer are shown in pink while E92, belonging to TM2-TM3 loop is shown in red; (b) Docking of Heme near cytoplasmic gate of HutCD IF; HutC dimer is shown in electrostatic surface representation whereas HutD dimer is shown in cartoon representation. (c) Zoomed view showing docked heme at the 'cytoplasmic gate' of HutCD dimer in IF state. HutD dimer is not shown here for clarity; (d) Zoomed view showing docking of heme near 'cytoplasmic gate' and its interactions with HutC residues; (e) Release pathway of heme from HutCD; (f) Snapshot at 133 ns shows interaction of Heme with Q-loop and D-loop residues of HutD; (g) Interaction of heme with F151 of HutC and S136, S138 of 'ABC signature motif' of HutD on the verge of release to cytosol; (h) Superposition of snapshots of HutCD IF at 85, 121, 410, 468 ns. HutC and HutD subunits undergo limited fluctuations during release of heme. (i) Zoomed view of superimposed snapshots reveals noticeable conformational shift ofTM5 helices (shown as cylinder) at 410 and 468 ns (red) especially in one TMD of HutC dimer compared to 1 (grey), 85 (green), 121 (blue) ns, leading to 'occluded' state during heme release.

Table 5.2: Heme interaction with HutD protomers in HutCD assembly:

Frames(ns)	Heme interaction with HutD2 Residue no.s and specific loop	Heme interaction with HutD1 Residue no.s and specific loop
123	[S88, L89, T90)], Q-loop • TM5, A-chain T156	-
172	S87,S88,T90, Q-loop	S88, Q-loop
289	S88, S138, SALD(170-174,D-loop)	-
414	S88, S138, SALD(170-174,D-loop)	Q85,Q86 (Q-loop), K49
1019	Q85, S88	S88
1063	Q85,Q86 (Q-loop), S88,E167, D170	-
1227	Q85,Q86 (Q-loop), S88,E167, D170	S88
1450	N40(P-loop), Q85,Q86, S88, Q143(ABC-signature motif),E167(WB),S170(D-loop)	-
1793	Q85, S170, A171, E167	Q86 S88
1903	G41, A42, G43, K44, K49, T46(P-loop), Q85	-
2852	K49, E167, S170, A171, Q85	-
3618	S17	-
4614	E167, S170, A171, Q85	-
5113	S88, E167, S170, Q85	-
6111	Q85,Q86, S87, S170, A171,G41, E167	T90, Q-loop
7608	L83, P84, Q85, S87, WB, Q143	-
9603	Q85,S88,L89,T90	Q86, S87, S88
12597	Q86-T90, Q-loop	-
14593	-	Q86, S88, L89, T90, L-loop
15092	-	S88 • HutC2-I342
16090	-	• HutC2-I342, HutC1-T156
26568	Q85	-
28564	Q86	-
34552	T90	-
38544	Q85, S87	-
40539	S87,S88,T90(Q-loop)	-
40884	S88,T90	-
41122	Q86,S88	-
43034	Q86,S87, S88	-
44032	Q-loop	-
44531	Q86, S88, L89	-
46883	Q19, A42, G43, K44, T46, Q217, G218, K219	P135, S136, L137, S138
47026	G41, A42, G43, K44(P-loop)	S132,L137, S138, E141
47143	-	S132, S136, L137, S138, G139
47160	-	S132,S135,S138
47162	N40, G41, A42 (P-loop)	S135,S138,G139
47168	K44	S138(ABC signature motif)
47205	-	S132,S135,S136 HEME IS MOVING OUT
47250	-	S132

Criteria: Selected all atoms/bonds of any residue that meet the criteria ≤ 4Å from heme.

Chapter 6

Contributions of HutD during heme internalization: Biochemical analysis

Summary

MD simulations previously envisaged that during internalization and release in cytosol, heme is first released in the pocket situated within two HutC and two HutD molecules. During that period, heme is expected to interact with the ABC signature motif, residues of D-loop, Walker-A, and Q-loop of the NBD, HutD, before it is released to the cytosol. However, that hypothesis was yet to be established experimentally. Therefore, we have investigated the interactions of heme with HutD and influence of these interactions on ATP binding/hydrolysis. Vis a vis, we have checked the influence of ATP binding/hydrolysis on the interactions of heme with HutD. This chapter contains the spectroscopic analysis, intrinsic fluorescence quenching, Malachite green ATPase assay and bioinformatics studies. Observations of these studies have corroborated with MD simulation results, and at the same time unveiled certain details of the interactions of heme and ATP with HutD.

6.1 Spectroscopic studies on HutD in occurrence of Heme

6.1.1 Methods: UV-visible Spectroscopy

For hemin titrations, the concentration of the purified 6×His-tagged HutD in 300 mM NaCl and 50 mM Tris–HCl (pH 7.0 and 8.0) was checked spectroscopically (ε_{280}=22920 $M^{-1}cm^{-1}$). For hemin titration, 10 μM of HutD was taken. A hemin stock solution of 3 mM was prepared in 100% DMSO. During titration, hemin was successively added from 2 μM to 56 μM into 10 μM of protein. After each hemin aliquot was added, samples were equilibrated for 10 minutes. UV/vis spectra were then recorded between 230 nm and 700 nm using a JASCO V-730 dual-beam spectrophotometer at 293 K. To obtain the difference spectra, the spectra of free hemin were subtracted from the spectra of HutD titrated with hemin. The same hemin titration of 10 μM of HutD was performed after prior incubation of HutD with the non-hydrolysable analogue of ATP, i.e., AMP.PNP from a stock solution of 50 mM, in the molar ratio of 1:2. Reproducibility of the results was confirmed by performing the experiments in triplicate.

6.1.2. Soret analysis indicated binding of hemin with HutD

This experiment aimed to assess the relative affinity of hemin for HutD using spectrophotometric hemin titration experiments. The absorption spectrum of hemin features a peak around 385 nm in the Soret band region (Fig. 6.1a). HutD alone does not exhibit absorption in the Soret region (Fig. 6.1a). However, upon titration with hemin, the Soret band

initially shifted to the right, with a maximum at 420 nm, and then experienced a minor blue shift to 415 nm (Fig. 6.1b). The ligand concentration was increased further to 56 μM to find if the increasing concentration of hemin affects the previous peak. However, the initial peak at 420 nm again obtained, followed by a similar extent of gradual blue shift to 418 nm (Fig. 6.1c). This experiments clearly indicated hemin binding with HutD.

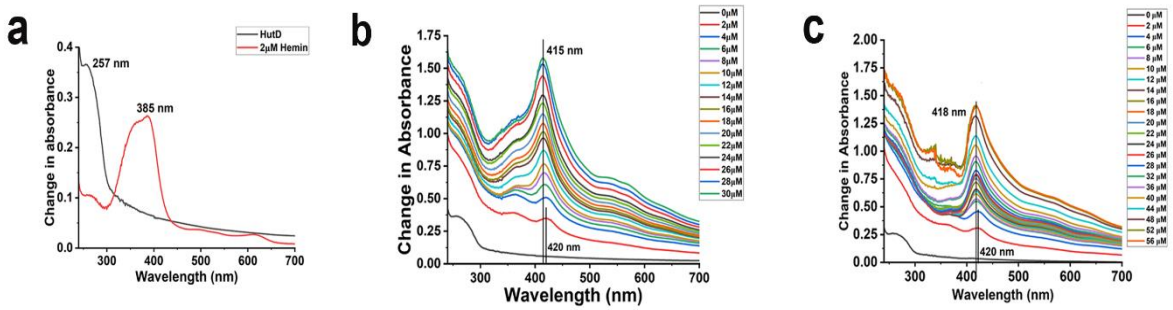

Figure 6.1: Hemin binding to HutD. (a) Hemin was subjected to UV-vis spectral scan and peak was observed at 385 nm. (b) HutD was titrated against increasing concentration of hemin (no protein in reference cell) and scanned after incremental addition of hemin till 30μM. Change in absorbance versus wavelength was plotted after subtracting blank (hemin titration in the absence of protein); (c) HutD was titrated with increasing concentration of hemin (no protein in reference cell) and scanned after incremental addition of hemin up to 56μM.

6.1.3 Soret analysis indicated that ATP does not hamper heme binding to HutD

We have further attempted to understand spectrophotometrically the effect of ATP on hemin binding by HutD. As previously noted, the absorption spectrum of hemin shows a peak around 385 nm in the Soret band region, whereas the protein lacks any peak in this region (Fig. 6.1b). Here we have titrated AMP.PNP incubated HutD with increasing concentrations of hemin that showed the initial peak at 418 nm, which gradually shifted to 416 nm producing saturation (Fig.6.2d). This study underscored that hemin binding with HutD was not essentially influenced by ATP binding.

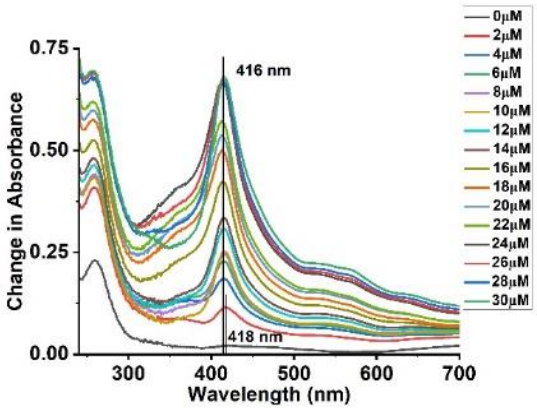

Figure 6.2: Hemin binding by AMP.PNP incubated HutD. AMP.PNP incubated HutD (1:2) was titrated with increasing concentrations of hemin till 30 μM. The resultant difference spectra (reference subtracted from sample) are shown here.

6.2 Affinity of Hemin towards HutD was measured by monitoring intrinsic fluorescence quenching

6.2.1 Methods: Fluorescence Spectroscopy

Following the procedure outlined in Chapter 3, fluorescence measurements were conducted using a Hitachi F-7000 spectrofluorometer with 1 cm path length quartz cuvettes. The fluorescence of tyrosine residues was monitored at an excitation wavelength of 280 nm, and emission spectra were recorded from 300 to 400 nm, with both excitation and emission slit widths set to 5 nm. All reactions were carried out in a buffer containing 50 mM Tris–HCl (pH 8.0), 300 mM NaCl and 5mM $MgCl_2$. Three sets of experiments have been conducted here: (i) HutD with Hemin as ligand, (ii) AMP.PNP incubated HutD with Hemin as ligand and (iii) Hemin incubated HutD with AMP.PNP as ligand. All the equilibrium titrations of HutD were carried out and the changes in fluorescence emission intensity were measured and recorded in the presence of increasing ligand concentration. The concentration of HutD was kept 5 μM of each reaction and hemin concentrations varied from 0 to 26 μM. For hemin incubated HutD experiment, the ligand AMP.PNP concentrations were varied from 0 to 625 μM. Maximum fluorescence (ΔF_{max}) value and apparent dissociation constant (K_d) for protein-ligand interactions were determined using non-linear regression.

6.2.2 Fluorescence quenching confirms hemin binding to HutD

Sequence and modelled structure of HutD depicted that Tyr15 is located close to ATP binding site. We have, therefore, measured the quenching of intrinsic fluorescence at λ_{ex}=280

nm and λ_{em}=300–400 nm. Significant quenching of fluorescence was observed with increasing concentrations of hemin from 0 to 26 µM indicating hemin binding to HutD. Plot of $\Delta F/\Delta F_{max}$ against hemin (µM) (using OriginPro 2024 software), produced K_d value of 2.15 ± 0.04 µM (Fig. 6.3a-b).

Similar fluorescence quenching was observed for AMP.PNP incubated HutD upon titration with increasing concentrations of hemin from 0 to 26 µM. In this case, plot of $\Delta F/\Delta F_{max}$ against hemin (µM) produced a K_d value of 2.18 ± 0.05 µM (Fig. 6.3c-d).

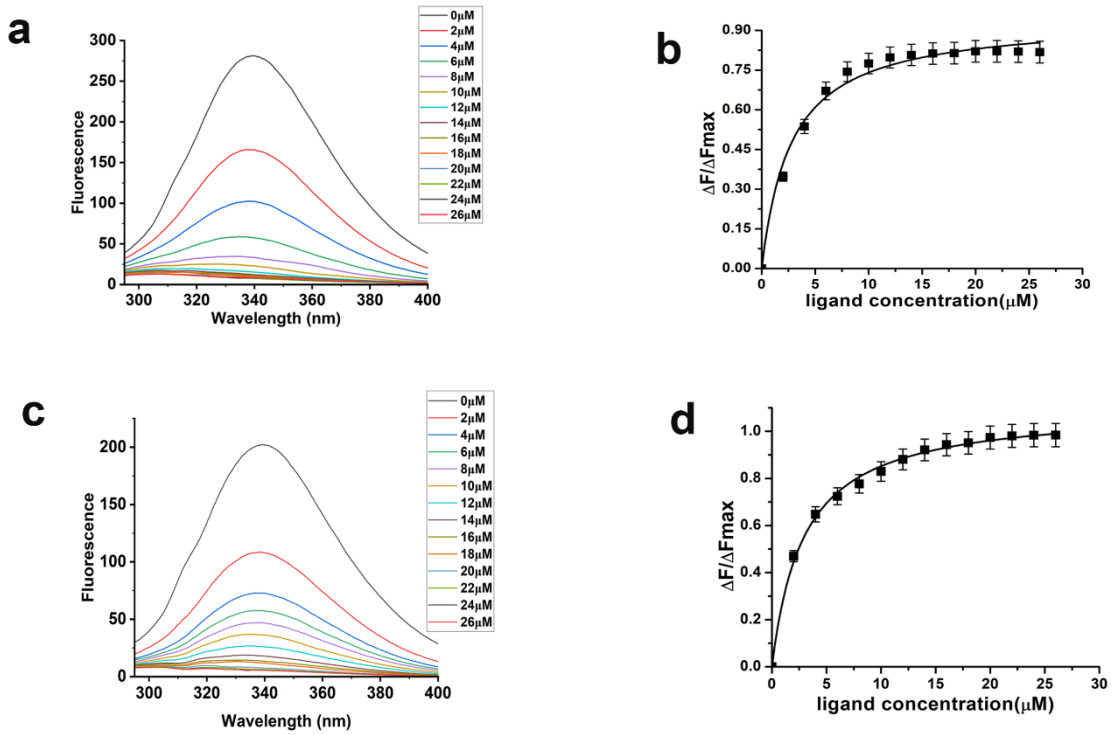

Figure 6.3: Hemin binding to HutD by fluorescence quenching. (a): Fluorescence quenching demonstrated significant change in fluorescence upon hemin binding to HutD; (λ_{ex} = 280 nm, λ_{em} = 300–400 nm) with slit widths of 5 nm for both excitation and emission. Concentration of hemin used was 0-26 µM. (b): Plot of $\Delta F/\Delta F_{max}$ against ligand hemin (µM) obtained a K_d value of 2.15 ± 0.04 µM. (c): Fluorescence quenching demonstrated significant change in fluorescence upon hemin binding to AMP.PNP incubated HutD; (λ_{ex} = 280 nm, λ_{em} = 300–400 nm) with slit widths of 5 nm for both excitation and emission. Concentration of hemin used was 0-26 µM. (d): Plot of $\Delta F/\Delta F_{max}$ against ligand hemin (µM) obtained a K_d value of 2.18 ± 0.05 µM.

6.2.3 Quenching confirms ATP binding to HutD even in the presence of Hemin

HutD, after incubation with hemin (1:1 molar ratio), titrated gradually with increasing concentration of AMP.PNP, showed significant fluorescence quenching, implying binding of

AMP.PNP to HutD in the presence of hemin (Fig. 6.4a). Plot of $\Delta F/\Delta F_{max}$ against AMP.PNP (mM) produced a K_d value of 153 ± 0.05 µM (Fig. 6.4b).

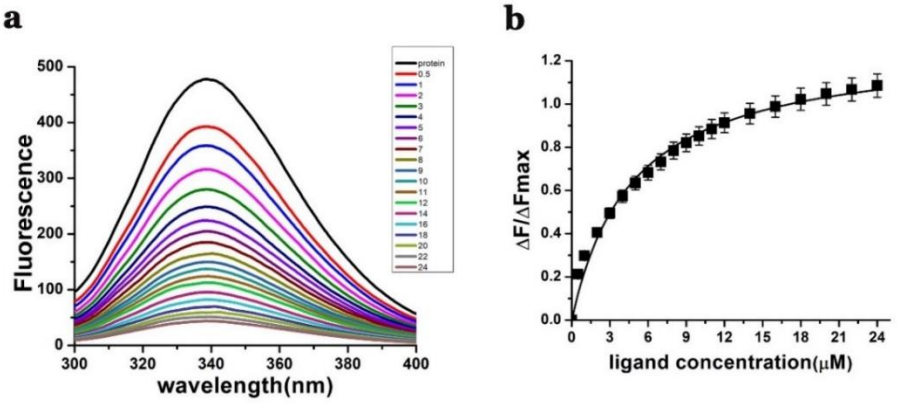

Figure 6.4: AMP.PNP binding by Hemin incubated HutD. (a): Fluorescence quenching demonstrated significant change in fluorescence upon AMP.PNP binding to hemin incubated HutD; (λ_{ex} = 280 nm, λ_{em} = 300–400 nm) with slit widths of 5 nm for both excitation and emission. Concentration of AMP.PNP used was 0-625 µM. (b): Plot of $\Delta F/\Delta F_{max}$ against ligand produced a K_d value of 153 ± 0.05 µM.

6.3 Measurement of ATP hydrolysis of HutD in the presence of Hemin

6.3.1 ATPase assay: methodology

As previously mentioned in Chapter 3, section 3.5.1, ATPase activity of HutD was investigated by Malachite green assay (92). Similar assay was performed for HutD incubated with 100 µM, 200 µM, 500 µM, and 1 mM of hemin (10mM were prepared in 100% DMSO). HutD incubated with different concentrations of hemin was assayed for its ATPase activity, where reaction mixtures containing 2.5 µM protein in buffer-R [made of 50mM Tris pH-8, 300mM NaCl, 5mM $MgCl_2$]. The Malachite green dye (composition as mentioned in Chapter 3.5.1) was freshly prepared. Pi standard curve was prepared by using KH_2PO_4 (Fig. 3.2g). All the experiments were minimally performed in triplicate.

6.3.2 Hemin impaired ATPase activity of HutD

The extent of ATP hydrolysis by hemin incubated HutD was much lesser compared to HutD. For 100 µM hemin, the first significant drop in amount of P_i released was seen, followed by a similar drop for 200 µM hemin (Fig. 6.5). ATPase activity gradually diminished further for 500 µM hemin, after which the amount of P_i released for 1 mM hemin did not decrease

noticeably. This observation suggested that saturation of HutD with hemin practically impairs ATPase activity of HutD.

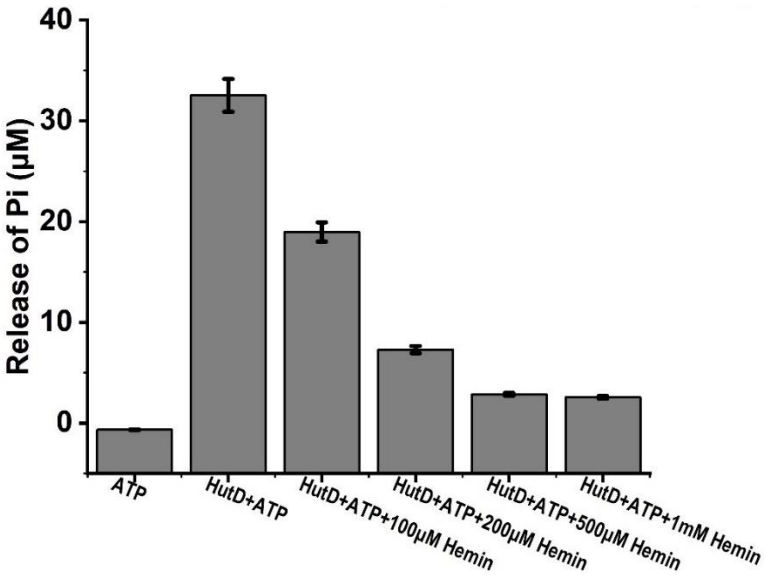

Figure 6.5: Hemin-incubated HutD showed a significant loss of ATPase activity during the Malachite Green assay, indicating that hemin binding affects ATP hydrolysis.

6.4 The effect of Protoporphyrin IX in ATP binding/ hydrolysis of HutD

6.4.1 Structure of Protoporphyrin IX

Protoporphyrin IX disodium salt (PubChem SID: 24855640, PpIX), lacking a metal ion, which belongs to the class of porphyrin family (Fig. 6.6). By studying how HutD interacts with Protoporphyrin IX (PpIX), which mimics the heme structure without the metal ion, we gain insights into the residues involved in binding, whether through the metal ion or not. This approach helps elucidate the molecular details of heme-binding proteins and their functional mechanisms. To validate our earlier findings that Heme strongly binds to HutD but hindered the ATPase activity, we assessed the binding affinity and ATP hydrolysis between PpIX and HutD through fluorescence quenching and Malachite green assay. Protoporphyrin IX disodium salt (Sigma) was first dissolved in 0.1 M Tris base, and then DMSO was added to make the concentration 3 mM. During our experiments, PpIX was diluted in buffer at pH 8.0.

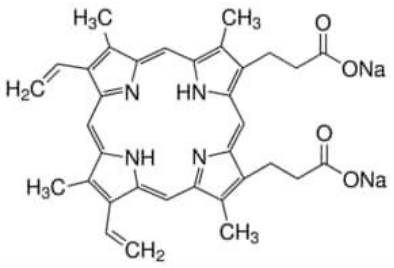

Figure 6.6: Structure of Protoporphyrin

6.4.2 HutD binds to Protoporphyrin IX as well

HutD showed intrinsic fluorescence quenching when titrated with increasing concentrations of PpIX (Fig. 6.7a), ranging from 0 to 16 µM. The results indicated that PpIX can intensely bind HutD to quench intrinsic fluorescence. Plot of $\Delta F/\Delta F_{max}$ against PpIX obtained a K_d value of 1.65 ± 0.03 µM (Fig. 6.7b). PpIX was devoid of metal ion and binding of this compound with HutD established that the binding of hemin with HutD takes places through hydrophobic and polar interactions and not through the axial coordination with the metal ion.

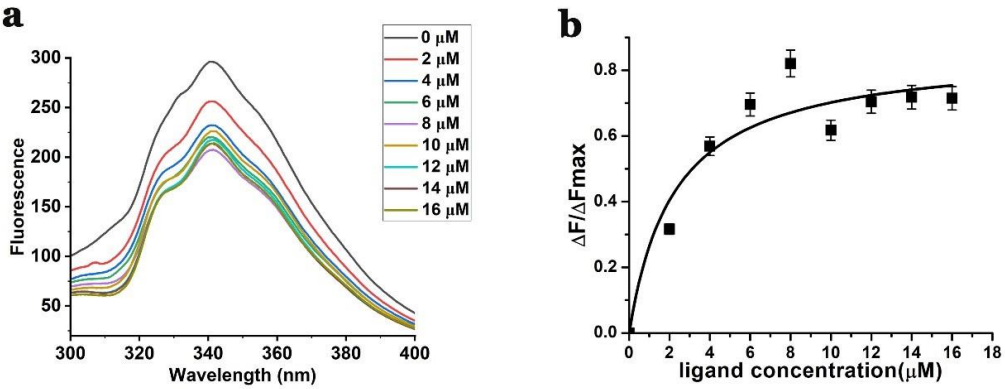

Figure 6.7: HutD binds to PpIX. (a) Fluorescence quenching demonstrated significant change in fluorescence upon PpIX binding to HutD; (λ_{ex} = 280 nm, λ_{em} = 300–400 nm) with slit widths of 5 nm for both excitation and emission. (b) Plot of $\Delta F/\Delta F_{max}$ against ligand PpIX (µM) produced a K_d value of 1.65 ± 0.03 µM.

6.4.3 Like Hemin, Protoporphyrin IX also impairs ATPase activity of HutD

The extent of ATP hydrolysis in the presence of PpIX incubated with HutD is significantly lower compared to HutD alone. The ATPase activity of the protein decreases notably as the concentration of PpIX increases (Fig. 6.8). A significant reduction in the amount of inorganic phosphate (Pi) released was observed at 100 µM PpIX. At a concentration of 500 µM PpIX, the amount of Pi released remained relatively unchanged (Fig. 6.8).

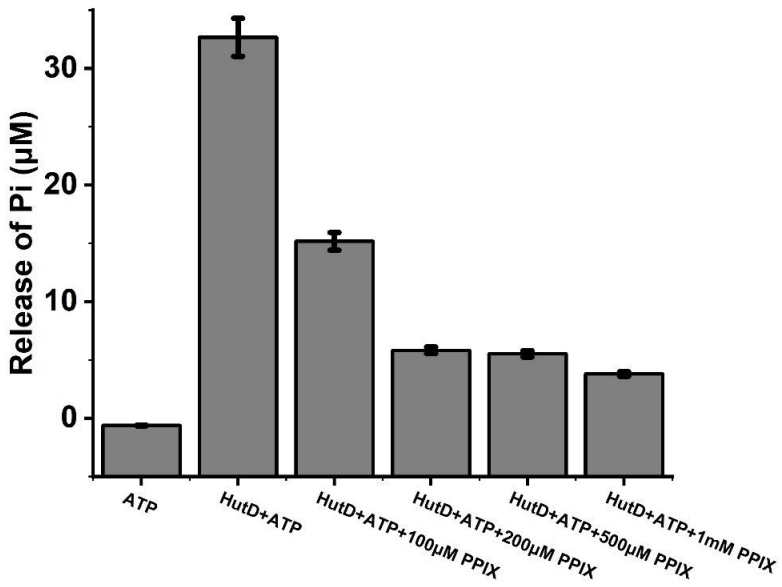

Figure 6.8: PpIX incubated HutD showed a significant loss of ATPase activity during the Malachite Green assay.

6.5 Sequence comparisons of HutD of *V. cholerae* with similar nucleotide binding proteins of Heme ABC importer of other gram-negative bacteria

6.5.1 Methodology

To structurally characterize HutD, a BLAST searches have been conducted using the amino acid sequences of HutD (Accession code: A0A0H3ADP8) against Protein Data Bank (PDB) and UniprotKB reference proteome and Swiss proteome.

6.5.2 Multiple sequence alignment showed conservation of sequence and structure across the hemin transporter family

The cytosolic ATPase HutD shares 55% identity (with 75% similarity over 254 amino acids) with the ATP binding protein of heme transporter from *Photobacterium damsela subsp. piscicida*, and 55% identity (with 74% similarity over 257 amino acids) with the ATP binding protein of heme transporting ABC transporter from *Psychromonas sp*. Sequences of the NBD of heme transporters from 20 other gram-negative organisms were obtained and aligned with the query sequence (HutD of *V. cholerae*) to analyse conservation of residues interacting with heme during its release into the cytosol through the translocation channel (Fig. 6.9). According to MD simulations discussed before, residues such as N40 of Walker-A, Q86, S88, L89, and T90 of the Q-loop, S138 of the ABC signature motif, H128, and S136 were observed interacting with heme prior to its movement towards cytosol (Fig. 5.8f-g). Residues N40, S88, L89, H128,

and S138 were highly conserved, whereas residues Q86, T90, and S136 were found to be substituted by similar amino acids in various gram-negative organisms (Fig. 6.9).

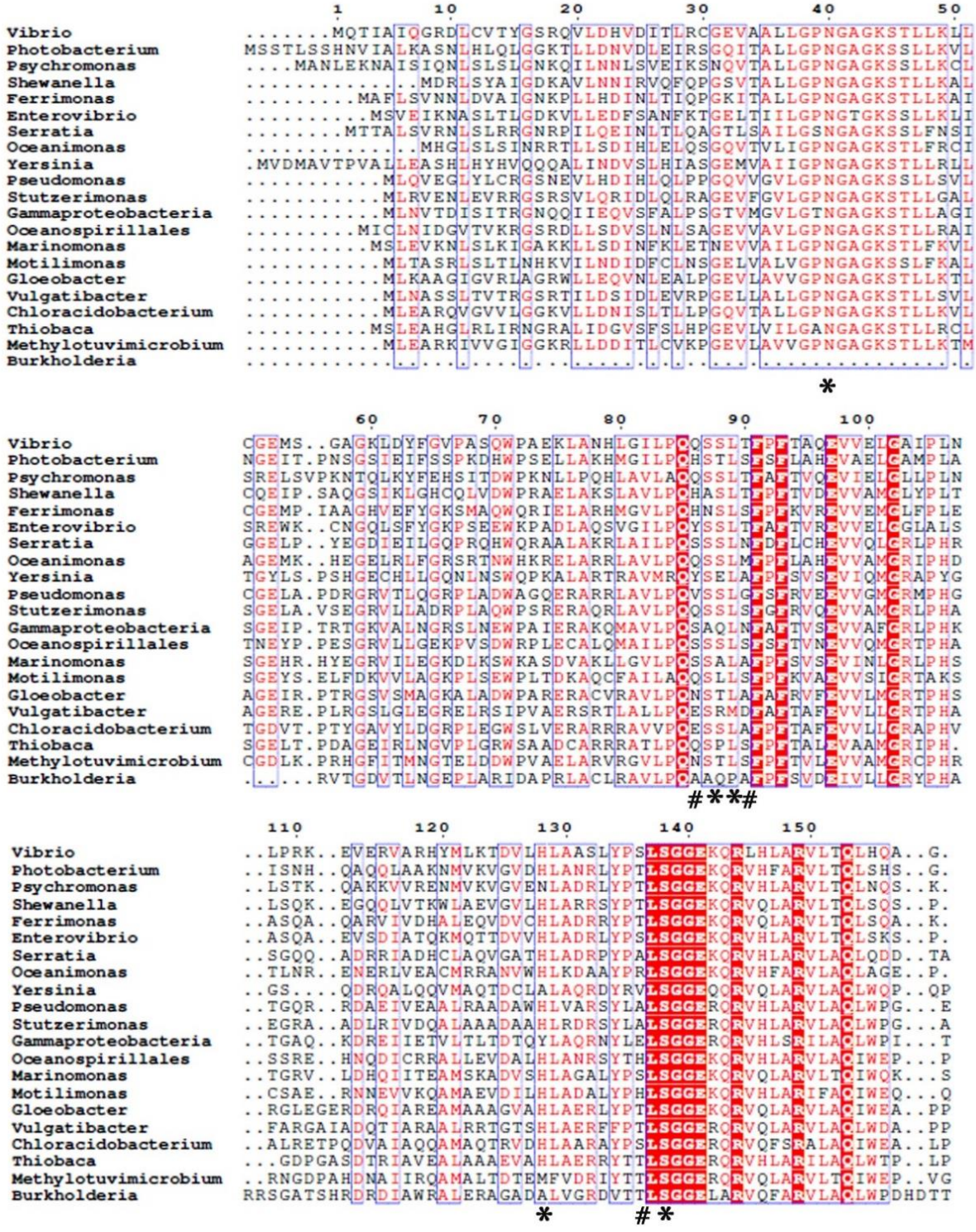

Figure 6.9: Sequence alignment of HutD from *Vibrio cholerae* with nucleotide binding domains of heme transporters from other gram-negative bacteria. Numbering is based on HutD sequence. Conserved residues are marked with "*" and the residues that are substituted by similar amino acids in the different organisms are marked by "#". The conserved regions are shown in red.

Chapter 7

Discussion: Type-II ABC importer HutCD-B

Dimerization of the NBDs in ABC importers of prokaryotes, whether nucleotide driven or independent, is indispensable, since this is a vital early event of ligand translocation. Our results authenticated HutD as a type-II ABC importer, since it forms dimer even in the absence of the permease, HutC (Fig. 3.2a-c). Based on the sequence comparisons, Y15 of the A-loop of HutD was predicted to pack with the adenine base of ATP (Fig. 4.1b). Substantial fluorescence quenching in the presence of AMP.PNP established significant binding of ATP with HutD in 1:1 stoichiometry with the involvement of Y15 (Fig. 3.2d-f). While HutD was an efficient ATPase, R18A, K44A, D166A and E167A turned out as loss-of-function mutants (Fig. 3.3a-b). Abrogation of ATPase activities in the mutants together with modeling, docking and MD simulations results suggested that R18 of the A-loop and K44 of Walker-A of HutD stabilize the ribose sugar and the β-phosphate of ATP respectively and hence, ATP binding is compromised upon removal of those side chains (Figs. 4.1b, 3.3a-b, 4.2c). Based on the sequence analysis (Fig. 4.1b) we presumed that D166 and E167 are crucial Walker-B residues for conducting ATP hydrolysis event. Our observations demonstrated that E167 is implicated in Mg^{+2} binding for ATP hydrolysis while neighbouring D166 interacts with S45 of Walker-A to facilitate ATP binding by stabilizing Walker-A. Rather, a network of polar interactions was observed between S45 of Walker-A and D166, E167 of Walker-B as evident from the snapshot of MD simulation (Fig. 5.3a). Mutation of D166 to Ala presumably generates more space for E167 side chain and at the same time turns E167 more flexible because of impaired polar interactions stated above, eventually disturbing Mg^{2+} binding/ATP hydrolysis.

MD simulation trajectory of HutD in ATP bound state depicted that D-loops of the two HutD monomers interact at the dimeric interface and H200 critically contributes to the dimerization by interacting with the *trans*-acting D-loop (Fig. 5.3c). MD simulation results further suggested that ATP binding to HutD does not need any assistance from the *trans*-acting 'ABC signature motif' (Fig. 5.3b), like it was observed before in the crystal structure of BtuCD-F (43). Rather, in HutCD, 'ABC signature motif' interacts with the heme during its ejection to the cytosol. Presumably, the translocation of bigger ligand vitamin B12 requires a wider channel compared to heme (HmuUV structure) and the NBDs need to dimerize accordingly. The difference in ATP binding mechanisms might be attributed to the differential inter dimeric interactions of BtuD and HutD, which are essential for the ligand- and species-specific transportation pathways.

In case of permeases, conformational shifts of certain transmembrane helices, especially the movable helices TM5 and H5a, regulate the ligand import processes through

ABC importers. Substrate translocations through the translocation channels of type-I ABC transporters MalK of *E. coli* are dictated by 'tweezer' like or 'twisting' motions of the NBDs (114, 115). For type-II importers, substrates translocation by the opening or closure of the cytoplasmic gate is thought to occur via 'peristaltic' motions of the TMDs (70). MD simulations suggested that in HutCD, a rotational motion occurs in the TMDs in synchronous manner with the inter NBD D-loop interactions (Table 5.1). The more the separation of the inter HutD D-loops, the more rotation of the NBDs occur which is then transmitted to the TMDs. The distance between the two HutC-HutD dimers was found to be altered accordingly. However, asymmetry has been observed in the interface interactions between HutC and HutD for each HutC-HutD duo.

The interaction of the SKF^{151} loop of HutC, located between TM4 and TM5 near the cytoplasmic gate, with ATP and the A-loop ($Y^{15}GSR$) of HutD is one of the most prominent facts that tie the event of ATP hydrolysis with the conformational change in HutCs to facilitate ligand translocation (Fig. 5.5c). Packing of F151 with the adenine base of ATP and Y15 of the A-loop of HutD leads to the widening of the cytoplasmic gate where the periplasmic side of the TM5 helices remained practically unchanged (Fig. 5.5c, 5.6c). Interestingly, in the later stage of the dynamics (~400 ns and beyond), which might be treated as post hydrolysis phase, continuous relaxation of the assembly was observed and, in this situation, TM5 helices prefers to acquire relatively parallel conformation. Inward facing assembly was also culminated to an occluded conformation, like it was observed before for vitamin B12 importer BtuCD (Fig. 5.7c-d). We, therefore, hypothesized that the occluded state is the most preferred conformation of HutCD.

H5a was seen to play a key role as a gating helix to form the interaction site for the PLBP, BhuT in the case of BhuUV-T assembly (46). Also, mutation of R176 in H5a of the permease, HmuU was reported to decrease affinity to the NBD, HmuT, and decrease heme-transport activity (33). Although TM5 helices showed visible transition near the cytoplasmic gate, conformation of H5a helices, located at the periplasmic side, practically remianed unchanged during the dynamics. We, therefore, hypothesize that the movement or change in orientation of H5A helices are most likely PLBP dependent, and subsequent separation of the PLBP from the TMDs may result in the transition of orientations of the H5A helices.

The heme release mechanism has been deciphered for the first time which was unknown so far. Our extensive simulation showed that the release of heme is primarily dictated by the

interaction of the propionate groups with the polar residues of HutC–HutD dimeric pocket (Fig. 5.8f-g). Interaction of heme with the residues of HutD (D-loop, Walker-A, Q-loop and 'ABC signature motif') (Fig. 5.8f-g, Table 5.2) further suggested that heme release event takes place in the absence of ATP. The parallel conformation of TM5 helices in HutC, in the occluded state probably leads to the squeezing of inter-dimeric pocket which eventually facilitates the heme release (Fig. 7). This suggests that type-II ABC importers, such as HutCD, adopt an occluded conformation as a preparatory step before initiating the subsequent cycle of ATP hydrolysis necessary for the translocation of heme. (Fig. 7).

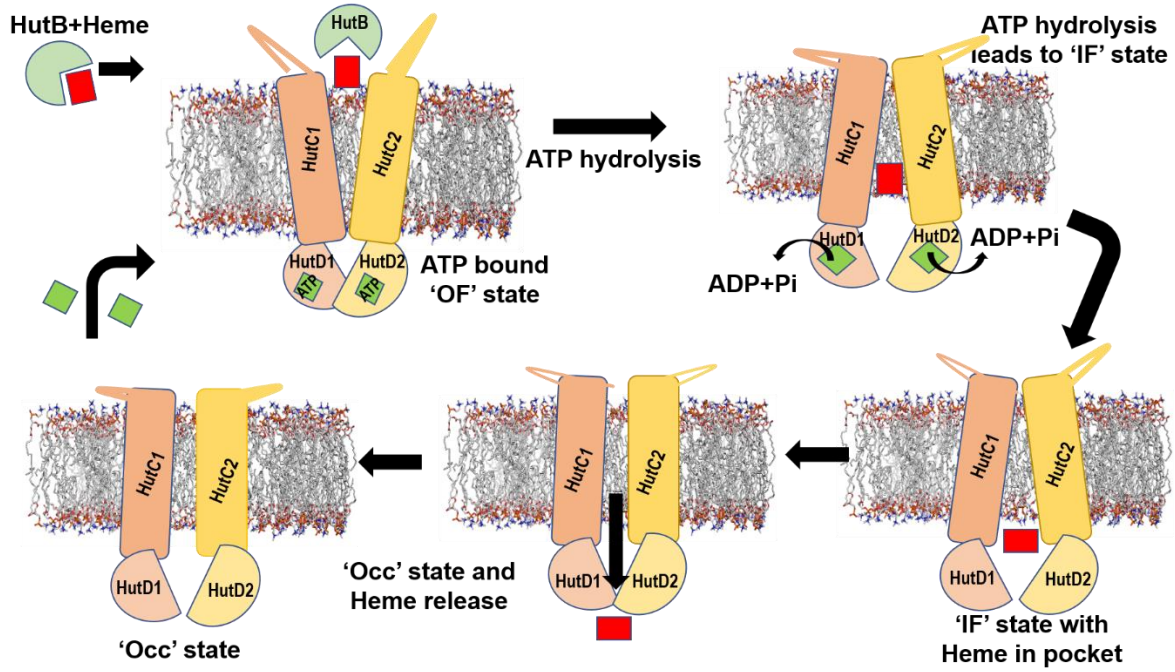

Figure 7: Proposed reaction mechanism. Involvement of TM4-TM5 loop in ATP hydrolysis causes cytoplasmic gate opening (IF state) easing heme release to the inter-dimeric pocket. Formation of occluded state constricts the pocket and releases heme.

Mechanistic differences based on subtle interactions are prevalent among type-II ABC importers like HutCD, HmuUV, BhuUV or BtuCD (33, 43, 46). Notably, Y15 of HutD or F151 of HutC, which stack with the adenine base of ATP leading to conformational changes in HutCD assembly, are not conserved in HmuV or BhuV (Fig. 4.1b). Although similar hydrophobic residues are observed in HmuUV in the close vicinity of the respective residues, BhuUV is quite different in this regard (Fig. 4.1). Furthermore, S170, the crucial D-loop residue of HutD is replaced by Ala in BhuV (Fig. 4.1b) generating a possibility of compromised D-loop interactions.

Our extensive simulation studies indicated that final release of heme to the cytosol is primarily dictated by the interaction of the propionate groups with the polar residues located in HutC-HutD dimeric pocket (Fig. 5.8f-g). Interaction of heme with the residues of D-loop, Walker-A, Q-loop and 'ABC signature motif' of the NBD, HutD (Fig. 5.8f-g, Table 5.2) further suggested that heme release event takes place in the absence of ATP. Because the presence of ATP would have hindered involvement of aforesaid motifs in the heme release process. Keeping this in mind, we wanted to investigate how heme binding with HutD affects ATP binding/hydrolysis, or vice versa. The shift of the Soret band upon titration of HutD with hemin (Fig. 6.1a) was indicative of perturbation in the electronic structure of hemin upon HutD binding. Binding of protoporphyrin IX (which is devoid of metal ion) with HutD confirmed that Fe^{2+} does not mediate the binding of hemin with HutD via axial coordination. Rather, hemin-protein interactions take place through hydrophobic and polar coordination.

Titration of AMP.PNP incubated HutD with increasing concentrations of hemin disclosed a similar binding. Fluorescence quenching data further established that hemin binds HutD, with a high K_d value (of 2.15 ± 0.04 μM) (Fig. 6.1c). In the presence of AMP.PNP, fluorescence quenching produced a similar K_d value of 2.18 ± 0.05 μM (Fig. 6.1d). Aforesaid observations implied that ATP binding does not interfere with or hinder heme binding to HutD. On the other hand, ATPase assay of heme incubated HutD showed impaired ATP hydrolysis. This observation raises two possibilities: (i) ATP is not binding to HutD in the presence of heme, at all, or (ii) ATP is binding to HutD in the presence of heme, but not getting hydrolysed. Previously it was observed that AMP.PNP binds HutD with an apparent K_d value of 94±0.02 μM (Fig. 3.3b). When HutD, incubated with hemin, was titrated with AMP.PNP, fluorescence quenching produced a K_d value of 153 ± 0.06 μM (Fig. 6.4b). This implied that ATP can bind weakly to HutD even in the presence of hemin, although the binding is slightly compromised.

Aforesaid results indicate that although ATP can bind HutD in the presence of hemin, hemin hinders ATP hydrolysis. According to MD simulation, heme was seen to remain bound to HutD for quite some time, where it continued to 'flip-flop' (Fig. 5.8a). Subsequently, it interacted with N40 of Walker-A and the D-loop residues of HutD. After that heme changed its orientation where the propionates were found to interact with S138 of HutD. MD simulation together with biophysical/biochemical analysis indulged us to infer that hemin binding does not obscure the ATP binding site of HutD. However, release of heme in the cytosol involves the Q-loop of HutD. Binding of hemin to Q-loop locks Walker-B in such conformation that the residues remain unavailable for ATP hydrolysis. This is the reason why ATP hydrolysis does

not occur during release of hemin to cytosol. BLAST search against UniprotKB reference proteome and Swiss proteome using the amino acid sequences of the HutD has shown high conservation of hemin binding residues such as N40, S138, L89 and H128 in the HutCD importer systems of many other gram-negative bacteria, further confirming the proposed mechanism of heme transport.

Chapter 8

Glucose-6-Phosphate internalisation in type-I VCA0625-27 ABC transporter of *Vibrio cholerae*

8.1 VCA0625-27: The ABC importer for Glucose-6-Phosphate uptake in *V. cholerae*

Internalization of nutrients across the plasma membrane of bacteria takes place via ATP binding cassette (ABC) transporters where PBP binds incoming ligand, and cytosolic ATPase NBD hydrolyse ATP to create large-scale conformational changes in the permease, accelerating nutrient uptake (18). Despite their common basic architecture, ABC importers are structurally and functionally diverse (37). The life cycle of *V. cholerae*, depend on transitions between the aquatic environments and human small intestine. In seawater, carbon sources are scarce, which poses challenges for *V. cholerae*. To overcome this, the bacterium employs various strategies, including the utilization of chitin from marine crustaceans and the storage of intracellular glycogen. Additionally, extracellular DNA and dissolved organic matter in seawater contribute to supporting the growth of *V. cholerae*. Despite these adaptations, the precise mechanisms that enable *V. cholerae* to efficiently uptake and metabolize carbon sources from seawater remain incompletely elucidated.

Glucose-6-Phosphate (G6P) is an essential nutrient as carbon source for various pathogenic bacteria. In *V. cholerae*, G6P serves as a substrate for intracellular pathogen replication and is required to prepare cells for better survival in phosphate-limiting environments (116-118). However, the mechanism of G6P uptake by different bacteria is less well understood yet. The VCA0622 to VCA0627 gene cluster was identified as in vivo induced in response to G6P, highlighting its role in adapting to phosphate-limited environments (118). Among these genes, the operon spanning VCA0625 to VCA0627 encodes an ABC transport system for hexose-6-phosphates. The presence of G6P induces the expression of an operon in *Vibrio cholerae*, which is regulated by the transcriptional activator VCA0622. This operon includes the putative ABC transporter system composed of the proteins PBP VCA0625, a membrane permease VCA0626, and ATPase VCA0627 (Fig. 8). Recent research has characterized this ABC transporter as being responsible for the uptake of hexose-6-phosphate, which *V. cholerae* utilizes as a carbon and phosphate source. This transporter system is crucial for the bacterium's survival, especially when transitioning from the host environment to environments with limited phosphate availability.

However, the structure, dynamics, and mechanism of sugar-phosphate internalization by this importer remained elusive. Understanding the molecular details of G6P import mechanisms in pathogenic bacteria is crucial for developing new therapeutic strategies.

Targeting these transport systems could potentially disrupt bacterial metabolism and virulence, offering novel approaches for antimicrobial therapy.

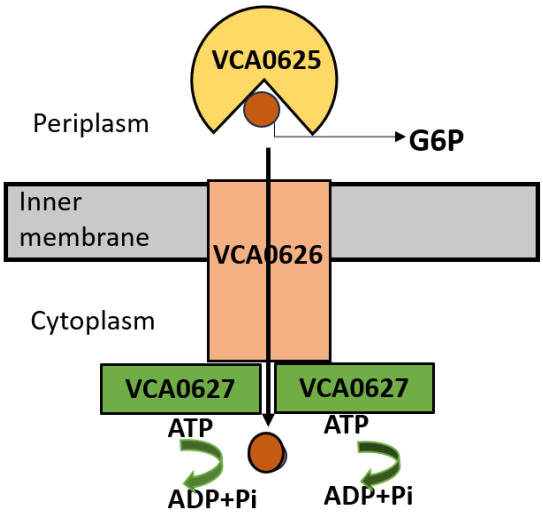

Figure 8: Type-I G6P VCA0625-27 ABC transporters of *Vibrio cholerae*

So far, structural, and mechanistic details of G6P uptake by ABC importer is largely restricted to the periplasmic ligand binding protein (PLBP) AfuA of AfuABC in *Actinobacillus pleuropneumoniae* (119) (PDB code: 4R73). Moreover, crystal structures of the best characterised type-I maltose transporter $MalFGK_2$-E from *E. coli*, demonstrated an 'inward-facing' (IF) conformation with the substrate translocation pathway open to the cytoplasmic side; 'pre-translocation state' (pre-T) a nucleotide-free semi-open intermediate state in which substrate initiates the transportation cycle by narrowing the translocation pathway close to the periplasmic side; an 'outward-facing' (OF) conformation in which permeases open towards the periplasmic side of the membrane (116-119).

8.2 Objectives: Revelation of the mechanism of G6P import

The efficient acquisition of extracellular nutrients is crucial for bacterial pathogenesis. The putative VCA0625-27 transporter of *V. cholerae* plays a critical role in enteric bacterial infection. However, the structure, dynamics, and mechanism of sugar-phosphate internalization by this importer remained elusive.

Therefore, the objectives of this part of my research were to: (i) elucidate the structure and mechanistic details of G6P binding by the PBP VCA0625, within the VCA0625-27 transporter of *V. cholerae*; (ii) characterize the ATPase activity of VCA0627, focusing on ATP binding and hydrolysis mechanisms using modeling and biochemical experiments; and (iii) characterisation of the permease VCA0626 through modeling and bioinformatic analyses.

Chapter 9

Cloning, Overexpression, Purification, Crystallisation and Structure determination of VCA0625

Summary

As an initial step to characterize VCA0625-27, we have cloned overexpressed and purified PLBP VCA0625. After that we have crystallized VCA0625 and diffraction data were collected up to 1.6 Å. This chapter covers the details of preparation of genomic DNA, cloning, overexpression, and purification of PBP VCA0625. It also contains crystallization, data collection, refinement, and structure determination of VCA0625.

9.1 Cloning, Overexpression and Purification of Glucose-6-Phosphate importing PBP VCA0625

9.1.1 Genomic DNA preparation

The genomic DNA for cloning was extracted from *V. cholerae* serotype O1 (strain ATCC 39541/Classical Ogawa 395 / O395) using a high salt SDS-based protocol (90). The extraction process involved TE buffer (Tris-EDTA), 10% (w/v) sodium dodecyl sulphate (SDS), 20 mg/ml proteinase-K, a 1:1 mixture of phenol and chloroform, a 10:1:0.6 solution of supernatant/3M sodium acetate/isopropanol, 70% ethanol, and TE-RNase (Fig. 3.1a).

9.1.2 Cloning, Overexpression and Purification of VCA0625

The gene region encoding VCA0625 (of 318 amino acids residues excluding signal-peptide of 1-26 residues; Accession code: A0A0H3AFK0) was amplified using genomic DNA from the *V. cholerae* O395 strain as the template. VCA0625 was cloned in pET28a$^+$ (Novagen) using specific primers (forward primer: 5′-GGAATTCGCATATGGAAGGCCGTTTGGTGGTTTA -3′, and reverse primer: 5′-CATTCGGGATCCTTAGTTACCCATTTTGA -3′) within *Nde1* and *BamH1* restriction sites. The clone was validated by restriction digestion analysis and commercial DNA sequencing. Protein was overexpressed by IPTG in *E. coli* BL21 (DE3) cells as N-terminal 6×His-tagged recombinant proteins (as per protocol mentioned in Chapter 3, section 3.1.1). Briefly, the pellet was resuspended in ice-cold lysis buffer-K (50 mM Tris–HCl pH 8.0, 300 mM NaCl, 5 mM $MgCl_2$) and lysed after adding PMSF (1 mM), lysozyme (1 mg/ml) and imidazole (5 mM). Protein was purified by Ni^+-NTA (Qiagen) affinity chromatography with increasing concentration of imidazole. The 6×His-tagged recombinant proteins were eluted with 50–150 mM imidazole gradient. Imidazole was removed subsequently by buffer exchange through centrifugation.

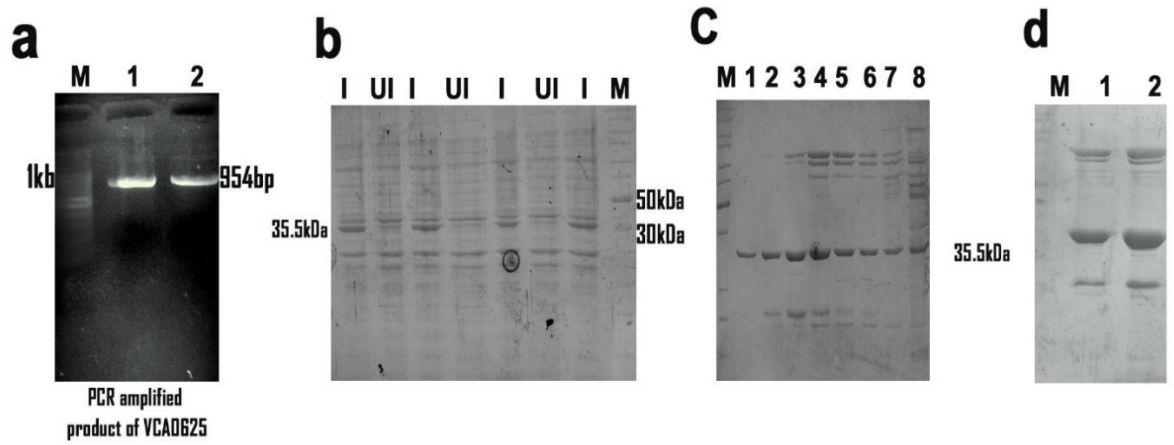

Figure 9.1: Cloning, Overexpression and purification profile of VCA0625. (a) 1% Agarose gel showing the band of PCR product of VCA0625; (b) 12% SDS PAGE profile of induced and uninduced VCA0625 expressing BL21(DE3) cells; (left) I: Induced cells, U: uninduced cells; M: Marker (right); (c) 12% SDS PAGE showing purification profile of VCA0625 (Lane 1: Marker, Lane 2-8: 10 – 150 mM imidazole gradient); (d) 12% SDS PAGE showing concentrated VCA0625 (Lane 1: Marker, Lane 2-3: 2µl and 4µl of concentrated protein.

9.2 Crystallization and diffraction data collection of VCA0625

For crystallization, VCA0625 (MW 35,376.77 Da) was concentrated to 10 mg/ml using an Amicon ultracentrifugation unit with a 10 kDa molecular-weight cutoff, in a buffer containing 50 mM Tris–HCl (pH 8.0), 300 mM NaCl, and 10% (v/v) glycerol. The protein concentration was determined spectrophotometrically with an extinction coefficient of 55,350 M^{-1} cm^{-1}. Initial crystallization trials were conducted using the hanging-drop vapor-diffusion method in 24-well crystallization trays (Hampton Research, Laguna Niguel, California, USA). The screening solutions included Grid Screen PEG 6000, Grid Screen Ammonium Sulfate from Hampton Research, and the JCSG+ suite from Qiagen. Typically, 2 µl of the protein solution was mixed with an equal volume of the screening solution and equilibrated against 500 µl of the latter as the reservoir. Optimal diffraction quality crystals of VCA0625 were obtained in sitting drop vapor diffusion process with precipitant containing 0.1 M Phosphate-citrate pH 7.0, 40% (v/v) PEG 300 after 72 h incubation at 20°C (Fig. 9.2). The crystals were quickly soaked in a cryo-protectant solution consisting of paratone oil in the mother liquor. Crystals were then flash-frozen and stored in liquid nitrogen until used for data collection. Diffraction data were collected up to 1.6 Å (Fig. 9.2b) using MARCCD detector at PX-BL21 (120) beamline of the Indus-2, RRCAT, Indore, India. Data integration was performed with XDS (121), followed by processing and scaling using AIMLESS from CCP4 (122). The statistics for data collection and processing are detailed in Table 9.1.

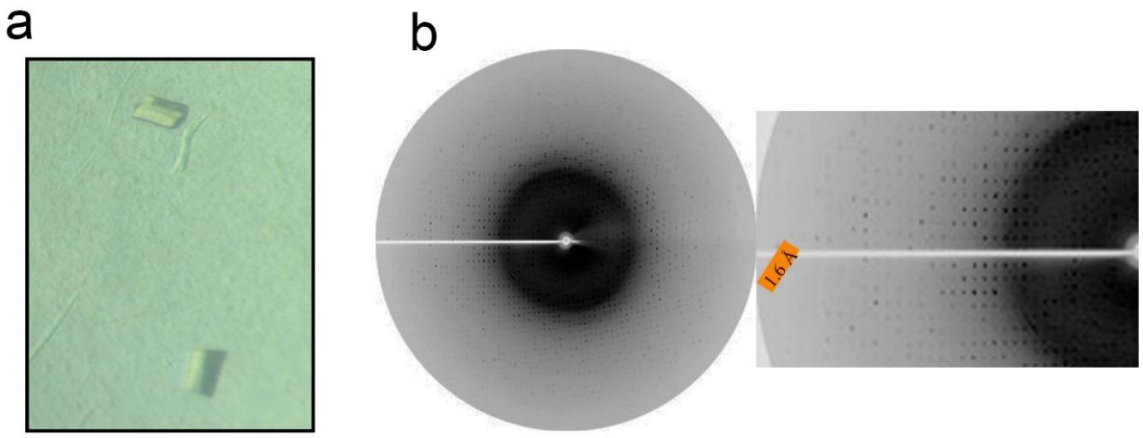

Figure 9.2: Crystallization and diffraction data collection profile of VCA0625. (a) Crystals of PLBP VCA0625;(b) X-ray diffraction image of VCA0625 crystals; the crystal diffracts to a highest resolution of 1.6 Å.

Table 9.1: Data collection statistics of VCA0625

Beamline	PXBL21, RRCAT, Indore, India
Wavelength (Å)	0.979
Detector	MAR345
Oscillation (°)	1
Space group	$P2_12_12_1$
Unit cell parameters (Å/°)	a=57.29, b=63.31, c=75.32 90,90,90
Resolution range (Å)	45.6-1.6
Number of reflections	35948
No. of molecules per asymmetric unit	1
Mathew's coefficient V_M ($Å^3$ Da^{-1})	1.90
Solvent content (%)	35.35
Completeness (%)	98.7(86.7)[a]
Averaged I/σ(I)	19.8(3.2)[a]
R_{merge} (%)	5.2 (39.0)[a]
Multiplicity	4.6 (4.0)
CC(1/2)	0.99(0.85)

[a] *Numbers in parentheses are values for the highest-resolution bin.*

9.3 Phasing and refinement of VCA0625

Molecular replacement (MR) calculations by Phaser-MR of PHENIX (123) with the ligand free coordinates of AfuA in G6P (Glucose-6-Phosphate) bound state (PDB code: 4R73) as search template, identified one molecule in the asymmetric unit. Further refinements were carried out using PHENIX (123) by including TLS refinement, B-group refinement, and

stimulated annealing. The quality of the electron density map improved significantly which allowed us to build the molecular model with fine corrections and mutating the alanine residues back to the residues. Anisotropic B factors and bulk solvent corrections were applied throughout the refinement. Automated water building was performed. The refinement cycles including XYZ and B-group were continued and the progress of the refinement was assessed by monitoring the R_{free} value. Non-crystallographic symmetry (NCS) was not applied during the refinement process. The 2Fo-Fc map, calculated using the refined model, was of high quality and aligned well with the model. Electron density appeared in 2Fo-Fc map as well as positive density appeared in the Fo-Fc map (contoured at 3σ) at the ligand binding pocket confirmed presence of bound ligand. Model fitting was performed using WinCoot (124). Data collection parameters and refinement statistics are given in Table 9.1 and Table 9.2. The electron density was well-defined throughout the molecules (Fig. 9.2b), and the quality of the structure aligns with the resolution of the diffraction data.

Table 9.2: Refinement statistics of VCA0625

Refinement	
R_{work}/R_{free} (%)	17.2/21.01
No of atoms Protein ligand	 2462 16
Average B-factor (all atoms) ($Å^2$)	16.46
RMSD Bond lengths (Å) bond angles (°)	 0.007 0.95
Ramachandran statistics (%) Most favoured Additionally allowed Disallowed	 98.7 1.9 0.3

9.4 Structure determination of the PBP, VCA0625

X-ray diffraction data were collected up to 1.6 Å resolution from the crystals of VCA0625, in space group $P2_12_12_1$ (Table 9.1). BLASTp search with the sequence of VCA0625 identified the PBP AfuA (of the ABC importer AfuABC, involved in hexose-6-Phosphate uptake from *A. pleuropneumoniae*) as nearest homolog with high identity of 72% for 321 amino acids excluding signal peptide. Despite that, MR calculations with the coordinates of AfuA in

apo state (PDB code: 4R72) as search template failed miserably to produce distinct solutions. Interestingly, the coordinates, of AfuA in Glucose-6-Phospate (G6P) bound state (PDB code: 4R73) produced clear-cut MR solution while used after removing the coordinates of bound ligand and waters from the search template. One molecule in the asymmetric unit produced R_{work} of 29.9% (R_{free} of 33.4%) (with RFZ = 25.9, TFZ = 39.0, and LLG = 2019). The continuous electron density (both in 2Fo-Fc and Fo-Fc maps), identified in the ligand binding pocket, was assigned as G6P bound during overexpression of protein in *E. coli*. (Fig. 9.3a). Further model building and refinements yielded final R_{work} of 17.2% and R_{free} of 21.01% respectively. The coordinates of the refined structure of VCA0625 have been submitted to RCSB with PDB code: 8X1A (Fig. 9.3b).

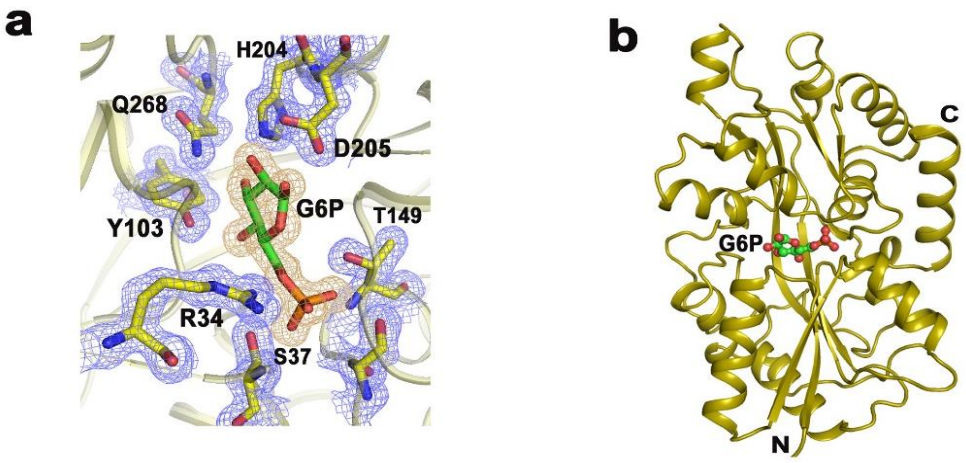

Figure 9.3: Structure determination of VCA0625. (a) $2F_0$-Fc density map (contoured at 1σ) around G6P bound to VCA0625; (b) Ribbon diagrams of VCA0625 complexed with β-G6P.

9.5 Interactions of G6P with VCA0625

Overall, the structure depicted that VCA0625 belongs to the class II/cluster-D PBP with two globular α/β domains linked by a β-stranded hinge (Fig. 9.4a). G6P fits snugly in the ligand binding cleft of VCA0625 through hydrogen bonding interactions between the hydroxyl groups of the pyranose ring and the side chains of Y103, H204, D205, E228 and Q268 (Fig. 9.4b). The phosphate moiety of G6P is stabilized through hydrogen bonds with the side chains of R34, S37, S147, T149 as well as backbone NH groups of T149 and G184 (Fig. 9.4b). G6P complex superposed well on the G6P bound AfuA with root-mean-square deviations (RMSD) of 0.5 Å (Fig. 9.4c).

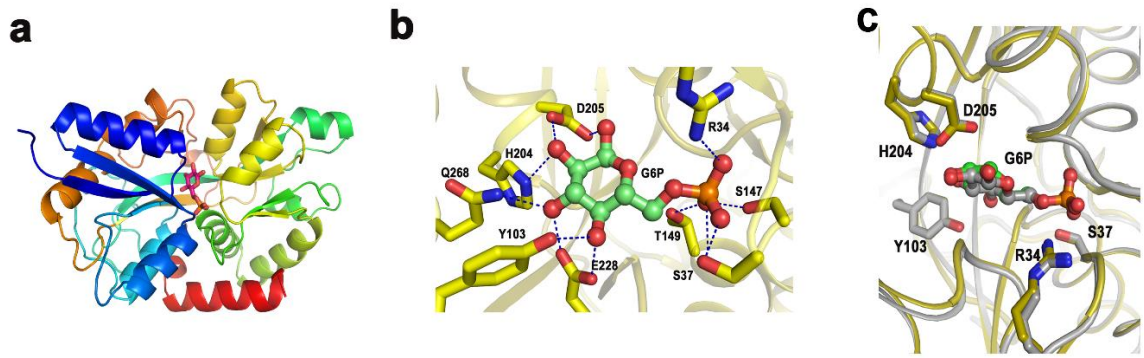

Figure 9.4 Interactions profile of VCA0625. (a) Crystal structure of Holo-VCA0625; (b) Ligand binding region in solved crystal structure of VCA0625; (c) Superposition of G6P bound AfuA structure (PDB code: 4R73) (gray) on VCA0625 (gold). G6P is shown in ball and stick.

Chapter 10

Molecular Dynamics simulation on VCA0625 in free, and ligand bound states

Summary

Structural and biophysical studies on the PLBP of VCA0625 helped us to determine their structures and ligand binding properties. Molecular Dynamic simulation was further performed on VCA0625 for understanding the dynamics of this PLBP in the free as well as in the ligand bound states. This chapter contains methods and results of MD simulations on VCA0625.

10.1 Methods: Molecular Dynamic Simulation steps and parameters

We performed all-atom molecular dynamics simulations on the VCA0625 both in the presence and absence of the coordinates of G6P using AMBER-2022 software suite at a temperature of 300 K. To accelerate the simulations, we used pmemd.cuda, a GPU-accelerated MD program within the AMBER suite (99), and cpptraj for analysis. The FF19SB force field (125) was used for the protein, and the TIP3P force field (100) for water. Three independent 1 μs simulations were run for both the bound and unbound states in explicit waters. The protein was solvated in a truncated octahedron box with periodic boundary conditions on all the three dimensions. The walls of the box was at least 10 Å away from the protein. Counter ions were added to achieve charge neutrality in the solvated system. To prevent steric clashes, we performed energy minimization for 2000 cycles using a combination of steepest descent and conjugate gradient algorithms. The temperature of the system was then equilibrated in the NVT ensemble and the pressure was brought to 1 atm by equilibrating in the NPT ensemble. The SHAKE algorithm (101) was used to constrain the stretching of bonds involving H-atoms. The temperature was regulated using Langevin thermostat (104) with a collision frequency of 2 ps^{-1}. The system was coupled to a Berendsen barostat (102) with a relaxation time of 2 ps to maintain a constant pressure of 1 atm. The particle mesh Ewald summation method (103) was employed for fast calculation the electrostatic interactions. The non-bonded interactions were calculated using a distance cut-off of 12 Å, and the time step for the integrator was 2 fs. The equilibration step was performed for 10 ns each in the NVT and NPT ensembles. Finally, the production run was performed in the NPT ensemble with the same parameters as the equilibration step, and the RMSD and RMSF were calculated with respect to the first frame in the trajectory.

10.2 Analysing the data

10.2.1 Dynamics of VCA0625 in free and in G6P bound states

MD simulation runs were carried out on VCA0625 in G6P bound and ligand free states to understand the dynamic nature of the molecule regarding ligand binding. Root mean square deviations (RMSDs) of the Cα atoms in apo and holo states of VCA0625 were calculated from the snapshots of the trajectories up to 1 μs, and were plotted (Fig. 10.1a). RMSD values converged well approximately within 70 ns. The RMSD values for the holo state remain steady around 1.5 to 2 Å, while in apo state, VCA0625 fluctuates more, ranging from 1 to 4.5 Å (Fig. 10.1a), indicating that VCA0625 gains stability upon G6P binding. Fig. 10.1b shows root mean square fluctuation (RMSF) values for the free and G6P bound VCA0625. Overall reductions in fluctuations after G6P binding are evident from the graphs. (Fig. 10.1b).

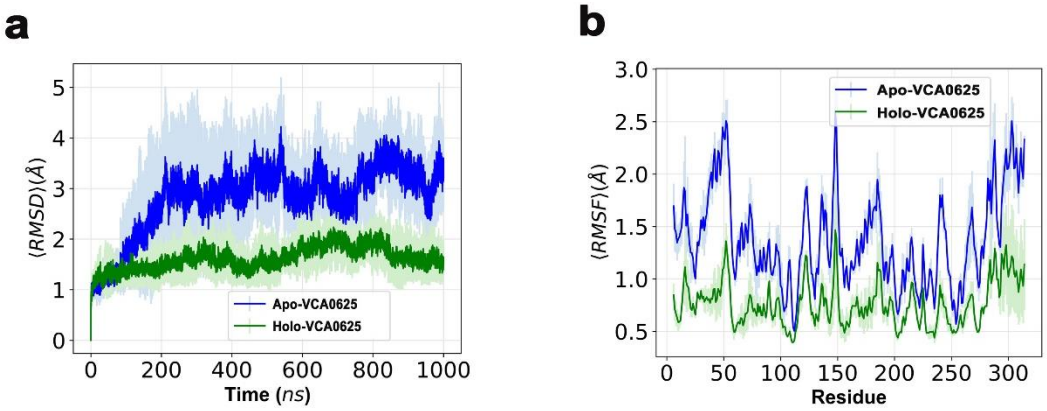

Figure 10.1: MD simulation results of VCA0625 in free and G6P bound state. (a) Plot of the RMSD values for the Cα atoms are shown for apo-VCA0625 (blue) and holo-VCA0625 (green) up to 1μs simulation range. (b) RMSF of the Cα atoms was calculated from the simulation trajectories.

10.2.2 VCA0625 execute both 'open to close' and swinging motions

Superposition of the snapshots of apo and G6P bound VCA0625 delineated the two lobes, of VCA0625 execute both 'open to close' and swinging motions (Fig. 10.2a–d). Both motions are prevalent in the case of ligand-free VCA0625 (Fig. 10.2a, c) compared to its G6P bound counterpart (Fig. 10.2b, d). Almost all interactions between G6P and VCA0625 remained preserved during dynamics. Interestingly, the side chain of R34 acquired multiple conformations, swinging from outside to inside of the binding pocket. In G6P-bound VCA0625, the distance between D205 and T11, located at the binding cleft, varied from 1.5

(57ns) to 6.27 Å (423ns). Upon proximity, they interacted with each other through H-bonding. However, this interaction is inversely related to interaction of R34 and G6P. Upon proximity of T11 and D205, the distance between R34 and G6P increased upto 14.08 Å (57ns) reflecting the 'closed' form. However, no such interaction between T11 and D205 or wide movement of R34 was observed in apo VCA0625.

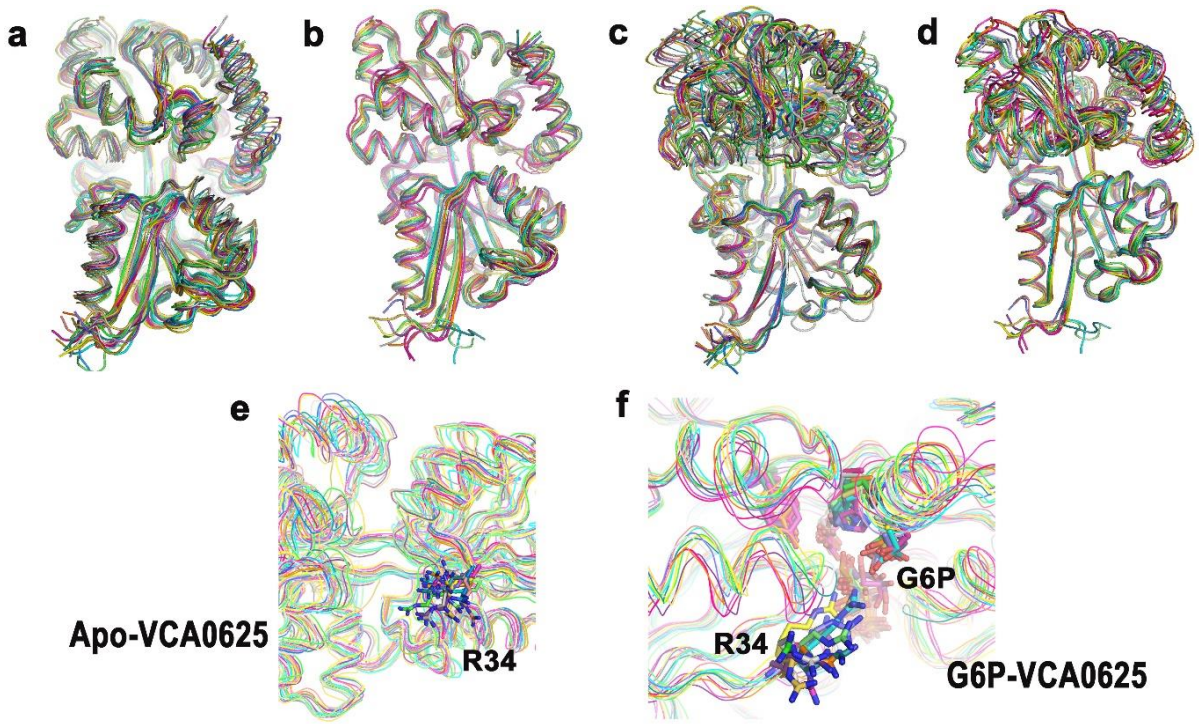

Figure 10.2: VCA0625 execute both 'open to close' and swinging motions. (a–b) Superposition of the snapshots of overall MD trajectories (a) in apo VCA0625 and (b) holo VCA0625; (c–d) Snapshots aligned with respect to the N-lobe to shows the inter-domain movement for apo VCA0625 in (c) and G6P bound VCA0625 in (d); (e–f) Movement of R34 side chain during simulation in apo and G6P bound VCA0625.

10.2.3 Software used for analysis

Software used for data analysis and presentations are Origin 8.5, PyMol (DeLano Scientific, Schrodinger, Inc., USA), UCSF Chimera 1.14, and Adobe photoshop CS3.

Chapter 11

Elucidation of the mode and efficacy of G6P binding by VCA0625 through mutagenesis studies

Summary

Structural and MD analyses have elucidated that R34 acts as a crucial gateway for binding G6P, while Y103 is positioned near G6P binding site. Therefore, we prepared two mutants, R34A and Y103A. Additionally, isothermal titration calorimetry (ITC) experiments were conducted to validate the impact of these mutations on binding affinity. This chapter covers cloning, overexpression, and purification of the R34A and Y103A mutants of VCA0625. Methods for the removal of G6P from native protein VCA0625 and its mutants are also outlined, alongside a description of the ITC experiments performed to assess binding characteristics.

11.1 Cloning, Overexpression and Purification of VCA0625 mutants R34A, and Y103A

The mutants R34A and Y103A were prepared by two-step PCR amplification using wild type VCA0625 as template. These mutant amplicons were also cloned in pET28a^{+} vector using *NdeI* and *BamHI* restriction sites. These mutant proteins were overexpressed with N-terminal 6×His tag in *E. coli* BL21(DE3) by IPTG induction and kanamycin resistance. The mutants were purified using the buffer containing 50 mM Tris–HCl pH 8.0, 300 mM NaCl, 10% (v/v) glycerol. The purified proteins R34A and Y103A were concentrated up to 300 μM and 350 μM respectively. The homogeneity of the purified mutant proteins was checked using SDS-PAGE with 12% polyacrylamide concentration. The constructs were verified by restriction digestion analysis and commercial DNA sequencing.

Table 11: Primers used to clone the mutants of VCA0625

VCA0625 mutants	**Primer sequence 5′ ➞ 3′**
R34A (27-344 aa)	FP: AACACCTCCTTTGTGGCCAACGGTTCAGGCAGT RP: ACTGCCTGAACCGTTGGCCACAAAGGAGGTGTT
Y103A(27-344 aa)	FP: TACTCTTCTGCGGTGGCCATGGGCATTTTGGGC RP: GCCCAAAATGCCCATGGCCACCGCAGAAGAGTA

11.2 Removal of ligand from VCA0625 and its mutants through partial denaturation

To investigate the role of VCA0625 independently of its ligand, we employed a strategy involving partial denaturation by urea to remove G6P from the protein. Removal of G6P from VCA0625 and its mutants were conducted through partial denaturation using 6M urea followed

by on-column refolding by washing with buffer with gradually reduced urea concentrations. In brief, the protein pellets were resuspended in ice-cold lysis buffer-L (having 50 mM Tris–HCl pH 8.0, 300 mM NaCl, 5 mM $MgCl_2$, 10% (v/v) glycerol). PMSF (1 mM) and lysozyme (1 mg/ml) were added to the resuspended solution and it was lysed by sonication on ice. The cell lysate was then centrifuged at 13,000 RPM for 45 min at 277 K. The collected supernatant was applied onto a nickel–nitrilotriacetic acid (Ni^{2+}-NTA) affinity chromatography media (Qiagen) that was previously equilibrated with buffer-L. A 6 M solution of urea was used to denature the bound protein. After that urea concentrations in the wash buffer were gradually decreased to 3 M, 1.5 M, 1 M and 0.75 M. Finally, wash buffer without urea was added to allow bound protein to refold. Protein was then eluted with elution buffer (with 50–150 mM imidazole gradient). The purified proteins were concentrated up to 200 μM and the homogeneity of the purified proteins was judged in 10% SDS-PAGE (Fig. 11.1).

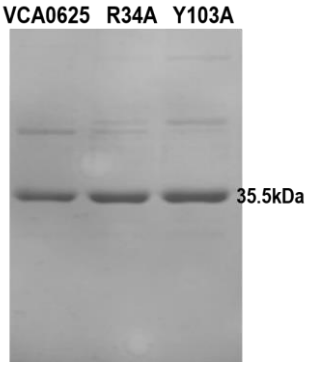

Figure 11.1: 10% SDS PAGE showing concentrated 4μl of VCA0625 and its mutants after removal of G6P from proteins through partial denaturation.

11.3 Measurement of binding affinity of VCA0625 and its mutants through Isothermal Titration Calorimetry (ITC)

11.3.1 Isothermal Titration Calorimetry: methodology

Isothermal Titration Calorimeters (ITC) measure the heat change associated with protein-ligand interactions. Before the experiments, proteins were dialyzed against a reaction buffer without glycerol. ITC measurements were conducted at 25°C using a Nano ITC (TA Instruments), with the ligand G6P being injected from the stirring syringe. The ligand was titrated against purified protein, loaded into the sample cell. The reactions were monitored for binding study with injections of 2.5 μl each for 20 injections of the ligand having interval of 180 sec between two injections. The results were analysed by the integration of the heat

released relative to the amount of protein-ligand interaction and curve-fitting based on a 'independent binding model' for G6P, using the default TA-analytical software provided. The data calculated binding constants (K_d), Stoichiometry (N) and thermodynamic parameters [Enthalpy (ΔH) and Entropy (ΔS)] which were referenced against runs performed with the G6P alone (ligand to buffer) as control for the heat of ligand solvation. All data are the mean of three independent experiments ± SD.

11.3.2 Measurement of G6P binding efficacy to VCA0625 and its mutants

ITC experiments demonstrated that titration of G6P against VCA0625 was exothermic. Binding isotherms were fitted using the one site binding model. Titration confirmed binding between G6P and VCA0625 with dissociation constant (K_d) of 17.45 ± 0.45 μM, for n = 1, ΔH = −1.63 kcal/mol (Fig. 11.2a). It was previously observed that (119) mutation of the residues of AfuA, corresponding to S37 and T149 of VCA0625, caused reduced binding of G6P, while binding was practically abolished upon mutations of the residues corresponding to H204, D205 and E228 of VCA0625. Since interaction patterns of G6P with VCA0625 is largely like G6P-AfuA complex, we envisaged a similar effect of the mutations of the aforesaid residues in VCA0625, and investigated the effect of Y103 through binding studies of G6P with Y103A. Furthermore, structure and dynamics of VCA0625 indicated that R34 is an important residue presumably taking part in recognition and binding of G6P, as well as in regulating the opened and closed form. Therefore, we have checked the G6P binding with the mutant R34A as well. Interestingly, binding was impaired both in case of R34A and Y103A (Fig. 11.2b-c).

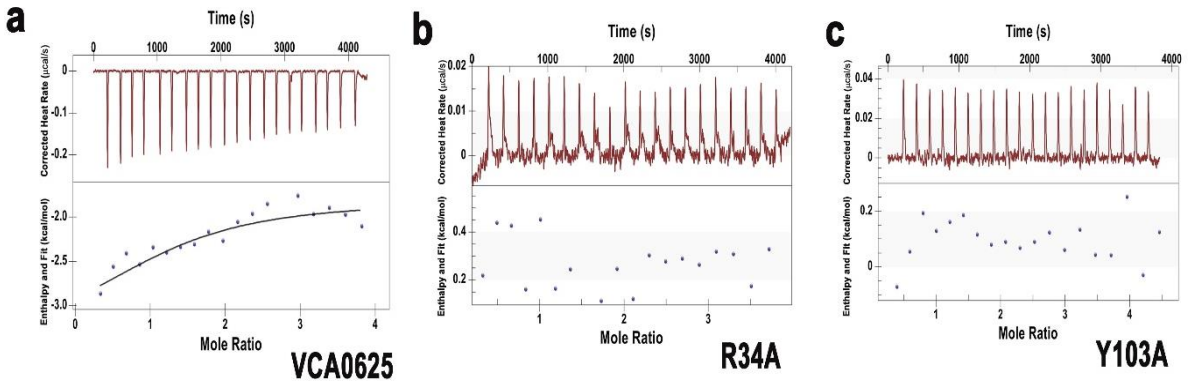

Figure 11.2: Binding affinity studies by ITC. (a) VCA0625 showed significant binding with G6P resulting a K_d value of 17.45 ± 0.45 μM; (b,c) Thermograms of R34A, Y103A indicated insignificant interaction.

Chapter 12

Characterisation of the NBD, VCA0627 and the permease, VCA0626

Summary

This chapter covers cloning, overexpression, and purification of the NBD VCA0627 from *V. cholerae*. Fluorescence spectroscopy indicated weak binding affinity towards AMP.PNP. Subsequent characterizations were carried out through sequence analysis and structural modeling. Although significant structural similarities were observed between VCA0627 and other NBDs, significant variations were observed in the regulatory domains. Negligible ATPase activity of VCA0627 suggested its functional dependence on the associated proteins VCA0625-26 of the ABC importer assembly.

12.1 Cloning, Overexpression and Purification of VCA0627

The full-length VCA0627 (residues 1-351) was cloned into the kanamycin-resistant pET28a+ vector (Novagen) using specific primers: forward primer 5'-GGAATTCGCATATGGTGGAAAAACAAAACTTTGT-3' and reverse primer 5'-CATTCGGGATCCCTATTCTGCGTAGGGCAGCA-3', synthesized by Sahagenes with *NdeI* and *BamHI* restriction sites. Genomic DNA from *V. cholerae* strain O395 (as detailed in Chapter 3, Section 3.1) used as the template for PCR amplification of the VCA0627 coding region (Fig. 12.1a). The 1053 bp PCR product and the pET28a^{+} vector were double-digested with *NdeI* and *BamHI*, and the fragments were purified from a 0.8% agarose gel using a Qiagen gel extraction kit. For protein overexpression, 100 ml of LB broth was inoculated with a single colony and grown overnight at 37°C. This culture was then used to inoculate 1 liter of LB broth, which was grown at 37°C until the OD_{600} reached 0.6. Protein expression was induced with 1 mM IPTG and the culture was incubated overnight at 20°C with slow shaking. After induction, cells were harvested by centrifugation at 4200×g for 15 minutes, and the pellet was resuspended in 7 ml of ice-cold lysis buffer (buffer-L). The resuspended cells were supplemented with 1 mM PMSF and 1 mg/ml lysozyme, then lysed by sonication on ice. The cell lysate was centrifuged at 12,000 rpm for 45 minutes at 4°C, and the supernatant was collected. The supernatant, containing 6×His-tagged VCA0627, was applied to Ni^{2+}–NTA (Qiagen) resin equilibrated with the lysis buffer. The protein was eluted with a gradient of 50 to 250 mM imidazole. SDS–PAGE analysis with a 10% polyacrylamide gel confirmed that the eluted fractions were nearly homogeneous (Fig. 12.1b). The pooled eluted protein was then buffer-exchanged against buffer-L and concentrated to 350 µM using an Amicon ultracentrifugation unit with a 10 kDa molecular-weight cutoff. The purity of the final VCA0627 preparation was again verified by SDS–PAGE (Fig. 12.1c).

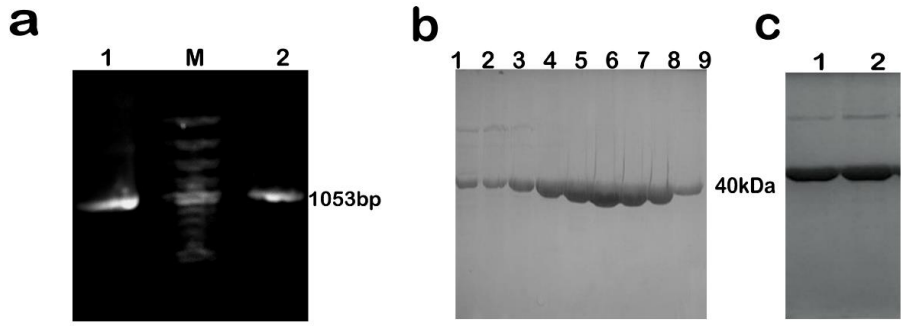

Figure 12.1: Cloning, Overexpression and purification profile of VCA0627. (a) 1% Agarose gel showing the band of PCR product of VCA0627; (b) 10% SDS PAGE showing purification profile of VCA0627(Lane 1-9: 10–250 mM imidazole gradient); (c) 10% SDS PAGE showing concentrated VCA0627 (Lane 1, 2: 2µl and 4µl of concentrated protein).

12.2 Characterization of VCA0627 through sequence analysis, modeling and AMP.PNP binding

12.2.1 *Sequence analysis and modeling of VCA0627 in Gram-negative bacteria*

To find out the nearest structural homolog of VCA0627, we performed BLASTp search against PDB with amino acid sequence of VCA0627 (Accession code: A0A0H3ADT9). VCA0627 showed 41% identity with CysA, the NBD of ABC-type sulphate importer from *Alicyclobacillus acidocaldarius* (PDB code: 1Z47) (126), 49% identity with PH0022, NBD of the multisugar transporter from *Pyrococcus horikoshii* (PDB code: 1VCI) (127), and 44% identity with MalK, the NBD of the maltose transporter from *E. coli* (PDB code: 1Q12) (114). CysA, PH0022, MalK belong to type-I importer and consist of an ATPase and a regulatory domain. Sequence alignment of VCA0627 with these NBDs indicated that the ATPase domain is primarily conserved. ATPase of VCA0627 contains several conserved functional motifs such as Walker-A (WA), Walker-B (WB) motifs, an ABC transporter-specific or 'signature' motif, Q-loop, D-loop and H-loop (Fig. 12.2a). Interestingly, substantial variations are observed in the regulatory domains of these NBDs (Fig. 12.2a).

Overall superposition of PH0022 on Alphafold (95) generated model of VCA0627 produced RMSD of 1.23 Å, while the other two NBDs have shown significantly high RMSD values (3.2 Å for CysA and 3.4 Å with MalK). However, the superposition of these structures only on the ATPase domain of VCA0627 produced RMSDs of 0.96 Å, 1.2 Å, and 1.45 Å for PH0022, CysA and MalK respectively (Fig. 12.2b). This implies that these structures primarily differ in the regulatory domain. Although the β-strands of the regulatory domains of CysA and MalK are significantly different from VCA0627, they match substantially well between PH0022 and VCA0627 (Fig. 12.2a).

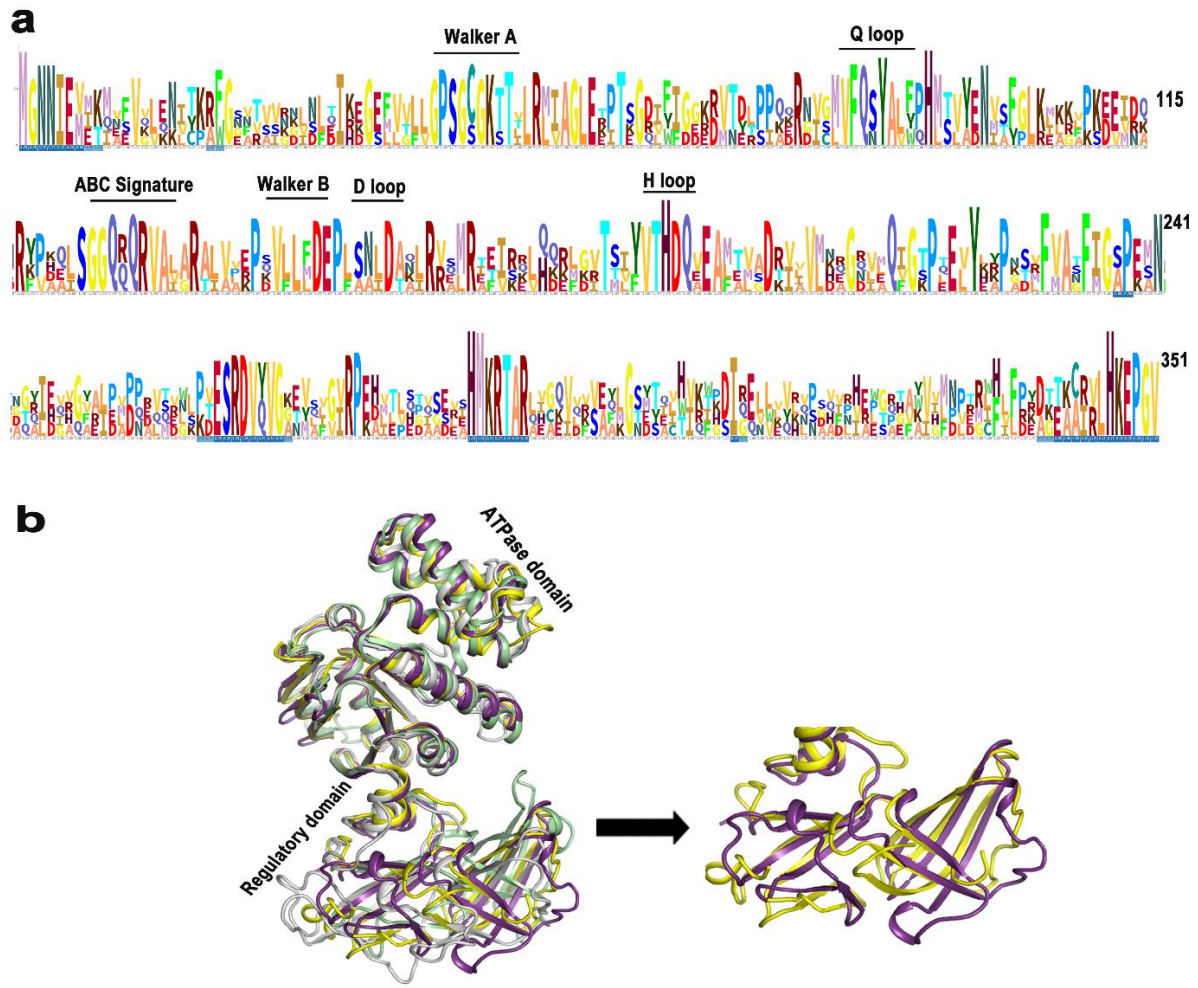

Figure 12.2: Bioinformatic analysis of VCA0627. (a) Consensus sequence logo generated (using Skylign followed by ClustalW alignment) from VCA0627 of *V. cholerae* and nearest structural homologs; (b) The overall superposition of CysA, PH0022, MalK, on model of VCA0627, whereas substantial similarities were observed between regulatory domains of PH0022 and VCA0627 (right panel).

12.2.2 Measurement of binding affinity of VCA0627 to AMP.PNP by Fluorescence Spectroscopy

12.2.2.1 Intrinsic fluorescence spectroscopy: methodology

The steady state fluorescence measurement was carried out in Hitachi F-7000 spectrofluorometer, as described previously in section 3.4.1 of Chapter 3. During reaction, the final concentration of the protein was 10 µM in the buffer containing 50 mM Tris–HCl pH 8.0, 300 mM NaCl, 5 mM $MgCl_2$. Equilibrium titration of VCA0627 was carried out with AMP.PNP (Sigma-Aldrich with a purity of ≥ 93% (HPLC) as ligand, dissolved in PCR grade Nuclease free Water. The effect of the ligand AMP.PNP on protein fluorescence intensities were monitored by titrating AMP.PNP against VCA0627. The fluorescence intensities were

corrected for dilution factors. Background quenching was eliminated by subtracting the signal obtained from a buffer solution that contained the appropriate quantity of the ligand.

12.2.2.2 Binding of AMP.PNP with VCA0627

Since ATP binding motifs of VCA0627 were found to be mostly conserved, we performed binding assays between VCA0627 and ATP analogue, AMP.PNP by measuring intrinsic fluorescence quenching of the protein (Fig. 12.3a) at λ_{ex}=280 nm, λ_{em}=295–400 nm, accounting the contributions of Tyrosines present at the ligand binding site. Apparent dissociation constant (K_d) value of 140 ± 0.043 µM (Fig.12.3b), thus obtained, indicated weak binding between VCA0627 and AMP.PNP (Fig. 12.3b).

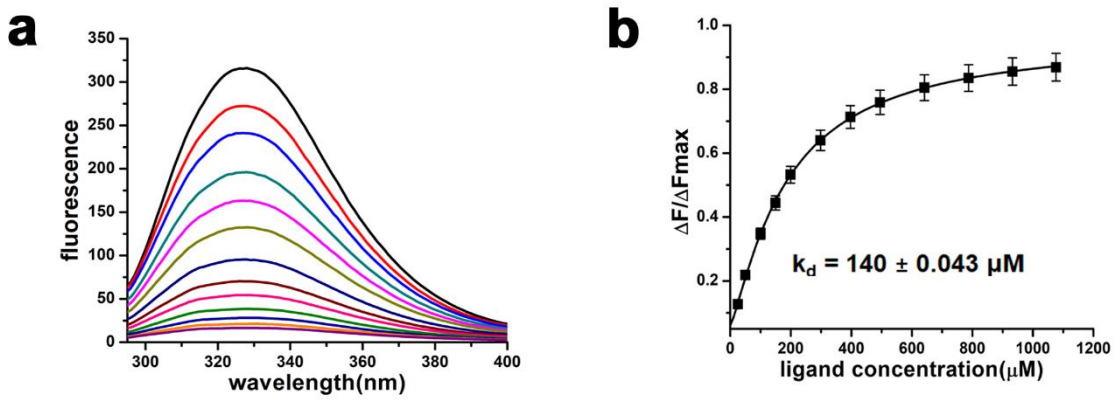

Figure 12.3: ATP binds to VCA0627. (a) Fluorescence quenching demonstrated significant change in fluorescence upon AMP.PNP binding to VCA0627; (λ_{exc}=280 nm, λ_{em} =295–400 nm) with slit widths of 5 nm for both excitation and emission; (b) Plots of $\Delta F/\Delta F_{max}$ against ligand AMP.PNP (µM) obtained a K_d value of 140±0.043 µM.

12.3 Measurement of ATPase activity of VCA0627

12.3.1 ATPase assay: methodology

As mentioned previously in section 3.5.1 of Chapter 3, ATPase activity of purified VCA0627 was determined spectrophotometrically using Malachite green assay by measuring the release of inorganic phosphate (Pi) upon ATP hydrolysis. Protein was assayed for its ATPase activity, where reaction mixtures containing 2.5 µM protein in buffer-R [composition of 50mM tris pH 8, 300mM NaCl, 5mM $MgCl_2$] was incubated with 0.1 mM ATP (Sigma-Aldrich) at 25°C for 20 minutes in a reaction volume of 1 ml. Addition of Malachite green was followed by the spectroscopic measurements. All the experiments were minimally performed in triplicate.

12.3.2 Absence of VCA0625-26 impairs ATPase activity of VCA0627

Observations of AMP.PNP binding directed us to check the ATPase activity of VCA0627 using malachite green assay. However, no ATP hydrolysis by VCA0627 was observed during Malachite green assay (Fig. 12.4). Insignificant *Pi* release by VCA0627 compared to the positive control (HutD) further established that VCA0627 is incapable of hydrolysing ATP in the absence of VCA0625 and VCA0626.

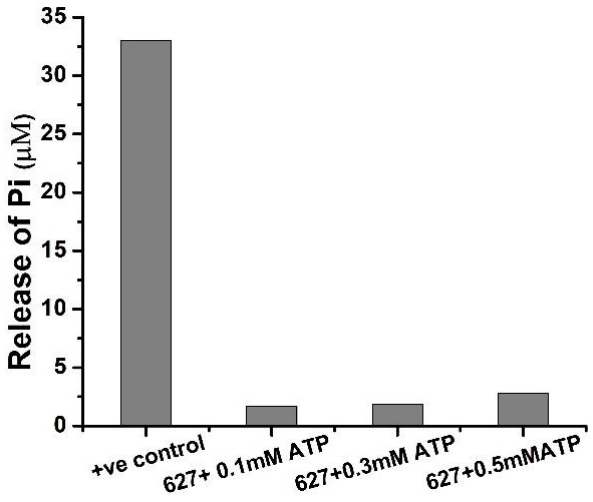

Figure 12.4: The ATPase domain VCA0627 showed negligible ATPase activities in Malachite green assay even with an elevation of ATP concentration to 0.5mM.

12.4 VCA0626 is an atypical fused monomeric permease

The permease VCA0626 (Accession code: A0A0H3AFF4) is found to be a fused monomer with 1–700 amino acids. No structure of such fused permease has been determined yet. Sequence similarity searches against PDB gave unsatisfactory results with very low sequence identity with other structurally characterized homodimer and heterodimer permeases of ABC type-I transporters. Interestingly, Alphafold (95) generated model of VCA0626 grossly resembles the structure of the heterodimeric permease MalFG in pre-translocation state (128), that belongs to MBP-Maltose transporter complex MalFGK-E (PDB code: 3PV0). N-terminal region of VCA0626 forms a four-helix bundle that apparently stays away from the transport channel (Fig. 12.5a). The other helices are involved in forming translocation channel (Fig. 12.5a). Since VCA0626 model matches with MalFG in pre-translocation state, we prepared an assembly model made of VCA0626 and the dimer of VCA0627 through structure-based docking (Fig. 12.5b). In MalFGK, the L-loop of MalFG interacts with NBD, MalK. Interestingly, during structure-based docking, two L-loops of VCA0626 containing 'EAS' motifs such as ^{316}EAS^{318} and ^{593}EAS^{595} were found to fit with the two monomers of VCA0627

(Fig. 12.5c). Our BLASTp search identified similar monomeric permeases in 27 other gram-negative bacteria. Sequence comparisons revealed that residue 240 onward the helices that are located in the transportation channel, or in the regions that interact with PLBP and NBD dimer are highly conserved (Fig. 12.5c). Interestingly, corresponding NBDs of these organisms also showed high degree of sequence identity specially in ATPase domain while the regulatory domains (RD) are relatively less conserved.

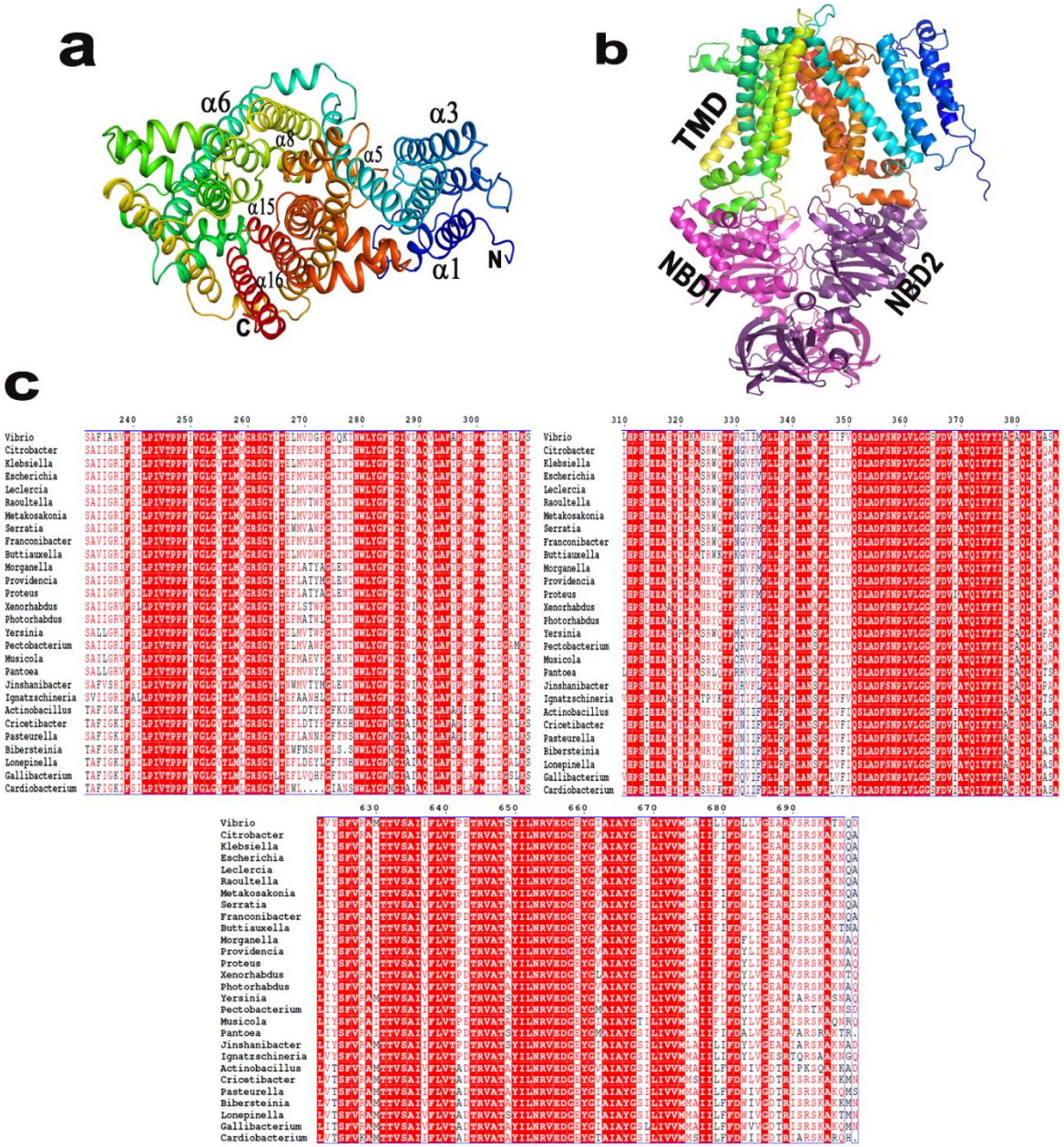

Figure 12.5: Bioinformatic studies on VCA0626. (a,b) The models of VCA0626 and VCA0626-27 assembly. Arrangements of transmembrane helices in atypical VCA0626 model is shown from the periplasmic side in (a); (c) Multiple sequence alignment of VCA0626 and similar transmembrane proteins of 27 gram-negative bacteria showed strict sequence conservation. Residue numbering is as per VCA0626 of *V. cholerae*.

Chapter 13

Discussion: Type-I ABC importer VCA0625-27

Usually, in bacteria, type-I importers internalize metabolites like sugars, amino acids, peptides or osmoprotectants where type-II importers import nutrients like vitamin B12 (cobalamin), metal chelates, or heme. Differences between these two kinds of importers are based not only on their nutrients but also on their structural characteristics (37). Our current study helped to gain insights into the hitherto unknown structure function of VCA0625-27 of *V. cholerae*. Crystal structure of the PLBP VCA0625 revealed that G6P binds efficiently to VCA0625 through polar interactions during its overexpression in *E. coli* cells (Fig. 11.2a). The structure and binding mode resemble with that of AfuA, the sugar phosphate importer of *A. pleuropneumoniae*. MD simulations further delineated that an 'open to close', and swinging motion occur between the lobes of VCA0625, the dimension of which reduces upon ligand binding. R34, located at the gate, plays a pivotal role in 'open to close' movement. The NBD, VCA0627 depicts considerable sequence identities with the other type-I importers. Type-II NBD dimers bind and hydrolyse ATP even in the absence of permeases (37). In contrast, type-I NBDs are functional only in the presence of permeases and PLBPs. Although VCA0627 contains all required motifs for ATP binding and hydrolysis, it showed weak ATP binding and no ATPase activity. Non-functionality of VCA0627 in the absence of VCA0625 and VCA0626 further establishes VCA0625-27 as type-I importer (Fig. 13). Despite VCA0626 is a fused monomeric permease, its model structure matches grossly the inward facing structure of hetero-dimeric MalFG of maltose transporter MalFGK-E (128). In general, the type-I importers contain fewer transmembrane helices compared to type-II (37). Type-I dimeric (homo or hetero) importers usually contain 5-6 helices per monomer, and therefore having around 12 helices per assembly. VCA0626 contains 12 helices which constitute the transport channel, along with PLBP and NBD binding sites. However, the homo or heterodimeric permeases often contain an extension in the periplasmic region to recognize and interact with PLBP. Instead, Alphafold (95) has predicted (with high confidence level) a four-helix bundle at the N-terminus of VCA0626 that apparently stays away from transportation channel (Fig. 12.5b-c). As observed before (129), ATP hydrolysis driven conformational changes propagate through the L-loop containing 'EAS' motif of the permease. Interestingly, the two L-loops of VCA0626 having 'EAS' motifs fit with the two monomers of VCA0627 to transmit ATPase induced conformational changes (Fig. 12.5b). Considering aforesaid observations, we hypothesize that VCA0625-27 of *V. cholerae* is an atypical type-I sugar phosphate importer of unique architecture (Fig. 13). Stunning sequence identities of VCA0626 and VCA0627 with 27 other gram-negative bacteria including AfuB of *A. pleuropneumoniae,* indulge us to anticipate similar G6P import mechanisms in these organisms as well (Figs. 12.5c). We envisage that

experimental structure of the assembly made of VCA0626 and VCA0627, along with revelation of the role of regulatory domain of VCA0627 in future will provide major breakthrough in the area of ABC importers that control metabolic and other important cellular processes in bacteria (Fig. 13).

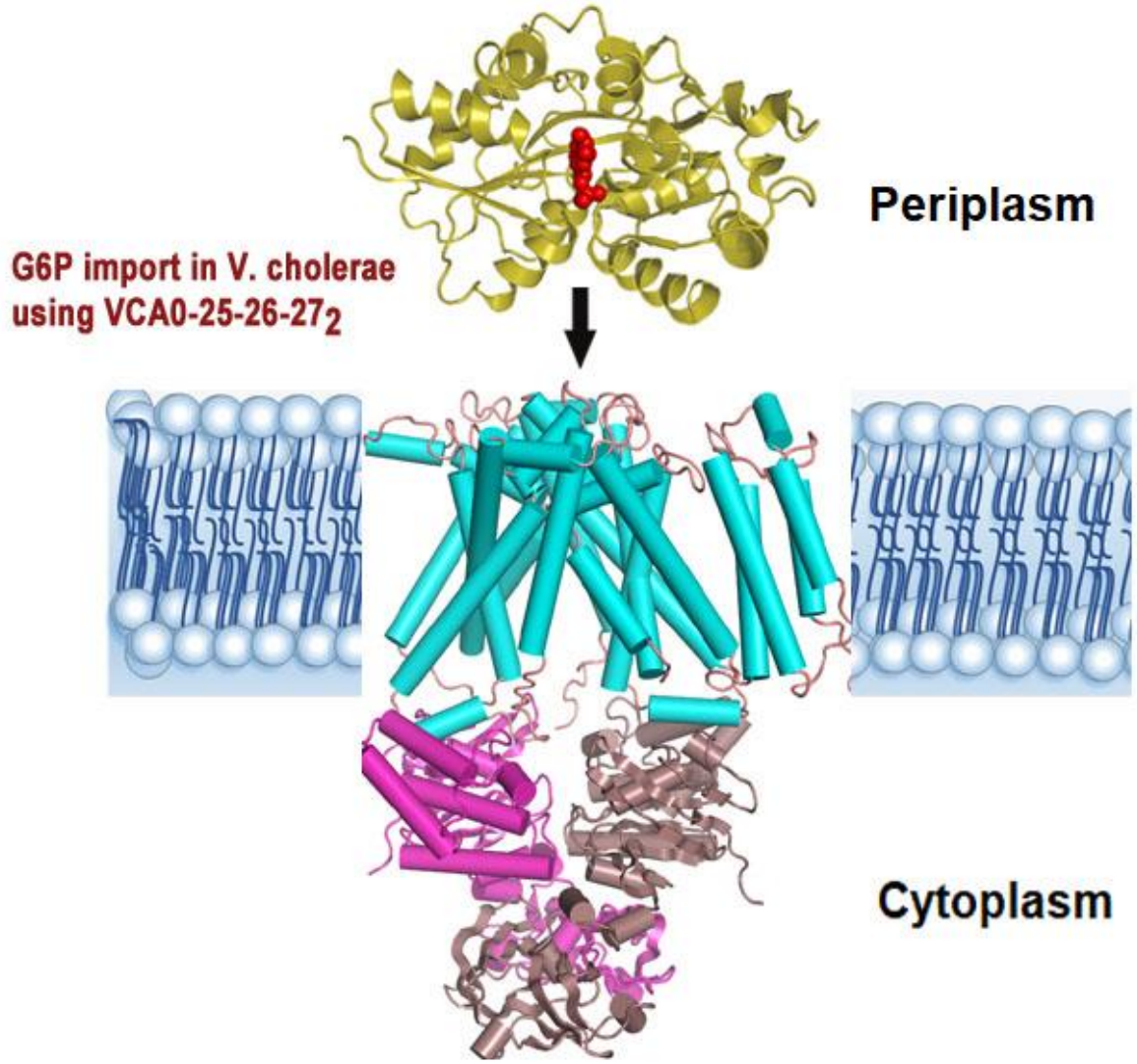

Figure 13: G6P importing type-I ABC transporter VCA0625-27 of *Vibrio cholerae*.

Conclusion

ABC transporters play crucial roles in nutrient uptake, maintaining cellular balance, and influencing bacterial virulence across different life forms. Their ability to utilize ATP to transport substrates makes them promising targets for developing drugs against bacterial infections. Specifically, *V. cholerae*, a gram-negative facultative bacterium causing cholera, relies on various ABC importers to internalize nutrients, crucial for its survival and propagation. Among these, my research focuses on understanding the mechanisms of two ABC importers of *V. cholerae*: (i) type-I G6P VCA0625-27 transporter and (ii) type-II heme HutCD-B transporter.

As an early step to unravel the molecular mechanisms of HutCD-B mediated heme transport, we previously solved the crystal structure of the PBP HutB in our laboratory. By constructing structural models of HutCD in both outward-facing (OF) and inward-facing (IF) states, I aimed to elucidate the functional dynamics of this transporter. Through biochemical assays, molecular modeling, docking, and extensive MD simulations on HutCD assemblies embedded in lipid bilayers, identified the residues crucial for ATP binding and hydrolysis in HutD. Biochemical results endorsed that the NBD, HutD forms dimer and like other type-II importers, each monomer binds one molecule of ATP. MD simulations on membrane embedded assemblies of HutCD delineated the intricate details required to execute coupled rotational motions between HutCs and HutDs in the IF and OF states. Probable pathway of internalization and interactions of heme with HutCD during ejection from the 'cytoplasmic gate' to the cytosol have been identified through MD simulations on the heme docked HutCD complex. Moreover, our findings underscored that while heme can bind independently to HutD, it modulates ATPase activity, suggesting a regulatory role in heme uptake. Importantly, interactions between HutD and heme were found to rely on hydrophobic and polar interactions rather than metal coordination, shedding light on the nuanced mechanisms of heme transport in *V. cholerae*.

However, deciphering the intricacies of these type-II ABC transporter requires preparation and study of membrane assemblies of this permease-ATPase complex HutCD. Understanding this transport pathway could open up possibilities for targeting this heme uptake pathway as a Trojan Horse for delivering antibacterial drugs into these pathogenic bacteria Moreover, it is known that *V. cholerae* uses hexose-6-Phosphate for biofilm formation as a carbon and phosphate source for subsequent survival under phosphate-limiting conditions. This

ABC type transport system VCA0625-27 has been identified for Glucose 6P transportation through the inner membrane. Analysis of the VCA0625-27 genes on the *Vibrio* species, I have determined high resolution crystal structure of VCA0625 in G6P bound state. Molecular dynamics (MD) simulations, performed on VCA0625 structure in the apo and G6P bound states, revealed bi-lobal movements. Site directed mutagenesis followed by isothermal titration calorimetry on VCA0625 delineated the roles of different residues in ligand binding efficacy. We have further characterized the ATPase VCA0627 in terms of ATP binding and hydrolysis. Structure analysis coupled with MD simulation results, different biochemical assays modeling, docking and systematic sequence analysis indulged us to believe that VCA0625-27 is an atypical type-I ABC importer involved in G6P internalization in *V. cholerae* as well as in 27 other gram-negative bacteria involved in diverse functions.

These collective insights lead to the conclusion that while a basic, universal process might exist for the internalization of certain nutrients, the intricate molecular mechanisms of uptake significantly depend on the specific nutrient requirements of different species.

.

References

1. Davies, J. S., Currie, M. J., Wright, J. D., Newton-Vesty, M. C., North, R. A., Mace, P. D., ... & Dobson, R. C. (2021). Selective nutrient transport in bacteria: multicomponent transporter systems reign supreme. *Frontiers in Molecular Biosciences*, *8*, 699222.

2. Saier Jr, M. H. (2000). A functional-phylogenetic classification system for transmembrane solute transporters. *Microbiology and molecular biology reviews*, *64*(2), 354-411.

3. Ellermann, M., & Arthur, J. C. (2017). Siderophore-mediated iron acquisition and modulation of host-bacterial interactions. *Free Radical Biology and Medicine*, *105*, 68-78.

4. Sheldon, J. R., Laakso, H. A., & Heinrichs, D. E. (2016). Iron acquisition strategies of bacterial pathogens. *Virulence Mechanisms of Bacterial Pathogens*, 43-85.

5. Eisenreich, W., Heesemann, J., Rudel, T., & Goebel, W. (2013). Metabolic host responses to infection by intracellular bacterial pathogens. *Frontiers in cellular and infection microbiology*, *3*, 24.

6. Richardson, A. R. (2019). Virulence and metabolism. *Microbiology spectrum*, *7*(2), 10-1128.

7. Allen, P. E., & Martinez, J. J. (2020). Modulation of host lipid pathways by pathogenic intracellular bacteria. *Pathogens*, *9*(8), 614.

8. Olive, A. J., & Sassetti, C. M. (2016). Metabolic crosstalk between host and pathogen: sensing, adapting and competing. *Nature Reviews Microbiology*, *14*(4), 221-234.

9. Uruén, C., Chopo-Escuin, G., Tommassen, J., Mainar-Jaime, R. C., & Arenas, J. (2020). Biofilms as promoters of bacterial antibiotic resistance and tolerance. *Antibiotics*, *10*(1), 3.

10. Maresso, A. W., & Maresso, A. W. (2019). The Acquisition and Consumption of Host Nutrients. *Bacterial Virulence: A Conceptual Primer*, 131-144.

11. Chen, I., & Lui, F. (2019). Physiology, active transport.

12. Berger, E. A. (1973). Different mechanisms of energy coupling for the active transport of proline and glutamine in Escherichia coli. *Proceedings of the National Academy of Sciences*, *70*(5), 1514-1518.

13. Saier Jr, M. H., Fagan, M. J., Hoischen, C., & Reizer, J. (1993). Transport mechanisms. *Bacillus subtilis and other gram-positive bacteria: Biochemistry, physiology, and molecular genetics*, 133-156.

14. Köster, W. (2001). ABC transporter-mediated uptake of iron, siderophores, heme and vitamin B12. *Research in microbiology*, *152*(3-4), 291-301.

15. Moeck, G. S., & Coulton, J. W. (1998). TonB-dependent iron acquisition: mechanisms of siderophore-mediated active transport. *Molecular microbiology*, *28*(4), 675-681.

16. Kadner, R. J. (1990). Vitamin B12 transport in Escherichia coli: energy coupling between membranes. *Molecular microbiology*, *4*(12), 2027-2033.

17. Wandersman, C., & Stojiljkovic, I. (2000). Bacterial heme sources: the role of heme, hemoprotein receptors and hemophores. *Current opinion in microbiology*, *3*(2), 215-220.

18. Cui, J., & Davidson, A. L. (2011). ABC solute importers in bacteria. *Essays in biochemistry*, *50*, 85-99.

19. Linton, K. J. (2007). Structure and function of ABC transporters. *Physiology*, *22*(2), 122-130.

20. Parrow, N. L., Fleming, R. E., & Minnick, M. F. (2013). Sequestration and scavenging of iron in infection. *Infection and immunity*, *81*(10), 3503-3514.

21. Szöllősi, D., Chiba, P., Szakács, G., Stockner, T., & Hegedűs, T. (2016). Mechanism of drug transport by ABC multidrug proteins in structural perspectives.

22. Coll, E. P., & Tieleman, D. P. (2011). ABC transporters. *Molecular machines*, 183-198.

23. Furuta, T. (2021). Structural dynamics of ABC transporters: Molecular simulation studies. *Biochemical Society Transactions*, *49*(1), 405-414.

24. Locher, K. P. (2016). Mechanistic diversity in ATP-binding cassette (ABC) transporters. *Nature structural & molecular biology*, *23*(6), 487-493.

25. Ter Beek, J., Guskov, A., & Slotboom, D. J. (2014). Structural diversity of ABC transporters. *Journal of General Physiology*, *143*(4), 419-435.

26. Tanaka, K. J., Song, S., Mason, K., & Pinkett, H. W. (2018). Selective substrate uptake: The role of ATP-binding cassette (ABC) importers in pathogenesis. *Biochimica et Biophysica Acta (BBA)-Biomembranes*, *1860*(4), 868-877.

27. Lewinson, O., & Livnat-Levanon, N. (2017). Mechanism of action of ABC importers: conservation, divergence, and physiological adaptations. *Journal of molecular biology*, *429*(5), 606-619.

28. Merino, G., Boos, W., Shuman, H. A., & Bohl, E. (1995). The Inhibition of Maltose Transport by the Unliganded Form of the Maltose-binding Protein of Escherichia coli: Experimental Findings and Mathematical Treatment. *Journal of theoretical biology*, *177*(2), 171-179.

29. Liu, C. E., Liu, P. Q., & Ames, G. F. L. (1997). Characterization of the adenosine triphosphatase activity of the periplasmic histidine permease, a traffic ATPase (ABC transporter). *Journal of Biological Chemistry*, *272*(35), 21883-21891.

30. Kadaba, N. S., Kaiser, J. T., Johnson, E., Lee, A., & Rees, D. C. (2008). The high-affinity E. coli methionine ABC transporter: structure and allosteric regulation. *Science*, *321*(5886), 250-253.

31. Lanfermeijer, F. C., Picon, A., Konings, W. N., & Poolman, B. (1999). Kinetics and consequences of binding of nona-and dodecapeptides to the oligopeptide binding protein (OppA) of Lactococcus lactis. *Biochemistry*, *38*(44), 14440-14450.

32. Vigonsky, E., Ovcharenko, E., & Lewinson, O. (2013). Two molybdate/tungstate ABC transporters that interact very differently with their substrate binding proteins. *Proceedings of the National Academy of Sciences*, *110*(14), 5440-5445.

33. Woo, J. S., Zeltina, A., Goetz, B. A., & Locher, K. P. (2012). X-ray structure of the Yersinia pestis heme transporter HmuUV. *Nature structural & molecular biology*, *19*(12), 1310-1315.

34. Lewinson, O., Lee, A. T., Locher, K. P., & Rees, D. C. (2010). A distinct mechanism for the ABC transporter BtuCD–BtuF revealed by the dynamics of complex formation. *Nature structural & molecular biology*, *17*(3), 332-338.

35. Rohrbach, M. R., Braun, V., & Köster, W. (1995). Ferrichrome transport in Escherichia coli K-12: altered substrate specificity of mutated periplasmic FhuD and interaction of FhuD with the integral membrane protein FhuB. *Journal of bacteriology*, *177*(24), 7186-7193.

36. Bao, H., & Duong, F. (2012). Discovery of an auto-regulation mechanism for the maltose ABC transporter MalFGK2. *PLoS One*, *7*(4), e34836.

37. Rice, A. J., Park, A., & Pinkett, H. W. (2014). Diversity in ABC transporters: type I, II and III importers. *Critical reviews in biochemistry and molecular biology*, *49*(5), 426-437.

38. Hollenstein, K., Frei, D. C., & Locher, K. P. (2007). Structure of an ABC transporter in complex with its binding protein. *Nature*, *446*(7132), 213-216.

39. Kadaba, N. S., Kaiser, J. T., Johnson, E., Lee, A., & Rees, D. C. (2008). The high-affinity E. coli methionine ABC transporter: structure and allosteric regulation. *Science*, *321*(5886), 250-253.

40. Gerber, S., Comellas-Bigler, M., Goetz, B. A., & Locher, K. P. (2008). Structural basis of trans-inhibition in a molybdate/tungstate ABC transporter. *Science*, *321*(5886), 246-250.

41. Sebulsky, M. T., Shilton, B. H., Speziali, C. D., & Heinrichs, D. E. (2003). The role of FhuD2 in iron (III)-hydroxamate transport in Staphylococcus aureus: demonstration that FhuD2 binds iron (III)-hydroxamates but with minimal conformational change and implication of mutations on transport. *Journal of Biological Chemistry*, *278*(50), 49890-49900.

42. Oldham, M. L., Davidson, A. L., & Chen, J. (2008). Structural insights into ABC transporter mechanism. *Current opinion in structural biology*, *18*(6), 726-733.

43. Korkhov, V. M., Mireku, S. A., & Locher, K. P. (2012). Structure of AMP-PNP-bound vitamin B12 transporter BtuCD–F. *Nature*, *490*(7420), 367-372.

44. Locher, K. P., Lee, A. T., & Rees, D. C. (2002). The E. coli BtuCD structure: a framework for ABC transporter architecture and mechanism. *Science*, *296*(5570), 1091-1098.

45. Grote, M., Polyhach, Y., Jeschke, G., Steinhoff, H. J., Schneider, E., & Bordignon, E. (2009). Transmembrane signaling in the maltose ABC transporter MalFGK2-E: periplasmic MalF-P2 loop communicates substrate availability to the ATP-bound MalK dimer. *Journal of Biological Chemistry*, *284*(26), 17521-17526.

46. Naoe, Y., Nakamura, N., Doi, A., Sawabe, M., Nakamura, H., Shiro, Y., & Sugimoto, H. (2016). Crystal structure of bacterial haem importer complex in the inward-facing conformation. *Nature Communications*, *7*(1), 13411.

47. Rodionov, D. A., Hebbeln, P., Eudes, A., ter Beek, J., Rodionova, I. A., Erkens, G. B., ... & Eitinger, T. (2009). A novel class of modular transporters for vitamins in prokaryotes. *Journal of bacteriology*, *191*(1), 42-51.

48. Duurkens, R. H., Tol, M. B., Geertsma, E. R., Permentier, H. P., & Slotboom, D. J. (2007). Flavin binding to the high affinity riboflavin transporter RibU. *Journal of Biological Chemistry*, *282*(14), 10380-10386.

49. Akhtar, A. A., & Turner, D. P. (2022). The role of bacterial ATP-binding cassette (ABC) transporters in pathogenesis and virulence: Therapeutic and vaccine potential. *Microbial pathogenesis*, *171*, 105734.

50. Baril, S. A., Gose, T., & Schuetz, J. D. (2023). How Cryo-EM has expanded our understanding of membrane transporters. *Drug Metabolism and Disposition*, *51*(8), 904-922.

51. Reidl, J., & Klose, K. E. (2002). Vibrio cholerae and cholera: out of the water and into the host. *FEMS microbiology reviews*, *26*(2), 125-139.

52. Holmgren, J., & Svennerholm, A. M. (1977). Mechanisms of disease and immunity in cholera: a review. *Journal of infectious diseases*, *136*(Supplement_1), S105-S112.

53. Herrington, D. A., Hall, R. H., Losonsky, G. E. N. E. V. I. E. V. E., Mekalanos, J. J., Taylor, R. K., & Levine, M. M. (1988). Toxin, toxin-coregulated pili, and the toxR regulon are essential for Vibrio cholerae pathogenesis in humans. *The Journal of experimental medicine*, *168*(4), 1487-1492.

54. Montero, D. A., Vidal, R. M., Velasco, J., George, S., Lucero, Y., Gómez, L. A., ... & O'Ryan, M. (2023). Vibrio cholerae, classification, pathogenesis, immune response, and trends in vaccine development. *Frontiers in Medicine*, *10*, 1155751.

55. Lospalluto, J. J., & Finkelstein, R. A. (1972). Chemical and physical properties of cholera exo-enterotoxin (choleragen) and its spontaneously formed toxoid (choleragenoid). *Biochimica et Biophysica Acta (BBA)-Protein Structure*, *257*(1), 158-166.

56. Mekalanos, J. J., Swartz, D. J., Pearson, G. D., Harford, N., Groyne, F., & de Wilde, M. (1983). Cholera toxin genes: nucleotide sequence, deletion analysis and vaccine development. *Nature*, *306*(5943), 551-557.

57. Wyckoff, E. E., Mey, A. R., & Payne, S. M. (2007). Iron acquisition in Vibrio cholerae. *Biometals*, *20*, 405-416.

58. Wachsmuth, K., Olsvik, Ø., Evins, G. M., & Popovic, T. (1994). Molecular epidemiology of cholera. *Vibrio cholerae and cholera: molecular to global perspectives*, 357-370.

59. Griffiths, G. L., Sigel, S. P., Payne, S. M., & Neilands, J. B. (1984). Vibriobactin, a siderophore from Vibrio cholerae. *Journal of Biological Chemistry*, *259*(1), 383-385.

60. Helton, E. A. (2010). FeoA, FeoB, and FeoC encode essential components of the Vibrio cholerae ferrous iron transport system.

61. Henderson, D. P., & Payne, S. M. (1994). Characterization of the Vibrio cholerae outer membrane heme transport protein HutA: sequence of the gene, regulation of expression, and homology to the family of TonB-dependent proteins. *Journal of bacteriology*, *176*(11), 3269-3277.

62. Agarwal, S., Dey, S., Ghosh, B., Biswas, M., & Dasgupta, J. (2017). Structure and dynamics of Type III periplasmic proteins Vc FhuD and Vc HutB reveal molecular basis of their distinctive ligand binding properties. *Scientific Reports*, *7*(1), 42812.

63. Li, N., Zhang, C., Li, B., Liu, X., Huang, Y., Xu, S., & Gu, L. (2012). Unique iron coordination in iron-chelating molecule vibriobactin helps Vibrio cholerae evade mammalian siderocalin-mediated immune response. *Journal of Biological Chemistry*, *287*(12), 8912-8919.

64. Sit, B., Crowley, S. M., Bhullar, K., Lai, C. C. L., Tang, C., Hooda, Y., ... & Moraes, T. F. (2015). Active transport of phosphorylated carbohydrates promotes intestinal colonization and transmission of a bacterial pathogen. *PLoS pathogens*, *11*(8), e1005107.

65. Skaar, E. P., Humayun, M., Bae, T., DeBord, K. L., & Schneewind, O. (2004). Iron-source preference of Staphylococcus aureus infections. *Science*, *305*(5690), 1626-1628.

66. Klose, K. E., & Mekalanos, J. J. (1997). Simultaneous prevention of glutamine synthesis and high-affinity transport attenuates Salmonella typhimurium virulence. *Infection and immunity*, *65*(2), 587-596.

67. Shelburne, S. A., Davenport, M. T., Keith, D. B., & Musser, J. M. (2008). The role of complex carbohydrate catabolism in the pathogenesis of invasive streptococci. *Trends in microbiology*, *16*(7), 318-325.

68. Agarwal, S., Biswas, M., & Dasgupta, J. (2015). Purification, crystallization and preliminary X-ray analysis of the periplasmic haem-binding protein HutB from Vibrio cholerae. *Acta Crystallographica Section F: Structural Biology Communications*, *71*(4), 401-404.

69. Agarwal, S., Dey, S., Ghosh, B., Biswas, M., & Dasgupta, J. (2019). Mechanistic basis of vitamin B12 and cobinamide salvaging by the Vibrio species. *Biochimica et Biophysica Acta (BBA)-Proteins and Proteomics*, *1867*(2), 140-151.

70. Tamura, K., Sugimoto, H., Shiro, Y., & Sugita, Y. (2019). Chemo-mechanical coupling in the transport cycle of a heme ABC transporter. *The Journal of Physical Chemistry B*, *123*(34), 7270-7281.

71. Tamura, K., & Sugita, Y. (2020). Free energy analysis of a conformational change of heme ABC transporter BhuUV-T. *The Journal of Physical Chemistry Letters*, *11*(8), 2824-2829.

72. Palmer, L. D., & Skaar, E. P. (2016). Transition metals and virulence in bacteria. *Annual review of genetics*, *50*(1), 67-91.

73. Cornelissen, C. N. (2018). Subversion of nutritional immunity by the pathogenic Neisseriae. *Pathogens and disease*, *76*(1), ftx112.

74. Raymond, K. N., Dertz, E. A., & Kim, S. S. (2003). Enterobactin: an archetype for microbial iron transport. *Proceedings of the national academy of sciences*, *100*(7), 3584-3588.

75. Eakanunkul, S., Lukat-Rodgers, G. S., Sumithran, S., Ghosh, A., Rodgers, K. R., Dawson, J. H., & Wilks, A. (2005). Characterization of the periplasmic heme-binding protein shut from the heme uptake system of Shigella dysenteriae. *Biochemistry*, *44*(39), 13179-13191.

76. Hider, R. C., & Kong, X. (2010). Chemistry and biology of siderophores. *Natural product reports*, *27*(5), 637-657.

77. Paoli, M., Marles-Wright, J., & Smith, A. N. N. (2002). Structure–function relationships in heme-proteins. *DNA and cell biology*, *21*(4), 271-280.

78. Choby, J. E., & Skaar, E. P. (2016). Heme synthesis and acquisition in bacterial pathogens. *Journal of molecular biology*, *428*(17), 3408-3428.

79. Starr, J., Brown, M. F., Aschenbrenner, L., Caspers, N., Che, Y., Gerstenberger, B. S., ... & Han, S. (2014). Siderophore receptor-mediated uptake of lactivicin analogues in gram-negative bacteria. *Journal of medicinal chemistry*, *57*(9), 3845-3855.

80. Wandersman, C., & Stojiljkovic, I. (2000). Bacterial heme sources: the role of heme, hemoprotein receptors and hemophores. *Current opinion in microbiology*, *3*(2), 215-220.

81. Schmitt, M. P. (1997). Utilization of host iron sources by Corynebacterium diphtheriae: identification of a gene whose product is homologous to eukaryotic heme oxygenases and is required for acquisition of iron from heme and hemoglobin. *Journal of bacteriology*, *179*(3), 838-845.

82. Schuller, D. J., Zhu, W., Stojiljkovic, I., Wilks, A., & Poulos, T. L. (2001). Crystal structure of heme oxygenase from the gram-negative pathogen Neisseria meningitidis and a comparison with mammalian heme oxygenase-1. *Biochemistry*, *40*(38), 11552-11558.

83. Ratliff, M., Zhu, W., Deshmukh, R., Wilks, A., & Stojiljkovic, I. (2001). Homologues of neisserial heme oxygenase in gram-negative bacteria: degradation of heme by the product of the pigA gene of Pseudomonas aeruginosa. *Journal of bacteriology*, *183*(21), 6394-6403.

84. Skaar, E. P., Gaspar, A. H., & Schneewind, O. (2004). IsdG and IsdI, heme-degrading enzymes in the cytoplasm of Staphylococcus aureus. *Journal of Biological Chemistry*, *279*(1), 436-443.

85. Wyckoff, E. E., Schmitt, M., Wilks, A., & Payne, S. M. (2004). HutZ is required for efficient heme utilization in Vibrio cholerae. *Journal of bacteriology*, *186*(13), 4142-4151.

86. Celia, H., Noinaj, N., Zakharov, S. D., Bordignon, E., Botos, I., Santamaria, M., ... & Buchanan, S. K. (2016). Structural insight into the role of the Ton complex in energy transduction. *Nature*, *538*(7623), 60-65.

87. Payne, S. M., Mey, A. R., & Wyckoff, E. E. (2016). Vibrio iron transport: evolutionary adaptation to life in multiple environments. *Microbiology and Molecular Biology Reviews*, *80*(1), 69-90.

88. Occhino, D. A., Wyckoff, E. E., Henderson, D. P., Wrona, T. J., & Payne, S. M. (1998). Vibrio cholerae iron transport: haem transport genes are linked to one of two sets of tonB, exbB, exbD genes. *Molecular microbiology*, *29*(6), 1493-1507.

89. Mey, A. R., Wyckoff, E. E., Oglesby, A. G., Rab, E., Taylor, R. K., & Payne, S. M. (2002). Identification of the Vibrio cholerae enterobactin receptors VctA and IrgA: IrgA is not required for virulence. *Infection and immunity*, *70*(7), 3419-3426.

90. Mirmohammadsadeghi, H., Abedi, D., Mohmoudpour, H. R., & Akbari, V. (2013). Comparison of five methods for extraction of genomic DNA from a marine Archaea, Pyrococcus furiosus.

91. Mani, R. S., Karimi-Busheri, F., Cass, C. E., & Weinfeld, M. (2001). Physical properties of human polynucleotide kinase: hydrodynamic and spectroscopic studies. *Biochemistry*, *40*(43), 12967-12973.

92. Dey, S., Biswas, M., Sen, U., & Dasgupta, J. (2015). Unique ATPase site architecture triggers cis-mediated synchronized ATP binding in heptameric AAA+-ATPase domain of flagellar regulatory protein FlrC. *Journal of Biological Chemistry*, *290*(14), 8734-8747.

93. Buckstein, M. H., He, J., & Rubin, H. (2008). Characterization of nucleotide pools as a function of physiological state in Escherichia coli. *Journal of bacteriology*, *190*(2), 718-726.

94. Chen, CC., Hwang, JK. & Yang, JM. (2009). $(PS)^2$-v2: template-based protein structure prediction server. *BMC Bioinformatics*, 10, 366.

95. Jumper, J., Evans, R., Pritzel, A., Green, T., Figurnov, M., Ronneberger, O., ... & Hassabis, D. (2021). Highly accurate protein structure prediction with AlphaFold. *nature*, *596*(7873), 583-589.

96. Rubenstein, A. B., Blacklock, K., Nguyen, H., Case, D. A., & Khare, S. D. (2018). Systematic comparison of Amber and Rosetta energy functions for protein structure evaluation. *Journal of chemical theory and computation*, *14*(11), 6015-6025.

97. Jo, S., Kim, T., Iyer, V. G., & Im, W. (2008). CHARMM-GUI: a web-based graphical user interface for CHARMM. *Journal of computational chemistry*, *29*(11), 1859-1865.

98. Maier, J. A., Martinez, C., Kasavajhala, K., Wickstrom, L., Hauser, K. E., & Simmerling, C. (2015). ff14SB: improving the accuracy of protein side chain and backbone parameters from ff99SB. *Journal of chemical theory and computation*, *11*(8), 3696-3713.

99. Dickson, C. J., Madej, B. D., Skjevik, Å. A., Betz, R. M., Teigen, K., Gould, I. R., & Walker, R. C. (2014). Lipid14: the amber lipid force field. *Journal of chemical theory and computation*, *10*(2), 865-879.

100. Price, D. J., & Brooks III, C. L. (2004). A modified TIP3P water potential for simulation with Ewald summation. *The Journal of chemical physics*, *121*(20), 10096-10103.

101. Kräutler, V., Van Gunsteren, W. F., & Hünenberger, P. H. (2001). A fast SHAKE algorithm to solve distance constraint equations for small molecules in molecular dynamics simulations. *Journal of computational chemistry*, *22*(5), 501-508.

102. Berendsen, H. J., Postma, J. V., Van Gunsteren, W. F., DiNola, A. R. H. J., & Haak, J. R. (1984). Molecular dynamics with coupling to an external bath. *The Journal of chemical physics*, *81*(8), 3684-3690.

103. Darden, T., York, D., & Pedersen, L. (1993). Particle mesh Ewald: An N· log (N) method for Ewald sums in large systems. *The Journal of chemical physics*, *98*(12), 10089-10092.

104. Pastor, R. W., Brooks, B. R., & Szabo, A. (1988). An analysis of the accuracy of Langevin and molecular dynamics algorithms. *Molecular Physics*, *65*(6), 1409-1419.

105. Roy, R., Ghosh, B., & Kar, P. (2020). Investigating conformational dynamics of Lewis Y oligosaccharides and elucidating blood group dependency of cholera using molecular dynamics. *ACS omega*, *5*(8), 3932-3942.

106. Zhang, Y., Feller, S. E., Brooks, B. R., & Pastor, R. W. (1995). Computer simulation of liquid/liquid interfaces. I. Theory and application to octane/water. *The Journal of chemical physics*, *103*(23), 10252-10266.

107. Gedeon, P. C., Thomas, J. R., & Madura, J. D. (2015). Accelerated molecular dynamics and protein conformational change: a theoretical and practical guide using a membrane embedded model neurotransmitter transporter. *Molecular modeling of proteins*, 253-287.

108. Moradi, S., Nowroozi, A., & Shahlaei, M. (2019). Correction: Shedding light on the structural properties of lipid bilayers using molecular dynamics simulation: A review study. *RSC advances*, *9*(14), 7687-7687.

109. Wang, J., Wang, W., Kollman, P. A., & Case, D. A. (2006). Automatic atom type and bond type perception in molecular mechanical calculations. *Journal of molecular graphics and modelling*, *25*(2), 247-260.

110. Li, P., & Merz Jr, K. M. (2016). MCPB. py: A python based metal center parameter builder.

111. Jakalian, A., Jack, D. B., & Bayly, C. I. (2002). Fast, efficient generation of high-quality atomic charges. AM1-BCC model: II. Parameterization and validation. *Journal of computational chemistry*, *23*(16), 1623-1641.

112. Wang, J., Wolf, R. M., Caldwell, J. W., Kollman, P. A., & Case, D. A. (2004). Development and testing of a general amber force field. *Journal of computational chemistry*, *25*(9), 1157-1174.

113. Trott, O., & Olson, A. J. (2010). AutoDock Vina: improving the speed and accuracy of docking with a new scoring function, efficient optimization, and multithreading. *Journal of computational chemistry*, *31*(2), 455-461.

114. Chen, J., Lu, G., Lin, J., Davidson, A. L., & Quiocho, F. A. (2003). A tweezers-like motion of the ATP-binding cassette dimer in an ABC transport cycle. *Molecular cell*, *12*(3), 651-661.

115. Moradi, M., & Tajkhorshid, E. (2013). Mechanistic picture for conformational transition of a membrane transporter at atomic resolution. *Proceedings of the National Academy of Sciences*, *110*(47), 18916-18921.

116. Liu, Y., Liu, B., Xu, T., Wang, Q., Li, W., Wu, J., ... & Wang, L. (2021). A fructose/H+ symporter controlled by a LacI-type regulator promotes survival of pandemic Vibrio cholerae in seawater. *Nature Communications*, *12*(1), 4649.

117. McDonough, E., Kamp, H., & Camilli, A. (2016). V ibrio cholerae phosphatases required for the utilization of nucleotides and extracellular DNA as phosphate sources. *Molecular microbiology*, *99*(3), 453-469.

118. Moisi, M., Lichtenegger, S., Tutz, S., Seper, A., Schild, S., & Reidl, J. (2013). Characterizing the hexose-6-phosphate transport system of Vibrio cholerae, a utilization system for carbon and phosphate sources. *Journal of bacteriology*, *195*(8), 1800-1808.

119. Sit, B., Crowley, S. M., Bhullar, K., Lai, C. C. L., Tang, C., Hooda, Y., ... & Moraes, T. F. (2015). Active transport of phosphorylated carbohydrates promotes intestinal colonization and transmission of a bacterial pathogen. *PLoS pathogens*, *11*(8), e1005107.

120. Kumar, A., Ghosh, B., Poswal, H. K., Pandey, K. K., Hosur, M. V., Dwivedi, A., ... & Sharma, S. M. (2016). Protein crystallography beamline (PX-BL21) at Indus-2 synchrotron. *Journal of synchrotron Radiation*, *23*(2), 629-634.

121. Kabsch, W. (2010). xds. *Acta Crystallographica Section D: Biological Crystallography*, *66*(2), 125-132.

122. Winn, M. D., Ballard, C. C., Cowtan, K. D., Dodson, E. J., Emsley, P., Evans, P. R., ... & Wilson, K. S. (2011). Overview of the CCP4 suite and current developments. *Acta Crystallographica Section D: Biological Crystallography*, *67*(4), 235-242.

123. Adams, P. D., Afonine, P. V., Bunkóczi, G., Chen, V. B., Davis, I. W., Echols, N., ... & Zwart, P. H. (2010). PHENIX: a comprehensive Python-based system for macromolecular structure solution. *Acta Crystallographica Section D: Biological Crystallography*, *66*(2), 213-221.

124. Emsley, P., & Cowtan, K. (2004). Coot: model-building tools for molecular graphics. *Acta crystallographica section D: biological crystallography*, *60*(12), 2126-2132.

125. Tian, C., Kasavajhala, K., Belfon, K. A., Raguette, L., Huang, H., Migues, A. N., ... & Simmerling, C. (2019). ff19SB: amino-acid-specific protein backbone parameters trained against quantum mechanics energy surfaces in solution. *Journal of chemical theory and computation*, *16*(1), 528-552.

126. Scheffel, F., Demmer, U., Warkentin, E., Hülsmann, A., Schneider, E., & Ermler, U. (2005). Structure of the ATPase subunit CysA of the putative sulfate ATP-binding cassette (ABC) transporter from Alicyclobacillus acidocaldarius. *FEBS letters*, *579*(13), 2953-2958.

127. Ose, T., Fujie, T., Yao, M., Watanabe, N., & Tanaka, I. (2004). Crystal structure of the ATP-binding cassette of multisugar transporter from Pyrococcus horikoshii OT3. *Proteins: Structure, Function, and Bioinformatics*, *57*(3), 635-638.

128. Oldham, M. L., Khare, D., Quiocho, F. A., Davidson, A. L., & Chen, J. (2007). Crystal structure of a catalytic intermediate of the maltose transporter. *Nature*, *450*(7169), 515-521.

129. Weng, J., Fan, K., & Wang, W. (2012). The conformational transition pathways of ATP-binding cassette transporter BtuCD revealed by targeted molecular dynamics simulation. *PLoS One*, *7*(1), e30465.

Publications

1. **Saha, I.**, Chakraborty, S., Agarwal, S., Mukherjee, P., Ghosh, B., & Dasgupta, J. (2022). Mechanistic insights of ABC importer HutCD involved in heme internalization by Vibrio cholerae. *Scientific Reports*, *12*(1), 7152.

2. **Saha, I.**, Ghosh, B., & Dasgupta, J. (2024). Structural insights in to the atypical type-I ABC Glucose-6-phosphate importer VCA0625-27 of Vibrio cholerae. *Biochemical and Biophysical Research Communications*, *716*, 150030.

3. **Saha, I.**, Biswas, A., Dasgupta, J. Insights into the interactions of heme with HutD, the ATPase domain of the ABC importer HutCD during heme internalization in Vibrio cholerae. (Manuscript under preparation)

scientific reports

Check for updates

OPEN

Mechanistic insights of ABC importer HutCD involved in heme internalization by *Vibrio cholerae*

Indrila Saha[1], Shrestha Chakraborty[1], Shubhangi Agarwal[1,3], Peeali Mukherjee[1], Biplab Ghosh[2]✉ & Jhimli Dasgupta[1]✉

Heme internalization by pathogenic bacteria inside a human host to accomplish the requirement of iron for important cellular processes is of paramount importance. Despite this, the mechanism of heme import by the ATP-binding-cassette (ABC) transporter HutCD in *Vibrio cholerae* remains unexplored. We have performed biochemical studies on ATPase HutD and its mutants, along with molecular modelling, docking and unbiased all-atom MD simulations on lipid-solvated models of permease-ATPase complex HutCD. The results demonstrated mechanisms of ATP binding/hydrolysis and trapped transient and global conformational changes in HutCD, necessary for heme internalization. ATPase HutD forms a dimer, independent of the permease HutC. Each HutD monomer canonically binds ATP in a 1:1 stoichiometry. MD simulations demonstrated that a rotational motion of HutC dimer occurs synchronously with the inter-dimeric D-loop interactions of HutDs. F151 of TM4–TM5 loop of HutC, packs with ATP and Y15 of HutD, initiating 'cytoplasmic gate opening' which mimics an 'outward-facing' to 'inward-facing' conformational switching upon ATP hydrolysis. The simulation on 'inward-facing' HutCD culminates to an 'occluded' state. The simulation on heme-docked HutCD indicated that the event of heme release occurs in ATP-free 'inward-facing' state. Gradual conformational changes of the TM5 helices of HutC towards the 'occluded' state facilitate ejection of heme.

Motile pathogenic bacteria acquire iron, the essential metal cofactor for several cellular processes, aiming at successful colonization and growth inside a host[1–3]. Animal hosts attempt to limit iron availability through 'nutritional immunity' thereby combating the colonization of pathogens[4]. This results in free-iron levels as low as 10^{-24} M[5]. To refute this, many pathogens develop various efficient strategies to obtain iron from the host-derived molecules during infection. The main strategies for iron acquisition by pathogenic bacteria include direct extraction of Fe^{3+} from specific iron-containing complexes of the hosts, such as lactoferrin, transferrin, haemoglobin or hemin, and/or production of small Fe^{3+}-chelating molecules called siderophores[6,7]. Heme or hemin is considered beneficial for pathogens due to its abundance within the host environment, especially when the pathogen lacks the ability to synthesize heme, as observed in the case of some heme auxotrophs[8]. The mechanisms of 'iron thievery' of pathogenic bacteria require special attention since these can be mimicked for the 'Trojan Horse' mechanism of antibiotic delivery to diminish permeability-mediated drug resistance[9].

The structure of the cellular envelope of gram-negative bacteria requires heme to be trafficked across the outer membrane, through the periplasm, and across the inner membrane before reaching the cytosol. Import of heme across the outer membrane of bacteria is accomplished by a TonB-dependent system with the help of proton motive force[10]. Active transport of the nutrients across the plasma membrane is achieved by various ATP binding cassette (ABC) transporters. Generally, periplasmic ligand binding protein (PLBP) captures nutrient, cytosolic nucleotide binding domains (NBDs) utilise ATP hydrolysis driven energy to cause large-scale conformational changes in the permeases to facilitate uptake of nutrients. Interestingly, despite their common basic architecture, molecular mechanisms of ATP binding and hydrolysis mediated alteration of nutrient translocation pathway are remarkably diverse even for the Type II importers, which are well known for the uptake of iron-siderophores, vitamin B12 and heme[11–15]. So far, structural details of heme transporting ABC importers are restricted to HmuUV of *Yersinia pestis* and BhuUV-T of *Burkholderia cenocepacia*[13,14]. Crystal structure of HmuUV of *Y. pestis*

[1]Department of Biotechnology, St. Xavier's College (Autonomous), 30, Mother Teresa Sarani, Kolkata 700016, India. [2]Macromolecular Crystallography Section, Beamline Development & Application Section, Bhabha Atomic Research Center, Trombay, Mumbai 400085, India. [3]Present address: Weill Cornell Medicine, Department of Anesthesiology, 1300 York Ave, New York, NY 10065, USA. ✉email: biplab@rrcat.gov.in; jhimli@sxccal.edu

demonstrated an 'outward-facing' (OF) conformation of the permeases with the translocation pathway opening to the periplasmic side of the membrane. The structure of BhuUV-T of *B. cenocepacia*, on the other hand, was obtained in 'inward-facing' (IF) conformation with the substrate translocation pathway open to the cytoplasm[14]. Recently, a targeted MD simulations on BhuUV-T with bound ATP in the IF state yielded an 'occluded' (Occ) state, in which both the cytoplasmic and periplasmic sides of heme translocation channel remained closed[16,17].

Vibrio cholerae, the causative agent of diarrheal disease cholera, encodes multiple iron acquisition systems, including the synthesis and transport of the catechol-type siderophore vibriobactin, transport of exogenous siderophores such as enterobactin and the acquisition of heme of the host system[18,19]. Analysis of the hut genes indicated that HutCD-B, which encodes a periplasmic binding protein (HutB), a cytoplasmic membrane permease (HutC) and an ATPase (HutD) are required to reconstitute the *V. cholerae* heme-transport system in *Escherichia coli*[20]. Based on that, ABC type transport system HutCD-B has been identified as the system of *V. cholerae* for heme transportation through the inner membrane[21]. However, the structure, dynamics and mechanism of ATP-dependent heme translocation through this system of *V. cholerae* remains unknown. As an early step to understand the molecular basis of HutCD-B mediated heme transport, we solved the crystal structure of periplasmic heme-binding protein HutB[22]. Structural studies coupled with biochemical analysis indicated parallel binding of two heme molecules to HutB in a pH-dependent manner which attributed to its storage[22]. MD simulation studies exhibited an unforeseen inter-lobe swinging motion that is presumably important for binding and/or ejection of heme to the permeases. Nonetheless, the mechanism of heme internalization is still unknown in *V. cholerae*.

In ABC transporters, the nature of conformational changes is largely specific to the species and the nutrients. Functional assays with HutD and its mutants along with molecular modelling, docking and MD simulations on HutCD assemblies were performed here to identify the pivotal residues involved in ATP binding/hydrolysis, as well as to trap the ATP hydrolysis driven transient and global conformational changes required for heme internalization. Here we have prepared structural models of HutCD in the OF and IF states. Two Mg^{2+}-ATP molecules were docked in HutDs of OF states. HutCD in the IF state was docked with heme. The HutCD assemblies in both the states were inserted into a solvated lipid (dimyristoyl phosphatidylcholine, DMPC) bilayer. To get insights into the conformational shifts expected to occur in the heme transportation pathway in ± Mg^{2+}-ATP states, unbiased MD simulations were performed on all the sets for 1 µs each. Biochemical results endorsed that the NBD, HutD forms dimer and like other type-II importers, each monomer binds one molecule of ATP. MD simulations on membrane embedded assemblies of HutCD delineated the intricate details required to execute coupled rotational motions between HutCs and HutDs in the IF and OF states. Probable pathway and interactions of heme with HutCD during ejection from the 'cytoplasmic gate' to the cytoplasm have been identified through MD simulations on the heme docked HutCD complex.

Results

Sequence analysis of HutC and HutD. To structurally characterize HutCD of *V. cholerae* we have performed a BLAST search against PDB with the amino acid sequences of the TMD, HutC (Accession code: C3LWH8) and the NBD, HutD (Accession code: A0A0H3ADP8) and aligned the sequences with their close structural homologs using Clustal Omega (Fig. 1). HutC has shown 45% identity and 67% similarity (for 303aa) with heme transporting permease HmuU of *Y. pestis* and 45% identity (63% similarity for 339 aa) with BhuU, of *B. cenocepacia* (Fig. 1a). In addition to the heme transporters, HutC sequence also showed 41% identity and 58% similarity (for 293 aa) with BtuC, the ABC transporter permease involved in vitamin B12 uptake. HutD, the cytosolic ATPase showed a maximum identity of 45% (62% similarity for 242 aa) with HmuV while identity with BhuV of *B. cenocepacia* was relatively less (36% identity and 51% similarity for 276 aa). Identity of HutD with BtuD of BtuCD was 36% (52% similarity for 217 aa). The significant extent of identity with the heme and B12 ABC transporters of different prokaryotic systems strongly indicates that HutCD is expected to possess a similar overall fold and belongs to the type II class of ABC transporter. The predicted topology of HutC with ten transmembrane helices appears to correspond to the transmembrane segment of the permeases of the type II class (marked in Fig. 1a). Similarly, HutD, like the other NBDs, exhibits sequence and structure conservation across the transporter family[23] and contains several conserved functional motifs such as Walker-A (WA), Walker-B (WB) motifs, an ABC transporter-specific or 'signature' motif, and two shorter sequences containing conserved glutamine and histidine residues (Q-loop and H-loop, respectively) (Fig. 1b).

Cross-linking and size exclusion chromatography suggest dimerization of HutD. To identify the oligomeric state of HutD, crosslinking experiments were carried out with HutD in the presence and absence of AMP.PNP, the non-hydrolysable analogue of ATP, using Glutaraldehyde as crosslinker (Fig. 2a, Fig. S1). Migration pattern, analysed by 10% SDS-PAGE gel, depicted the presence of dimer (~ 60 kDa) along with monomer of HutD (30 kDa) both in the presence and absence of AMP.PNP (Fig. 2a, Fig. S1). However, tendency of forming dimer is prevalent in the presence of AMP.PNP (Fig. 2a). Little bit of anomaly in movement of proteins in SDS-PAGE (which is observed in case of HutD dimer) is not very uncommon upon cross-linking or chemical modifications of proteins. Moreover. HutD, that was used for cross-linking experiments was pure and functional, and hence the band near ~ 60 kDa has been considered as dimeric band.

To further validate the results of cross-linking experiments, we performed size exclusion chromatography (SEC) using Superdex 200 increase column 10/300 with HutD in free and AMP.PNP treated states (Fig. 2b,c; free state and AMP.PNP treated HutD are shown in red and green colours respectively). In free state, peak II of Fig. 2b having elution volume of 15.36 ml was indicative of monomer along with a trace amount of dimer. However, incubation with AMP.PNP showed a clear shift of peak-II towards dimer with elution volume of 14.68 ml (Fig. 2b,c). This indicates that AMP.PNP binding facilitates dimerization which corroborates with the

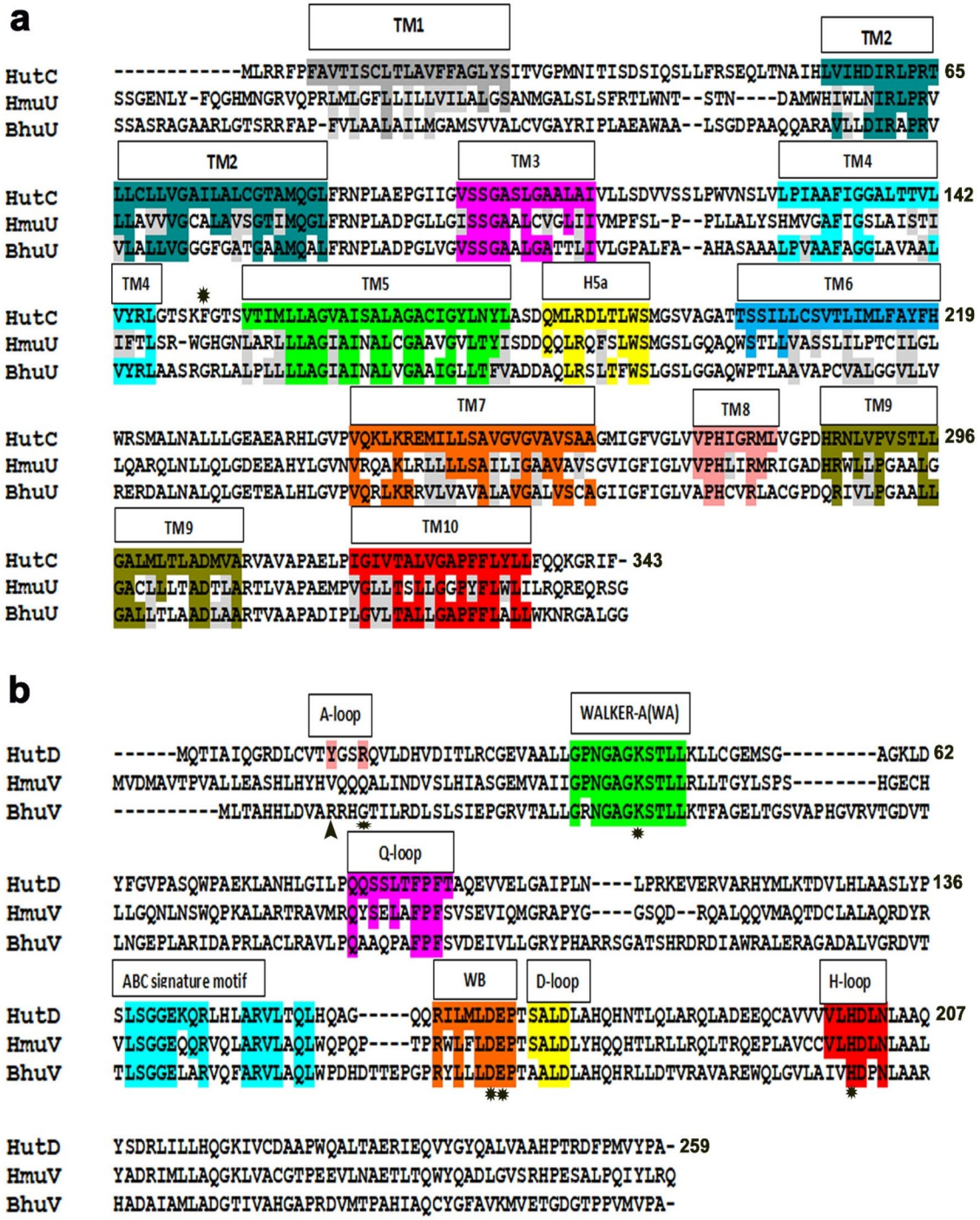

Figure 1. Sequence analysis of HutC and HutD. (**a**) Sequence alignment of HutC from *Vibrio cholerae*, HmuU from *Yersinia pestis* and BhuU from *Burkholderia cenocepacia*. Numbering is based on HutC sequence. (**b**) Sequence alignment of HutD from *Vibrio cholerae*, HmuV from *Yersinia pestis* and BhuV from *Burkholderia cenocepacia*. Numbering is based on HutD sequence. Important motifs and conserved residues are individually coloured/marked. Semi-conservation inside important motifs are shaded in grey. Some important residues are marked with '*'.

observations of cross-linking experiments (Fig. 2a). In both experiments of SEC, peak-I probably denotes little impurities in the samples and/or soluble aggerates.

So far, HutCD was known as a putative type-II ABC importer of heme, based on sequence comparisons. Our observations authenticated that like other type-II importers HutD is capable of forming dimer in the absence of the permease, HutC, and ATP binding facilitates dimerization of HutD.

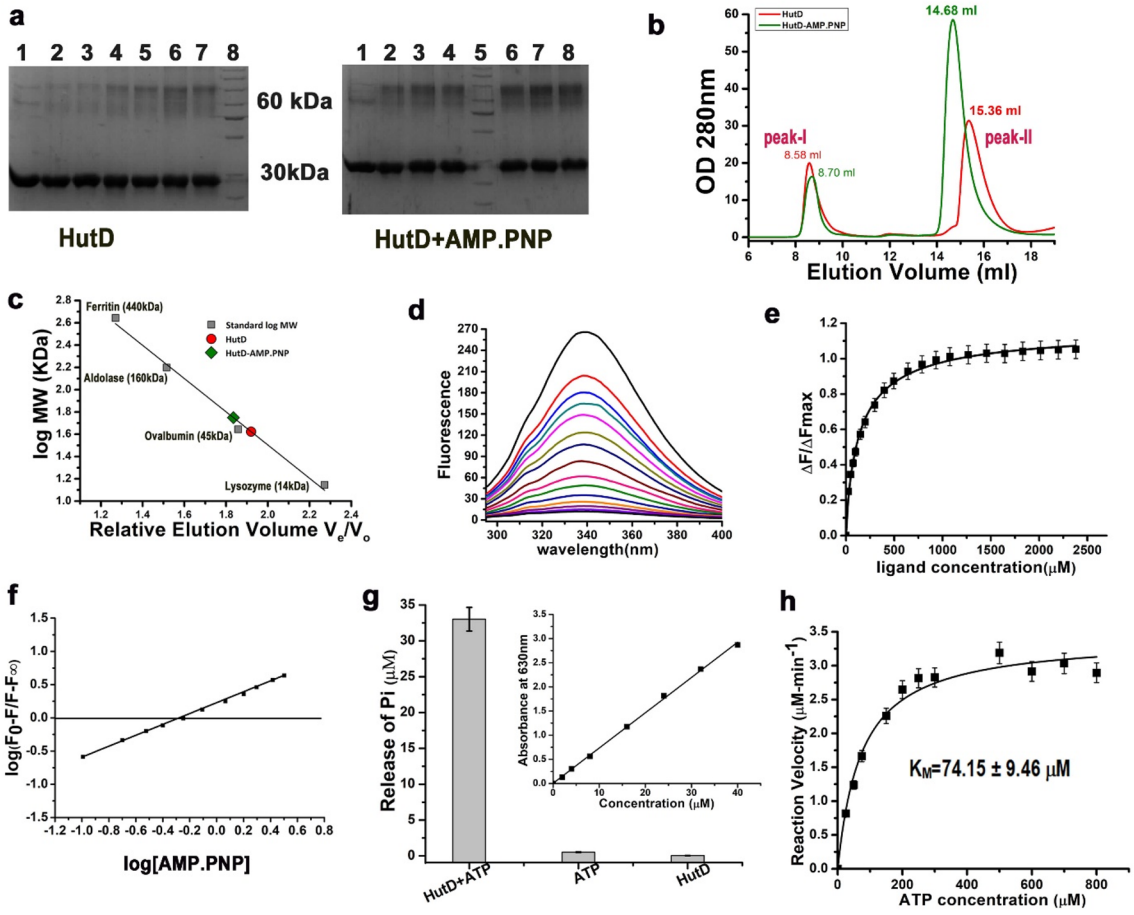

Figure 2. Dimerization and ATP binding/hydrolysis by HutD. (**a**) Crosslinking of HutD with Glutaraldehyde in Nt-free state (left) and after incubation with AMP.PNP showed prevalent dimerization upon incubation with AMP.PNP; *left:* (L1: Control, L2–L7: after treatment with 0.005–0.04% of Glutaraldehyde, L8: MWM), right: (L1: Control, L2–L4: after treatment with 0.005%, 0.01%, and 0.02% of Glutaraldehyde, L5: MWM, L6–L8: after treatment with 0.03%, 0.035%, and 0.04% of Glutaraldehyde). A cropped version is used here to reduce space and to maintain clarity. Original gel pictures are available in Fig. S1; (**b**) size exclusion chromatography elution profiles of HutD in Nt-free and upon incubation with AMP.PNP; (**c**) the molecular weights of the peaks were determined from the calibration curve prepared using molecular weight standards. Elution volumes suggest strong dimeric shift upon AMP.PNP binding to HutD. (**d,e**) Fluorescence quenching demonstrated significant change in fluorescence upon AMP.PNP binding to HutD; (λ_{exc} = 280 nm, λ_{em} = 295–400 nm) with slit widths of 5 nm for both excitation and emission. Plots of $\Delta F/\ \Delta F_{max}$ against ligand AMP.PNP (mM) obtained a K_d value of 94 ± 0.024 μM; (**f**) slope of the *straight line* indicates 1:1 binding stoichiometry between HutD and AMP.PNP; (**g**) significant ATP hydrolysis of HutD were observed in Malachite green assay and the release of inorganic phosphate (*Pi*) was estimated against the standard curve of KH_2PO_4 (*Inset*); (**h**) reaction velocity of HutD, measured at a protein concentration of 2.5 μM, were plotted against ATP concentrations (μM) as per Michaelis–Menten equation $y = Vmax \times x^n/(k^n + x^n)$ with 'One site-specific binding' model. Error bars in (**e,g,h**) are SD values obtained from at least three replicates.

Binding of AMP.PNP with HutD. Participation of A-loop, Walker-A and Walker-B is well known in the ATP binding in the NBDs of type-II ABC importers (PDB codes: 4G1U, 1L2T). Sequence alignment (Fig. 1b) indicated proximity of Y15 of A-loop to the ATP binding site (Fig. 1b). We, therefore, decided to investigate the interactions of AMP.PNP, the non-hydrolysable ATP analog, with HutD by monitoring the intrinsic fluorescence quenching at an excitation wavelength of 280 nm (λ_{exc} = 280 nm, λ_{em} = 295–400 nm) accounting the contributions of tryptophans and tyrosines present at the ligand binding site. Interestingly, with significant fluorescence quenching, HutD has shown considerable interactions with AMP.PNP with a dissociation constant, K_d of 94 ± 0.024 μM (Fig. 2d,e). Calculation of stoichiometry indicated binding between HutD and AMP.PNP in a 1:1 molar ratio (Fig. 2f). Negligible quenching upon excitation at wavelength of 295 nm (λ_{exc} = 295 nm, λ_{em} = 308–400 nm), that accounts the contribution of Trp only, ruled out the participation of the Trp residues in ATP binding (Fig. S2) and established that the Trp residues are located beyond the foster distance of ATP binding site of HutD. In turn, these results established the proximity and participation of Y15 in ATP binding.

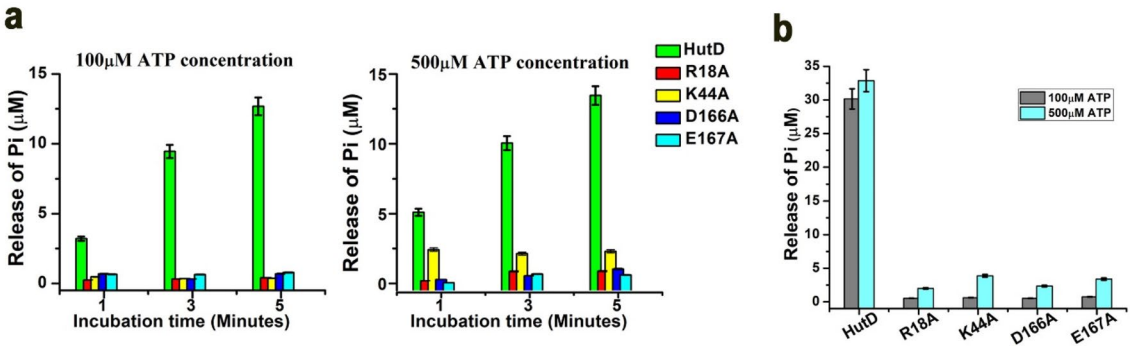

Figure 3. Identification of functionally crucial residues of HutD by mutagenesis. (**a**) Loss of function of the mutants R18A, K44A, D166A, E167A compared to HutD, as evident from the measurement of ATPase activities with 100 μM and 500 μM ATP at three time points (1, 3, 5 min). (**b**) ATPase activities of HutD and mutants measured with an extended incubation time of 20 min with 100 μM and 500 μM of ATP.

ATP hydrolysis by HutD and calculations of V_{max} and K_M. HutD has shown substantial ATP hydrolysis while tested using Malachite green assay (Fig. 2g). 2.5 μM HutD and 100 μM ATP (Sigma Aldrich) were incubated at 298 K for 20 min (Fig. 2g). The release of inorganic phosphate (Pi) was measured at 630 nm upon incubation with Malachite green as per the protocol described earlier[24]. Released Pi from each reaction was quantified by comparing with a Pi standard curve prepared using KH_2PO_4 (inset of Fig. 2g). HutD without ATP addition served as the control reaction. The experiments were minimally performed in triplicates.

We have determined maximal velocity (V_{max}) and Michaelis constant (K_M) through time course ATPase assays of HutD. Considering linearity of Pi production during time course experiment, reaction velocity was measured upon incubation of HutD with increasing ATP concentrations (up to 800 μM) through a time scan up to 5 min. Reaction velocity (V_0) in terms of Pi release was then plotted against ATP concentrations (Fig. 2h). Fitting of ATPase activities in Michaelis–Menten equation resulted in V_{max} of 3.42 ± 0.10 μM/min and K_M of 74.15 ± 9.46 μM for HutD (Fig. 2h).

Identification of pivotal functional residues of HutD through mutagenesis. Based on sequence similarity, we could presume functionally important residues of HutD (Fig. 1b, Table S1). To confirm our propositions, we have prepared four point mutants of HutD namely R18A, K44A, D166A and E167A, and investigated their ATP hydrolysis capacity using Malachite green assays. Time course experiments showed that the amount of Pi produced by wild type (wt) HutD during ATP hydrolysis increased approximately linearly with incubation time for the first 5 min (Fig. 3a). However, the ATPase activity using 100 μM of ATP of the mutants R18A, K44A, D166A and E167A were drastically low compared to wt HutD and remained constant throughout for different incubation times varying from 1 to 5 min (Fig. 3a). The concentration of ATP inside the bacterial host may elevate up to 1 mM under certain conditions[25]. Therefore, we have measured ATPase activities of wt HutD and the variants upon elevating ATP concentrations to 500 μM as well. All four mutants showed negligible ATPase activities even with an elevation of ATP concentration to 500 μM (Fig. 3a *right panel*). The increase of incubation time to 20 min also did not affect the ATP hydrolysis pattern of the mutants compared to wt HutD (Fig. 3b).

Modelling of HutD and HutCD in OF and IF conformational states. Oligomeric states of NBD of ABC transporters and mechanism of ATP binding/hydrolysis differ significantly in the case of type-I and type-II importers. While in the case of the type-I importers dimerization of NBDs are influenced by interactions with permeases, type-II NBDs can form dimer independently[23]. Sequence comparisons proposed HutCD as a type-II importer (Fig. 1). Our biochemical results established that HutD forms stable functional dimer (that can bind and hydrolyse ATP) in the absence of the permease HutC (Fig. 2a–c). Therefore, we decided to investigate the dynamic nature of HutD dimers in the OF and IF states.

The structures of the two type-II Heme importers, HmuUV of *Y. pestis* (PDB code: 4G1U) and BhuUV from *B. cenocepacia* (PDB code: 5B57), in two different conformational states, served as templates to prepare the models of HutD and HutCD in the OF and IF states. First, we prepared the models of HutD dimers in OF and IF conformations (Fig. 4a,b). Previous studies on type-II ABC transporters suggested that ATP hydrolysis mainly occurs in the OF state[26]. Therefore, knowledge-based docking of two Mg^{2+}-ATP molecules was performed with HutD in OF state (Fig. 4a,c) where coordinates and binding mode of ATP in MJ0796 NBD dimer (PDB code 1L2T) was treated as template. Dimers of HutC in OF and IF states were also modelled in a similar manner. All models were prepared initially using ps2v2[27] and later verified by Alphafold2[28]. HutCD assemblies in IF and OF states were then generated considering the assembly structures of HmuUV and BhuUV (Fig. 4d–i).

Altogether, we have prepared five sets of complexes: (1) Mg^{2+}-ATP bound HutD dimer in OF state; (2) HutD dimer in IF state; (3) lipid bilayer embedded Mg^{2+}-ATP bound HutCD assembly in OF state; (4) lipid bilayer embedded HutCD in IF state; (5) Heme bound lipid bilayer embedded HutCD in IF state. MD simulations, each of 1 μs, were carried out on all complexes with the Amber-18 and AmberTools-18 software packages[29]. We have used DMPC (1,2-dimyristoyl-sn-glycero-3-phosphocholine) molecules for constructing the bilayer and CHARMM-GUI[30] was used to prepare the solvated protein-embedded lipid bilayer system before simulations.

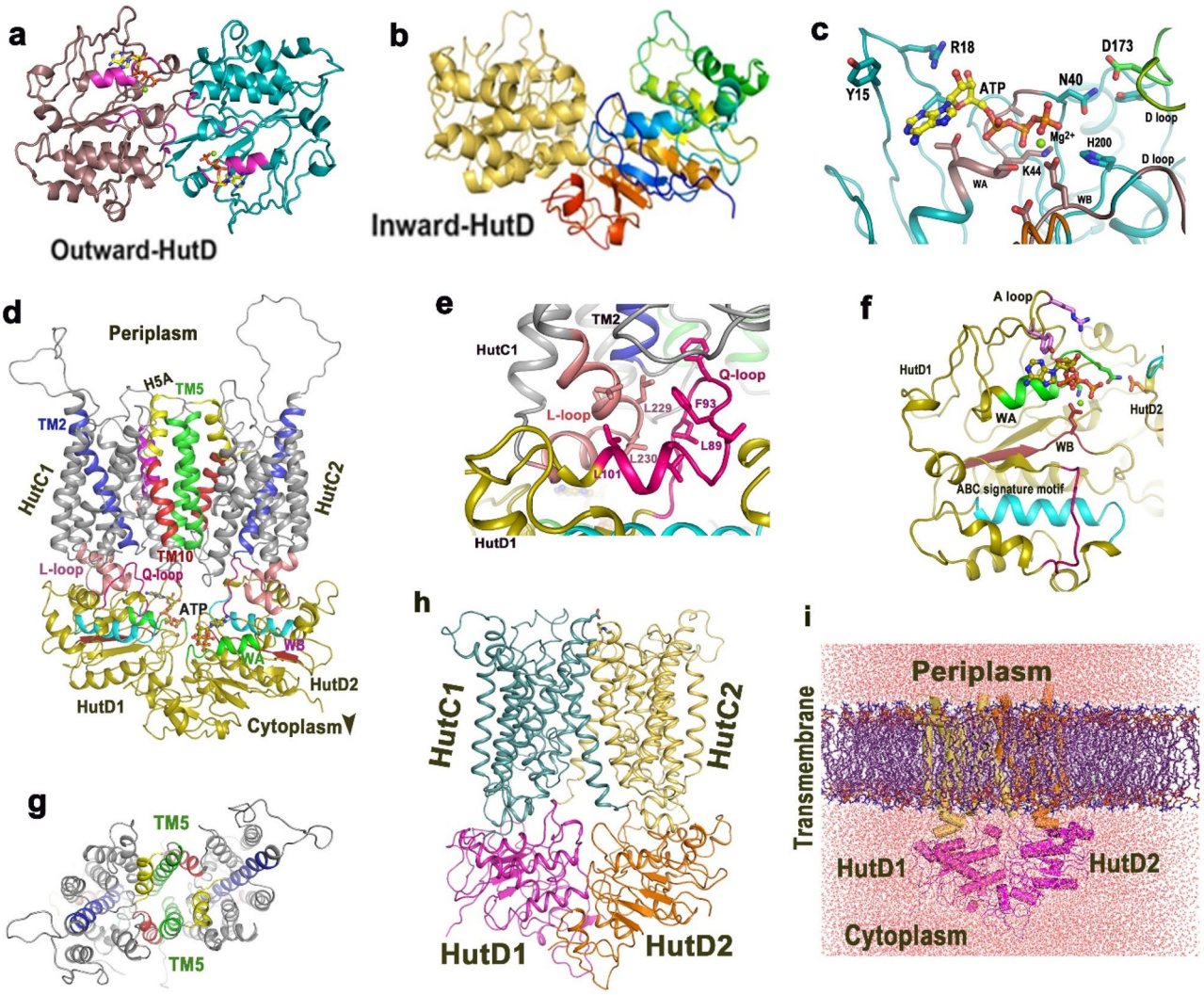

Figure 4. Models of HutD, HutC in different states and lipid embedded assembly. Ribbon representation of the models of (**a**) HutD dimer in the OF state, Nucleotide-binding domains (NBDs, dimer of HutD) are shown in brown and cyan, conserved Walker-A motif or P-Loop is shown in magenta of each NBD. Two ATP molecules are shown in stick; (**b**) HutD dimer in the IF state; (**c**) zoomed view of the docking of Mg^{2+}-ATP in HutD OF dimer and related interactions; (**d**) Mg^{2+}-ATP bound HutCD dimeric assembly in the OF state; zoomed view of different regions of HutCD are shown in (**e–g**). (**e**) Interactions between L-loop of HutC1 (salmon) with Q-loop of HutD1 (magenta); (**f**) disposition of binding motifs such as A-loop, Walker-A (green), Walker-B (maroon) around Mg^{2+}-ATP. ABC signature motif is shown in cyan; (**g**) arrangements of transmembrane helices in HutCD-OF model is shown from the periplasmic side. TM5 helices of each TMD is shown in green, H5a in yellow; (**h**) Model of HutCD assembly in IF state. (**i**) Model of HutCD assembly embedded in solvated DMPC lipid bilayer.

An embedded model is shown in Fig. 4i. However, the lipid bilayer and the solvents molecules were not shown in the subsequent figures to maintain clarity.

Dynamics of HutD dimer in free and in HutC bound states. In order to understand the collective internal motions of HutD dimers in the OF and IF states, we have calculated root-mean-square deviations (RMSDs) of the Cα atoms from the snapshots of the trajectories up to 1 μs for the two chains of NBDs of HutD dimer and HutCD dimer (Fig. 5a,b). In all cases, RMSD values converged well to a constant value after approximately 75 ns. RMSD values of the two HutD protomers (named as HutD1 and HutD2) were plotted separately (Fig. 5a,b). The RMSD values for HutD1 of HutCD OF, HutCD IF, and HutD IF and OF were steady around 3.0 to 3.5 Å (Fig. 5a). However, HutD2 in OF state showed relatively lower RMSDs ranging around 2 Å (Fig. 5b). This indicates that NBDs acquire stability upon Mg^{2+}-ATP binding, although asymmetric movements were observed between the monomers (Fig. 5a,b).

B-factors of the two chains of HutD were also plotted separately. The highest B-factors were observed for HutD and the B-factors were lowest for HutD of HutCD in ATP-Mg^{2+} bound state (Fig. 5c,d). HutD of HutCD IF state showed intermediate flexibility (Fig. 5c,d). Further analysis of B-factors of the two monomers of HutD

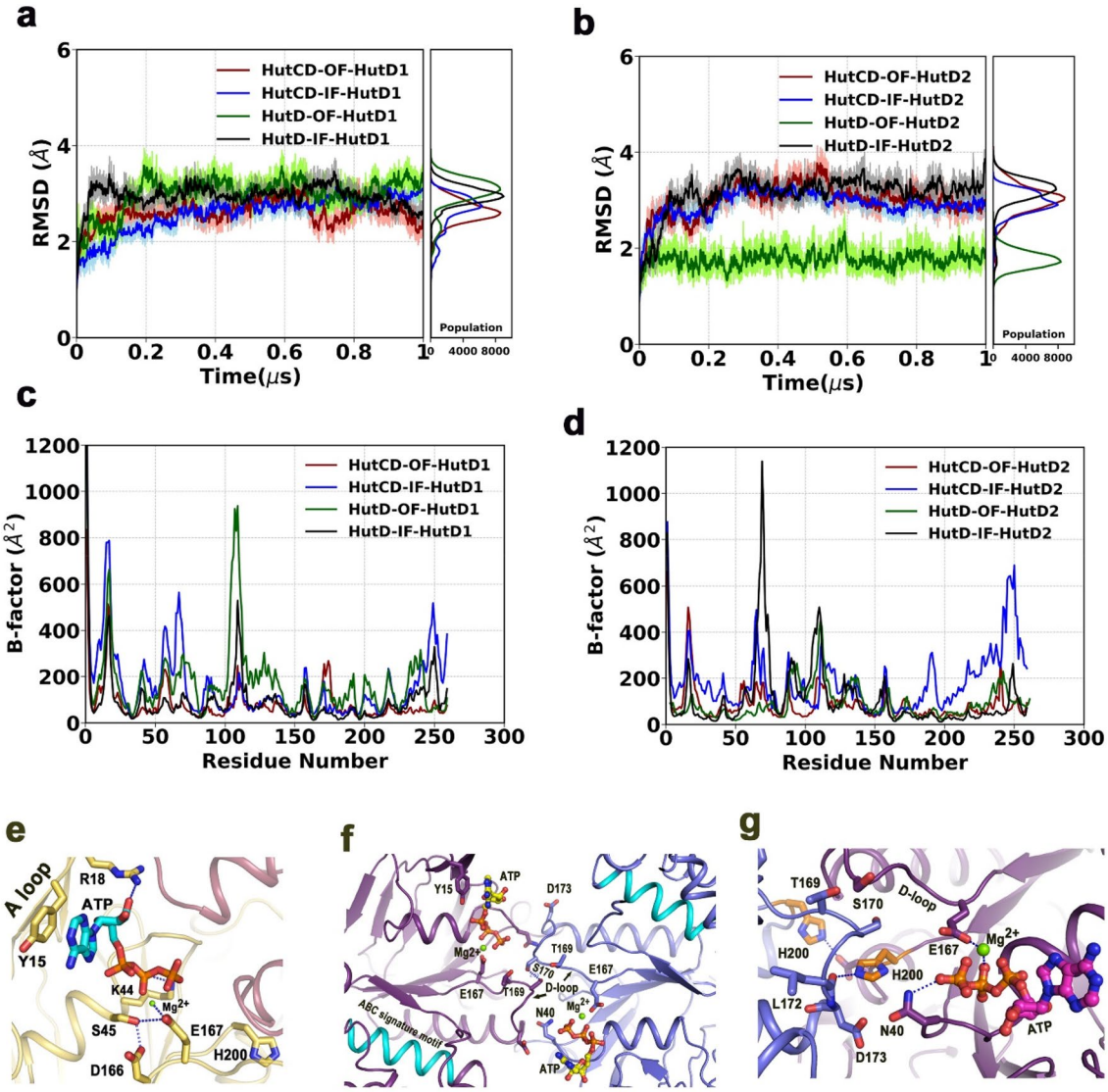

Figure 5. MD simulation results of HutD in the OF state. (**a,b**) Cα-RMSD values of HutD1 and HutD2 as part of HutD dimers and as part of HutCD assemblies in the IF and OF states; (**c,d**) B-factors of HutD1 and HutD2 as part of HutD dimers and as part of HutCD assemblies in the IF and OF states; (**e**) ATP binding in HutD OF at 200 ns showing involvement of the residues of A-loop, Walker-A and Walker-B motifs; (**f**) interaction between D-loops of two HutD monomers at 108 ns of simulation run on HutD dimer in the OF state; (**g**) disposition of H200 at 150 ns of the simulation run on HutD dimer in the OF state.

showed asymmetry/dissimilar movements. Reduction in fluctuations in the residues 100–115 of HutD1 in HutCD indicates that not only ATP-Mg^{2+} but the TMDs also help in stabilization of the complex, because of the interactions between L-loop of HutC and Q-loop of HutD (Figs. 4e, 5c,d). The flexibility and asymmetric nature of the A-loop (residues 12–23, Fig. 1b) are also evident for all the states, which is more distinct in case of HutD1 compared to HutD2 (Fig. 5c,d). As evident from large B-factor values, high flexibility were observed in certain surface exposed regions of HutD (Fig. 5c,d).

Interactions near ATP binding site of HutD dimer. Analysis of the simulation trajectory of HutD dimer in the presence of Mg^{2+}-ATP bound OF state revealed that Y15 of the A-loop packs hydrophobically with the adenine base of ATP where R18 interacts with the ribose sugar of ATP (Fig. 5e). During dynamics, Mg^{2+} consistently remains bound to E167 of Walker-B and is poised to hydrolyze ATP (Fig. 5e,f). D166, the neighboring residue, interacts with S45 of Walker-A and thereby stabilizes the Walker-A conformation. K44 acts as the pivotal residue of Walker-A that interacts and stabilizes β- and γ-phosphates of ATP (Fig. 5e). These observations corroborate with abrogation of ATP hydrolysis of R18, K44, D166 and E167 to Ala (Fig. 3).

In the OF state, the D-loops of the two HutD monomers interact with each other at the dimeric interface which is mediated primarily by T169 and S170 (Fig. 5f). H200 also participates in dimerization (Fig. 5g). H200 of both the chains interacts with the D-loops belonging to the *trans* protomer (Fig. 5g). N40 is found to play a

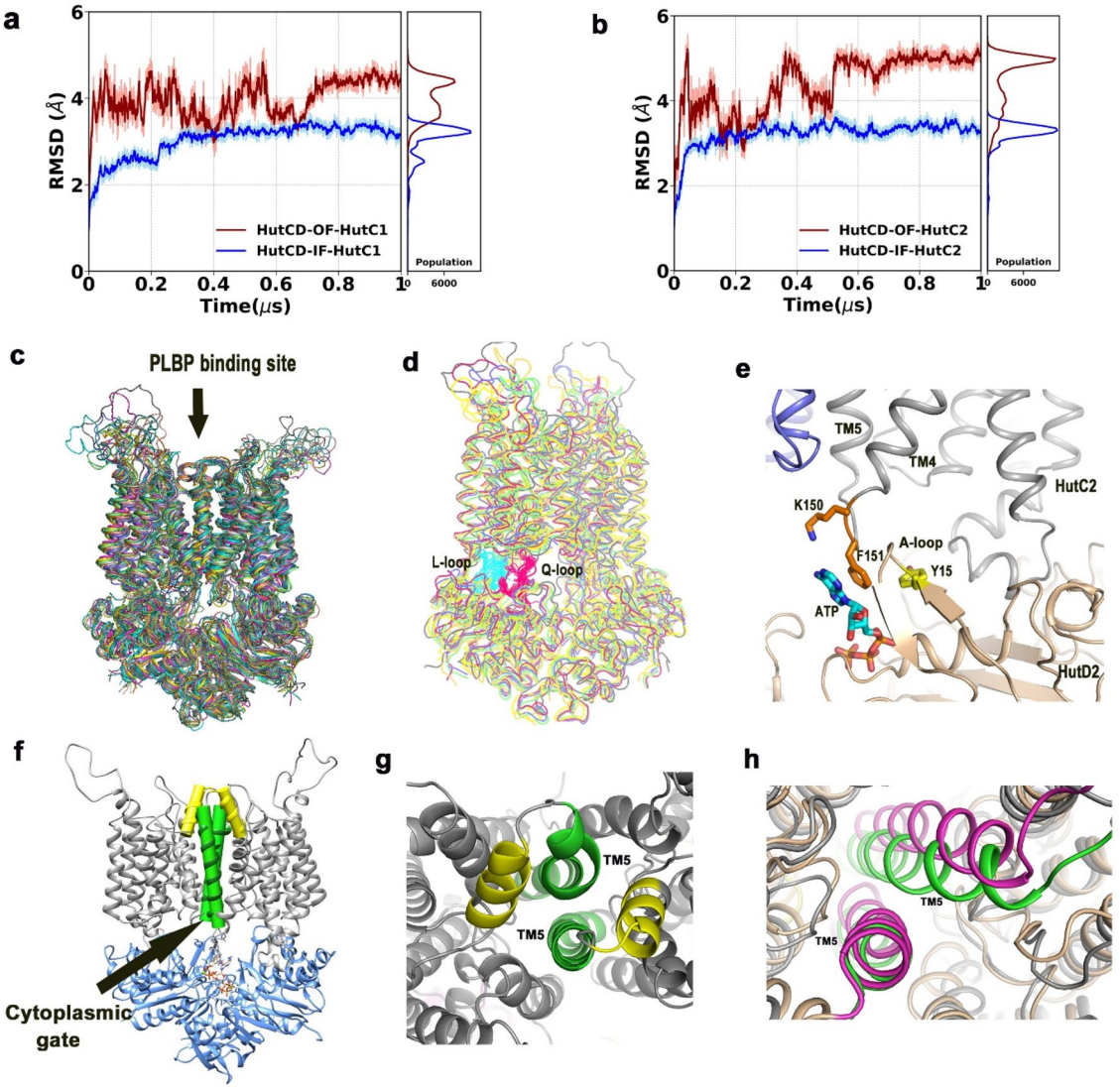

Figure 6. MD simulation showed OF to IF transition in HutCD. (**a,b**) Cα-RMSD values of HutC1 and HutC2 as part of HutCD assemblies in IF and OF states; (**c**) superposition of snapshots showing overall movement in HutCD OF state. PLBP binding site using an arrow; (**d**) superposition of snapshots showing proximity between L-loop (cyan) of HutC and Q-loop (pink) of HutD during dynamics; (**e**) snapshot of 150 ns shows interaction of F151 of HutC with ATP and Y15 of A-loop of HutD that causes cytoplasmic gate opening; (**f**) TM5 helices (green) of HutCD OF at the beginning of MD run; (**g**) zoomed view of TM5 helices (green) and H5a (yellow) of the beginning frame from periplasmic side; (**h**) superposition of snapshots of HutCD OF starting frame (green) and 150 ns (magenta) shows increased inter TM5–TM5 distance at 150 ns leading to cytoplasmic gate opening.

dual role. This residue is capable of interacting both with the γ-phosphate of bound ATP and D173 of the D-loop belonging to the *trans*-acting HutD (Fig. 5f,g). ATP binding was found to be assisted by 'ABC signature motif' in BtuCDF[26]. However, we have hardly observed any contribution of 'ABC signature motif' in ATP binding for HutCD (Fig. 5f).

Dynamics of HutCD in the OF state. We observed that RMSDs of the two HutD chains of HutCD converged after 75 ns and remained steady around 2.5 Å and 3 Å respectively. To investigate the flexibility and conformational shift of TMDs in HutCD, we have calculated the RMSDs of HutC1 and HutC2 in OF and IF states from MD trajectories run up to 1 μs. RMSD plots of two TMD chains (Fig. 6a,b) indicated that the values converged after approximately 75 ns. While RMSD values of HutCs in the IF state remained stable around 3 Å (Fig. 6a,b), significant fluctuations were observed in the RMSDs of HutCs in the OF state, ranging between 4 and 5 Å. Overall superposition of the snapshots in OF state (ranging between 100 and 750 ns) demonstrated high flexibility of the loops exposed to periplasmic side and encompassing the PLBP binding site (aa 30–55 of HutC) (Fig. 6c). Although these loops of both HutC monomers were apparently in the upright conformation in the staring model (Fig. 4d), after dynamics they culminated in different conformations (Fig. 6c). In one HutC monomer, this loop region was found in upright conformation whereas in the other it acquired an inclined con-

Trajectory of HutCD OF state (ns)	S170 of HutD1/N40 of HutD2 (Å)	N40 of HutD1/S170 of HutD2 (Å)	D-loop distance S170–S170
79	11.65	5.49	4.6
98	11.15	5.21	5.0
103	7.2	5.38	2.92
117	10.7	7.2	3.5
127	7.64	7.56	2.93
136	5.15	4.17	9.48
141	4.02	2.81	8.65
151	4.79	2.63	8.24
184	3.88	5.15	8.09
342	4.67	4.92	11.69
381	2.89	4.47	9.93
400	4.70	2.92	10.30
420	3.71	3.88	11.22
450	3.36	4.96	10.020
481	4.70	4.76	11.889
500	3.36	3.158	11.550
553	4.863	4.653	12.052
595	4.66	4.82	12.299
606	5.80	6.9	17.26

Table 1. Random frames taken in order to see any proximities between S170 of HutD1:N40 of HutD2, N40 of HutD1:S170 of HutD2 and S170 of HutD1:S170 HutD2.

formation (Fig. 6c). Asymmetric movement of this loop in two HutC monomers might be attributed to ease the accommodation of the PLBP.

Synchronized conformational shift of HutD and HutC in ATP-Mg^{2+} bound OF state HutCD. Analysis of the simulation trajectory of HutCD OF state indicated that the interactions between the D-loops of the two HutD monomers are instrumental in the transmission of conformational shift to HutC. In HutCD, the distance between S170 of the SALD motif of the D-loops of the two monomers varied from 2.9 (103 ns) to 17 Å (606 ns) (Table 1). Upon proximity, the D-loops interacted with each other through H-bonding between S170 and/or T169 (Fig. 5f). N40 stabilized the γ-phosphate of ATP and interacted with D173 belonging to the 'SALD motif' of the D-loop of *trans*-acting protomer (Fig. 5f,g). However, this interaction was inversely related to inter HutD interactions through the D-loops, which is evident from Table 1. Upon proximity of the D-loops of the two monomers of HutD, N40 interacted with the γ-phosphate of ATP practically facilitating ATP hydrolysis.

Available structures suggest that a cytoplasmic loop, called L-loop that is located between TM6 and TM7 helices of TMD, shares extensive contacts with the complementary groove on the NBD surface and is proposed to be critical in TMD-NBD communication[31]. Such interactions were evident in HutCD as well (Fig. 4d). Superposition of the snapshots, collected from 50 to 580 ns of the simulation run of HutCD, established retention of proximity and hydrophobic interactions between L-loop of HutC and Q-loop of HutD (Fig. 6d). The conserved Q85 of the Q-loop of HutD was also found to interact with the *cis*-acting D-loop. The conformational shifts in HutD dimer, caused by the position and the interactions of the D-loops, therefore, relayed to the L-loop of HutC through the Q loop of HutD. Trajectories of HutCD in OF state between 140 and 300 ns showed vigorous structural movements, and after 300 ns there has been a continuous loosening and widening of the overall structure, with concomitant dissociation of HutD1–HutD2 interface by distancing of D-loops (Table 1).

Opening of the 'cytoplasmic gate'. The 'cytoplasmic gate' that resides in cytoplasmic side of TM5 is known to be instrumental in heme translocation, as evident from the structures of HmuUV and BhuUV[13,14]. F151 that belongs to the loop between TM4 and TM5 of HutC located near cytoplasmic gate is found to be important in terms of transmission of the signal. At the beginning of simulation, this loop was 13 Å away from HutDs. During dynamics, F151 was seen to pack with adenine base of ATP and Y15 of the A-loop of HutD (Fig. 6e). Interestingly, the involvement of F151 in such hydrophobic packing is not consistently simultaneous in each HutC–HutD duo. In early stage of simulation, such as 80 ns to 150 ns, the interaction remained simultaneous in both HutC1–HutD1 and HutC2–HutD2. However, after 200 ns the interactions were not that consistent. Subsequently, F151 of HutC packs with Y15 of HutD but adenine base of ATP remains sufficiently away from those residues. In these stages of the trajectory, such interaction was observed in one HutC–HutD while in the other the TM4-TM5 loop was away from the ATP binding site. At the beginning of MD simulation 'cytoplasmic gate' was closed (Fig. 6f) and as expected with OF structure, periplasmic side of the heme uptake channel was open (Fig. 6g). During the progress of the simulation run, packing of F151 of HutC with ATP and Y15 of HutD increases the distance of TM5 in cytoplasmic side essentially opening the cytoplasmic gate (Fig. 6h). A superpo-

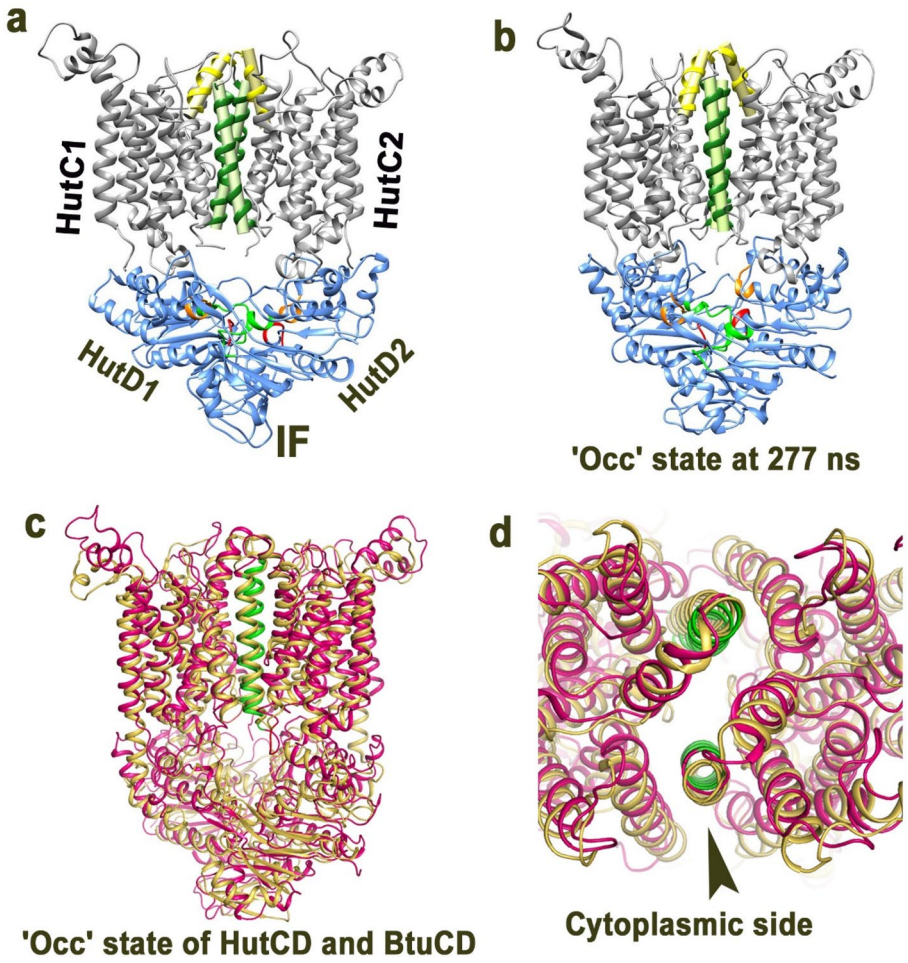

Figure 7. IF state of HutCD culminated to occluded state. (**a**) Ribbon representation of HutCD-IF model at 1 ns, showing axes of H5A (yellow), and TM5 (green), of each TMD in HutC dimer. (**b**) HutCD IF turned to 'occluded' state, snapshot taken at 277 ns from the unbiased MD study. Both in (**a,b**), D-loop, Walker-A and 'ABC signature motif' of HutD are shown in red, green and orange respectively. (**c**) Superposition of the 'occluded' state snapshot of HutCD IF at 277 ns on the 'occluded' state crystal structure of BtuCD (PDB code: 4FI3) (**d**) Zoomed view of (**c**) from cytoplasmic side showing similar orientation of TM5 helices (shown in green in case of HutCD).

sition of the snapshots at 150 ns on that of frame 1 depicts such opening of the 'cytoplasmic gate' (Fig. 6h). This conformational shift made us hypothesise that ATP binding and hydrolysis facilitates opening of the 'cytoplasmic gate' for heme uptake.

Occluded state is observed in the simulation of ATP-free IF state of HutCD. As expected, the HutCD IF model showed inward facing orientation of the TM5 helices (Fig. 7a). Overall RMSD values of HutC and HutD dimers remained around ~ 3 Å during simulation. Throughout the dynamics, the periplasmic side remained tightly sealed by salt bridge interactions between D182 and R186 along with hydrophobic packing between L185 of two H5a helices. Although the crossing angle of H5a–H5a was little lower (50.8°) than the structure of BhuUV (73.1°), like BhuUV, the position of H5a helices remained almost unchanged during dynamics. Notable transition in the orientation of the TM5 helices was observed from 277 ns. At this stage and onward, drastic reduction in the inter TM5–TM5 crossing angle occurred from 23.9° to 6.4° (Fig. 7b). Superposition of the snapshots of HutCD IF, collected at ~ 277 ns, with the occluded ATP bound crystal structure of vitamin B12 importer BtuCD (PDB Code: 4FI3) showed a RMSD of 3 Å (Fig. 7c). Maximum differences were observed among the NBDs, while orientation of the TM5 helices of the two structures were outstandingly similar to each other (Fig. 7c,d). The crossing angle/distance of TM5 axes was 6.4°/16.2 Å in case of HutCD, and that of the ATP bound occluded structure of BtuCD is 11.2°/19.0 Å (PDB Code: 4FI3). These observations suggest that unbiased MD simulation of the HutCD in IF state leads to gradual transition to the ostensible occluded state from ~ 277 ns by exclusive movement of the inter TM5 helices (Fig. 7).

The NBD domains of HutCD IF state remained oriented throughout dynamics, where the main flexible portion was the A-loops (Fig. 5c). In IF state, the *trans*-acting 'ABC signature motif' was found near the Walker-A, although the distance was not equal in case of the two protomers. Gradual proximilty of Walker-A and

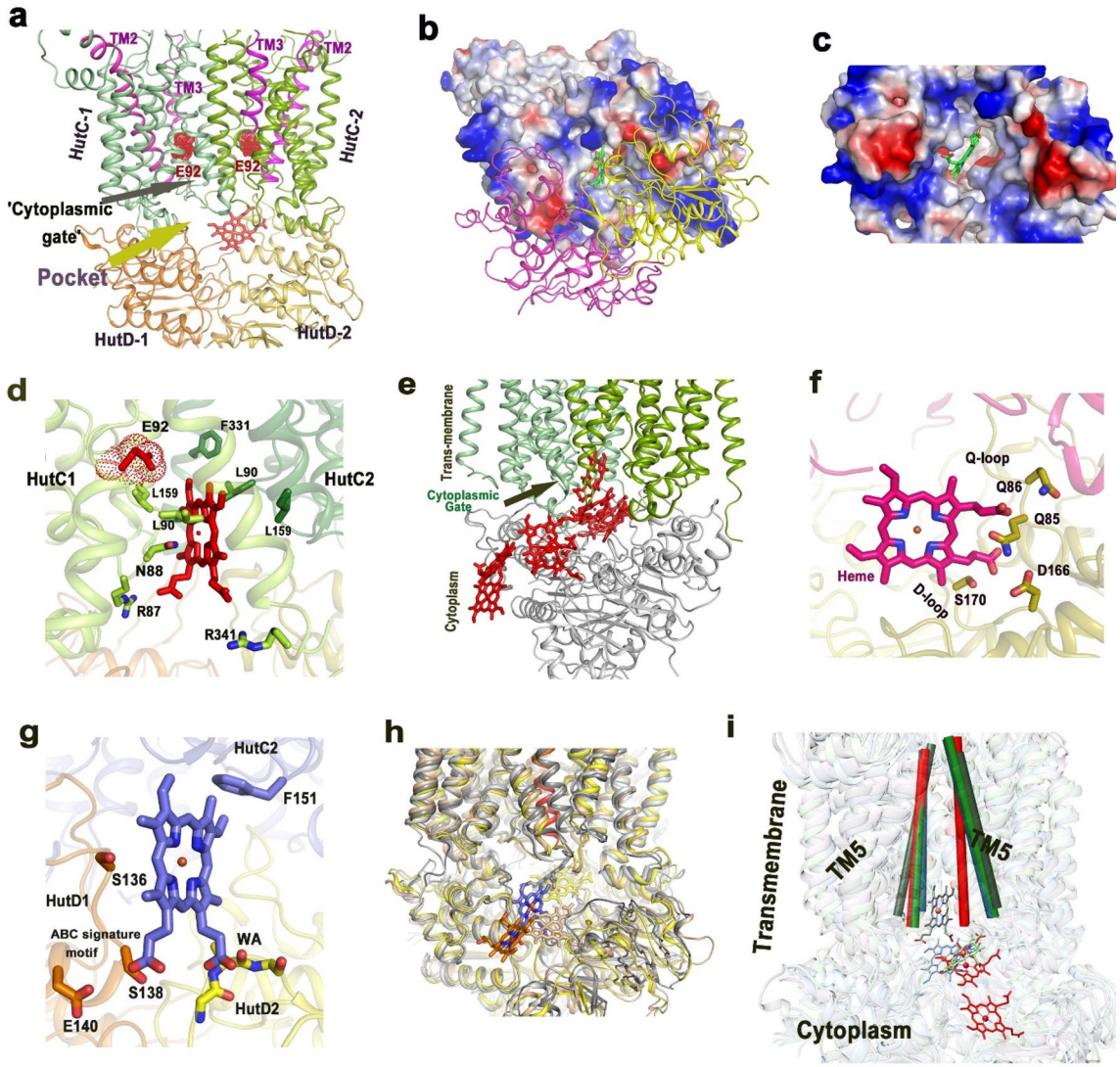

Figure 8. Heme release pathway from 'cytoplasmic gate' to cytosol. (**a**) Ligand release pocket between the two dimers, HutC1–HutD1 and HutC2–HutD2 and cytoplasmic gate are shown here.TM2, TM3 of each HutC monomer are shown in pink while E92, belonging to TM2–TM3 loop is shown in red; (**b**) Docking of Heme near cytoplasmic gate of HutCD IF; HutC dimer is shown in electrostatic surface representation whereas HutD dimer is shown in cartoon representation. Docked heme is shown as green sticks; (**c**) Zoomed view showing docked heme at 'cytoplasmic gate' of HutC dimer of HutCD in the IF state. HutD dimer is not shown here for clarity; (**d**) Zoomed view showing docking of heme near 'cytoplasmic gate' and its interactions with HutC residues; (**e**) Release pathway of heme from HutCD; (**f**) Snapshot at 133 ns shows interaction of Heme with Q-loop and D-loop residues of HutD; (**g**) Interaction of heme with F151 of HutC and S136, S138 of 'ABC signature motif' of HutD on the verge of release to cytosol; (**h**) Superposition of snapshots of HutCD IF at 85, 121, 410, 468 ns. HutC and HutD subunits undergo limited fluctuations during release of heme. (**i**) Zoomed view of superimposed snapshots reveals noticeable conformational shift ofTM5 helices (shown as cylinder) at 410 and 468 ns (red) especially in one TMD of HutC dimer compared to 1 (grey), 85 (green), 121 (blue) ns, leading to 'occluded' state during heme release.

trans-acting 'ABC signature motif' with the progress of simulation provided compactness to the NBD dimer. The D-loops at the NBD interface were less flexible than the D-loops of Mg^{2+}-ATP bound OF state HutCD. In contrust to the OF state where D-loops of HutDs were found to interact, in the IF state, inter D-loop distance was ranging from 6 to 11 Å in most of the frames.

Identification of heme release pathway in HutCD IF state. Naoe et al. stated that D112 of the TM2–TM3 loop of the permease BhuU of *B. cenocepacia* is the only charged residue exposed to the inward facing heme translocation pathway of BhuUV and plays critical role in the heme translocation process, because mutation of this residue to the hydrophobic residues impaired transport activity[14]. Corresponding residue of HutC is E92 and as expected, this residue of both the HutC monomers are exposed to the heme translocation channel in the IF model of HutCD to impart polarity (Figs. 1a, 8a). We, therefore, intended to investigate the binding pattern

and movement of heme, after it reaches the 'cytoplasmic gate'. For that reason, heme was docked near the cytoplasmic gate of inward facing HutCD using Autodock Vina[32] (Fig. 8b,c). The hydrophobic site was made of L159 and V163 of TM5 along with L90 of TM2–TM3 loop. One propionate group was hydrogen bonded with R87 of the TM2–TM3 loop (Fig. 8d).

Soon after beginning of simulation, the heme molecule moved to the pocket between two HutC-HutD dimers (Fig. 8e–g). At this stage, the propionate group was interacting with the backbone NH groups of the Q-loop residues L89 and T90 of HutD1. Heme stayed inside this pocket 'flip flopping' around for a significant period of time. Subsequently, heme was found to interact with N40 of Walker-A and the D-loop residues of HutD. Polar interactions of the propionates of heme with Q86, S88, T90 of HutD (HutD1) were steady from 350 to 430 ns (Fig. 8f). Additionally, F151 of HutC was found to pack with heme (Fig. 8g). Notably, F151 of HutC was crucial for cytoplasmic gate opening during ATP hydrolysis by HutCD in OF state. The pocket between two HutC-HutD dimers started squeezing around 455 ns. Around 465 ns the heme changed orientation and moved near the other HutD monomer (HutD2) where the propionates were interacting with S138 of HutD2 (Fig. 8g). Heme was on the verge of release to cytosol around 472 ns where heme was in contact with S138 of the 'ABC signature motif' of HutD2. At 473 ns, the propionate group of heme had polar interaction with S136 followed by H128 and the molecule is finally released to the cytosol (Fig. 8e–i). A detailed list of interactions between HutCD and heme is given as Table S2.

During the process of heme release, no significant structural change occurred in the TMDs except orientation of TM5 (Fig. 8h). After 400 ns, the TM5 helices started acquiring an occluded conformation which was prominent around 460 ns (Fig. 8i). Attainment of occluded state is evident from the superposition of the snapshots collected at 85, 121, 410 and 468 ns (Fig. 8i). Here, conformation of TM5 remained unchanged in HutC1 where cytoplasmic side of TM5 of HutC2 shifted about 5 Å towards central axis of the translocation channel (Fig. 8i).

Discussion

Dimerization of the NBDs in ABC importers of prokaryotes, whether nucleotide driven or independent, is indispensable, since this is a vital early event of ligand translocation. Our results authenticated HutD as a type-II ABC importer, since it forms dimer even in the absence of the permease HutC (Fig. 2a–c). Based on the sequence comparisons, Y15 of the A-loop of HutD was predicted to pack with the adenine base of ATP (Fig. 1b). Substantial fluorescence quenching in the presence of AMP.PNP established significant binding of ATP with HutD in 1:1 stoichiometry with the involvement of Y15 (Fig. 2d–f). While wt HutD was an efficient ATPase, R18A, K44A, D166A and E167A turned out as loss-of-function mutants (Fig. 3a,b). Abrogation of ATPase activities in the mutants together with modelling, docking and MD simulations results suggested that R18 of the A-loop and K44 of Walker-A of HutD stabilize the ribose sugar and the β-phosphate of ATP respectively and hence, ATP binding is compromised upon removal of those side chains (Figs. 1b, 3a,b, 4c, 5e). Based on the sequence analysis (Fig. 1b) we presumed that D166 and E167 are crucial Walker-B residues for conducting ATP hydrolysis event. Our observations demonstrated that E167 is implicated in Mg^{+2} binding for ATP hydrolysis while neighbouring D166 interacts with S45 of Walker-A to facilitate ATP binding by stabilizing Walker-A. Rather, a network of polar interactions was observed between S45 of Walker-A and D166, E167 of Walker-B as evident from the snapshot of MD simulation (Fig. 5e). Mutation of D166 to Ala presumably generates more space for E167 side chain and at the same time turns E167 more flexible because of impaired polar interactions stated above, eventually disturbing Mg^{+2} binding/ATP hydrolysis.

MD simulation trajectory of HutD in ATP bound state depicted that D-loops of the two HutD monomers interact at the dimeric interface and H200 critically contributes to the dimerization by interacting with the *trans*-acting D-loop (Fig. 5g). MD simulation results further suggested that ATP binding to HutD does not need any assistance from the *trans*-acting 'ABC signature motif' (Fig. 5f), like it was observed before in the crystal structure of BtuCD-F[26]. Rather, in HutCD, 'ABC signature motif' interacts with the heme during its ejection to the cytosol. Presumably, the translocation of bigger ligand vitamin B12 requires a wider channel compared to heme (HmuUV structure) and the NBDs need to dimerize accordingly. The difference in ATP binding mechanisms might be attributed to the differential inter dimeric interactions of BtuD and HutD which are essential for the ligand- and species-specific transportation pathways.

Conformational shifts of certain transmembrane helices, especially the movable helices TM5 and H5a regulate the ligand import processes through ABC importers. Substrate translocations through the translocation channels of type-I ABC transporters MalK of *E. coli* are dictated by 'tweezer' like or 'twisting' motions of the NBDs[33,34]. For type II importers, substrates translocation by open/closure of the cytoplasmic gate is thought to occur via 'peristaltic' motions of the TMDs[16]. In HutCD, a rotational motion occurs in the TMDs in synchronous manner with the inter NBD D-loop interactions (Table 1). The more the separation of the inter HutD D-loops, the more rotation of the NBDs which is then transmitted to the TMDs. The distance between the two HutC–HutD dimers was found to be altered accordingly. However, asymmetry has been observed in the interface interactions between HutC and HutD for each HutC–HutD duo.

The interaction of the SKF^{151} loop of HutC, located between TM4 and TM5 near the cytoplasmic gate, with ATP and the A-loop (Y^{15}GSR) of HutD is one of the most prominent facts that tie the event of ATP hydrolysis with the conformational change in HutCs to facilitate ligand translocation (Fig. 6e). Packing of F151 with the adenine base of ATP and Y15 of the A-loop of HutD leads to the widening of the cytoplasmic gate where the periplasmic side of the TM5 helices remained practically unchanged (Fig. 6e,h). Interestingly, in the later stage of the dynamics (~ 400 ns and beyond), which might be treated as post hydrolysis phase, continuous relaxation of the assembly was observed and, in this situation, TM5 helices prefers to acquire relatively parallel conformation. Inward facing assembly was also culminated to an occluded conformation, similar to that observed before for

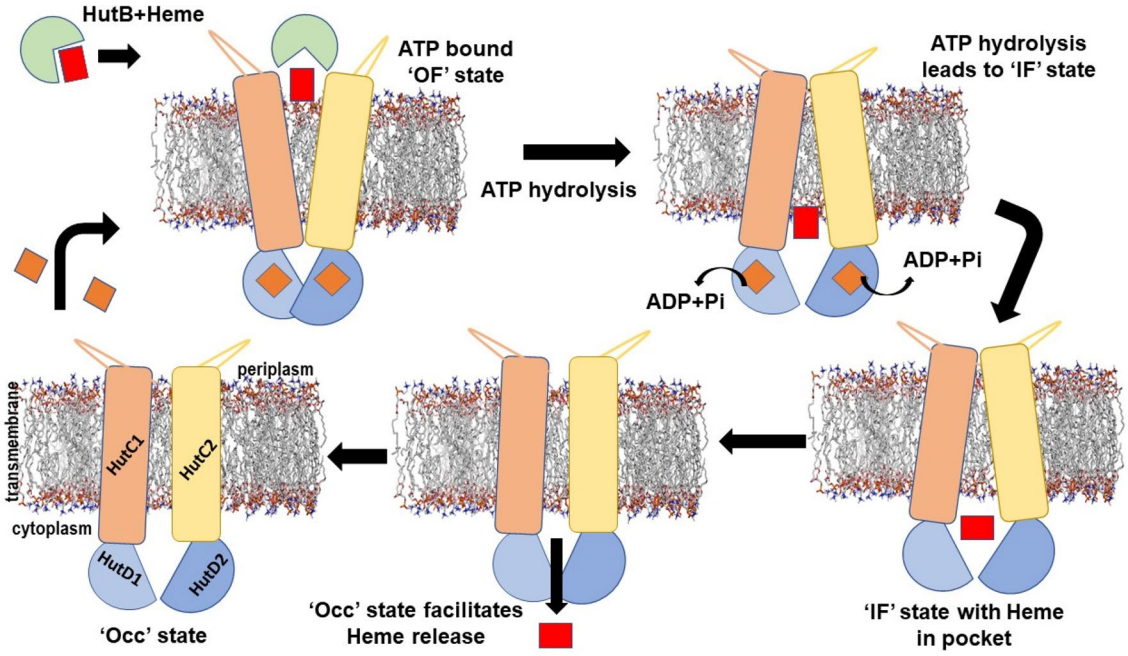

Figure 9. Proposed reaction mechanism. Involvement of TM4–TM5 loop in ATP hydrolysis causes cytoplasmic gate opening (IF state) easing heme release to the inter-dimeric pocket. Heme release to cytoplasm takes place in the absence of ATP. Formation of occluded state constricts the pocket and releases heme.

vitamin B12 importer BtuCD (Fig. 7c,d). We, therefore, hypothesize that the occluded state is the most preferred conformation of HutCD.

H5a was seen to play a key role as a gating helix to forming the interaction site for the PLBP, BhuT in the case of BhuUV-T assembly[14]. Also, mutation of R176 in H5a of HmuU was reported to decrease affinity to HmuT and decrease heme-transport activity[13]. Although TM5 helices showed visible transition near the cytoplasmic gate, conformation of H5a helices, located at the periplasmic side, practically remianed unchanged during the dynamics. We, therefore, hypothesize that the movement or change in orientation of H5A helices are most likely PLBP dependent, and subsequent separation of the PLBP from the TMDs may result in the transition of orientations of the H5A helices.

The heme release mechanism has been deciphered for the first time which was unknown so far. Our extensive simulation showed that the release of heme is primarily dictated by the interaction of the propionate groups with the polar residues of HutC–HutD dimeric pocket (Fig. 8f,g). Interaction of heme with the residues of D-loop, Walker-A, Q-loop and 'ABC signature motif' (Fig. 8f,g, Table S2) further suggested that heme release event takes place in the absence of ATP. Because the presence of ATP would have hindered involvement of these motifs in the heme release process. As observed in case of heme-free HutCD in the IF state, heme bound form also acquired occluded state at the verge of heme release. Parallel conformation of TM5 helices in the occluded state probably leads to the squeezing of inter-dimeric pocket which eventually facilitates the heme release (Fig. 9). Hence ABC importers like HutCD prefers to acquire occluded conformation before starting the next cycle of ATP hydrolysis dependent heme translocation (Fig. 9).

Type-II importers HmuUV, BhuUV or BtuCD were predominantly in different states while trapped in the crystal lattice[13,14,26]. Notably, Y15 of HutD or F151 of HutC, which stack with the adenine base of ATP leading to conformational changes in HutCD assembly, are not conserved in HmuV or BhuV (Fig. 1b). Although similar hydrophobic residues are observed in HmuUV in the close vicinity of the respective residues, BhuUV is quite different in this regard (Fig. 1). Furthermore, S170, the crucial D-loop residue of HutD is replaced by Ala in BhuV (Fig. 1b) generating a possibility of compromised D-loop interactions. Collectively, the observations intend us to believe that although there is a common minimum procedure to internalize a specific nutrient, detailed mechanism of uptake is primarily dictated by the requirement of that specific nutrient in the respective species.

Methods

Cloning, site-directed-mutagenesis, overexpression, and purification. Chromosomal DNA of *V. cholerae* strain O395 was used as the template to amplify the region encoding Full length HutD of 259 aa (Accession code: A0A0H3ADP8). The 780 bp HutD PCR amplicon and the pET28a$^+$ vector (Novagen) with *NdeI* and *BamHI* restriction sites were ligated using T4 DNA ligase and the appropriate clones were selected using *E. coli* XL1-Blue cells with kanamycin resistance. The cDNA of HutD (amino acids 1–259) was PCR amplified and was cloned in pET28a$^+$ within *NdeI* and *BamHI* restriction sites. The recombinant protein with N-terminal His_6-tag was overexpressed in BL21 (DE3) by IPTG induction and purified by Ni–NTA affinity chromatography. The construct was verified by restriction digestion analysis and commercial DNA sequencing. The mutants R18A, K44A, D166A and E167A were prepared by two-step PCR amplification using previously cloned WT HutD

plasmid as template. These mutant amplicons were also cloned in pET28a$^+$ vector using *NdeI* and *BamHI* as restriction sites. Sequences of the variants were verified by commercial sequencing. These recombinant proteins with N-terminal His_6 tag were overexpressed in *E. coli* BL21 (DE3) cells in the presence of IPTG.

Overexpression and purification of recombinant proteins were performed as per protocol described by Dey et al.[24]. In brief, 10 ml of LB broth, supplemented with kanamycin, was inoculated by a single colony, and grown by overnight shaking at 310 K. 1 l LB broth with kanamycin was inoculated with 10 ml of the overnight culture and the culture was grown further at 310 K until the OD_{600} reached 0.6. The cells were induced by 1 mM IPTG and grown at 310 K for another 3 h. The cells were then harvested at 4500×*g* for 20 min at 277 K and the pellet was resuspended in 10 ml ice-cold lysis buffer-L (having 50 mM Tris–HCl pH 8.0, 300 mM NaCl, 5 mM $MgCl_2$, 10% (v/v) glycerol). PMSF (1 mM) and lysozyme (1 mg/ml) were added to the resuspended solution and it was lysed by sonication on ice. The cell lysate was then centrifuged at (12,000 RPM for 45 min) at 277 K. The collected supernatant was applied onto a nickel–nitrilotriacetic acid (Ni^{2+}-NTA) affinity chromatography media (Qiagen) that was previously equilibrated with buffer-L. The 6× His-tagged recombinant proteins were eluted with 50–200 mM imidazole gradient. Subsequently, imidazole was removed from proteins through buffer exchange using Amicon centrifugation units. The wt HutD was concentrated up to 300 µM. All mutants were purified using the buffer containing 50 mM Tris–HCl pH 8.0, 300 mM NaCl, 10% (v/v) glycerol with the same protocol and concentrated up to 250 µM. The homogeneity of the purified proteins was checked using SDS-PAGE with 12% polyacrylamide concentration.

Cross-linking experiments. Crosslinking experiments had been carried out with WT HutD and WT HutD in the presence of non-hydrolysable ATP analogue AMP-PNP using Glutaraldehyde (Sigma-aldrich) as crosslinker. HutD was purified in cross-linking buffer (50 mM Na-Phosphate pH 8.0 and 150 mM NaCl) followed by incubation with AMP.PNP (20 mM) on ice for 1.5 h. Increasing amounts of glutaraldehyde were added to the mix to a final concentration range of 0.0025–0.04%. The reaction mixture was further incubated at room temperature for 15 min. Crosslinking reactions were quenched by adding 50 mM Tris–HCL pH 8.0, followed by incubation at 97 °C for 10 min in standard SDS loading dye. Reaction products were separated by electrophoresis and analysed on 10% SDS-PAGE polyacrylamide gel.

Gel filtration assay. Size Exclusion chromatography experiments were performed in a Superdex 200 Increase 10/300 GL using AKTA purifier (cytiva). Blue dextran was used to identify the void volume. The column was further calibrated with standard molecular weight calibration kit (GE Healthcare) containing Ferritin (440 kDa), Aldolase (160 kDa), Ovalbumin (45 kDa) and Lysozyme (14.3 kDa). The standard graph was prepared against relative elution volume (V_e/V_o) in X-axis [where V_e is the elution volume and V_o is the void volume] and the log molecular weight in Y-axis. For the AMP.PNP bound state, 250 µM HutD was preincubated for 1.5 h at 4 °C with 500 µM AMP.PNP in the same buffer-L. For analysis of HutD and HutD with AMP.PNP, in each run, 500 µl of protein was injected to the SEC column pre-equilibrated with buffer containing 50 mM Tris–HCl (pH 8.0), 300 mM NaCl, and 5 mM $MgCl_2$ and ran at a flow rate of 0.5 ml/min. The peak fractions were collected and analysed in 12% SDS-PAGE.

Fluorescence quenching study. As per protocol described by Agarwal et al.[22], fluorescence measurements were carried out in Hitachi F-7000 spectrofluorometer, using quartz cuvettes of 1 cm path length. Changes in fluorescence of tryptophan and tyrosine residues were measured at an excitation wavelength of 280 nm and the emission spectra were recorded between 295 and 400 nm. Sole contribution of Trp residues upon AMP.PNP binding was also monitored with an excitation at 295 nm and emission between 308 and 400 nm. In both the cases, slit widths was kept consistently at 5 nm. All reactions were carried out at 298 K. The reactions were performed in a buffer containing 50 mM Tris–HCl (pH 8.0) and 300 mM NaCl. Equilibrium titration of HutD was carried out with AMP-PNP as ligand and the changes in fluorescence emission intensity were measured in the presence of increasing concentration of ligand. The concentration of HutD was 2.5 µM and ligand concentrations varied from 0 to 2 mM.

The binding stoichiometry was determined using the protocol described by Mani et al.[35]. The plot of $\log(F_0 - F)/(F - F_\infty)$ against log [AMP-PNP], where F_0, F, and F_∞ are the fluorescence intensities of HutD alone, HutD, in the presence of various concentrations of AMP-PNP, and HutD saturated with AMP-PNP, respectively, yielded a straight line whose slope was a measure of the binding stoichiometry. The dissociation constant, K_d was determined using nonlinear curve fitting analysis as per Eqs. (1) and (2). All experimental points for the binding isotherms were fitted by the least-squares method:

$$K_d = \{[C_0 - (\Delta F/\Delta F_{max}) \cdot C_0] \cdot [C_P - (\Delta F/\Delta F_{max}) \cdot C_0]\}/\{(\Delta F/\Delta F_{max}) \cdot C_0\}, \quad (1)$$

$$C_0 \cdot (\Delta F/\Delta F_{max})^2 - [(C_0 + C_P + K_d) \cdot (\Delta F/\Delta F_{max})] + C_P = 0. \quad (2)$$

where C_0 and C_p denotes the input concentrations of the ligand and VcHutD respectively. ΔF is the change in fluorescence intensity at 334 nm ($\lambda_{ex} = 280$ nm) for each point of titration curve and ΔF_{max} is the same parameter when ligand is totally bound to the protein. A double-reciprocal plot of $1/\Delta F$ against $1/(C_p - C_0)$, as shown in Eq. (3) was used to determine the ΔF_{max}.

$$1/\Delta F = 1/\Delta F_{max} + K_d/[\Delta F_{max}(C_P - C_0)]. \quad (3)$$

ΔF_{max} was calculated from the slope of the best fit line corresponding to the above plot[22]. All experimental points for the binding isotherms are fitted by least square methods using OriginPro 8.0 software.

ATPase assay. ATPase activities of purified HutD and its mutants R18A, K44A, D166A and E167A were determined spectrophotometrically using malachite green assay by measuring the release of inorganic phosphate (Pi). As per protocol described before in Dey et al.[24], each reaction mixture with final protein of 2.5 µM and buffer containing 50 mM Tris–HCl (pH 8.0), 300 mM NaCl, and 5 mM $MgCl_2$ were incubated with ATP (Sigma Aldrich), of concentration ranging from 100 to 500 µM at 298 K. Malachite Green solution was freshly prepared by adding 0.44 g of Malachite green in 0.3 M H_2SO_4, 2.5 ml of 7.5% ammonium molybdate, and 0.2 ml of 11% Tween 20 to a final volume of 10 ml. 200 µl of aforesaid solution was added to the reaction mixture to a final volume of 1 ml. The absorbance was measured at 630 nm within 5 min of adding the colouring reagent. Pi standard curve was prepared by using KH_2PO_4 and plotting OD_{630} against release of Pi using OriginPro 8.0 software[24]. The total Pi released by each protein upon ATP hydrolysis was obtained from the standard curve. Each protein was checked with Malachite green dye without ATP to measure the contaminant inorganic phosphate if any, and the minor absorbance thus obtained at 630 nm was subtracted from the absorbance produced by that protein upon hydrolysis of added ATP. The ATP hydrolysis without protein has served as another negative control to nullify the effect of the contaminating inorganic phosphate with ATP. All the experiments were minimally performed in triplicate.

Docking. Docking of heme with HutCD in the IF state has been performed using AutoDock Vina[32] software. Coordinates of heme was retrieved from Docking of Heme molecule in the pocket of HutCD was performed using a grid box of dimension 65 Å × 40 Å × 52 Å centered at (− 29, + 14, + 15) Å.

Building the lipid-protein system. The principal axis of the HutCD complex was aligned with the Z-axis, while the lipid bilayer spanned the XY plane. The HutCD complex was translated by 20 Å along the Z-axis to correctly place the TMD part within the hydrophobic region of the bilayer such that the polar head groups and hydrophilic lipid trails make contact with the specific residues of the transmembrane protein[36] The multicomponent complex was enclosed in a tetrahedral box (approximate dimensions: a = 120 Å, b = 120 Å, c = 170 Å) and solvated in explicit water with a minimum water thickness of 22.5 Å on the top and bottom of the complex. A suitable number of neutralizing ions (Na^+ or Cl^-, depending upon the cases) were added by replacing solvent molecules using the Monte Carlo method. The number of DMPC molecules in a leaflet was in the range of 180 to 210, depending upon the protein being embedded (Fig. S3). The number of DMPC molecules on the upper and lower leaflets was slightly different (the maximum difference was 10). The area per lipid was calculated[37] by multiplying the sides of the simulation box in the XY-plane and dividing it by the average number of lipid molecules in a leaflet (Fig. S4). The coordinate of the solvated multicomponent system was saved in PDB format and was modified afterward to make it consistent with the AMBER naming scheme.

Force field for the ligands. All atom force field (FF) for the ATP cofactor was taken from the AMBER parameter database[38] maintained by the Bryce group. ATP molecules were first made fully deprotonated and then hydrogens were added using "reduce" available in the Amber Tools. All the phosphate atoms in ATP were deprotonated and the total charge was − 4*e*. The atom names in ATP were also changed to match the naming convention of this FF. We used antechamber[39] and MCPB.py[40] to create the FF for the heme group. In the heme group, the iron metal coordinates to four nitrogen atoms. We have used a bonded model[41] where Fe is bonded to four sp3 hybridised nitrogen. The antechamber program was used with the AM1-BCC charge method[42] to assign charge by treating heme as having a charge of − 4*e* and the atoms were treated with GAFF atom types[43]. The procedure we followed to treat the heme group within the AMBER software package is described with great detail in one of the Amber tutorials[41].

MD simulation steps and parameters. Unbiased MD simulation in this work was carried out using pmemd.cuda, the GPU version (10) of MD engine within the Amber package. The protein backbone and side chains were treated with the FF parameters from ff14SB[44], and lipid14 FF[45] was used for the DMPC bilayer. All the simulations were carried out in explicit solvent with the three-point transferable interatomic potential (TIP3P) for waters[46]. In simulations involving only protein (i.e., the cases where bilayer was absent), a truncated octahedron box was used for solvation such that the edge of the box was at-least 10 Å away from the protein. A suitable number of Na^+ or Cl^- ions were added to neutralize the solvated system. Periodic boundary condition was applied on all the sides of the solvated box. Bonds containing H-atoms were restrained using the SHAKE algorithm[47] which enabled us to use a time step of 2 fs for the integrator. The pressure and temperature were controlled using a weak coupling to an external bath. The solvated system was coupled to a Berendsen barostat[48] with a relaxation time of 2 ps, for maintaining a constant pressure of 1 atm. The particle mesh Ewald summation[49] was employed for calculating the electrostatic interactions part of the total Hamiltonian. We applied a distance cutoff of 10 Å for calculations of the long-range electrostatic interactions. The temperature of the system was allowed to fluctuate around a mean of 310 K by employing Langevin dynamics[50] with a collision frequency of 2/ps. Standard simulation protocols were used for the solvated protein cases[51].

For the protein-lipid multicomponent system, the following simulation protocols were used. We followed rigorous energy minimization steps (3) to "relax" the system by eliminating any energetically unfavourable interactions that might have occurred while preparing the system using CHARMM-GUI. Minimisation was done in three steps: (1) minimised the solvent molecules holding the lipids and protein fixed by using position restraints with a force constant of 250 kcal/mol/$Å^2$, (2) minimised the solvent and the lipid keeping the protein fixed and (3) finally all the atoms in the systems were set free of restraints and allowed to relax. We ran 5000 cycles of minimization steps in all three steps. The temperature of the energy minimised system was increased to 310 K linearly in two steps (0–100 K, 100–310 K). To avoid excessive solute fluctuations, we applied a weak

restraint (10 kcal/mol/Å^2) on the protein and lipid residues. Langevin dynamics with a collision frequency of 1.0/ps was applied for temperature equilibration at constant volume. Each of the equilibration steps involved 100 ps of MD runs in NVT ensembles. After the heating steps, the weak restraints on the protein and lipid residues were released in steps by carrying out four MD simulations, each of 500 ps, in NPT ensembles. Monte Carlo barostat (barostat = 2) with pure semi-isotropic (ntp = 3) pressure scaling was used to achieve a constant pressure of 1 atm. To reduce buckling of the bi-layer, a constant surface tension (0.0 dyne/cm) was applied at the membrane-liquid (csurften = 3) interface[52]. Finally, we ran MD "production run" for 1000 ns with an integration time step of 2 ps in NPT ensemble.

Software used for analysis. Software used for data analysis and presentations are Origin, PyMol, UCSF chimera and Adobe photoshop.

Data availability

The pdb coordinates generated and/or analysed during the current study are not publicly available because these are generated through homology modelling. But these coordinate files will be available from the corresponding author on reasonable request. An important result of molecular dynamics simulation has been provided in the form of a movie as supplementary material. Other MD simulation results presented here will also be available in the form of movie on reasonable request.

Received: 9 January 2022; Accepted: 24 March 2022
Published online: 03 May 2022

References

1. Meneghetti, F. *et al.* Iron acquisition pathways as targets for antitubercular drugs. *Curr. Med. Chem.* **23**, 4009–4026 (2016).
2. Palmer, L. D. & Skaar, E. P. Transition metals and virulence in bacteria. *Annu. Rev. Genet.* **50**, 67–91 (2016).
3. Sheldon, J. R., Laakso, H. A. & Heinrichs, D. E. Iron acquisition strategies of bacterial pathogens. *Microbiol. Spectr.* https://doi.org/10.1128/microbiolspec.VMBF-0010-201 (2016).
4. Cornelissen, C. N. Subversion of nutritional immunity by the pathogenic Neisseriae. *Pathog. Dis.* **76**, 112 (2018).
5. Raymond, K. N., Dertz, E. A. & Kim, S. S. Enterobactin: An archetype for microbial iron transport. *Proc. Natl. Acad. Sci.* **100**, 3584–3588 (2003).
6. Eakanunkul, S. *et al.* Characterization of the periplasmic heme-binding protein ShuT from the heme uptake system of *Shigella dysenteriae*. *Biochemistry* **44**, 13179–13191 (2005).
7. Hider, R. C. & Kong, X. Chemistry and biology of siderophores. *Nat. Prod. Rep.* **27**, 637 (2010).
8. Choby, J. E. & Skaar, E. P. Heme synthesis and acquisition in bacterial pathogens. *J. Mol. Biol.* **428**, 3408–3428 (2016).
9. Starr, J. *et al.* Siderophore receptor-mediated uptake of lactivicin analogues in gram-negative bacteria. *J. Med. Chem.* **57**, 3845–3855 (2014).
10. Celia, H. *et al.* Structural insight into the role of the Ton complex in energy transduction. *Nature* **538**, 60–65 (2016).
11. Hollenstein, K., Dawson, R. J. & Locher, K. P. Structure and mechanism of ABC transporter proteins. *Curr. Opin. Struct. Biol.* **17**, 412–418 (2007).
12. Borths, E. L., Poolman, B., Hvorup, R. N., Locher, K. P. & Rees, D. C. In vitro functional characterization of BtuCD-F, the *Escherichia coli* ABC transporter for vitamin B 12 uptake. *Biochemistry* **44**, 16301–16309 (2005).
13. Woo, J. S., Zeltina, A., Goetz, B. A. & Locher, K. P. X-ray structure of the *Yersinia pestis* heme transporter HmuUV. *Nat. Struct. Mol. Biol.* **19**, 1310–1315 (2012).
14. Naoe, Y. *et al.* Crystal structure of bacterial haem importer complex in the inward-facing conformation. *Nat. Commun.* **7**, 13411 (2016).
15. Qasem-Abdullah, H., Perach, M., Livnat-Levanon, N. & Lewinson, O. ATP binding and hydrolysis disrupt the high-affinity interaction between the heme ABC transporter HmuUV and its cognate substrate-binding protein. *J. Biol. Chem.* **292**, 14617–14624 (2017).
16. Tamura, K., Sugimoto, H., Shiro, Y. & Sugita, Y. Chemo-mechanical coupling in the transport cycle of a heme ABC transporter. *J. Phys. Chem. B* **123**, 7270–7281 (2019).
17. Tamura, K. & Sugita, Y. Free energy analysis of a conformational change of heme ABC transporter BhuUV-T. *J. Phys. Chem. Lett.* **11**, 2824–2829 (2020).
18. Wyckoff, E. E., Stoebner, J. A., Reed, K. E. & Payne, S. M. Cloning of a *Vibrio cholerae* vibriobactin gene cluster: Identification of genes required for early steps in siderophore biosynthesis. *J. Bacteriol.* **179**, 7055–7062 (1997).
19. Payne, S. M., Mey, A. R. & Wyckoff, E. E. Vibrio iron transport: Evolutionary adaptation to life in multiple environments. *Microbiol. Mol. Biol. Rev.* **80**, 69–90 (2016).
20. Occhino, D. A., Wyckoff, E. E., Henderson, D. P., Wrona, T. J. & Payne, S. M. *Vibrio cholerae* iron transport: Haem transport genes are linked to one of two sets of tonB, exbB, exbD genes. *Mol. Microbiol.* **29**, 1493–1507 (1998).
21. Wyckoff, E. E., Schmitt, M., Wilks, A. & Payne, S. M. HutZ is required for efficient heme utilization in *Vibrio cholerae*. *J. Bacteriol.* **186**, 4142–4151 (2004).
22. Agarwal, S., Dey, S., Ghosh, B., Biswas, M. & Dasgupta, J. Structure and dynamics of Type III periplasmic proteins VcFhuD and VcHutB reveal molecular basis of their distinctive ligand binding properties. *Sci. Rep.* **7**, 42812 (2017).
23. Rice, A. J., Park, A. & Pinkett, H. W. Diversity in ABC transporters: Type I, II and III importers. *Crit. Rev. Biochem. Mol. Biol.* **49**, 426–437 (2014).
24. Dey, S., Biswas, M., Sen, U. & Dasgupta, J. Unique ATPase site architecture triggers cis-mediated synchronized ATP binding in heptameric AAA+-ATPase domain of flagellar regulatory protein FlrC. *J. Biol. Chem.* **290**, 8734–8747 (2015).
25. Buckstein, M. H., He, J. & Rubin, H. Characterization of nucleotide pools as a function of physiological state in *Escherichia coli*. *J. Bacteriol.* **190**, 718–726 (2008).
26. Korkhov, V. M., Mireku, S. A., Veprintsev, D. B. & Locher, K. P. Structure of AMP-PNP-bound BtuCD and mechanism of ATP-powered vitamin B12 transport by BtuCD-F. *Nat. Struct. Mol. Biol.* **21**, 1097–1099 (2014).
27. Chen, C. C., Hwang, J. K. & Yang, J. M. (PS)2–v2: Template-based protein structure prediction server. *BMC Bioinform.* **10**, 366 (2009).
28. Jumper, J. *et al.* Highly accurate protein structure prediction with AlphaFold. *Nature* **596**, 1–11 (2021).
29. Case, D. A. *et al. AMBER 2018* (University of California, 2018).
30. Jo, S., Kim, T., Iyer, V. G. & Im, W. CHARMM-GUI: A web-based graphical user interface for CHARMM. *J. Comput. Chem.* **29**, 1859–1865 (2008).

31. Weng, J., Fan, K. & Wang, W. The conformational transition pathways of ATP-binding cassette transporter BtuCD revealed by targeted molecular dynamics simulation. *PLoS ONE* **7**, e30465 (2012).
32. Trott, O. & Olson, A. J. AutoDock Vina: Improving the speed and accuracy of docking with a new scoring function, efficient optimization, and multithreading. *J. Comput. Chem.* **31**, 455–461 (2009).
33. Chen, J., Lu, G., Lin, J., Davidson, A. L. & Quiocho, F. A. A tweezers-like motion of the ATP-binding cassette dimer in an ABC transport cycle. *Mol. Cell* **12**, 651–661 (2003).
34. Moradi, M. & Tajkhorshid, E. Mechanistic picture for conformational transition of a membrane transporter at atomic resolution. *Proc. Natl. Acad. Sci.* **110**, 18916–18921 (2013).
35. Mani, R. S., Karimi-Busheri, F., Cass, C. E. & Weinfeld, M. Physical properties of human polynucleotide kinase: Hydrodynamic and spectroscopic studies. *Biochemistry* **40**, 12967–12973 (2001).
36. Gedeon, P. C., Thomas, J. R. & Madura, J. D. Accelerated molecular dynamics and protein conformational changes: A theoretical and practical guide using a membrane embedded model neurotransmitter transporter. *Methods Mol. Biol.* **1215**, 253–287 (2015).
37. Moradi, S., Nowroozi, A. & Shahlaei, M. Correction: Shedding light on the structural properties of lipid bilayers using molecular dynamics simulation: A review study. *RSC Adv.* **9**, 7687–7687 (2019).
38. Meagher, K. L., Redman, L. T. & Carlson, H. A. Development of polyphosphate parameters for use with the AMBER force field. *J. Comput. Chem.* **24**, 1016–1025 (2003).
39. Wang, J., Wang, W., Kollman, P. A. & Case, D. A. Automatic atom type and bond type perception in molecular mechanical calculations. *J. Mol. Graph. Model.* **25**, 247–260 (2006).
40. Li, P. & Merz, K. M. MCPB.py: A python based metal center parameter builder. *J. Chem. Inf. Model.* **56**, 599–604 (2016).
41. Li, P. & Merz, K. M. *Building Bonded Model for a Heme Group with MCPB.py* (2015). http://ambermd.org/tutorials/advanced/tutorial20/mcpbpy_heme.htm (Accessed 8 August 2021).
42. Jakalian, A., Jack, D. B. & Bayly, C. I. Fast, efficient generation of high-quality atomic charges. AM1-BCC model: II. Parameterization and validation. *J. Comput. Chem.* **23**, 1623–1641 (2002).
43. Wang, J., Wolf, R. M., Caldwell, J. W., Kollman, P. A. & Case, D. A. Development and testing of a general amber force field. *J. Comput. Chem.* **25**, 1157–1174 (2004).
44. Maier, J. A. *et al.* ff14SB: Improving the accuracy of protein side chain and backbone parameters from ff99SB. *J. Chem. Theory Comput.* **11**, 3696–3713 (2015).
45. Dickson, C. J. *et al.* Lipid14: The Amber lipid force field. *J. Chem. Theory Comput.* **10**, 865–879 (2014).
46. Price, D. J. & Brooks, C. L. A modified TIP3P water potential for simulation with Ewald summation. *J. Chem. Phys.* **121**, 10096–10103 (2004).
47. Kräutler, V., van Gunsteren, W. F. & Hünenberger, P. H. A fast SHAKE algorithm to solve distance constraint equations for small molecules in molecular dynamics simulations. *J. Comput. Chem.* **22**, 501–508 (2001).
48. Berendsen, H. J. C., Postma, J. P. M., van Gunsteren, W. F., DiNola, A. & Haak, J. R. Molecular dynamics with coupling to an external bath. *J. Chem. Phys.* **81**, 3684–3690 (1984).
49. Darden, T., York, D. & Pedersen, L. Particle mesh Ewald: An N ·log(N) method for Ewald sums in large systems. *J. Chem. Phys.* **98**, 10089–10092 (1993).
50. Pastor, R. W., Brooks, B. R. & Szabo, A. An analysis of the accuracy of Langevin and molecular dynamics algorithms. *Mol. Phys.* **65**, 1409–1419 (1988).
51. Roy, R., Ghosh, B. & Kar, P. Investigating conformational dynamics of Lewis Y Oligosaccharides and elucidating blood group dependency of cholera using molecular dynamics. *ACS Omega* **5**, 3932–3942 (2020).
52. Zhang, Y., Feller, S. E., Brooks, B. R. & Pastor, R. W. Computer simulation of liquid/liquid interfaces. I. Theory and application to octane/water. *J. Chem. Phys.* **103**, 10252–10266 (1995).

Acknowledgements

We are thankful to Prof. U. Sen of SINP, Kolkata, India for his support and advice at various stages of this work. We are grateful to Rev. Dr. Dominic Savio, SJ, Principal, St. Xavier's College, Kolkata, for his constant support and encouragement. This work is supported by UGC-DAE-CSR Grant No. CSR-IC/BL-76/CRS-193/2016-2017/857 of Govt. of India. We also acknowledge DST Grant No. SR/FST/COLLEGE-014/2010(C), WBDBT BOOST Grant No. 335/WBBDC/1P-2/2013 and DBT BUILDER Grant No. BT/INF/22/SP41296/2020 for infrastructural support.

Author contributions

I.S.: Data curation; Formal analysis; Investigation; Methodology. S.C.: Formal analysis; Investigation; Methodology; Writing—original draft. S.A.: Investigation, Writing—review & editing. P.M.: Investigation; Methodology. B.G.: Investigation, Funding acquisition; Supervision; Validation; Visualization; Roles/Writing—original draft; J.D.: Conceptualization; Funding acquisition; Supervision; Validation; Visualization; Roles/Writing—original draft. All authors reviewed the manuscript.

Competing interests

The authors declare no competing interests.

Additional information

Supplementary Information The online version contains supplementary material available at https://doi.org/10.1038/s41598-022-11213-9.

Correspondence and requests for materials should be addressed to B.G. or J.D.

Biochemical and Biophysical Research Communications 716 (2024) 150030

Contents lists available at ScienceDirect

Biochemical and Biophysical Research Communications

journal homepage: www.elsevier.com/locate/ybbrc

Structural insights in to the atypical type-I ABC Glucose-6-phosphate importer VCA0625-27 of *Vibrio cholerae*

Indrila Saha [a], Biplab Ghosh [b,c,**], Jhimli Dasgupta [a,*]

[a] Department of Biotechnology, St. Xavier's College (Autonomous), 30, Mother Teresa Sarani, Kolkata, 700016, India
[b] Macromolecular Crystallography Section, Beamline Development & Application Section, Bhabha Atomic Research Center, Trombay, Mumbai, 400085, India
[c] Homi Bhabha National Institute, Anushaktinagar, Mumbai, 400094, India

ARTICLE INFO

Keywords:
Vibrio cholerae
ABC transporter
Glucose-6-phosphate
Crystal structure
MD simulation
Mutagenesis

ABSTRACT

Sugar phosphates are potential sources of carbon and phosphate for bacteria. Despite that the process of internalization of Glucose-6-Phosphate (G6P) through plasma membrane remained elusive in several bacteria. VCA0625-27, made of periplasmic ligand binding protein (PLBP) VCA0625, an atypical monomeric permease VCA0626, and a cytosolic ATPase VCA0627, recently emerged as hexose-6-phosphate uptake system of *Vibrio cholerae*. Here we report high resolution crystal structure of VCA0625 in G6P bound state that largely resembles AfuA of *Actinobacillus pleuropneumoniae*. MD simulations on VCA0625 in apo and G6P bound states unraveled an 'open to close' and swinging bi-lobal motions, which are diminished upon G6P binding. Mutagenesis followed by biochemical assays on VCA0625 underscored that R34 works as gateway to bind G6P. Although VCA0627 binds ATP, it is ATPase deficient in the absence of VCA0625 and VCA0626, which is a signature phenomenon of type-I ABC importer. Further, modeling, docking and systematic sequence analysis allowed us to envisage the existence of similar atypical type-I G6P importer with fused monomeric permease in 27 other gram-negative bacteria.

1. Introduction

Internalization of nutrients across the plasma membrane of bacteria takes place via ATP binding cassette (ABC) transporters where periplasmic ligand binding protein (PLBP) binds incoming ligand and cytosolic ATPase/nucleotide binding domains (NBDs) hydrolyze ATP to create large-scale conformational changes in the permease, accelerating nutrient uptake [1]. Despite their common basic architecture, ABC importers are structurally and functionally diverse [2]. The life cycle of *Vibrio cholerae*, the cholera causing gram-negative flagellated bacteria depend on transitions between the aquatic environments and human small intestine. Glucose-6-Phosphate (G6P) is an essential nutrient as carbon source for various pathogenic bacteria. In *V. cholerae,* G6P serves as a substrate for intracellular pathogen replication and is required to prepare cells for better survival in phosphate-limiting environments [3–5]. However, the mechanism of G6P uptake by different bacteria is less well understood yet. So far, structural, and mechanistic details of G6P uptake by ABC importer is largely restricted to the periplasmic ligand binding protein (PLBP) AfuA of AfuABC in *Actinobacillus pleuropneumoniae* (PDB code: 4R73) [6].

The putative ABC transporter VCA0625-27 of *V. cholerae*, made of the PLBP VCA0625, a fused monomeric membrane permease VCA0626 and ATPase VCA0627, has been recently characterized for hexose-6P uptake to utilize it as carbon and phosphate sources [5]. However, the structure, dynamics, and mechanism of sugar-phosphate internalization by this importer remained elusive. We have determined high resolution crystal structure of VCA0625 in G6P bound state. Molecular dynamics (MD) simulations, performed on VCA0625 structure in the apo and G6P bound states, revealed bi-lobal movements. Site directed mutagenesis followed by isothermal titration calorimetry on VCA0625 delineated the roles of different residues in ligand binding efficacy. We have further characterized the ATPase VCA0627 in terms of ATP binding and hydrolysis. Structure analysis coupled with MD simulation results, different biochemical assays modeling, docking and systematic sequence analysis indulged us to believe that VCA0625-27 is an atypical type-I ABC importer involved in G6P internalization in *V. cholerae* as well as in 27 other gram-negative bacteria involved in diverse functions.

* Corresponding author.
** Corresponding author. Macromolecular Crystallography Section, Beamline Development & Application Section, Bhabha Atomic Research Center, Trombay, Mumbai, 400085, India.
E-mail addresses: biplab@rrcat.gov.in (B. Ghosh), jhimli@sxccal.edu (J. Dasgupta).

https://doi.org/10.1016/j.bbrc.2024.150030
Received 18 April 2024; Accepted 28 April 2024
Available online 1 May 2024

2. Materials and methods

2.1. Cloning, site-directed-mutagenesis, overexpression, and purification

Genomic DNA of *V. cholerae* O395 strain was used as the template to amplify the region encoding VCA0625 (of 318 amino acids residues excluding signal-peptide of 1–26 residues; Accession code: A0A0H3AFK0), and full length VCA0627 of 351 residues (Accession code: A0A0H3ADT9). The amplicons of VCA0625 mutants were prepared using two step PCR method. Each amplicon was cloned in pET28a^{+} (Novagen) within *Nde1* and *BamH1* restriction sites. The clones were validated by restriction digestion analysis and commercial DNA sequencing. Proteins were overexpressed by IPTG in *E. coli* BL21 (DE3) cells as N-terminal 6×His-tagged recombinant proteins, as per protocol described in Dey et al. [7]. Briefly, the pellet was resuspended in ice-cold lysis buffer-L (50 mM Tris–HCl pH 8.0, 300 mM NaCl, 5 mM $MgCl_2$, 10% (v/v) glycerol) and lysed after adding PMSF (1 mM) and lysozyme (1 mg/ml). Proteins were purified by Ni^{+}-NTA (Qiagen) affinity chromatography with increasing concentration of imidazole. Imidazole was removed subsequently by buffer exchange through centrifugation. Removal of ligand from VCA0625 and its mutants were conducted through partial denaturation using 6 M urea followed by on-column refolding by washing with buffer with gradually reduced urea concentrations. The homogeneity of the purified proteins was judged in 10% SDS-PAGE.

2.2. Fluorescence quenching study

To monitor intrinsic fluorescence quenching of protein upon addition of ligand, experiments were performed in Hitachi F-7000 spectrofluorometer using quartz cuvettes of 1 cm path length at an excitation wavelength $\lambda_{ex} = 280$ nm and emission wavelength (λ_{em}) between 295 nm and 400 nm. All reactions were carried out at 298 K. The reactions were performed in buffer-L. Equilibrium titration of VCA0627 was carried out with AMP.PNP as ligand. In case of the mutants of VCA0625 and its mutants the ligand was G6P. For all experiments protein concentration was of 2.5 μM and ligand concentrations varied up to 2 mM. The binding stoichiometry was determined using the protocol described in Dey et al. [7].

Table 1
Data collection and refinement statistics of VCA0625 structure.

Data collection	
Beamline	PXBL21, RRCAT, Indore, India
Wavelength (Å)	0.979
Detector	MAR345
Oscillation (°)	1
Space group	$P2_12_12_1$
Unit cell parameters (Å/°)	a = 57.29, b = 63.31, c = 75.32 90,90,90
Resolution range (Å)	45.6–1.6
Number of reflections	35948
No. of molecules per asymmetric unit	1
Mathew's coefficient V_M ($Å^3$ Da^{-1})	1.90
Solvent content (%)	35.35
Completeness (%)	98.7 (86.7)[a]
Averaged I/σ(I)	19.8 (3.2)[a]
R_{merge} (%)	5.2 (39.0)[a]
Multiplicity	4.6 (4.0)
CC(1/2)	0.99 (0.85)
Refinement	
R_{work}/R_{free} (%)	17.2/21.01
No of atoms	
Protein	2462
ligand	16
Average B-factor (all atoms) ($Å^2$)	16.46
RMSD	
Bond lengths (Å)	0.007
bond angles (°)	0.95
Ramachandran statistics (%)	
Most favoured	98.7
Additionally allowed	1.9
Disallowed	0.3

[a] Numbers in parentheses are values for the highest-resolution bin.

2.3. Isothermal titration calorimetry

ITC experiments were performed using Nano ITC (TA Waters) at 25 °C by injecting ligand (G6P) loaded into the stirring syringe titrated against purified VCA0625 and its mutants, loaded into the sample cell. The reactions were monitored for binding study with injections of 2.5 μl each for 20 injections having 180 s of interval between them. The results were analyzed by the integration of the heat released relative to the amount of protein-ligand interaction and curve-fitting based on a 'independent binding model' for G6P, using the default TA-analytical software provided. Binding constants (K^d), Stoichiometry (N) and thermodynamic parameters [Enthalpy (ΔH) and Entropy (ΔS)] were referenced against runs performed with the ligands alone (ligand to buffer) as control for the heat of ligands solvation.

2.4. Malachite green assay

ATPase activity of purified VCA0627 was spectrophotometrically determined by measuring the release of inorganic phosphate (Pi) using malachite green assay as per protocol described before [7,8]. The final protein concentration of 2.5 μM. Each reaction mixture was incubated with ATP (Sigma Aldrich), of concentration ranging from 100 to 500 μM at 298 K. The ATP hydrolysis without protein was performed to nullify the effect of the contaminating inorganic phosphate with ATP.The Pi released by each reaction was calculated from the standard curve. Experiments were performed in triplicate.

2.5. Crystallization, diffraction data collection

Optimal diffraction quality crystals of VCA0625 were obtained in sitting drop vapor diffusion process with precipitant containing 0.1 M Phosphate-citrate pH 7.0, 40% (v/v) PEG 300 after 72 h incubation at 20 °C. Diffraction data on the cryo-cooled crystals were collected using MARCCD detector at PX-BL21 beamline at Indus-2 synchrotron, RRCAT, Indore [9].

2.6. Phasing and refinement

Molecular replacement (MR) calculations by Phaser-MR of PHENIX [10] with the ligand free coordinates of AfuA in G6P bound state (PDB code: 4R73) as search template, identified one molecule in the asymmetric unit. Further refinements were carried out using PHENIX [10]. 2Fo-Fc map calculated with the refined model was of good quality and overlaid well with the model. Electron density appeared in 2Fo-Fc map as well as positive density appeared in the Fo-Fc map (contoured at 3σ) at the ligand binding pocket confirmed presence of bound ligand. Model fitting was performed using Coot [11]. The coordinates of the refined structure of VCA0625 have been submitted to RCSB with PDB code: 8×1A.

2.7. MD simulation steps and parameters

We performed all-atom molecular dynamics simulations on both the bound and unbound structures of the VCA0625 using the AMBER-2022 suite at a temperature of 300 K. To accelerate the simulations, we used pmemd.cuda, a GPU-accelerated MD program within the AMBER suite [12], and cpptraj for analysis. The FF19SB force field [13] was used for the protein and the TIP3P force field [14] for water. Five independent 1 μs simulations were run for both the bound and unbound states in explicit waters. The protein was solvated in a truncated octahedron box

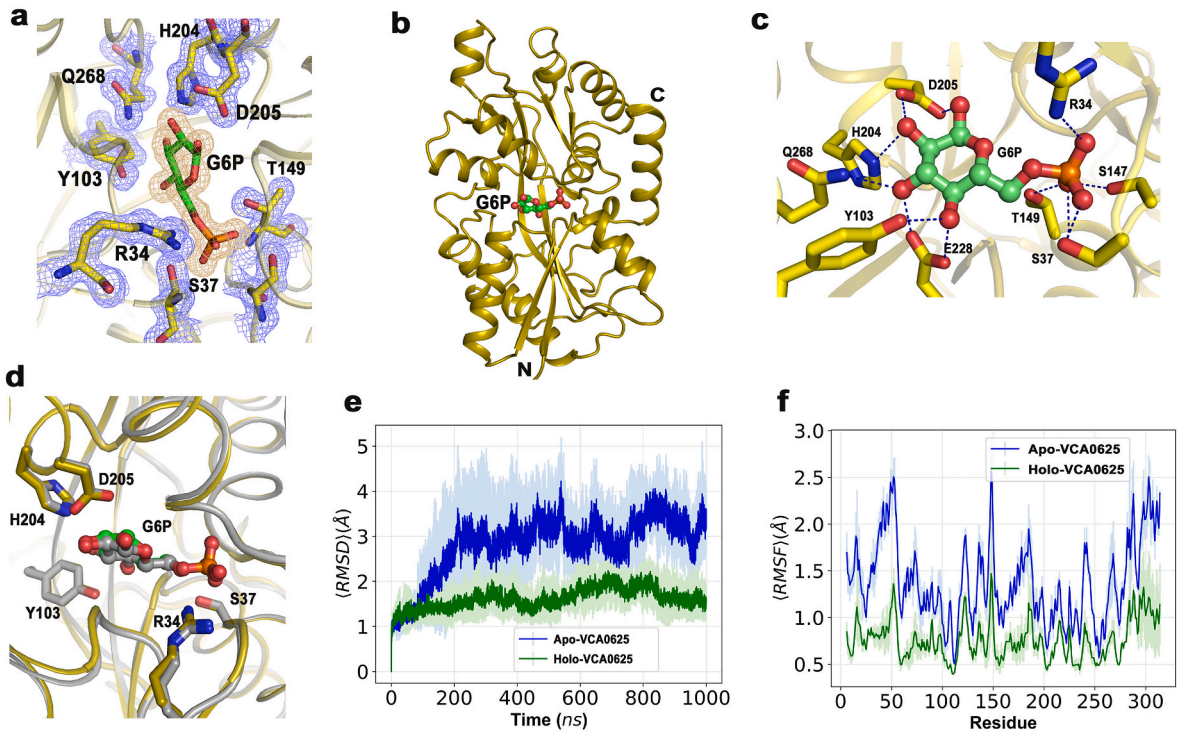

Fig. 1. (a) $2F_0$-Fc density map (contoured at 1σ) around G6P bound to VCA0625; (b) Ribbon diagrams of *V. cholerae* VCA0625 complexed with β-G6P; (c) Ligand binding region in solved crystal structure of VCA0625; (d) Superposition of G6P bound AfuA structure (PDB code: 4R73) (gray) on VCA0625 (gold). G6P is shown in ball and stick; (e) Plot of the RMSD values for the Cα atoms are shown for apo-VCA0625 (blue) and holo-VCA0625 (green) up to 1μs simulation range. (f) RMSF of the Cα atoms was calculated from the simulation trajectories. (For interpretation of the references to colour in this figure legend, the reader is referred to the Web version of this article.)

with periodic boundary conditions on all the three dimensions. The walls of the box were at least 10 Å away from the protein. Counter ions were added to achieve charge neutrality in the solvated system. To prevent steric clashes, we performed energy minimization for 2000 cycles, first using the steepest descent method followed by the conjugate gradient method. The temperature of the system was then equilibrated in the NVT ensemble and the pressure was brought to 1 atm by equilibrating in the NPT ensemble. The non-bonded interactions were calculated using a distance cut-off of 12 Å, and the time step for the integrator was 2 fs. The equilibration step was performed for 10 ns each in the NVT and NPT ensembles. Finally, the production run was performed in the NPT ensemble with the same parameters as the equilibration step. The Standard simulation protocol was followed as per protocol described before [8] and the RMSD and RMSF were calculated with respect to the first frame in the trajectory.

2.8. Software used for analysis

Software used for data analysis and presentations are Origin 8.5, PyMol (DeLano Scientific, Schrödinger, Inc., USA), UCSF Chimera 1.14, and Adobe photoshop CS3.

3. Results

3.1. Structure determination of the PLBP, VCA0625

X-ray diffraction data were collected up to 1.6 Å resolution from the crystals of VCA0625, in space group $P2_12_12_1$ (Table 1). BLASTp search with the sequence of VCA0625 identified the PLBP AfuA (of the ABC importer AfuABC, involved in hexose-6-Phosphate uptake from *A. pleuropneumoniae*) as nearest homolog with high identity of 72% for 321 amino acids excluding signal peptide. Despite that, MR calculations with the coordinates of AfuA in apo state (PDB code: 4R72) as search template failed miserably to produce distinct solutions. Interestingly, the coordinates, of AfuA in G6P bound state (PDB code: 4R73) produced clear-cut MR solution while used after removing the coordinates of bound ligand and waters from the search template. One molecule in the asymmetric unit produced R_{work} of 29.9% (R_{free} of 33.4%) (with RFZ = 25.9, TFZ = 39.0, and LLG = 2019). The continuous electron density (both in $2F_o$-F_c and F_o-F_c maps) identified in the ligand binding pocket was assigned as Glucose-6-Phospate bound during overexpression of protein in *E. coli*. (Fig. 1a). Further model building and refinements yielded final R_{work} of 17.2% and R_{free} of 21.01% respectively (PDB code: 8×1A). Data collections and refinement statistics are given in Table 1.

3.2. Interactions of G6P with VCA0625

Overall structure depicted that VCA0625 belongs to the class II/cluster-D PLBP with two globular α/β domains linked by a β-stranded hinge (Fig. 1b). G6P fits snugly in the ligand binding cleft of VCA0625 through hydrogen bonding interactions between the hydroxyl groups of the pyranose ring and the side chains of Y103, H204, D205, E228 and Q268 (Fig. 1c). The phosphate moiety of G6P is stabilized through hydrogen bonds with the side chains of R34, S37, S147, T149 as well as backbone NH groups of T149 and G184 (Fig. 1c). G6P complex superposed well on the G6P bound AfuA with root-mean-square deviations (RMSD) of 0.5 Å (Fig. 1d).

3.3. Dynamics of VCA0625 in free and in G6P bound states

MD simulation runs were carried out on VCA0625 in G6P bound and ligand free states to understand the dynamic nature of the molecule regarding ligand binding. RMSDs of the Cα atoms in apo and holo states of VCA0625 were calculated from the snapshots of the trajectories up to 1 μs, and were plotted (Fig. 1e). RMSD values converged well approximately within 70 ns. The RMSD values for the holo state remain steady

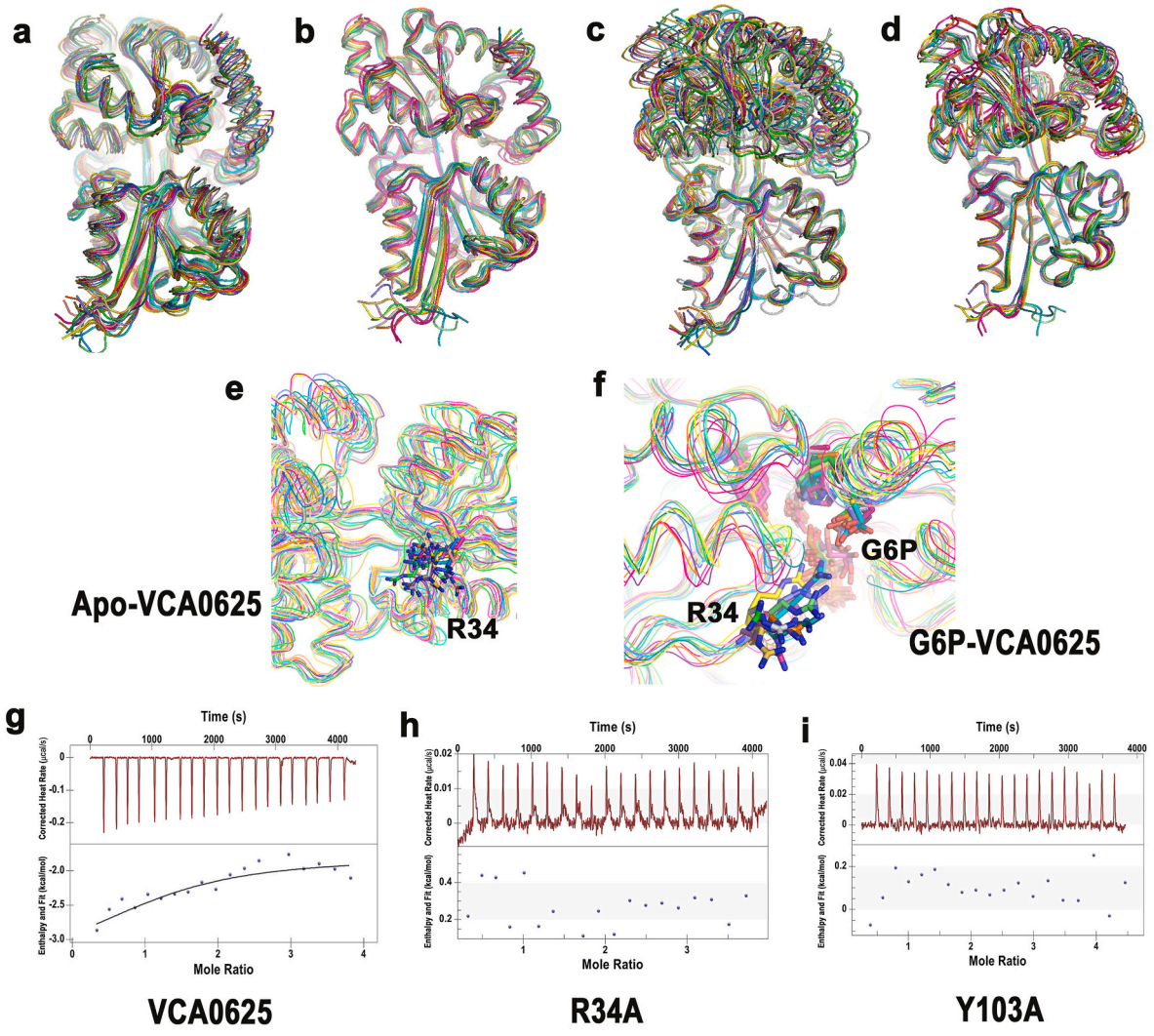

Fig. 2. (a–b) Superposition of the snapshots of overall MD trajectories (a) in apo VCA0625 and (b) holo VCA0625; (c–d) Snapshots aligned with respect to the N-lobe to shows the inter-domain movement for apo VCA0625 in (c) and G6P bound VCA0625 in (d); (e–f) Movement of R34 side chain during simulation in apo and G6P bound VCA0625; (g–i) Binding affinity studies by ITC to judge interaction of G6P with VCA0625, R34A, Y103A. VCA0625 showed significant binding with G6P resulting a K_d value of 17.45 ± 0.45 μM; Thermograms of R34A, Y103A indicated insignificant interaction.

around 1.5 to 2 Å, while in apo state, VCA0625 fluctuates more, ranging from 1 to 4.5 Å (Fig. 1e), indicating that VCA0625 gains stability upon G6P binding. Fig. 1f shows Root Mean Square Fluctuation (RMSF) values for the free and G6P bound VCA0625. Overall reductions in fluctuations after G6P binding are evident from the graphs. (Fig. 1f).

Superposition of the snapshots of apo and G6P bound VCA0625 delineated the two lobes, of VCA0625 execute both 'open to close' and swinging motions (Fig. 2a–d). Both motions are prevalent in the case of ligand-free VCA0625 (Fig. 2a, c) compared to its G6P bound counterpart (Fig. 2b, d).

Almost all interactions between G6P and VCA0625 remained preserved during dynamics. Interestingly, the side chain of R34 acquired multiple conformations, swinging from outside to inside of the binding pocket. In G6P-bound VCA0625, the distance between D205 and T11, located at the binding cleft, varied from 1.5 (57ns) to 6.27 Å (423ns). Upon proximity, they interacted with each other through H-bonding. However, this interaction is inversely related to interaction of R34 and G6P. Upon proximity of T11 and D205, the distance between R34 and G6P increased upto 14.08 Å (57ns) reflecting the 'closed' form. However, no such interaction between T11 and D205 or wide movement of R34 was observed in apo VCA0625.

3.4. Measurement of G6P binding efficacy to VCA0625 and its mutants

Binding of G6P with VCA0625 was monitored using ITC. Titration between VCA0625 and G6P was exothermic. Binding isotherm were fitted using the one site binding model. Titration confirmed binding between G6P and VCA0625 with dissociation constant K_d of 17.45 ± 0.45 μM, for n = 1, ΔH = - 1.63 kcal/mol (Fig. 2g). It was previously observed that [6] while mutation of the residues of AfuA, corresponding to S37 and T149 of VCA0625, caused reduced binding of G6P, binding was practically abolished upon mutations of the residues corresponding to H204, D205 and E228 of VCA0625 (Fig. 1c–d). Since interaction patterns of G6P with VCA0625 is largely like G6P-AfuA complex, we investigated the effect of Y103. Furthermore, structure and dynamics of VCA0625 indicated that R34 is an important residue presumably recognition and binding of G6P as well as regulating the opened and closed form. Therefore, we have checked the G6P binding with the mutant R34A. Interestingly, binding was impaired in R34A and Y103A (Fig. 2h–i).

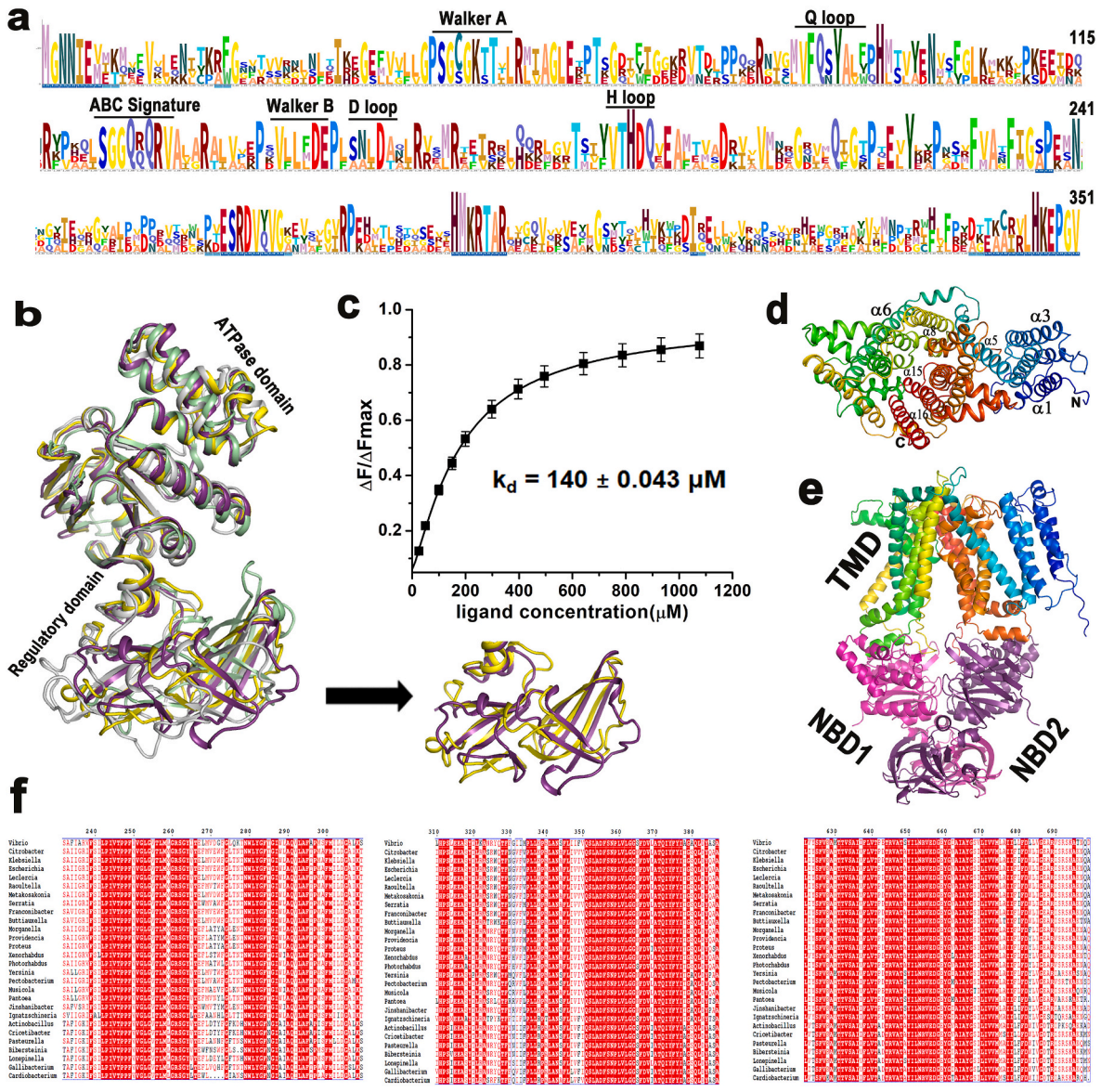

Fig. 3. (a) Consensus sequence logo generated (using Skylign followed by ClustalW alignment) from VCA0627 of *V. cholerae* and nearest structural homologs; (b) The overall superposition of CysA, PH0022, MalK, on model of VCA0627, whereas substantial similarities were observed between regulatory domains of PH0022 and VCA0627 (right panel); (c) Intrinsic fluorescence quenching of VCA0627 with λ_{ex}=280 nm, λ_{em}=295–400 nm produced a plots of $\Delta F/\Delta F_{max}$ against AMP.PNP (μM); (d, e) The models of VCA0626 and VCA0626-27 assembly. Arrangements of transmembrane helices in atypical VCA0626 model is shown from the periplasmic side in (d); (f) Multiple sequence alignment of VCA0626 and similar transmembrane proteins of 27 gram-negative bacteria showed strict sequence conservation. Residue numbering is as per VCA0626 of *V. cholerae*.

3.5. Characterization of VCA0627 through sequence analysis, modelling and AMP.PNP binding

To find out the nearest structural homolog of VCA0627, we performed BLASTP search against PDB with amino acid sequence of VCA0627 (Accession code: A0A0H3ADT9). VCA0627 showed 41% identity with CysA, the NBD of ABC-type sulfate importer from *Alicyclobacillus acidocaldarius* (PDB code: 1Z47) [15], 49% identity with PH0022, NBD of the multisugar transporter from *Pyrococcus horikoshii* (PDB code: 1VCI) [16], and 44% identity with MalK, the NBD of the maltose transporter from *E. coli* (PDB code: 1Q12) [17]. CysA, PH0022, MalK belong to type-I importer and consist of an ATPase and a regulatory domain. Sequence alignment of VCA0627 with these NBDs indicated that the ATPase domain is primarily conserved. ATPase of VCA0627 contains several conserved functional motifs such as Walker-A (WA), Walker-B (WB) motifs, an ABC transporter-specific or 'signature' motif, Q-loop, D-loop and H-loop (Fig. 3a). Interestingly, substantial variations are observed in the regulatory domains of these NBDs (Fig. 3a). Overall superposition of PH0022 on Alphafold [18] generated model of VCA0627 produced RMSD of 1.23 Å, while the other two NBDs have shown significantly high RMSD values (3.2 Å for CysA and 3.4 Å with MalK). However, the superposition of these structures only on the ATPase domain of VCA0627 produced RMSDs of 0.96 Å, 1.2 Å, and 1.45 Å for PH0022, CysA, MalK respectively (Fig. 3b), implying that these differs primarily in the structure of regulatory domain. Although the β-strands of the regulatory domains of CysA and MalK are significantly different from VCA0627, they match substantially between PH0022 and VCA0627 (Fig. 3a).

Since ATP binding motifs of VCA0627 were found to be mostly conserved, we performed binding assays between VCA0627 and ATP analog AMP.PNP by measuring intrinsic fluorescence quenching (Fig. 3c). Intrinsic fluorescence quenching with λ_{ex}=280 nm,

λ_{em}=295–400 nm produced apparent K_d value of 140 ± 0.043 μM, indicating weak binding between VCA0627 and AMP.PNP (Fig. 3c,S1). However, no ATP hydrolysis by VCA0627 was observed during Malachite green assay (Fig. S4).

3.6. VCA0626 is an atypical fused monomeric permease

The permease VCA0626 (Accession code: A0A0H3AFF4) is found to be a fused monomer with 1–700 amino acids. No structure of such fused permease has been determined yet. Sequence similarity searches against PDB gave unsatisfactory results with very low sequence identity with other structurally characterized homodimer and heterodimer permeases of ABC type-I transporters. Interestingly, Alphafold [18] generated model of VCA0626 grossly resembles the structure of the heterodimeric permease MalFG in pre-translocation state [19], that belongs to MBP-Maltose transporter complex MalFGK-E (PDB code: 3PV0). N-terminal region of VCA0626 forms a four-helix bundle that apparently stays away from the transport channel (Fig. 3d). The other helices are involved in forming translocation channel (Fig. 3d). Since VCA0626 model matches with MalFG in pre-translocation state, we prepared an assembly model made of VCA0626 and the dimer of VCA0627 through structure-based docking (Fig. 3e). In MalFGK, the L-loop of MalFG interacts with NBD, MalK. Interestingly, during structure-based docking, two L-loops of VCA0626 containing 'EAS' motifs such as ^{316}EAS^{318} and ^{593}EAS^{595} were found to fit with the two monomers of VCA0627 (Fig. 3e, S2).

Our BLASTp search identified similar monomeric permeases in 27 other gram-negative bacteria. Sequence comparisons revealed that residue 240 onward the helices that are located in the transportation channel, or in the regions that interact with PLBP and NBD dimer are highly conserved (Fig. 3f,S2). Interestingly, corresponding NBDs of these organisms also showed high degree of sequence identity specially in ATPase domain while the regulatory domains (RD) are relatively less conserved.

4. Discussion

Usually, in bacteria, type-I importers internalize metabolites like sugars, amino acids, and peptides or osmoprotectants where type-II importers import micronutrients, such as vitamin B12 (cobalamin), metal chelates, or heme. Differences between these two kinds of importers are based not only on their nutrients but also on their structural characteristics [2]. Our current study helped to gain insights into the hitherto unknown structure function of VCA0625-27 of *V. cholerae*. Crystal structure of the PLBP VCA0625 revealed that G6P binds efficiently to VCA0625 through polar interactions during its overexpression in *E. coli* cells (Fig. 1c). The structure and binding mode resemble with that of AfuA, the sugar phosphate importer of *A. pleuropneumoniae*. MD simulations further delineated that an 'open to close', as well as swinging motion occur between the lobes of VCA0625, the dimension of which reduces upon ligand binding. R34 located at the gate plays a pivotal role in 'open to close' movement.

The NBD, VCA0627 depicts considerable sequence identities with the other type-I importers. Type-II NBD dimers bind and hydrolyze ATP even in the absence of permeases [8]. In contrast, type-I NBDs are functional only in the presence of permeases and PLBPs. Although VCA0627 contains all required motifs for ATP binding and hydrolysis, it showed weak ATP binding and no ATPase activity. Non-functionality of VCA0627 in the absence of VCA0625 and VCA0626 further establishes VCA0625-27 as type-I importer.

Despite VCA0626 is a fused monomeric permease, its model structure matches grossly the inward facing structure of hetero dimeric MalFG of maltose transporter MalFGK-E [19]. In general, the type-I importers contain fewer transmembrane helices compared to type-II [2]. Type-I dimeric (homo or hetero) importers usually contain 5-6 helices per monomer, and therefore having around 12 helices in the assembly. VCA0626 contains 12 helices which constitute the transport channel, as well as PLBP and NBD binding sites. However, the homo or heterodimeric permeases often contain an extension in the periplasmic region to recognize and interact with PLBP. Instead, Alphafold [18] has predicted (with high confidence level) a four-helix bundle at the N-terminus of VCA0626 that apparently stays away from transportation channel (Fig. 3d–e).

As observed before [20], ATP hydrolysis driven conformational changes propagate through the L-loop containing 'EAS' motif of the permease. Interestingly, the two L-loops of VCA0626 having 'EAS' motifs fit with the two monomers of VCA0627 to transmit ATPase induced conformational changes (Fig. 3e). Considering aforesaid observations, we hypothesize that VCA0625-27 of *V. cholerae* is an atypical type-I sugar phosphate importer of unique architecture. Stunning sequence identities of VCA0626 and VCA0627 with 27 other gram-negative bacteria including AfuB of *A. pleuropneumoniae*, indulge us to anticipate similar G6P import mechanisms in these organisms as well (Figs. S2,S3). We envisage that experimental structure of the assembly made of VCA0626 and VCA0627, along with revelation of the role of regulatory domain of VCA0627 in future will provide major breakthrough in the area of ABC importers that control metabolic and other important cellular processes in bacteria.

CRediT authorship contribution statement

Indrila Saha: Data curation, Formal analysis, Investigation. **Biplab Ghosh:** Data curation, Formal analysis, Writing – review & editing. **Jhimli Dasgupta:** Conceptualization, Project administration, Supervision, Writing – original draft, Writing – review & editing.

Declaration of competing interest

The authors declare that they have no known competing financial interests or personal relationships that could have appeared to influence the work reported in this paper.

Acknowledgements

We are grateful to Rev. Dr. Dominic Savio, SJ, Principal, St. Xavier's College, Kolkata, for his constant support and encouragement. We are thankful to Prof. Udayaditya Sen of SINP, Kolkata, India for his support and advice. IS is thankful to her lab mates for their support. We acknowledge DST Grant No. SR/FST/COLLEGE-014/2010(C), WBDBT BOOST Grant No. 335/WBBDC/1P-2/2013 and DBT BUILDER Grant No. BT/INF/22/SP41296/2020 for infrastructural support.

Appendix A. Supplementary data

Supplementary data to this article can be found online at https://doi.org/10.1016/j.bbrc.2024.150030.

References

[1] M.L. Oldham, A.L. Davidson, J. Chen, Structural insights into ABC transporter mechanism, Curr. Opin. Struct. Biol. 18 (2008) 726–733, https://doi.org/10.1016/j.sbi.2008.09.007.
[2] A.J. Rice, A. Park, H.W. Pinkett, Diversity in ABC transporters: type I, II and III importers, Crit. Rev. Biochem. Mol. Biol. 49 (2014) 426–437, https://doi.org/10.3109/10409238.2014.953626.
[3] Y. Liu, B. Liu, T. Xu, Q. Wang, W. Li, J. Wu, X. Zheng, B. Liu, R. Liu, X. Liu, X. Guo, L. Feng, L. Wang, A fructose/H+ symporter controlled by a LacI-type regulator promotes survival of pandemic Vibrio cholerae in seawater, Nat. Commun. 12 (2021) 4649, https://doi.org/10.1038/s41467-021-24971-3.
[4] E. McDonough, H. Kamp, A. Camilli, *vibrio cholerae* phosphatases required for the utilization of nucleotides and extracellular DNA as phosphate sources, Mol. Microbiol. 99 (2016) 453–469, https://doi.org/10.1111/mmi.13128.
[5] M. Moisi, S. Lichtenegger, S. Tutz, A. Seper, S. Schild, J. Reidl, Characterizing the hexose-6-phosphate transport system of Vibrio cholerae, a utilization system for carbon and phosphate sources, J. Bacteriol. 195 (2013) 1800–1808, https://doi.org/10.1128/JB.01952-12.

[6] B. Sit, S.M. Crowley, K. Bhullar, C.C.-L. Lai, C. Tang, Y. Hooda, C. Calmettes, H. Khambati, C. Ma, J.H. Brumell, A.B. Schryvers, B.A. Vallance, T.F. Moraes, Active transport of phosphorylated carbohydrates promotes intestinal colonization and transmission of a bacterial pathogen, PLoS Pathog. 11 (2015) e1005107, https://doi.org/10.1371/journal.ppat.1005107.

[7] S. Dey, M. Biswas, U. Sen, J. Dasgupta, Unique ATPase site architecture triggers cis-mediated synchronized ATP binding in heptameric AAA+-ATPase domain of flagellar regulatory protein FlrC, J. Biol. Chem. 290 (2015) 8734–8747, https://doi.org/10.1074/jbc.M114.611434.

[8] I. Saha, S. Chakraborty, S. Agarwal, P. Mukherjee, B. Ghosh, J. Dasgupta, Mechanistic insights of ABC importer HutCD involved in heme internalization by Vibrio cholerae, Sci. Rep. 12 (2022) 7152, https://doi.org/10.1038/s41598-022-11213-9.

[9] A. Kumar, B. Ghosh, H.K. Poswal, K.K. Pandey, Jagannath, M.V. Hosur, A. Dwivedi, R.D. Makde, S.M. Sharma, Protein crystallography beamline (PX-BL21) at Indus-2 synchrotron, J. Synchrotron Radiat. 23 (2016) 629–634, https://doi.org/10.1107/S160057751600076X.

[10] P.D. Adams, P.V. Afonine, G. Bunkóczi, V.B. Chen, I.W. Davis, N. Echols, J. J. Headd, L.-W. Hung, G.J. Kapral, R.W. Grosse-Kunstleve, A.J. McCoy, N. W. Moriarty, R. Oeffner, R.J. Read, D.C. Richardson, J.S. Richardson, T. C. Terwilliger, P.H. Zwart, Phenix : a comprehensive Python-based system for macromolecular structure solution, Acta Crystallogr. Sect. D Biol. Crystallogr. 66 (2010) 213–221, https://doi.org/10.1107/S0907444909052925.

[11] P. Emsley, K. Cowtan, Coot : model-building tools for molecular graphics, Acta Crystallogr. Sect. D Biol. Crystallogr. 60 (2004) 2126–2132, https://doi.org/10.1107/S0907444904019158.

[12] R. Salomon-Ferrer, A.W. Götz, D. Poole, S. Le Grand, R.C. Walker, Routine microsecond molecular dynamics simulations with AMBER on GPUs. 2. Explicit solvent particle mesh ewald, J. Chem. Theor. Comput. 9 (2013) 3878–3888, https://doi.org/10.1021/ct400314y.

[13] C. Tian, K. Kasavajhala, K.A.A. Belfon, L. Raguette, H. Huang, A.N. Migues, J. Bickel, Y. Wang, J. Pincay, Q. Wu, C. Simmerling, ff19SB: amino-acid-specific protein backbone parameters trained against quantum mechanics energy surfaces in solution, J. Chem. Theor. Comput. 16 (2020) 528–552, https://doi.org/10.1021/acs.jctc.9b00591.

[14] D.J. Price, C.L. Brooks, A modified TIP3P water potential for simulation with Ewald summation, J. Chem. Phys. 121 (2004) 10096–10103, https://doi.org/10.1063/1.1808117.

[15] F. Scheffel, U. Demmer, E. Warkentin, A. Hülsmann, E. Schneider, U. Ermler, Structure of the ATPase subunit CysA of the putative sulfate ATP-binding cassette (ABC) transporter from Alicyclobacillus acidocaldarius, FEBS Lett. 579 (2005) 2953–2958, https://doi.org/10.1016/j.febslet.2005.04.017.

[16] T. Ose, T. Fujie, M. Yao, N. Watanabe, I. Tanaka, Crystal structure of the ATP-binding cassette of multisugar transporter from Pyrococcus horikoshii OT3, Proteins: Struct., Funct., Bioinf. 57 (2004) 635–638, https://doi.org/10.1002/prot.20206.

[17] J. Chen, G. Lu, J. Lin, A.L. Davidson, F.A. Quiocho, A tweezers-like motion of the ATP-binding cassette dimer in an ABC transport cycle, Mol. Cell. 12 (2003) 651–661, https://doi.org/10.1016/j.molcel.2003.08.004.

[18] J. Jumper, R. Evans, A. Pritzel, T. Green, M. Figurnov, O. Ronneberger, K. Tunyasuvunakool, R. Bates, A. Žídek, A. Potapenko, A. Bridgland, C. Meyer, S.A. A. Kohl, A.J. Ballard, A. Cowie, B. Romera-Paredes, S. Nikolov, R. Jain, J. Adler, T. Back, S. Petersen, D. Reiman, E. Clancy, M. Zielinski, M. Steinegger, M. Pacholska, T. Berghammer, S. Bodenstein, D. Silver, O. Vinyals, A.W. Senior, K. Kavukcuoglu, P. Kohli, D. Hassabis, Highly accurate protein structure prediction with AlphaFold, Nature 596 (2021) 583–589, https://doi.org/10.1038/s41586-021-03819-2.

[19] M.L. Oldham, D. Khare, F.A. Quiocho, A.L. Davidson, J. Chen, Crystal structure of a catalytic intermediate of the maltose transporter, Nature 450 (2007) 515–521, https://doi.org/10.1038/nature06264.

[20] J. Weng, K. Fan, W. Wang, The conformational transition pathways of ATP-binding cassette transporter BtuCD revealed by targeted molecular dynamics simulation, PLoS One 7 (2012) e30465, https://doi.org/10.1371/journal.pone.0030465.